NANOTECHNOLOGY: NOVEL FLUORESCENT NANOCONSTRUCTS FOR EARLY DIAGNOSIS, THERAPY AND SENSING

LAKSHMI. V. NAIR

PHD THESIS

2016

SREE CHITRA TIRUNAL INSTITUTE FOR

MEDICAL SCIENCES AND TECHNOLOGY, TRIVANDRUM

Thiruvananthapuram

NANOTECHNOLOGY: NOVEL FLUORESCENT NANOCONSTRUCTS FOR EARLY DIAGNOSIS, THERAPY AND SENSING

A THESIS PRESENTED BY

LAKSHMI. V. NAIR

TO

SREE CHITRA TIRUNAL INSTITUTE FOR

MEDICAL SCIENCES AND TECHNOLOGY, TRIVANDRUM

Thiruvananthapuram

IN PARTIAL FULFILMENT OF THE REQUIREMENTS

FOR THE AWARD OF

DOCTOR OF PHILOSOPHY

2016

DECLARATION

I, Lakshmi. V. Nair, hereby certify that I had personally carried out the work depicted in the thesis entitled, **"Nanotechnology: Novel Fluorescent Nanoconstructs for Early Diagnosis, Therapy and Sensing",** except where due acknowledgment has been made in the text. No part of the thesis has been submitted for the award of any other degree or diploma prior to this date.

Date: 18.02.2016

Lakshmi. V. Nair
Reg.No:2011/PhD/01

SREE CHITRA TIRUNAL INSTITUTE FOR MEDICAL SCIENCES & TECHNOLOGY, TRIVANDRUM

Thiruvananthapuram – 695011, INDIA
(An Institute of National Importance under Govt. of India)
Phone-(91)0471-2520248 Fax-(91)0471-2341814
Email: jayasree@sctimst.ac.in Web site – www.sctimst.ac.in

Dr. R. S. Jayasree

Biophotonics and Imaging Laboratory

BMT Wing, SCTIMST

This is to certify that **Ms. Lakshmi. V. Nair**, in the Biophotonics and Imaging Laboratory of this Institute has fulfilled the requirements prescribed for the PhD. degree of the Sree Chitra Tirunal Institute for Medical Sciences and Technology, Thiruvananthapuram. The thesis entitled, **"Nanotechnology: Novel Fluorescent Nanoconstructs for Early Diagnosis, Therapy and Sensing"**was carried out under my direct supervision. No part of the thesis was submitted for the award of any degree or diploma prior to this date.

*Clearance was obtained from the Institutional Ethics Committee/ Institutional Animal Ethics Committee for carrying out the study.

Date:18.02.2016

Dr. R.S. Jayasree

(Research Supervisor)

The thesis entitled

"NANOTECHNOLOGY: NOVEL FLUORESCENT NANOCONSTRUCTS FOR EARLY DIAGNOSIS, THERAPY AND SENSING"

Submitted by

Lakshmi. V. Nair

for the degree of

Doctor of Philosophy

Of

SREE CHITRA TIRUNAL INSTITUTE
FOR MEDICAL SCIENCES AND TECHNOLOGY,
TRIVANDRUM

Is evaluated and approved by

…… ……..

Dedicated to my
Parents and teachers

ACKNOWLEDGEMENT

I express my sincere gratitude to my research guide Dr. R. S. Jayasree for the continuous support, encouragement and invaluable suggestions during the entire course of my work. I am thankful to her for all the moral support and help she has given to me throughout my days in the lab. I appreciate her immense contributions of novel ideas to make my Ph.D. experience productive and stimulating.

I owe my sincere gratitude to The Director of our institute and Head BMT Wing for the fellowship and all the facilities provided during the course of my work. I extend my thanks to Deputy Registrar, Associate Dean for PhD affairs, Dean and all members of academic division and Director's office for their support and help.

I thank my doctoral advisory committee members Dr. K. Sreenivasan, Dr. T. Anoop Kumar and Dr. C.P. Sharma for the valuable suggestions and critical comments. I also thank them for extending their laboratory facilities for my study.

I am grateful to Prof. A. Ajayaghosh, CSIR-NIIST TVM for his valuable time and contributions to my studies and allowing me to use his laboratory facilities.

I thank Prof. Sakti Kumar and Prof. Toru Maekawa of Bio-Nano Electronics Research Center, Toyo University, Japan for providing me the facilities and help for my study as a part of the Indo-Japan project.

I gratefully acknowledge Dr. T.V. Kumary for giving me training in cell culture studies and providing the lab facility for cell culture studies. The help from all the members of Tissue Culture lab is acknowledged.

I also thank Dr. M. R. Rekha for her sincere support and encouragement during my cell culture studies and animal experiments. I am grateful to Dr. Prabha D. Nair for permitting me to use the fluorescence spectroscopy and fluorescence microscopy facility of DTRT for my studies. I thank Dr. Annie John and Ms. Susan Mani (TEM lab BMT Wing) and Mr.Kiran, NIIST for TEM studies. I thank Mrs.Viji, NIIST for helping me with MALDI analysis. I thank Dr. T.V. Anilkumar for the training in

confocal microscope and the help in histopathological analysis. I extent my sincere thanks to Dr. V. Kalyanakrishnan, Dr. Lissy K. Krishnan and Dr. Roy Joseph for their inspiration, constant support and laboratory help throughout my stay in SCTIMST. I extent my gratitude to Dr. Sachin J. Shenoy (DIMT) and Dr.Hari Krishnan and all members DLAS for their help in the animal experiments.

I thank Mr. Vijayan, Mr. Nishad, Mr. Sreekanth, Mr. Suresh, Dr. Manoj Komath of Bioceramic lab, Dr. C. Radhakumary, Mr. Rowsen Mosses, Mr. P. R. Hari, Dr. Gopu of laboratory for polymer analysis, Mr. Vinod, Mrs. Usha Vasudev, Mr. Tilak of tissue culture, Dr. Renjith P. Nair, Mrs Tara, MrRenjith Kartha, Mrs. Priyanka of thrombosis research lab for all their timely support and help during the entire course of the work. I gratefully acknowledge their understanding, patience and friendship that helped me a lot during my research work. I extended my thanks to Mr. Arun Anirudhan for all the software related assistance.

My sincere thanks also go to former and present fellow Mrs. Arya Saraswathy, Mr. Shiju, Mrs. Nimi, Ms. Nimmi Francis, Ms. Madhumol. Mrs. Aneesha, Ms. Parvathy, Ms. Hema, Ms. Nisha of Biophotonics and Imaging Lab and Dr.Vidya, Dr.Manju, Dr. Sonia, Ms. Susan, Ms. Radhika , Dr. Durgadas, Mr. Arun, Mr. Rejin, Mr. Satheesh, Mr. Sunil for all the help, support and encouragement. I am grateful to all the members of photochemistry NIIST TVM for their help, friendship and support. I also thank all my friends in Toyo University for the help and support during my stay in Japan. I also thank all staff of BMT Wing, who directly or indirectly helped me for my PhD program. The help from accounts, store and library is greatly acknowledged. I also thank the security staff for their kind support.

I owe my deep sense of gratitude and regards to my parents and sister for their prayers, affection, patience and support, which smoothly paved my path towards the successful completion of the work. I thank God Almighty for standing with me in all the stages of my life.

Lakshmi V Nair

Contents

List of Figures

List of Tables

Abbreviations

AuC	Gold Quantum/ Nano Cluster
NIR	Near Infra Red
BBB	Blood Brain Barrier
NCD	Non Communicable Disease
CT	Computer Tomography
MRI	Magnetic Resonance Imaging
PTT	Photothermal Therapy
PDT	Photodynamic Therapy
PS	Photosensitizer
GSH	Glutathione
MSA	Mercaptosuccinic acid
GMSA	Gold nanoparticle with MSA
LA	Lipoic acid
FA	Folic acid
PPIX	Protoporphyrin IX
HMDA	Hexamethylene diamine
DPBF	1,3-diphenylisobenzofuran
GAuC	Glutathione stabilized AuC
LAuC	Lipoic acid stabilized AuC
Urease@GAuC	Urease immobilized GAuC
FLAuC	Folic acid conjugated LAuC
PFLAuC	Porphyrin conjugated FLAuC
LAT	Large Amino acid Transport

CNT	Carbon nanotube
SWCNT	Single Wall Carbon Nanotube
Qd	Quantum dot
Qd@CNT	Qd conjugated SWCNT
FaQd@CNT	Folic acid conjugated Qd@CNT
QY	Quantum Yield
SPR	Surface Plasmon Resonance
FT-IR	Fourier Transform Infrared
TEM	Transmission Electron Microscopy
SEM	Scanning Electron Microscopy
XRD	X-ray diffraction
XPS	X-ray photoelectron Spectroscopy
MALDI	Matrix Assisted Laser Desorption Ionization

SYNOPSIS

The interdisciplinary branch of science viz “nanoscience” has many applications in the day-to-day life of mankind spanning almost all fields. Among these, nanobiotechnology and nanomedicine is the emerging branch of science contributed from multiple scientific areas. This comparatively new branch of science and technology opens a wide door to address many problems that remained unsolved in various fields of life, not only for human beings but for other living organisms also.

Timely and accurate disease diagnosis, and sensing or identification of analytes or disease markers is the most important factors for the proper management of any disease. Bio molecules and minerals present in the body play a vital role in the overall activity of the body. For example, urea is a bi product formed in the kidney and liver and is excreted through the urine or sweat. The high level of urea present in the blood is an indications for renal and liver failures. Similarly, glucose, creatinine, lipids, salts and many minerals play important roles in the proper functioning of an organism. Any mismatch from the normal level affects the routine functioning of the system that can even lead to death, in more dangerous situation.

Cancer and brain diseases are the concern of modern world in one way or the other. Cancer is the leading cause of death in developed countries and brain related diseases face threat due to the changes in the socio economic life style. According to WHO the death due to cancer is increasing tremendously. Main challenge with cancer diagnosis is the inadequacy of the current diagnostic tools to identify them at an early stage. In the case of brain disease, blood brain barrier (BBB), which is an interface between blood and brain restricts the entry of contrast agents and drugs

posing hurdles in the diagnosis and therapy. Changes that take place in the brain during the disease progression are still not explored completely. In this thesis, an attempt is made to support the continued efforts by the scientific community to address the above mentioned challenges. For this, novel nano systems have been designed to enable early detection of disease markers from body fluids, early diagnosis of cancer and brain diseases using these imaging probes and therapy.

The synopsis includes chapters that give an introduction to the topic, an extensive review of literature on the concerned topics, methodologies adopted for the different studies, results of these studies and the discussion based on the major findings.

The first chapter provides the introduction of the topic of research and the second chapter describes literature review on the major research publications with appropriate citations. Rest of the thesis is divided into five parts. The first part of this thesis explains the synthesis of NIR emitting gold quantum cluster (AuC) using glutathione (GSH) and lipoic acid (LA) by varying the reaction conditions. NIR emitting nanoparticle has got wide attention in biomedical field due to the favorable optical and biocompatible properties. The main objective of this part of the thesis is the synthesis and optimization of NIR emitting AuC whose emission property will be utilized for the imaging applications along with additional molecule for targeting and therapeutic potential. AuC with distinct fluorescence property were developed using GSH for evaluating their structural and physical properties. By the etching of gold nanoparticle with glutathione, three different Au_{33} clusters and one Au_8 cluster were prepared. These clusters having size in the range 0.7 to 2 nm were synthesized

by changing reaction temperature from 0^{o}C to 70^{o}C and pH between 1.5 and 10. Self-assembly of atoms with different geometrical arrangement was evident in the TEM images of three clusters. MALDI-MS and XPS studies supported this finding. Properties of these clusters indicate that the self-assembly of atoms and its arrangement is an important factor in determining their characteristics. Similarly a second AuC using lipoic acid (LAuC- λ_{em} = 720 nm) with 18 atoms and a size of 1.4 nm were developed. Both batches of clusters showed X- ray and optical imaging capability.

The main objective of the second part of this thesis is the designing of AuC (glutathione stabilized AuC- GAuC) for model analyte sensing. For this, an NIR emitting (λ_{em} = 750 nm) nanobiosensor was developed by conjugating urease enzyme to GAuC (Urease@GAuC) for the selective detection of urea in whole blood. The detection is based on the fluorescence quenching of AuC in the presence of urea. The blood urea level estimated in whole blood and blood serum was comparable with the currently used clinical method for blood serum. This sensor could also detect urea in adulterated milk and hence has wide-range of applications. Since the detection is based on the change in the NIR emission associated with an enzyme specific conversion of urea leading to a pH induced aggregation of GAuC, the method does not interfere with other analytes.

Third part of the thesis highlight the development of a biocompatible gold cluster based multifunctional nanosystem for fluorescence imaging directed photodynamic therapeutic (PDT) applications. The main aim of this section is tumor diagnosis and targeted therapy using AuC. For this, NIR emitting LAuC based nanoplatform (λ_{em}

= 720 nm) were developed by incorporating folic acid (FA) and a photosensitizer (PS) which exhibited excellent tumor reduction upon laser irradiation. This system showed 80% triplet quantum yield when compared to that of the PS alone (63%). 60 µg of PS in GAuC is sufficient to kill 50% of cell population. PDT efficiency of this system has also been demonstrated *in vivo* in tumor-induced animals.The NIR emission of the nanocarrier also facilitated real time tracking of the progress of PDT, using live animal imaging system.

Fourth part of the thesis deals with the designing of AuC for BBB targeted brain imaging and drug delivery. L dopa conjugated AuC based BBB targeting nanocarrier is synthesized. NIR emission of AuC was retained after functionalization, enabling optical imaging. Time dependent *in vitro* studies for BBB permeability showed that 44% of Dop@GAuC crossed the *in vitro* barrier in 3h compared to 14 % of GAuC. The barrier potential remained in the normal level with in 30 min of particle incubation indicating the non distruption of BBB during the crossing of nanosystem. Live animal imaging study showed the particle internalization in the brain. Model drug delivery through BBB was demonstrated by the behavioural changes (changes in the behaviour like movement, tail stiffness, salivation, general activity etc) of the animal.

Fifth part deals with the use of hybrid nanosystem for imaging and targeted therapy. The main objective of this part is the development of a biocompatible hybrid nanomaterial using CdSe quantum dot (Qd) and single walled carbon nanotube (SWCNT) for targeted cellular imaging and therapy (Qd@CNT). FA conjugated hybrid system, FaQd@CNT, enables the selective targeting of the same inside the

cancer cell. The imaging capability of Qd and the therapeutic potential of SWCNT are available in a single system along with cancer targeting property. Heat generated by this system within 4 min laser irradiation was found to be high to facilitate cancer cell death. Specific photothermal destruction of cancer cells has been achieved with the developed FaQd@CNT compared to Qd@CNT hybrid nanosystem.

Last chapter of the thesis gives the overall summary and conclusion. The whole thesis is focused on the use of nanotechnology in the field of disease diagnosis, sensing of bio analyte and targeted distruction of the disease at its early stage using non toxic fluorescing nanocarriers. Moreover, nanoformulations for cancer and brain related diseases have been developed/ engineered without affecting normal cells.

CHAPTER 1

INTRODUCTION

The present era of scientific research has made significant attention on the applications of Nanoscience and Nanotechnology. This interdisciplinary area of science has got significance after the well celebrated talk of Richard P. Feynman (Nobel Laureate in physics-1965) *"There's plenty of Room at the Bottom",* in the annual meeting of American Physical Society at California Institute of Technology, on December 29th 1959. The talk focused on the miniaturization of materials, which may solve many scientific problems that exist. Nanoscience deals with the manipulation of materials of nanoscale size, creating various properties. The nanoscience to technology was developed later and the term was coined by Prof. Norio Taniguchi and Prof. K Eric Drexler, who discussed the applications of nanomaterials. One nanometer is one billionth, 10^{-9} of a meter. The well accepted definitions of nanomaterials are materials where the size of the individual building blocks is less than 100 nm. Nanomaterials may be zero dimensional (spherical nanoparticle), one dimensional (nanorod or nanotubes) or two dimensional (film or stack of thin film) in nature.

Usually chemistry synonyms the nanoscience as it deals with manipulation of material properties in atomic scale. Nanoparticles are number of atoms or molecules bonded together (these particles usually contain 10^6 atoms or less) and their size is intermediate between individual atoms and aggregates large enough to be called bulk

material (Ghosh and Pal, 2007). As nanoparticles are much larger than individual atoms and molecules but are smaller than bulk solid materials, their behavior is in between a macroscopic solid and an atomic or molecular system. As a consequence of reducing the size and the dimensionality of a material, its electronic properties change drastically as the density of states and the spatial length scale of the electronic motion are reduced with decreasing size. The energy eigen states of nanomaterials are determined by the boundary conditions of the systems, and therefore surface effects become very important. There are three major factors responsible for the drastic property change of these materials in comparison with their bulk counter parts

- High surface to volume ratio.
- Quantum size effect.
- Electrodynamics interaction.

1.1 Nanotechnology In Biomedical Field

Timely diagnosis of the diseases and their proper management is one of the major challenges in medical field. The use of nanoparticles for biological and biomedical applications include bio-imaging, single molecule tracking, bio sensing, drug delivery, gene delivery, transfection, and diagnosis. Engineered nanoparticle with proper functionalization can be used to accumulate in tumor cells using targeting ligands, providing a tool for cancer diagnosis and its treatment. Such sensor arrays have been developed to differentiate normal, cancerous, and metastatic cells by detecting the changes in the intrinsic properties of these materials. The interactions

and fate of a broad range of functionalized nanoparticles is currently under investigation. The needs of intracellular delivery depend on the mode of applications. For example, if the main requirement of a nanoparticles is for cancer cell targeting and killing, it should identify the cell and internalize independently of the ultimate localization. However, in the case of intracellular imaging and sensing, cell recognition is less important, whereas the ultimate intracellular localization of the nanomaterial is crucial and needs to be fully addressed. For any biomedical application, the developed nanomaterial should be non toxic in nature. It should retain its property once internalized into a cell or tissue (Lévy et al., 2010). A typical configuration for nanomaterial intended for biomedical application is shown in figure 1.

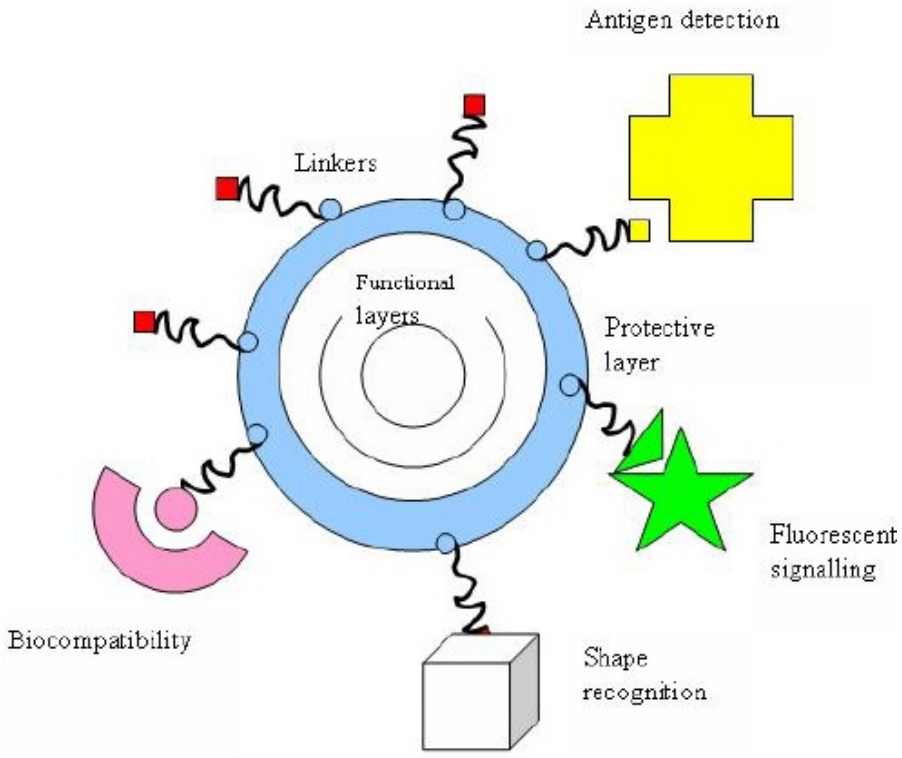

Figure 1: Typical configurations utilised in nano-bio materials applied to bio medical problems. Reprinted from (OV Salata, 2004)

1.1.1 Nanomaterials For Sensing, Imaging And Therapy

A sensor is a device capable of undergoing any change upon interaction with analytes of interest. Nanosensors are any biological, chemical, or surgical sensory system used to convey information about analyte to the macroscopic world. Main methods of manufacturing of these nano sensors are top down lithography, bottom up assembly and molecular self assembly (Alagarasi, 2015). The first working synthetic nano sensor was developed in Georgia Institute of technology using carbon nanotube for sensing the mass of the attached particle by measuring the vibrational frequency of the nanotube (Foster, 2006).

Early stage disease diagnosis can also be achieved by making use of nanotechnology. Nanotechnology is a field of applied science and technology, which controls matter on molecular level in scales within the 1-100 nm and the preparation of devices in that size range. Living organisms are built up of cells that are typically 10 μm across. However, the cell parts are much smaller and are in the sub-micron size domain. Proteins are even smaller than cells (typical size of 5 nm), which is comparable with the dimensions of smallest manmade nanoparticles. This simple size comparison gives an idea of using nanoparticles as very small probes that would allow to spy at the cellular machinery without introducing too much interference (OV Salata, 2004). Due to the above said reason nanomaterials will be an ideal option to reach in the diseased region without disturbing the overall functioning of the body.

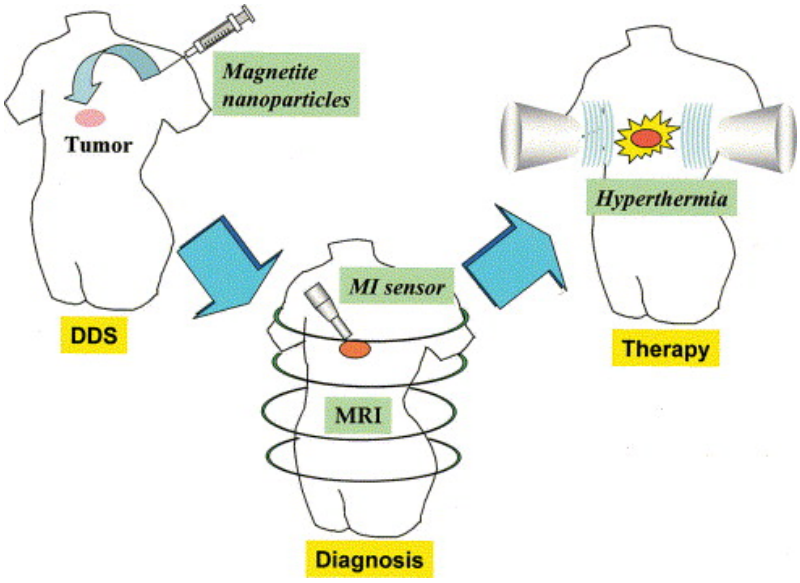

Figure 2: Schematic representation of magnetic nanoparticle mediated disease diagnosis and therapy.

Because of the properties offered by the nano particle in the size regime, the therapeutic efficacy offered by them is much higher than conventional treatment strategies. They have the ability to hide themselves from the immune system. As a result they can retain in the body for a longer period of time (Roy et al., 1999), (Peer et al., 2007). This allows the use of these materials for therapeutic purposes. For example, PEGylated gold nanorod in nu/nu mice treatment observed 57% tumor reduction (Dickerson et al., 2008). Similarly photosensitizer linked gold nanorod resulted in 79% reduction in photo dynamic therapy alone and 95% reduction in the combined therapy (Jang et al., 2011). Schematic illustration of nanomaterial mediated disease diagnosis and treatment is shown in figure 2.

1.1.2 Fluorescing Nano Materials

Fluorescing material is always a beneficial tool in various fields of biomedical application. This helps the surgeons for the direct visualization during surgery (fluorescence image guided surgery), and also during diagnosis. Use of conventional fluorescent materials suffers from toxicity, lesser solubility in the physiological media and its photo bleachability. This restricts its use in a broader range. Also, the

limitation due to auto-fluorescence and the inability of the light source to penetrate to the deeper tissue restricts the use of fluorescing material in clinical use.

The size dependent unique property offered by the nanomaterials allow to overcome the above said limitations to a great extent. Nanomaterials of different origin are (metallic, polymeric, semiconducting etc) available with different morphology (spherical, rod, star etc). Among them metallic and semiconducting materials got wide importance in biomedical field because of the size tunable optical property and nontoxicity (Eustis and El-Sayed, 2006).

They show unique optical, electronic, chemical and magnetic properties that are entirely different from that of their bulk materials. Colloidal solutions of metallic (Au, Ag, Cu etc) nanoparticles and quantum dots show characteristic color in visible light. For example, compared to bulk gold which has a yellow color caused by a reduction in reflectivity for light at the end of the spectrum, the colloidal gold shows a bright wine red color caused by the free surface electrons at the nanoparticle surface. Among the noble metals, gold has always attracted humans. Until the middle ages, the soluble gold was used to disclose fabulous curative powers for various diseases, such as venereal problems, dysentery, epilepsy, and tumors, and for diagnosis of syphilis (Daniel and Astruc, 2004). Thus, the remarkable features exhibited by colloidal gold have been utilized for centuries. Metallic quantum clusters with size of the order of few nanometers (0.1-2nm) are another class of metallic nano material which is having higher quantum yield in comparison with metallic nano materials. When the size of gold nanoparticles is reduced to the smaller length scale (< 2 nm), it shows quantum confinement, similar to quantum dot rather

than the SPR property (Shang and Nienhaus, 2012) (Xavier et al., 2012). Because of the non toxicity and higher quantum yield, metallic nano clusters will be a better substitute in biomedical application.

1.1.3. Hybrid Nanomaterials

Hybrid nanomaterials are one of the most promising classes of material, where more than one nanoparticle are incorporated to form a single system that can be used for different applications. Assembly of more than one nanostructured components with precise control over the size, shape, composition, and spatial orientation is desirable for the combination of different functionalities and also for advanced properties that can arise independent of the single-component materials (Sanchez et al., 2011) . A hybrid nanosystem made of magnetic iron oxide and semiconducting quantum dot shows the properties of both nano systems. Iron oxide fascilitate magnetic resonance imaging where as Qd provides optical imaging (Park et al., 2008). Engineering of multicomponent nanostructures with more than one nanoconstruct opens a new avenue in various fields by completely avoiding ligands with nanoparticles itself.

In a hybrid nanomaterial, surface chemical properties of the core nanoparticle can be modified by coating with another nanomaterial to provide improved colloidal stability or resistance to oxidation. Additional functionality may also be imparted to a hybrid nanoparticle by attaching an antibody, for example, to enable biological targeting.

1.2. Basic Concept Of Nano Sensor In Disease Diagnosis.

Bio molecules present in the body play a vital role in the overall activity of the body. For example, urea is a bi product formed in the kidney and liver which is excreted through urine or sweat. The high level of urea present in the blood clearly indicates the renal failure and liver failure chances. Similar to urea, glucose, creatinine, lipids, salts and minerals play important roles in the proper functioning of an organism. Any mismatch from the normal level will adversly affect the routine life and a significant variation is more dangerous situation where death can occur.

Different techniques and strategies are available for the detection of bio chemical parameters. But the main limitations of these techniques are its low selectivity and non specificity of the analyte of interest. The lowest detection limit of most of the systems is very high and the high cost of the detection of each analyte also restricts the people to perform the test at its early stage. As a result, most of these analytes were detected only in the late stage in developing and under developed countries.

Nanomaterials have attracted wide attention in the field of sensing because of their specific features that differ from bulk materials. The application of nanomaterials to the design of chemical sensors is nowadays one of the most active research fields because of their high reactivity, selectivity, small size and tremendous possibility to modify the surface for specificity. Major research are now focusing on chemical sensors utilizing electrochemical methods, including the individual single-walled carbon nanotube (SWNT)-based chemical sensors that are capable of detecting small concentrations of gas molecules. Boron-doped silicon nanowire nanosensors have been demonstrated to be capable of highly sensitive and selective detection of

biological and chemical species. Palladium mesowire arrays for the detection of hydrogen based upon the resistivity changes caused by structural changes in the wire itself has been tried (Luo et al., 2006).

Compared to electro chemical sensors, optical sensors are cheap and less time consuming. Nanomaterial based optical sensors are among the most important types of chemical sensors that have been studied in the recent past for the continuous, real time monitoring of diverse analytes. Depending on the origin of the optical signals, these sensors may be roughly classified into luminescence-based and absorbance-based sensors (Shi et al., 2004).

Most of the diseases and diseased conditions are associated with the elevated expression of certain biochemical parameters in the body. Proper identification of these bio chemicals at its early stage is very important as the treatment is more effective if detected at its initial stages. Moreover, in some diseased conditions continous monitoring of these biochemicals are demanded for the effective management of the condition. Because of the high reactivity, selectivity, sensitivity and very low limit of detection of nanomaterials help to identify them at its early stage. These sensors are fast, reliable and with low cost.

1.3. Basic Concept Of Cancer And Brain Diseases.

1.3.1. Cancer

Non communicable diseases (NCD) are the fast growing threats for developing and under-developed countries. According to WHO; diabetics, cardiovascular diseases, cancer, brain diseases etc. comes under NCDs. Among them cancer is the second leading cause of death in most of the developed and developing countries. There are mainly two types of tumors - benign and malignent. In which benign tumors are just

solid mass of cells of a specific origin which lack the capability to invade surrounding tissues (non metastatic). While malignant tumors invade the surrounding tissues and to the blood stream leading to secondary infections (metastatic). According to the latest report of WHO, once metastasis has occurred, the survival rate plummets to 23%.

Cancer is a class of diseases characterized by uncontrolled growth of abnormal cells. There are more than hundred distinct type of cancers, which can vary substantially in their behaviour and response to treatment. Cancer arises as a consequence of deregulated growth-controlling pathways, due to mutations or epigenetic alterations affecting gene coding for the protein components (Sadikovic et al., 2008).Various stages of tumor progressein is shown in figure 3.

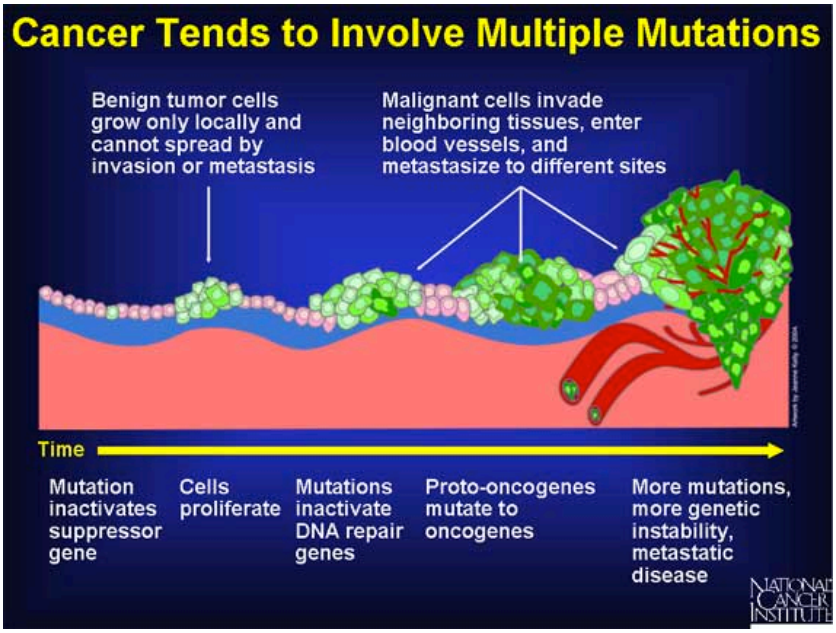

Figure 3: Schematic representation of tumor progression from a single cell to cancerous one. Reproduced from National Cancer Institute USA

1.3.2. Cancer Diagnosis And Nanotechnology.

For the proper management of any disease first we need to identify the disease. Different imaging modalities are used for the disease diagnosis in medical fields. The most commonly used imaging systems are X ray, CT, MRI, ultra sound, PET etc. These imaging techniques allow real-time visualization of living organisms and in few cases, the molecular interaction details, and, importantly, they are all non-invasive. These techniques help to diagnose diseases and give biological information and functions at preclinical stages.

Disease diagnosis using the above said imaging modalities require the administration of contrast agents for the better understanding of the diseases by the clinicians. Lack of efficient contrast agents and its non specific nature restricts the use of these imaging modalities. High cost and use of radiation induced side effect also restricts its use.

In comparison with the above said diagnostic tool, optical imaging posesses high spatial resolution and is cheap and less time consuming. It is harmless to the patients in all respects. But the main limitation of this technique is the auto fluorescence and inability of the light source to penetrate the tissue in the visible region.

Fluorescence probes suitable for imaging applications should meet the following requirements: (1) they should be non-toxic to cells and other organisms; (2) they should be smaller than the biomolecules of interest, so that normal biological functions such as biomolecular interactions are not disturbed; (3) they should have optimal photophysical properties including low photobleaching, absence of blinking, and high quantum yield; and, finally, (4) they should be simple to synthesize and use

for labelling biomolecules. Each of these attributes is essential for marker application in advanced imaging techniques aimed at unravelling the molecular details underlying biological processes (Fernández-Suárez and Ting, 2008)

But the main problem in cancer diagnosis is that most of the above said imaging modalities are not efficient in detecting tumors and metastatic cancer that are smaller than 0.5 cm and also they cannot distinguish between benign and malignant lesion.

Nanotechnology opens a new platform for disease diagnosis because of the inherent optical, magnetic and electrical properties imparted due to the extremely small size and quantum confinement of nanoparticles. The extremely smaller size allows it to escape from the immune system and because of the specificity towards the organ of interest allows the particle to accumulate in the desired organ. Enhanced absorption cross section and enhanced scattering cross section of metallic and semiconducting nanoparticles can be used for the imaging of target organ of interest, because of its inherent size dependent optical property. In comparison with conventional dyes, they are highly photostable.

1.3.3. Cancer Therapy And Nanotechnology.

Successful and accurate diagnosis of disease is the first step of disease management, which needs to be followed by proper therapy. From olden days heat therapy was widely used for treating diseases and the process is termed as hyperthermia. Heating of tissues to a temperature in the range of 41-47^{o}C using radiofrequency (RF), ultra sound and microwave for several minutes is called as hyperthermia. But conventionally used heating sources had the limitation of damaging of healthy tissue.

After the invention of LASER, its use came in therapeutic field due to the controlled and confined damage in the tumor cells. But the usage of very high output power (10- 100 watts) for a longer period of time for curing the disease restricts its use because of the chance of killing the normal tissues.

Chemotherapy is the most commonly used treatment strategy for cancer treatment. But the multi drug resistance of the body restricts its use after two or three doses. Most of the drugs are non-specific to cancer tissue and hence there is a chance of accumulation of these drugs in the normal tissues. Most adverse part of this therapy is the side effect associated with this treatment, like excessive hair fall and weight lose.

Photothermal (PTT) and photodynamic therapy (PDT) are the two promising therapy for proper disease management. Here also photobleachability, low absorption of natural dye molecule and photo sensitizers restricts its use. Also non- specific uptake of these molecules by normal cells adversely affects the treatment by damaging the normal healthy cells. In the case of PDT, conventionally used photosensitizing molecules stays in the body for a long period, rendering the patient to be highly sensitive to light (Huang et al., 2008b).

Several researches were focused on the use of above said therapeutic strategy in combination with nanotechnology. Gold nanomaterials and carbon nanotubes were found to be a suitable candidate for PTT because of its ability to convert incoming energy into heat either via electron- electron interaction or electron- phonon interaction.

1.3.4. Brain Diseases

Brain and brain related diseases are also becoming one of the major life threatening problem nowadays. Alzheimer's disease, dementia, Parkinson's disease etc are the most common diseases affecting elderly brain where as autism, dyslexia etc are congenital in nature. Brain tumour is most common in almost all age groups. So far there is no proper technique available for the early stage diagnosis of brain related diseases. Also there is only vague idea regarding the cause of these diseases and the biochemical changes that may occur in the brain during these diseases. According to WHO 2012 annual report, 5.4 million people in the US have Alzheimer's disease (AD) and by 2050, it estimates that between 11 million and 16 million Americans will have the disease, with one new case appearing every 33 seconds. Considering the drug industry, even after 20^{th} century, there are only few drugs available that can reach the brain. This is mainly because of the existence of natural gatekeeper (blood brain barrier- BBB), which blocks the entry of foreign and unwanted molecules into the brain. BBB, which acts as an interface between blood and brain, play a major role in the same.

1.3.5. Blood Brain Barrier (BBB) And Nanothechnology

The blood–brain barrier (BBB) formed by brain capillary endothelial cells is an important physiological barrier in the central nervous system that regulates the passage of molecules from the circulatory system into the brain. This barrier protects the brain from the invasion of various deleterious agents. However, it also hinders the delivery of diagnostic and therapeutic agents to the brain. Although various strategies have been proposed to overcome this barrier, including biochemical modification, osmotic opening of the cerebral capillary endothelium, as well as

alternative routes for administration, they are largely limited by the chemical structures of the agents and the existence of efflux pumps. Therefore, delivery of diagnostic and therapeutic agents across the BBB is still a major challenge for neurological disorders (Ballabh et al., 2004), (Weiss et al., 2009) (Abbott et al., 2006).

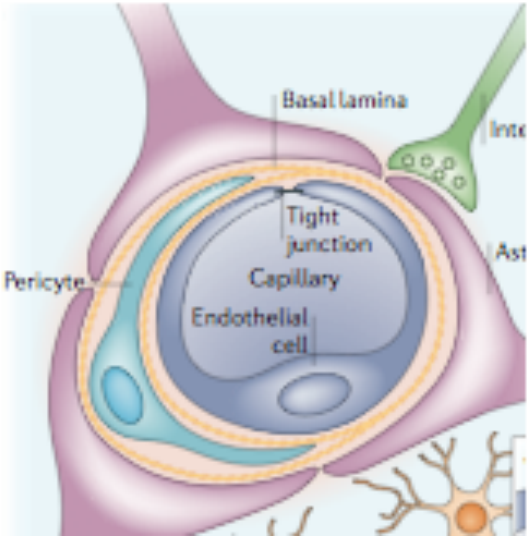

Figure 4: The BBB morphology. Adapted from (Abbott et al., 2006)

With the advent of nanotechnology, nanoparticles (NPs) with high chemical and biological stability and functionalized by protective ligands are increasingly demonstrating superior to other strategies in BBB transport. Nanoparticles with sizes between 1 and 100 nm serve as nanocarriers to enhance the delivery of agents across the BBB for imaging and therapy. The underlying mechanisms of how NPs cross the BBB may include receptor or absorptive mediated transcytosis by endothelial cells, opening of the tight junctions and inhibition of the trans membrane efflux systems, as well as other unknown mechanisms. Transport of NPs across the BBB may depend

on various factors, such as the surrounding surfactants, NP size, and electric charge (Ferrari, 2005)(Lockman et al., 2002) (Silva, 2008).

1.4 Gold Quantum Cluster (AuC)

Quantum confined condensed phase clusters of noble metals such as gold and silver have been of recent interest due to their intriguing properties such as photoluminescence, non-photobleachability, photon anti-bunching, longer lifetime when compared to the conventional organic fluorophores and versatility in applications. Clusters are basically a new type of materials referred as an intermediate to the individual molecules and the nano dimension. There are atomic and molecular clusters depending upon their constituents. Nano clusters include species existing in gas phase or condensed phase or in both. They can have a net charge or no charge (neutral clusters). There are clusters formed out of metals, semiconductors and even of noble gases. They have remarkably higher optical properties. At condensed phase, it shows properties like luminescence and optical absorbance. The luminescent spectrum also depends upon nature and size of the nano clusters. The information related to gas phase clusters can be determined by photo detachment spectroscopy. Ionization potential (IP) is one of the well studied properties of the cluster and using this IP, shell structure and stability of the clusters are confirmed. Among the colloidal gold nanocrystals, gold quantum clusters are remarkably a new class of material. The particle size lies between nano and atomic dimension (Shang and Nienhaus, 2012), (Xavier et al., 2012), (Chaudhari et al., 2011).

These nano clusters shows discrete energy level rather than the continuous energy state because of the extremely smaller size (sub nano dimension). Gold quantum/

nano clusters (AuCs) show size dependent fluorescence emission from UV- visible to NIR region. In addition to the non toxicity of gold, comparatively high quantum yield of GAUC with respect to gold nanoparticles makes an important candidate in the medical imaging fields. Hierarchy of material from atoms to bulk is shown below (figure 5)

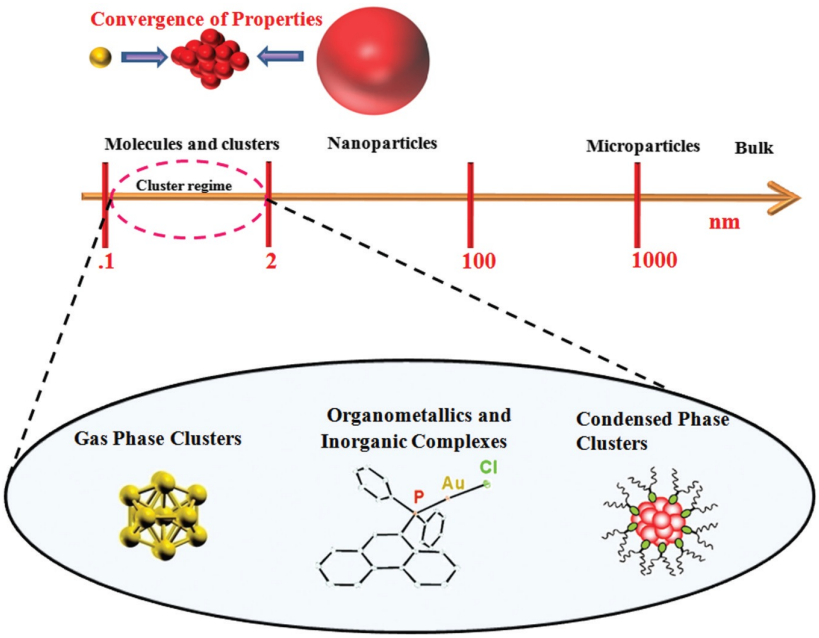

Figure 5: Hierarchy of materials from atoms to bulk, especially in the case of noble metals. Reprinted from (Xavier et al., 2012)

Metallic nanoclusters can be broadly classified into two groups as monolayer protected and template protected AuCs. In monolayer protected AuCs, the core atoms are stabilized with small molecules like glutathione, lipoic acid, octane thiols etc where as in template protected AuCs, core atoms are stabilized in proteins and dendrimers.

1.4.1 Glutathione Stabilized Gold Quantum Cluster

Glutathione (GSH) protected nano clusters are the well studied one among the monolayer protected AuCs (figure 6). GSH clusters with emission from blue to red region were developed and evaluated in great details (Habeeb Muhammed et al., 2008) (Negishi et al., 2005).

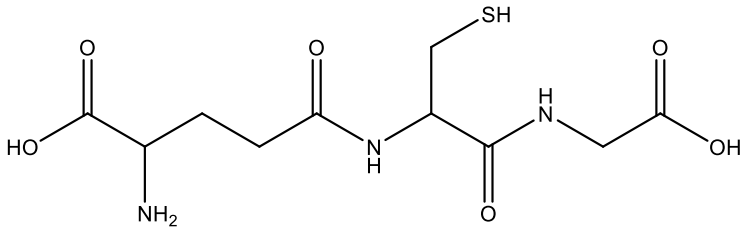

Figure 6: Structure of glutathione

GSH is a tri-peptide with a gamma peptide linkage between the carboxyl group of the glutamate side-chain and the amine group of cysteine. The thiol group present in the cysteine residue makes it suitable for easy binding with gold because of the strong affinity of Au and SH.

GSH plays an important biological functions by keeping the cysteine thiol group in proteins in the reduced state and also protect the cells from oxidative stress by trapping free radicals that damage DNA and RNA.

1.4.2 Lipoic Acid (LA) Stabilized Gold Cluster

LA (figure 7) is an organo sulphur compound derived from octanoic acid. It is widely used as an antioxidant and pharmaceutical drugs in biomedical field.

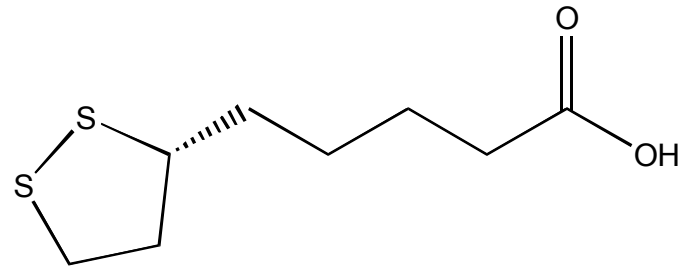

Figure 7: Structure of α- lipoic acid

At C6 and C8, LA contains two sulphur atoms connected by a disulfide bond and is thus considered to be oxidized although either sulphur atom can exist in higher oxidation states. Chemically LA consists of two enantiomers. (*R*)-(+)-lipoic acid (RLA) and (*S*)-(-)-lipoic acid (SLA) and as a racemic mixture (*R*/*S*)-lipoic acid (R/S-LA). RLA form exists in nature and is essential for aerobic metabolism because this form of LA is an essential cofactor of many enzyme complexes.

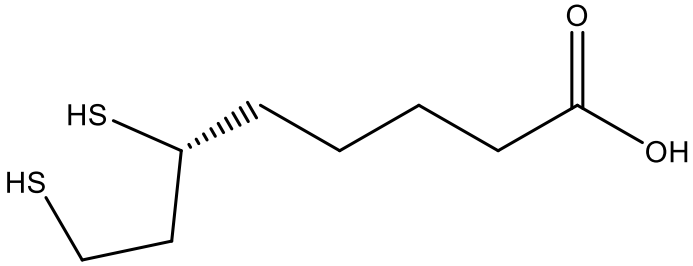

Figure 8: Structure of reduced lipoic acid

Once the lipoic acid is reduced (figure 8), it has two thiol groups and attachment of reduced LA is much easier in gold because of the strong interaction of Au and SH groups.

1.4.3 Synthesis And Optimization Of NIR Emitting Gold Quantum Cluster

NIR emitting materials are of great importance in modern science, because of its ability to avoid auto fluorescence from the tissue, especially in medical field. Inherent fluorescence and non-cytotoxic nature of gold quantum cluster are the important properties that make it an ideal candidate for this field. Well-known interaction between gold and thiol has attracted wide interests throughout the world of chemistry as well as in other fields of modern science. Gold thiol binary system exhibit unique structural and functional characteristics based on the degree of aggregation, which in turn is useful for various applications, like water purification, sensing of toxic elements and biomedical applications (Retnakumari et al., 2010) (Liu et al., 2010) (Roy et al., 2012). The ratio of gold and thiol usually plays an important role in the properties of the material, as it depends on the degree of polymerization of gold thiol system. Another factor, which determines the structural and functional properties of the system, is the Au (I) atoms with d^{10} closed-shell electronic configuration that tend to form aggregation due to aurophilic interaction (Negishi et al., 2004), (Negishi et al., 2005).

By making use of the gold thiol interaction, by changing reaction condition and temperature of reaction, tuning of optical property is possible. Because of the presence of thiol moiety on GSH and LA helps in the strong interaction with gold to form cluster. Also this system will be ideal for evaluating and unraveling the unknown parameters behind the properties of metallic cluster.

1.5 Urea Detection Using Urease Immobilized Gold Quantum Cluster

Urea is a byproduct of protein metabolism that is formed in the liver, carried by the blood and excreted through the kidney in urine. Therefore, urea is an important marker for evaluating uremic toxin levels and kidney and hepatocellular functions. Urea detection is also important in the estimation of non-protein nitrogen in food products such as milk since it is known that urea adulteration is utilized as an indicator of protein feeding efficiency. Nanosensors based on metal nanoparticles (NPs) have got wide attention during the past couple of decades because of their enhanced selectivity and sensitivity towards specific analytes. There are several reports on nanosensors for the detection of urea, most of which are based on electrochemical or amperometric sensing (Barhoumi et al., 2005) (Srivastava et al., 2012)

Hydrolysis of urea into carbondioxide and ammonia is catalyzed by urease enzyme. In clinical diagnosis the formed bi products reacts with colorimetric reagent to form colored compound and is estimated spectrometrically for quantifying urea. Urease (figure 9) is functionally, belong to the super family of amidohydrolases and phosphotriestreases. Ureases are found in numerous bacteria, fungi, algae, plants and some invertebrates, as well as in soils, as a soil enzyme. They are nickel-containing metalloenzymes of high molecular weight. .

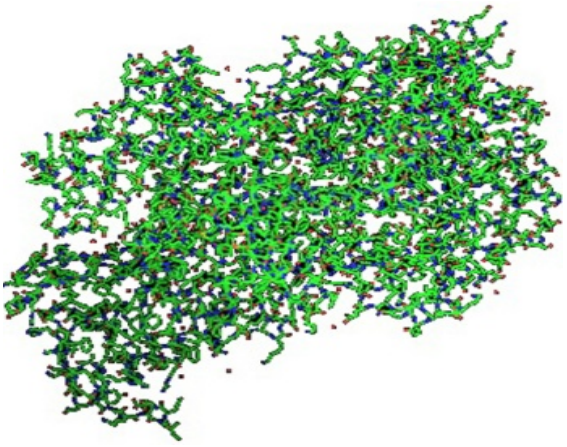

Figure 9: Structure of urease enzyme

1.6. Tumor Imaging And Targeted PDT Using Gold Quantum Cluster

1.6.1. Targeted Tumor Imaging Using Folic Acid Conjugated Gold Cluster

Cancer cells can be distinguished from normal cells through their over expression of certain receptors and proteins over the cell surface. Epidermal growth factor receptor and $\alpha_v\beta_3$ integrin proteins are over expressed in most of the cancer cell irrespective of its origin.

Folate receptor is one of the most widely studied receptor in most of the cancer cells because of the low cost and ready availability of folic acid, ligand of folate receptor.

Folic acid (figure 10) is derived from the Latin word *folium*, which means "leaf". Chemically it contains NH_3 and COOH moieties which easily allow the binding with nanoparticles using suitable chemistry to fascilitate targeted imaging or therapy.

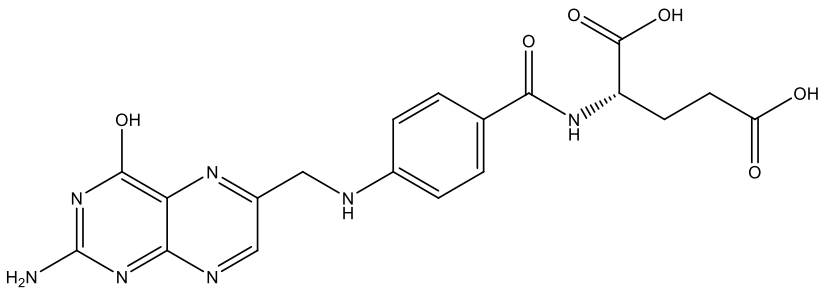

Figure 10: Structure of folic acid

1.6.2. Tumor Therapy Using Gold Nanocluster (Targeted PDT)

An ideal cancer therapy not only destroys the primary tumour, but also triggers the immune system to recognize, track down and destroy remaining tumour cells, whether in the primary or metastasized sites. PDT is a promising treatment modality for a variety of oncological conditions. It is based on the concept that photosensitizer molecules can be preferentially localized in tumor tissues upon systemic administration. PDT has a direct effect on cancer cells, producing cell death either by necrosis or by apoptosis. Reactive oxygen species, such as singlet oxygen, or free radicals are the main cytotoxic substances, which can irreversibly damage the cancer tissues. The main advantages of PDT are its ability to arrest tumour vasculature and metastasis, blocking of oxygen and other nutrients by the production of ROS and its non-immune suppressiveness. In spite of the greater potential over other treatment modalities, PDT faces the limitations due to the unintended destruction of normal cells due to the non selectivity of the currently available photosensitizers (PS). High dose administration becomes inevitable due to the non selectivity of PS resulting high level of dark toxicity. Another major limitation of majority of currently available sensitizers is the difficulty in the administration and effective delivery to the cancer site due to their very low solubility in water and physiological media. As most of the PS are non traceable under conventional imaging techniques, the speculative nature of the accumulation of PS at the cancer site and subsequent lack of follow up of therapy keeps away this effective treatment modality from real practice.

Gold-based nanomaterials were widely used for the photothermal destruction of cancer cell both *in vitro* and *in vivo* by El sayed and his group. Very little studies have been done on the use of gold nano cluster for therapeutic application especially PDT.

Photosensitizers (PS) are the major group of molecules used for PDT. A photosensitizer is a chemical compound that can be promoted to an excited state upon absorption of light and undergo intersystem crossing with oxygen to produce singlet oxygen. Singlet oxygen is highly toxic to the cells and that kills the tumor cells. It is rapidly eliminated from the cells because of its lesser lifetime. Porphyrin and Pthalocyanine based molecules are most widely used PS

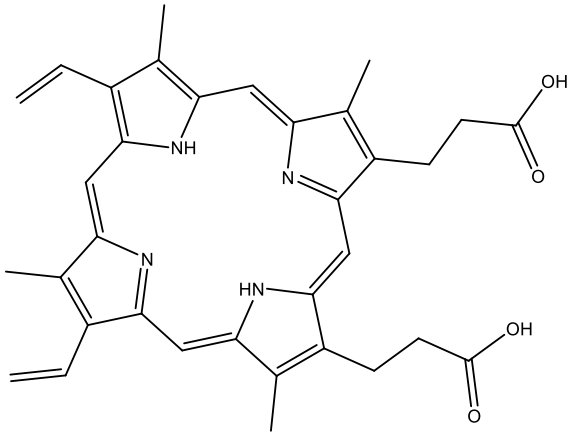

Figure 11: Structure of Protoporphyrin IX

Protoporphyrin IX (PPIX- figure 11) is a clinically approved PS for PDT. It is shown to have a triplet quantum yield of 63%. Reactive acid functionality on PPIX will helps to modify the nanocluster.

1.7. BBB Targeted Brain Imaging Using Nano Cluster Of Gold

Brain disorders are the major concern of the modern world in terms of economic cost and human suffering with increasing number of aged population as a result of the long life span. The main challenge in the treatment of many of the neurodegenerative diseases is the presence of a polarized layer of endothelial cells that comprise the blood–brain barrier (BBB) which precludes access of systemically administered medicines to brain tissue. Currently more than 98% of all small molecules and 100% of large-molecule pharmaceutics do not cross the blood brain barrier in cases where there is no disruption or loosening of the same. As a result, effective therapy becomes possible only at later stage of the disease when the integrity of the barrier is compromised. BBB also restricts the possibility of early diagnosis of the diseases as the imaging contrast agents are prevented from entry. However, despite the tight protection given to the brain, BBB allows selective transport of essential nutrients and oxygen to the brain. Specific membrane transport proteins are relatively higher in BBB, which allows the entry of essential nutrients, such as glucose and certain amino acids or related molecules, including L-DOPA.

Certain receptors present on BBB also allow the entry of macromolecules into the brain through receptor-mediated pathways. These pathways may be explored for an effective delivery of imaging moiety or drug to the brain facilitating early diagnosis and effective therapy.

Brain endothelium and astroglia contain millimolar concentrations of GSH. Since cysteine and GSH levels in plasma are of the same order of magnitude. As an alternative to plasma cysteine, plasma GSH might play an important role in brain

homeostasis. Brain capillaries contain gamma-glutamyltranspeptidase (GGT) activity on the luminal membrane which may serve to break down plasma GSH.

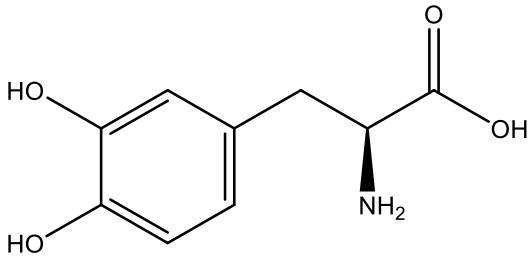

Figure 12: Structure of L- dopa

L- Dopa (figure 12) is one of the most common drugs used for the treatment of Parkinson's diseases clinically. Specific membrane protein (large neutral amino acid transporter (LAT1) is present on BBB to enable the entry of L dopa into the brain. Lots of side effects have been reported for the use of L dopa. To avoid the adverse effect and also to increase the bioavailability of L dopa, it is usually administrated along with carbidopa. The acid and amine functionality of L dopa enables the easy conjugation of the same with nanoparticles.

1.7.1 Drug Delivery In Brain- Main Challenges

Once the disease is diagnosed, a therapeutic approach is mandatory for the betterment of disease in brain. Delivering of therapeutic drugs in brain is the major challenge in brain related diseases. The BBB prevents most of the large as well as small molecules owing to its unique epithelial like non-porous tight junctions within the capillary endothelium and its limited efficiency for pinocytosis. Hence, the molecules can access to the brain either through lipid-mediated diffusion or carrier or receptor mediated active transport (Pardridge, 2012).

1.8 Single Wall Carbon Nanotube (SWCNT) Quantum Dot (Qd) Hybrid Nanosystem For Targeted Imaging And PTT

Single wall carbon nanotube (SWCNT) is one of the interesting candidates in various fields in the last few decades. Unique electrical transport properties of carbon nanotubes suggest that they have many advantages over conventional materials for use as superior nanometer scale wires. Metallic SWNTs can act as ballistic conductors and can carry current densities larger than copper wires of the same diameter.

SWCNT is efficient in converting the absorbed energy into heat. So it is highly efficient in photothermal therapy (PTT). But solubility of SWCNT restricts its use in biological application. In order to increase the solubility several methods are adopted through the functionalization with suitable ligand. Since SWCNT doesn't have any inherent optical property, it is not a good candidate for imaging applications. However by conjugating with fluorescent molecules, its imaging potential can be activated.

Qd is another major class of nanomaterials that attracts in the researches even after 30^{th} years of its discovery, because of its enhanced optical characteristics. Because of the higher quantum yield in comparison with organic dye and non photoblechability makes an appropriate element in the bio imaging field. But for therapeutic application, Qd must be conjugated with photo sensitizers or chemotherapeutic drugs. By conjugating SWCNT with Qd is an ideal alternation for imaging and PTT.

1.9 Hypothesis

It is hypothesized that nanotechnology is a glowing edge technology in various fields of applications especially in the field of medical diagnosis, sensing and therapy. By properly manipulating, the nonmaterial will provide a suitable vehicle for major threats facing in the field of disease diagnosis and its proper management/ therapy. It is also possible to understand the biochemical changes of brain that happened during the early stage of disease progression with the help of nanomaterials.

1.10 Objective

Based on the background literature and our hypothesis, we propose the main objectives as follows

- Synthesis and optimization of monolayer protected NIR emitting gold quantum clusters
- Designing of gold quantum clusters for model analyte sensing
- Tumor diagnosis and targeted therapy using gold quantum cluster
- Designing of gold quantum clusters for BBB targeted brain Imaging and drug delivery
- Development of hybrid nanomaterial for cellular imaging and therapy.

CHAPTER 2

REVIEW OF LITERATURE

Nanotechnology and nano engineering are capable to produce significant scientific and technological advances in diverse fields including biomedical field. In a broad sense, it is defined as the science and engineering involved in the design, synthesis, characterization, and application of materials and devices whose smallest functional unit is in the nanometer scale, ranging from a few to several hundred nanometers. The specialty of such a material is that, it can be designed to exhibit very specific and controlled chemical and physical properties as a result of the control over their molecular synthesis and assembly (Shrivastava and Dash, 2009).

Living cells are full of complex structures and are composed of macromolecules, including proteins. They are involved in all the process in the cell, such as information transfer, metabolism, and transport of substances (Zandonella, 2003) . Nanotechnologies offer a new platform for observing the operation at the level of individual molecules, even in the living cell.

Most of the proteins and biomolecules in the living organism are of nearly 10's of nm in size (Rosi and Mirkin, 2005). The chemical tuneability and high surface area of nanoparticles helps to accurately design and develop nano device and can be incorporated into biological systems, due to the similar size scales (Shenhar and Rotello, 2003). Synthesis, structure and function of biological systems are too complex. The ability to rationally design structures on the same size as biological molecules generates the ability to probe and modify biological systems. Also these

biological systems are often used to build up nanomaterials of specific shape and function. Nanostructures are being widely used as drug delivery agents, labeling agents and sensors (Katz and Willner, 2004).

The field of nanotechnology has received increasing attention over the last 30 years in various fields of science and technology. The whole study of this thesis is designed to use fluorescing nanomaterials for sensing, imaging and therapeutic field. Gold based nanoclusters and hybrid nanomaterilas were selected for the study. This chapter presents a complete review on the studies related to metallic quantum cluster and hybrid nanomaterials- synthesis and its applications in sensing, imaging (cancer and brain) and therapy.

2.1. Near Infra Red Emitting Gold Quantum Cluster

Metallic nonmaterials especially gold nanomaterials were attracted in biomedical field because of its biocompatibility and its enhanced absorption and scattering cross section (Eustis and El-Sayed, 2006), (Daniel and Astruc, 2004). However gold quantum cluster (size less than 2nm) is realatively a newer class of material (Chaudhari et al., 2011).

Analogous to semiconductor quantum dots (Qd) when particle sizes are smaller than the Bohr exciton radius (Alivisatos, 1996), gold nanoparticles show a size-dependent plasmon absorption band when their conduction electrons are confined to dimensions smaller than the electron mean free path (Link and El-Sayed, 2003). But plasmon

absorption disappears completely for nanoparticles less than 2 nm where Mie's theory no longer is valid (Hostetler et al., 1998). Fascinatingly, metal nanoclusters confined to a second critical regime having sizes comparable to the Fermi wavelength of the electron (ca. 0.7 nm), results in molecule-like properties of discrete electronic states (Lee et al., 2004) and size-dependent fluorescence (Huang et al., 2007).

In contrast to Qds, noble metal quantum clusters (AuCs) are highly attractive for bioimaging and biolabeling applications due to their low toxicity and smaller size. Increasing use of metal-containing compounds in therapy and diagnosis (Abrams and Murrer, 1993) also make the metal nanoclusters as an alternative building block of biomedical probes using their luminescent properties.

2.1.1 Optical Properties And Synthesis Of Gold Quantum Clusters (AuC)

The ultra-small size imparted quantum confinement of AuCs give rise to discrete electronic energy levels, molecule-like electronic transitions, enhanced photoluminescence, intrinsic magnetism, and other effects . Compared to gold nanoparticles, AuCs are too small and possess discrete enrgy levels (Qian et al., 2012). AuCs have much enhanced fluorescence quantum yield of 10^{-3}–10^{-1} in comparison with their bulk counterpart. The energy level diagram of photoluminescence in gold nanoclusters is shown in figure 13. These fluorescent nontoxic brighter AuCs will be an efficient substitute for fluorescence based sensing and imaging applications. Dendrimer encapsulated AuCs having 70 % quantum yield were developed by the Dickson group (Zheng et al., 2004). By controlling physicochemical parameters like size and chemical composition, the fluorescence

emission of AuCs can be easily tuned from the visible to the near infrared region (Huang et al., 2009b).

Ramakrishna et al. (Ramakrishna et al., 2008) and Khandelia et al. (Khandelia et al., 2015) have demonstrated the two photon absorbance efficacy of AuCs. The two-photon absorption cross-section of AuCs was found to be 105 Göppert-Mayer units (Polavarapu et al., 2011). AuCs possess better photostability than organic dyes (Polavarapu et al., 2011), (Lin et al., 2009). Lipoic acid-coated AuCs exhibited a much slower photobleaching rate than fluorescein and rhodamine 6G (Lin et al., 2009). The unique photophysical properties of these AuCs are beneficial to their biological application, giving the possibility of multiplexed detection of molecular targets, and continuous, real-time imaging of single molecules or cells over long periods.

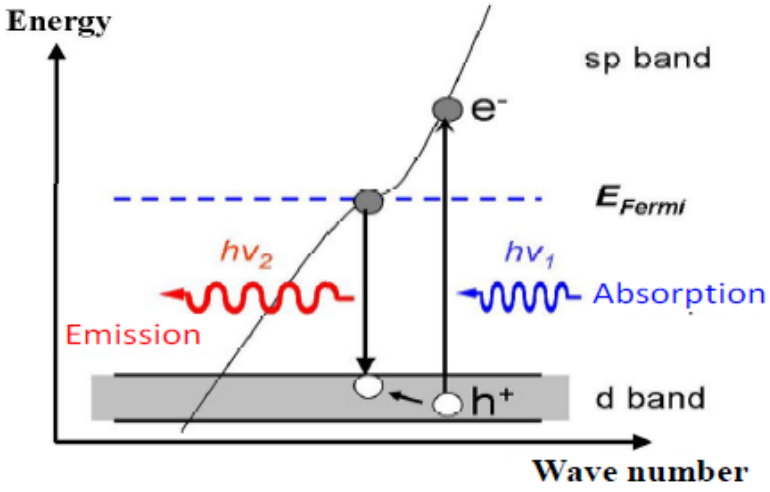

Figure 13: Photoluminescence of AuC's. Adapted from (Apell et al., 1988)

Synthesis of AuCs with excellent and unique optical properties is the fundamental requirement for any applications. A wide variety of synthetic methods for the synthesis of water-soluble, fluorescent AuCs have been adopted for the last decades. The synthesis of these AuCs comes under two categories. The first route involves the production of small clusters from large nanoparticles by etching with thiols (Huang et al., 2007), (Lin et al., 2009), (Muhammed et al., 2009), biomolecules (Zhou et al., 2009)(Muhammed and Pradeep, 2010) or multivalent polymers (Duan and Nie, 2007). This route is capable of synthesizing AuCs with different ligands through the involvement of multi-step process makes the synthesis little complicated and tedious. In comparison with the above synthetic route, a one-step method, in which AuCs are synthesized by reducing gold salt with a suitable reducing agents like sodium borohydride (Schaeffer et al., 2008), (Shang et al., 2011a), tetrakis(hydroxymethyl)phosphonium chloride (Shang et al., 2011b), or proteins (Xie et al., 2009) (Xavier et al., 2010), is more favourable and has lately been widely adopted. Yuan et al. (Yuan et al., 2012) reported a new synthetic strategy for the development of atomically precise AuCs by using surfactant induced protection-deprotection method. On variying the proptecting ligand over AuCs impart different properties and color (figure 14).

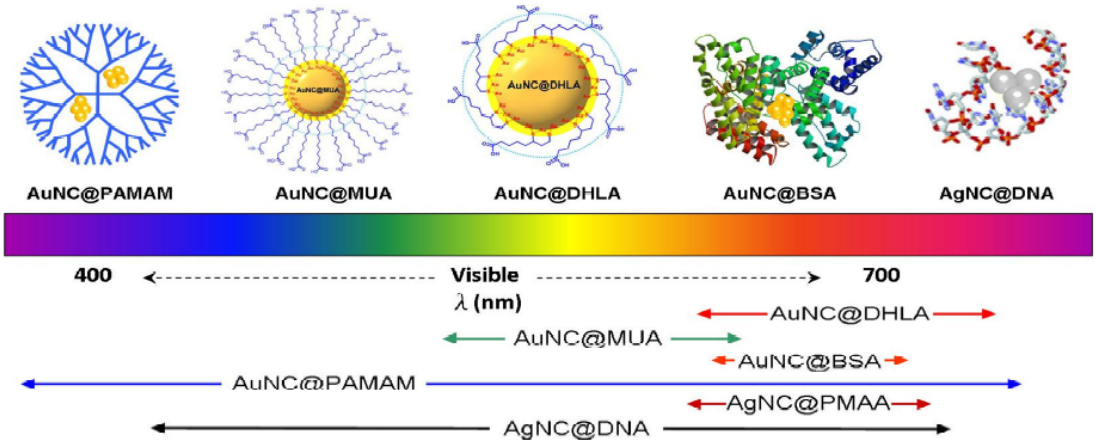

Figure 14: Representative fluorescent noble-metal nanoclusters scaled as a function of their emission wavelength superimposed over the spectrum. Reprinted from (Shang and Nienhaus, 2012)

NIR emitting nanomaterials attained wide importance in the biomedical field because of its ability to avoid autofluorescence. Most of the biomolecules and proteins emit in the visible range. Octanethiol capped AuCs shows emission in the 750 nm with a lesser quantum yield of 0.1% (Muhammed et al., 2009). In the previous studies it is evident that changing the capping agent, and reaction conditions affect the properties of these AuCs. Changes in the number of core atom, number of ligands and pH also affects the property. As an example, on changing the pH of the reaction (Habeeb Muhammed et al., 2008) during etching with glutathione resulted in blue emitting (Au_8) and red emitting (Au_{25}) cluster. Au_{25} clusters synthesized in various routes using albumin, glutathione and other ligands are having different optical behaviour and different quantum yields. There is no unified theory to clearly address how the optical property changes by varying reaction condition. Very recently, dodecanethiol protected gold cluster (figure 15) were utilized for the evaluation of nonbulk electronic and geometrical structure of clusters (Negishi et al., 2015).

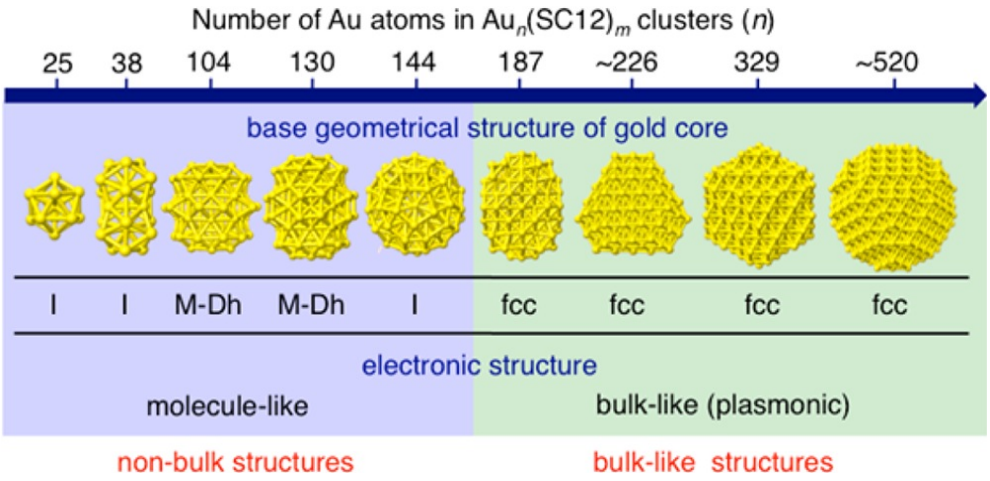

Figure 15: Geometric and structural evaluation of non-bulk structures form bulk like structures. Reprinted from (Negishi et al., 2015)

2.2. Gold Cluster As A Novel Sensor

Biosensors capable of detecting chemical and biological agents in their environment are active areas of research using nanomaterials especially gold nanoparticles, quantum dots, carbon nanotube etc. But, studies based on fluorescent noble-metal nanoclusters are limited owing to the lack of knowledge of their optical physics. First report of AuC was demonstrated for the detection of mercury (II) ion based on fluorescence quenching of the AuCs through Hg(II)-induced aggregation (Huang et al., 2007). L-cysteinyl-L-cysteine AuCs with 41.3% quantum yield were developed for the selective detection of arsenic in aqueous solution with a detection limit of 53.7 nM (Roy et al., 2012). Similarly, glutathione-protected AuCs (Chen et al., 2009), albumin stabilized gold clusters (Durgadas et al., 2011) and lactoferrin conjugated AuCs (Xavier et al., 2010) were used for the highly sensitive and selective detection of Cu^{2+} ions based on aggregation-induced fluorescent quenching.

Blue shift in the emission of cyclodextran capped Au_{15} cluster were utilized for the selective detection of Cu ions (Shibu and Pradeep, 2011). A donar acceptor system based on Au nanodots and Au nanoparticles were demonstrated for the analysis of proteins by a new competitive homogeneous photoluminescence quenching of Au nanodots (Huang et al., 2008a). Huang et al (Huang et al., 2009a) developed mannose protected fluorescing gold nanocluster for the selective detection of Concanavalin A over other proteins and lectin. These clusters have the capability of binding mannose-specific adhesion Fim H of type 1 in *E. coli* bacteria, yielding brightly fluorescent cell clusters. Wei et al. developed a highly fluorescing gold nanocluster by using lysozyme for the selective detection of Hg^{2+} ions based on fluorescence quenching with a detection limit of 10 nM (Wei et al., 2010). Cyanide etching induced fluorescence quenching based sensor platform were demonstrated for the selective and sensitive detection of cyanide (figure 16) in aqueous environment (Liu et al., 2010). The limit of detection of the developed sensor is 200 nM which is approximately 14 times lower than the maximum level of cyanide in drinking water permitted by the World Health Organization.

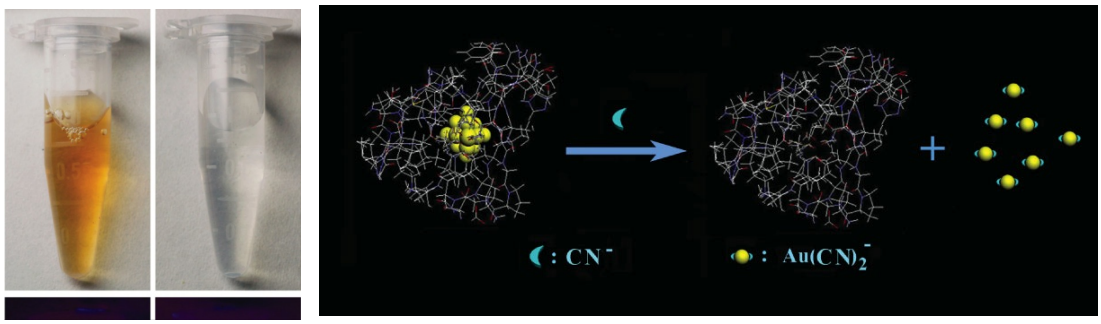

Figure 16: Gold nanocluster based sensing platform for the detection of cyanide. Reprinted from (Liu et al., 2010)

2.3. Gold Quantum Clusters For Targeted Tumor Imaging And Photodynamic Therapy

Comparatively higher quantum yield and photostability of gold quantum cluster make it suitable for cell markers for long-term studies such as cell-cell interactions, cell differentiation, and tracking. These AuCs can be internalized by cells for either by receptor-mediated (Yu et al., 2008) or nonspecific endocytosis (Lin et al., 2009). With the advances in synthetic strategies, AuCs were successfully employed as fluorescence labels for a variety of biological purposes, such as biomolecule detection (Huang et al., 2009a), (Liu et al., 2010), intracellular metal ion sensing (Huang et al., 2007), (Shibu and Pradeep, 2011), live cell labeling (Lin et al., 2009), (Huang et al., 2011), cellular apoptosis studies (Lin et al., 2010), and targeting notorious pathogenic bacteria (Chen et al., 2010). Among the various applications of AuCs, fluorescence imaging has made the most progress and attracted the greatest interest. Lin et al. reported the use of AuCs as a probe for nuclear targeting and intracellular delivery. Blue-emitting Au nanoclusters functionalized with SV40 NLS peptide can enter the cytoplasm of living HeLa cells (figure 17), where non-functionalized ones shows no intracellular signals for 1.5 hr treatment (Lin et al., 2008). Human aortic endothelial cells can uptake lipoic acid conjugated AuCs after 5 hr incubation (Lin et al., 2009).

NIR light provides number of advantages for cellular imaging, such as weak autofluorescence, negligible photobleaching. So, imaging agents having emission in the NIR region is particularly attractive for high sensitivity fluorescence based bioimaging (Frangioni, 2003). Pradeep and coworkers (Muhammed et al., 2009)

demonstrated streptavidin bound NIR emitting Au_{23} quantum cluster to selectively stain human hepatoma cells (HepG2). These cells contain a large amount of biotin, which binds to streptavidin with high specificity and affinity. Receptor-targeted NIR imaging of oral carcinoma KB cells was reported using folic acid-conjugated Au_{25} AuCs (Retnakumari et al., 2010). Folic acid conjugated AuCs were found to become internalized in significantly higher concentration compared with the negative control cell lines. The characteristic NIR emission from AuCs made it possible to image the clusters, where the optical properties of blood and tissue are highly favourable for imaging application. NIR emitting multidentate polymer capped AuCs were used as biomarkers to label the hematopoietic cells (Huang et al., 2011). Here the cancer cells incorporated more AuCs than normal cells.

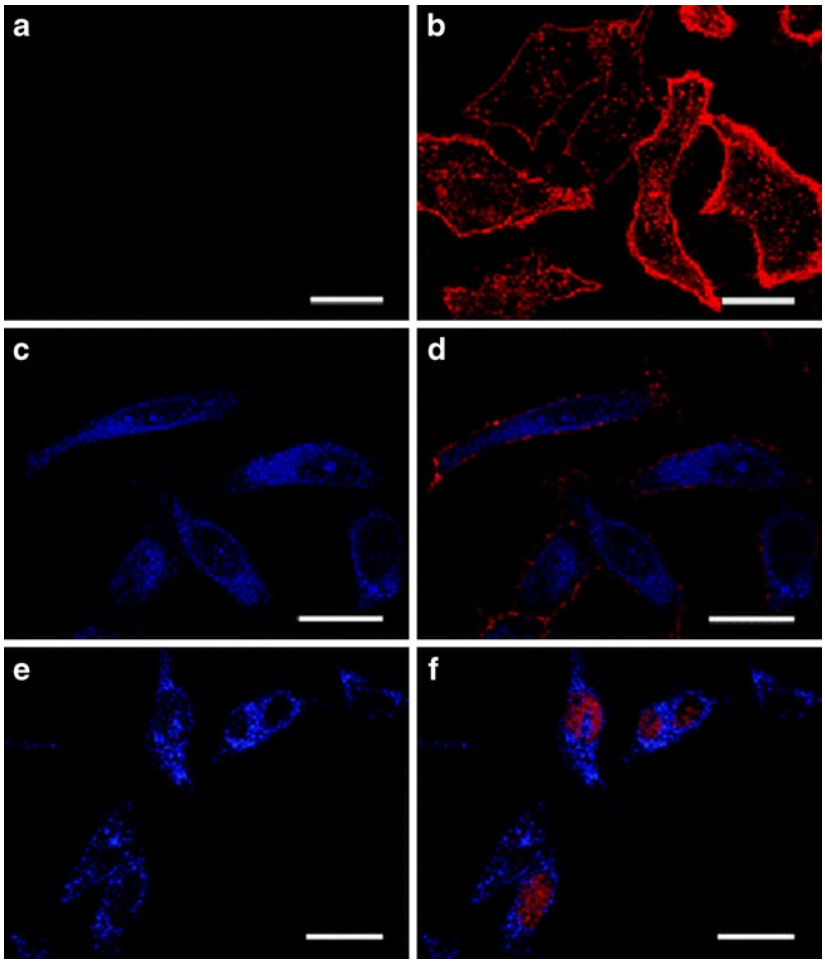

Figure 17: Confocal microscopy images of intracellular delivery of AuCs. HeLa cells were treated with 11- mercaptoundecanonic acid capped AuCs (a, b) and peptide– functionalized AuCs (c–f) for 1.5 h. Adapted from (Lin et al., 2008)

The excellent two photon absorption cross-sections of AuCs make them promising markers for two-photon cellular imaging for deep tissue imaging. Two-photon imaging of human mesenchymal stem cells (hMSCs) using dextran encapsulated AuCs were demonstrated by Chou and coworkers (Liu et al., 2009). Upon two-photon excitation with 800 nm laser, bright luminescence from AuCs was observed in the cells. Higher two photon crosssection and photostability of GSH capper AuCs is shown to have two-photon excitation in live cell imaging (Polavarapu et al., 2011).

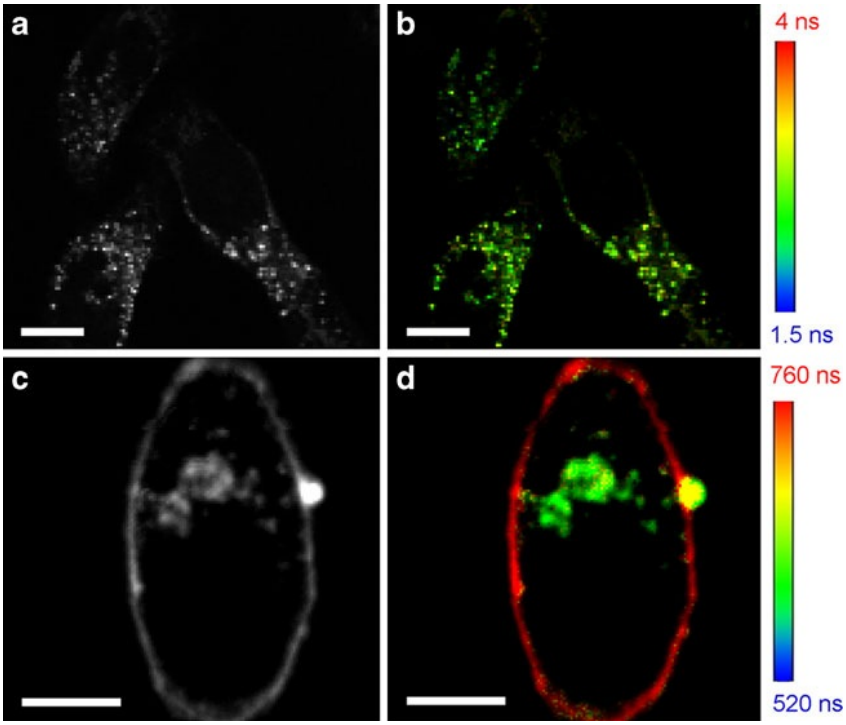

Figure 18: Fluorescence life time imaging of HeLa cells incubated with (c & d) and without(a & b) lipoic acid conjugated AuCs. Reprinted from (Shang et al., 2011a)

Compared to fluorescence based imaging, fluorescence life time imaging is independent of the concentration of fluorophore and the intensity of laser source. Fluorescence lifetime of the fluorophores can be highly sensitive to the local environment. Due to this, fluorescence lifetime imaging provide contrast due to spatial variations of the lifetime and yield valuable additional information (Borst and Visser, 2010). Lipoic acid stabilized AuCs with good colloidal stability and biocompatibility possess high fluorescence life time, much longer than that of cellular autofluorescence (Shang et al., 2011a). On exposing HeLa cells to AuCs for 1 h, luminescent emission with long fluorescence lifetimes were observed inside the cells indicating the internalization of AuC (figure 18). The fluorescence decay of lipoic acid coated AuCs in the cells is slower than in aqueous solution indicate the formation of protein corona round the AuCs during uptake process (Röcker et al.,

2009). Fluorescence lifetime images (figure 18) clearly show that the nanocluster near the cell membrane display longer lifetimes than inside the cells. Thus, lifetime imaging reveals the cellular uptake of AuCs and provides information on changes in their local environment.

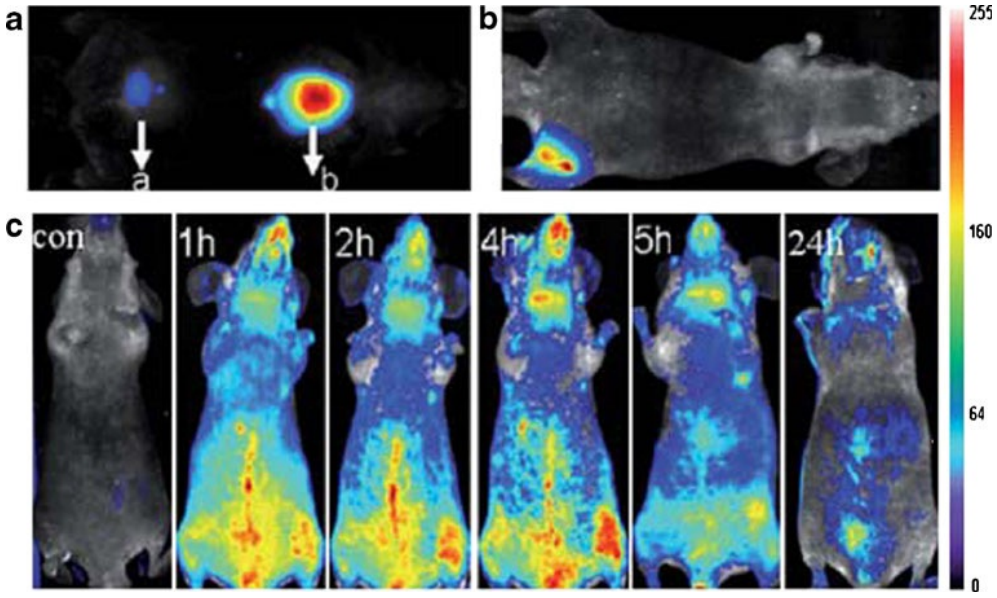

Figure 19: In vivo tumor imaging using albumin stabilized AuCs subcutaneously (a), intramuscularly (b). Real time in vivo abdomen image taken with intravenous injection of AuCs (c). Adapted from (Wu et al., 2010)

NIR emitting bovine serum albumin stabilized AuCs were demonstrated for the *in vivo* tumor diagnosis for the first time by Wu et al (Wu et al., 2010). The NIR fluorescence of the AuCs was visualized upon injection into the muscle and also through the intravenous injection. They observed a fluorescence from the mice upto 5h of post injection (figure 19).The *ex vivo* studies showed that these AuCs accumulated mostly in tumor sites resulting from the enhanced permeability and retention effect. Quantitative biodistribution of these clusters in the liver and spleens

is relatively small in comparison with other nanoparticle-based contrast agents due to their ultrasmall hydrodynamic size (ca. 2.7 nm). Similar to this study, kidney target specific AuCs were developed by conjugating with ferritin (Sun et al., 2011). Intravenous injection of these AuCs to female nude mice through tail vein reveals the internalization of the particle in the kidney after 30 min of post injection (figure 20). These particle remained in the kidney after 7h of post injection. Such a long time retention of AuCs in kidneys reveal the existence of certain ferritin receptors in kidney. In addition to kidney fluorescence, strong signals were also observed from liver and spleen. Quantification of AuCs shows that liver, kidney, and spleen were the major target tissues of ferritin-encapsulated AuCs after 2 h of post-injection with very low Au level in lung and heart (figure 20 b &c).

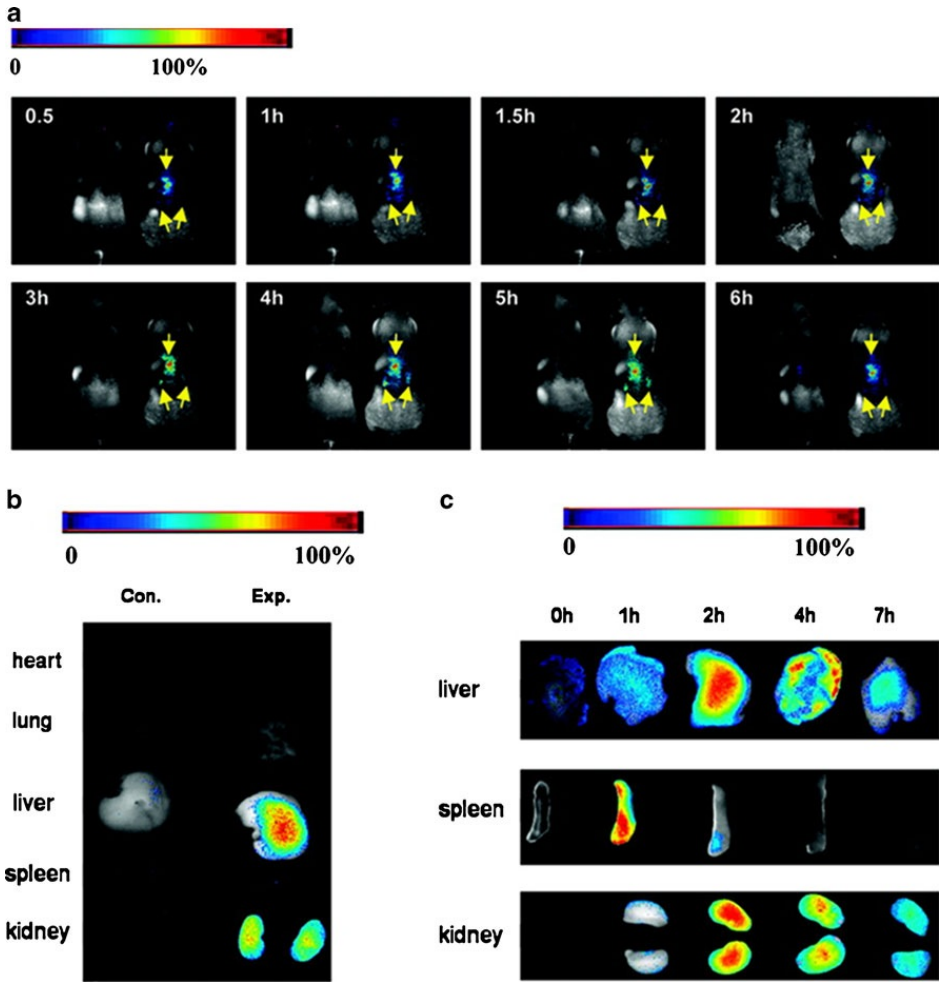

Figure 20: Whole body dorsal fluorescence images at different time points after AuC injection in comparison with the control (a) at different time point. Fluorescence images of mouse organs 6 h after AuCs injection (b). Fluorescence images of mouse organs at different time points after injection (c). Adapted from (Sun et al., 2011)

Very little effort has been made for the use of AuCs based therapeutic platform especially in the photodynamic approach. Recently, Huang *et al.* reported the use of silica functionalized gold cluster with covalently incorporated chlorin e6 (Ce6) molecules for NIR fluorescence imaging and PDT (Huang et al., 2013). The cluster based theranostic probe possesses high loading, no nonspecific release during its circulation, significantly enhanced cellular uptake efficiency, offering a remarkably improved photodynamic therapeutic efficacy compared to free Ce6 (figure 21). This

system shows good stability, high water dispersibility and solubility, non-cytotoxicity, and good biocompatibility.

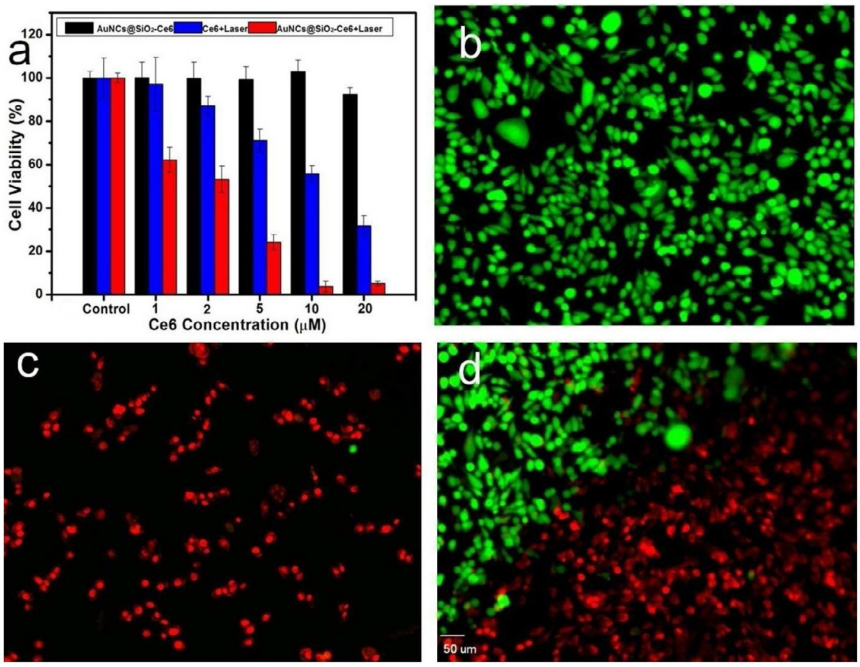

Figure 21: Cell viability at different concentrations of free Ce6 and AuCs@SiO2- Ce6 for 12 h at 37 °C with or without irradiation with a 671 nm laser (a). Live dead assay (b to d), cells without irradiation (b), with irradiation (c) laser boundary (d). Reproduced from (Huang et al., 2013).

2.4. BBB Targeted Brain Imaging Using Gold Quantum Cluster

The BBB is a selective barrier formed by the endothelial cells that line cerebral microvessels (Abbott et al., 2006). It acts as a 'physical barrier' between adjacent endothelial cells and this complex tight junction force most molecular traffic to take a transcellular route across the BBB, rather than moving paracellularly through the junctions, as in most endothelia (Hawkins and Davis, 2005). Small gaseous molecules such as O_2 and CO_2 can diffuse freely through the lipid membranes, and this is also a route of entry for small lipophilic agents, including drugs such as barbiturates and ethanol. The presence of specific transport systems on the luminal

and abluminal membranes (figure 22) regulates the transcellular traffic of small hydrophilic molecules, which provides a selective 'transport barrier', permitting or facilitating the entry of required nutrients, and excluding or effluxing potentially harmful compounds (Begley and Brightman, 2003).

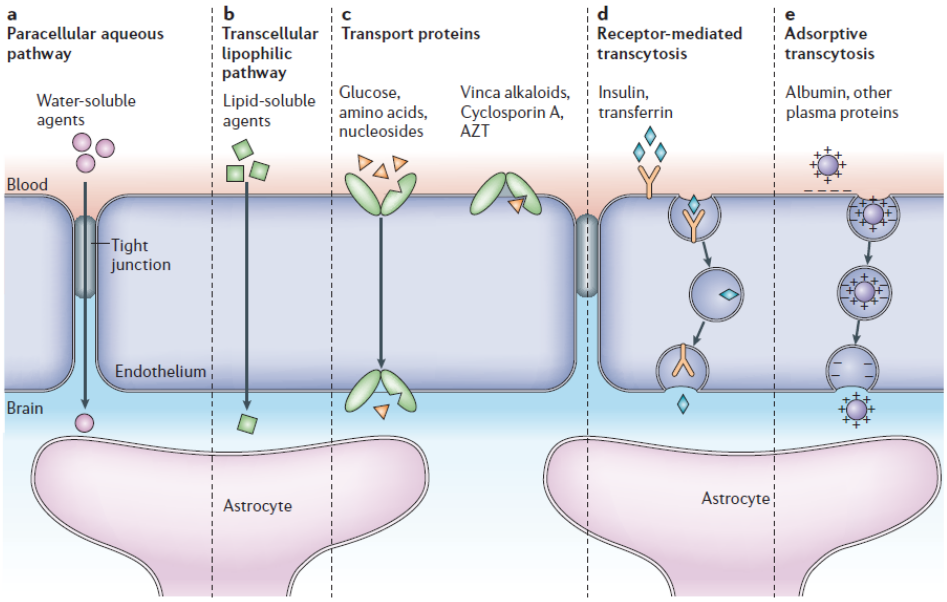

Figure 22: Different pathways across BBB. Adapted from (Hawkins and Davis, 2005).

Suitable modification of the nano construct to use any of the permissible pathways will facilitate efficient entry of them into the brain without disturbing BBB.

So far there are no studies reported for the use of gold cluster for BBB targeted brain imaging. But Santra et al demonstrated TAT peptide conjugated quantum dots for the effective labelling of brain cells (Santra et al., 2005). TAT peptide conjugated PEGylated nanomaterials were used as a carrier for antibiotics into the brain (Liu et al., 2008). PAMAM- G5 dendrimer conjugated with RGD peptide and angiopep were used for the detection of brain tumor imaging using optical imaging and MRI

(Yan et al., 2012)**.** Here RGD peptide is utilized for tumor targeting and angiopep is for BBB targeting.

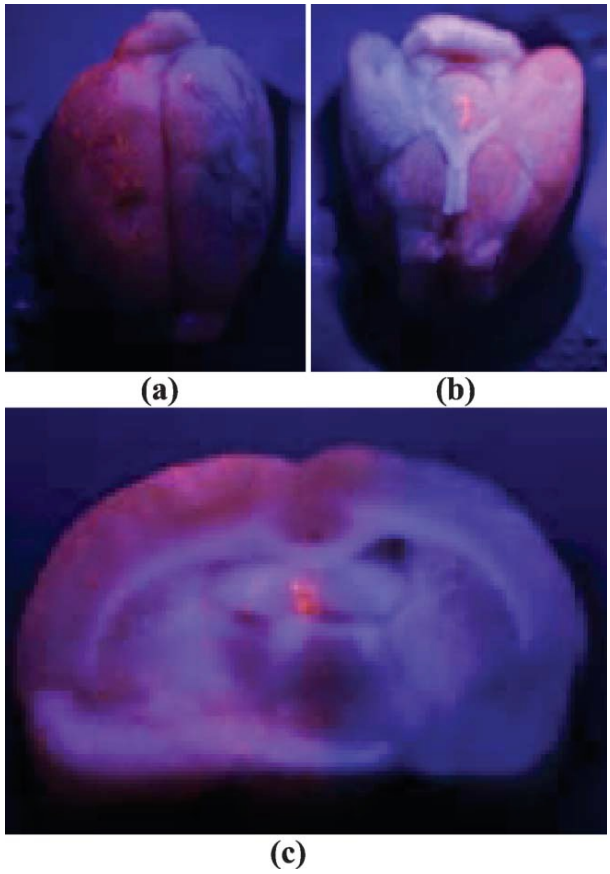

Figure 23: Gross views of a rat brain labelled with TAT-conjugated Qd; (a) and (b) represent dorsal views and (c) represents coronal section. Reprinted from (Santra et al., 2005)

Recently Pahuja et al demonstrated trans BBB delivery of dopamine loaded nanoparticles reverse functional deficit in parkinsonian rat. They have developed dopamine-loaded PLGA nanoparticles to deliver dopamine to the brain. Slow and consistent release of dopamine from PLGA nanoparticles, showed reduced clearance of dopamine in plasma, reduced quinone adduct formation, and decreased dopamine autoxidation. The nanoparticles internalized SH-SY5Y cells shows that dopaminergic neurons in the substantia nigra and striatum, regions are affected during parkinsonism. Treatment with these nanoparticles did not cause any reduction

in cell viability and morphological deterioration in SH-SY5Y, as compared to bulk dopamine-treated cells. This study demonstrate that these particles were able to cross the BBB and capillary endothelium in the striatum and substantia nigra in a 6-hydroxydopamine induced rat model of Parkinson disease. Systemic intravenous administration caused increased levels of dopamine and its metabolites and reduced dopamine-D2 receptor super sensitivity in the striatum of parkinsonian rats (figure 24). Dopamine delivered through this nanoformulation did not cause additional generation of ROS, dopaminergic neuron degeneration, and ultrastructural changes in the striatum and substantia nigra as compared to 6-hydroxydopamine induced rats. Dopamine delivery through nanoformulation neither caused alterations in the heart rate and blood pressure nor showed any abrupt pathological change in the brain and other peripheral organs (Pahuja et al., 2015).

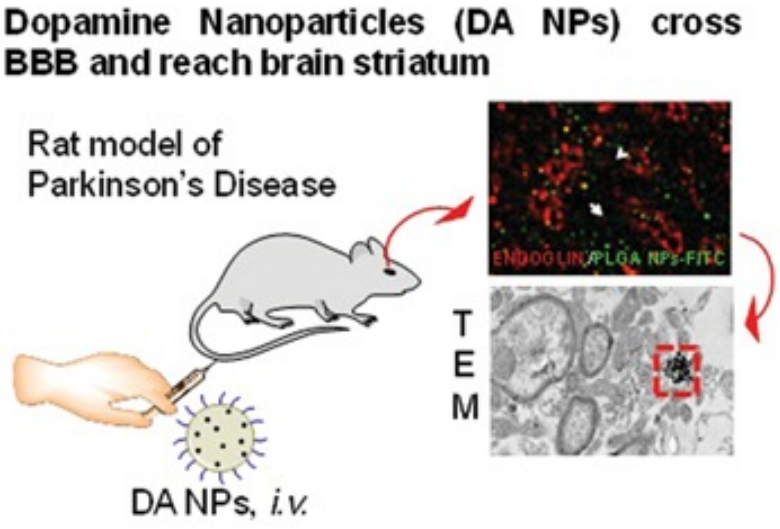

Figure 24: Delivery of dopamine nanoparticles across the BBB using dopamine loaded PLGA nanoparticles in Parkinson rat. Reprinted from (Pahuja et al., 2015)

2.5. Hybrid Nanomaterials For Imaging And Therapy

Multifunctional nanoparticles that can combine various properties have attracted a great deal of attention due to their increasing and important applications in the biomedical field. Hybrid nanosystems are the outcome of recent efforts to incorporate multiple functions into a single unit. If more than one type of nanostructure can be incorporated in a system, they have great potential to achieve multiple functions. These nanosystems which can be used as carriers for diagnostic and therapeutic agents usually exhibit the properties of all the parental systems.These materials are of great interest in biomedical applications due to their potential use in multiple parallel applications.

Lot of studies were reported on the use of hybrid nanomaterials for various applications in the last few years. In 2003 Banarjee et al (Banerjee and Wong, 2003) demonstrated a rational approach for in situ mineralization of crystalline CdTe quantum dots on the surfaces of oxidized multiwalled carbon nanotubes (MWNTs) through chemical recognition (figure 25).

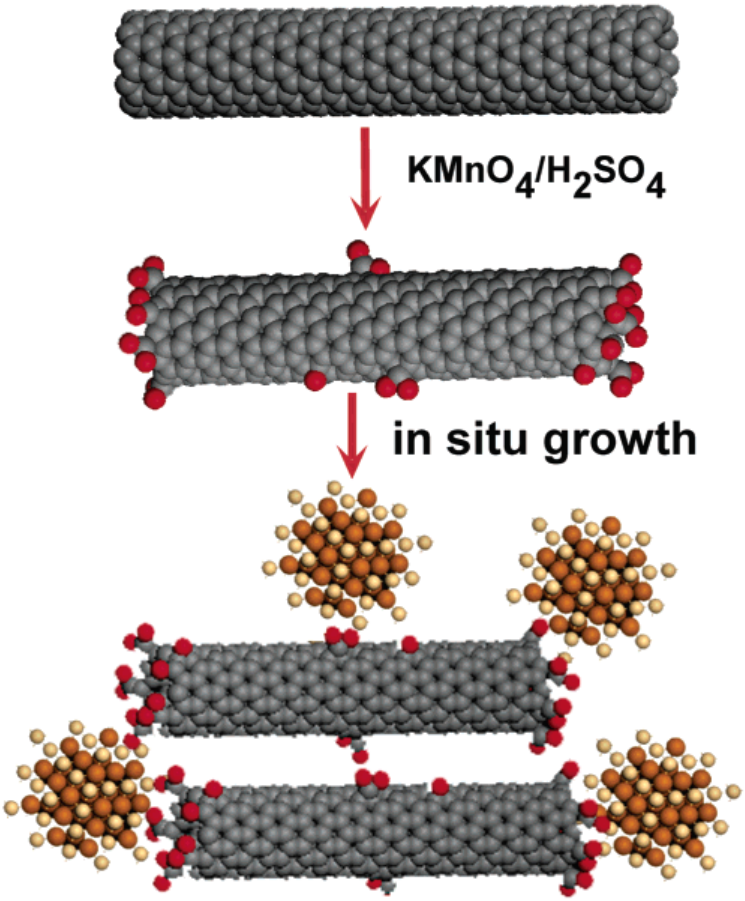

Figure 25: Schematic illustration of various steps in the growth of the nanotube- nanocrystal heterostructure. Reprinted from (Banerjee and Wong, 2003)

Quantum dot activated fluorescent multiwalled carbon nanotubes were demonstrated for the fluorescence imaging application *in vivo* (Shi et al., 2007). Similarly Jia et al explored dual functionalized carbon nanotube delivery system containing antisense oligodeoxynucleotides as a therapeutic gene and CdTe quantum dots as fluorescent labeling probes via electrostatical layer-by-layer assembly (Jia et al., 2007).

Micellar hybrid nanoparticles (MHNs) with magnetic iron oxide and quantum dot with doxorubicin having long-circulation, provide simultaneous targeted drug delivery and dual-mode NIR fluorescence imaging and MRI (figure 26) of diseased tissue in vitro and in vivo (Park et al., 2008). Quantum dots Conjugated with Fe_3O_4-filled CNT for cancer targeted imaging and magnetically guided drug delivery was

demonstrated which facilitates magnetically guided delivery and improved the synergetic targeting efficiency (Chen et al., 2012).

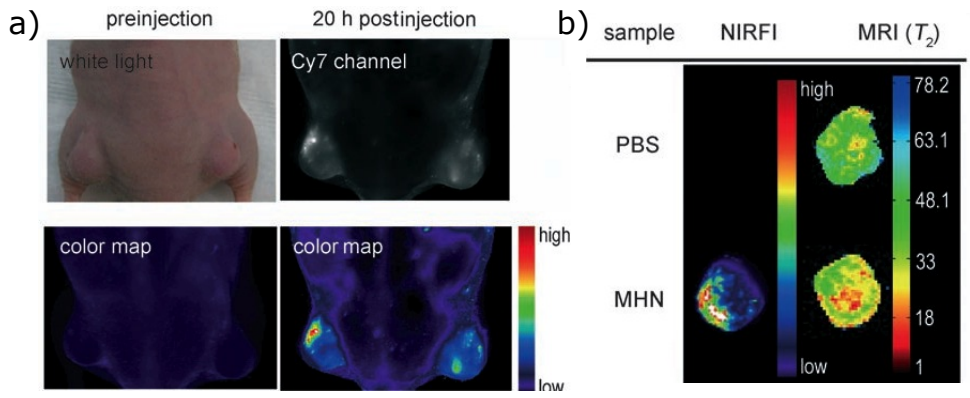

Figure 26: NIR fluorescence images showing the passive accumulation of MHNs containing QDs in a mouse with MDA-MB-435 tumors (a). Image table describing the results of multimodal imaging (by MRI and NIR fluorescence) of the tumor harvested from the mouse of control and treated mice group (b). Adapted from (Park et al., 2008)

A series of studies have been repeated recently based on various application of hybrid nanomaterials. Some of them include gold nanoparticles quantum dot (Kulakovich et al., 2002) (Oh et al., 2005), (Pons et al., 2007), gold nanoparticles iron oxide (Bao et al., 2007), (Xu et al., 2007), gold nanorod iron oxide (Gole et al., 2008), gold nanorod quantum dot (Xia et al., 2011), iron oxide carbon dot (Wang et al., 2014), single wall carbon nanotube gold nanparticle (Wang et al., 2012), iron oxide quantum dot (Yi et al., 2005) (Sathe et al., 2006) (Fan et al., 2010) which were used for imaging and therapeutic application.

CHAPTER 3

MATERIALS AND METHODS

In order to meet the objectives of the proposed study, NIR emitting gold quantum clusters with glutathione and lipoic acid and a hybrid nanomaterials with single wall carbon nanotube and quantum dots were developed. Detailed synthesis procedure and experimental characterizations are explained in this chapter.

3.1 Synthesis Of NIR Emitting Gold Cluster

3.1.1. Synthesis Of Gold Quantum Cluster (AuC) With Gutathione (GAuC)

3.1.1.1. Materials

Chloroauric acid, glutathione reduced (GSH), mercaptosuccinic acid (MSA) were purchased from sigma, Bangalore, India. Sodium borohydride, was purchased from Merck India Pvt.Ltd. All the chemicals were used as such without any further purification unless stated. All the glass wares were cleaned using aqua regia (1:3 ratios of HCl and HNO_3). The water used in all experiment was Millipore Milli Q grade (18MΩ-cm).

3.1.1.2. Synthesis Of Gold Nanoparticles (GMSA)

Four different gold clusters were synthesized by etching of gold nanoparticles with reduced glutathione. In a typical experiment, 49 mg $HAuCl_4$ and 37 mg MSA were dissolved in 25 mL Milli Q water and allowed to keep for 30 minutes. To this system 0.2 M sodium borohydride was added at 0^oC and allowed to react for another 1 h.

The resulting brown colored solution was precipitated in methanol and centrifuged 4 times to get MSA gold nanoparticle (GMSA). GMSA particles were lyophilized and the powdered samples were kept in vacuum desiccators.

3.1.1.3 Synthesis Of Different Sized Gold Quantum Cluster (AuC)

Different sized AuC's were synthesized by etching of GMSA with GSH by varying reaction temperature and pH of the reaction. For the preparation of the entire sample 1: 4 (w/w) ratio of GMSA and GSH were used. For the preparation of sample 1, GSH was mixed with GMSA at room temperature and pH was adjusted to 1.5. The reaction was continued for 12 h in room temperature.

Sample 2 were synthesized in the same procedure explained for sample 1 except 12 h reaction was continued at 70^{o}C after adding GSH at room temperature. Similarly sample 3 was prepared by adding GSH at 0^{o}C to GMSA and the reaction was continued for 12 h at a temperature 70^{o}C. Sample 4 was prepared by the addition of GMSA and GSH at room temperature and the pH was adjusted to 10 and the etching process was allowed to complete for 12 h at 70^{o}C.

For the synthesis of NIR fluorescing gold nano cluster, GMSA was treated with GSH at 0^{o}C. All the AuC's were purified at 3000 rpm for 5 min to remove heavy particles. Supernatants were precipitated in 1:1 ratio of methanol isopropanol to get crude cluster.

3.1.1.4 Description Of Experimental Techniques

3.1.1.4.1 Absorbance Spectral Measurements.

Absorbance of the materials were observed for the diluted samples using UV-1800 schimandzu UV Spectrometer.

3.1.1.4.2 Emission Spectral Measurements.

Photoluminescence study was conducted using a dilute solution of AuC. PL spectra were recorded using a Cary Bio 500 instrument using a 1 cm pathlength quartz cuvette.

3.1.1.4.3 Fourier Transform Infra Red Spectroscopy.

FT IR spectra were recorded using Thermo Nicolet, Madison, USA. Spectra were recorded by KBr pellet method.

3.1.1.4.4 Zeta Potential And Particle Size Analysis.

Zeta potential of the materials were measured using nano ZS (Malvern, UK).

3.1.1.4.5 Matrix Assisted Laser Deposition Mass Spectroscopy (MALDI).

The synthesized clusters were characterized using MALDI. MALDI was recorded using a Shimadzu KRATOS analytical AXIMA- CFR plus. 20µL of the synthesized cluster in 1:1 water methanol mixture was used for the study. α- cyanohydroxy cinnamic acid matrix was used and the spectrum was recorded from 2000 to 25000 at 160 mW laser power. Mass analysis was confirmed using m mass software (mass spectrometry tool, www.mmass.org).

3.1.1.4.6 High Resolution TEM.

TEM images of the samples were recorded using JEOL 3010; 300 KV HRTEM. Diluted samples were drop casted on a formvar coated copper grid and dried it in room temperature and imaged .

3.1.1.4.7 X Ray Photo Electron Spectroscopy (XPS).

XPS spectra of the developed nanoclusters were measured by drying the sample on silica substrate at room temperature. XPS measurement was performed using an electron spectrometer (XPS, Kratos Analytical, Shimadzu, Japan). The X-rays from the Al Kα line at 1253.6 eV (15 kV, 20 mA) were used for excitation. Photoelectrons were collected in the constant analyzer energy mode with a pass energy of 20 eV.

3.1.1.4.8 Quantum Yield (QY) Measurement.

QY of the developed material were evaluated spectro fluorimetrically by comparing with a dye which is having an emission overlapping with that of the developed materials. Here Nile blue was chosen as a standard dye. For the QY of nano clusters, absorbance of cluster and Nile blue was kept as 0.1. Fluorescence were recorded using fluorolog 3 spectrofluorimeter and the area under the curve is evaluated using the software. QY was calculated using

$$QY = QY_{ref} (\eta / \eta_{ref})^2 (I / I_{ref})$$

3.1.1.4.9 X Ray –CT Imaging.

X ray attenuation of the developed materials were monitored using clinical X ray CT scanner (Philips iCT 256). 1 mg/ mL of the samples were taken in an eppendorf tube and bare tube served as control.

3.1.1.4.10 Optical Imaging.

Optical imaging capability of the developed nanoparticles were evaluated using Xenogen IVIS spectra (Caliper life sciences, USA) instrument using 450 nm excitation filter and 750 nm emission filters. For this 1 mg/ mL concentration of the nanoparticles were taken in a black colored well plate and the image were acquired.

3.1.2 Synthesis Of NIR Emitting Gold Quantum Cluster Using Lipoic Acid (LAuC)

3.1.2.1 Materials

Chloroauric acid and lipoic acid (LA) were purchased from Sigma, Bangalore, India. Sodium borohydride, sodium hydroxide and hydrochloric acid were obtained from Merck India Pvt. Ltd. All the chemicals were used as such without any further purification unless stated. All the glass wares were cleaned using aqua regia (1:3 ratios of HCl and HNO_3). The water used in all experiment was Millipore Milli Q grade (18 MΩ.cm).

3.1.2.2 Synthesis Of Lipoic Acid Cluster (LAuC).

2.4 mg of LA (1.5 mM) was dissolved in 8 mL de-ionized (DI) water and stirred at room temperature (25 °C). To this, 40 µL of NaOH (1 M) was added and stirred for 30 min, followed by the drop-wise addition of 80 µL $HAuCl_4$ (50 mM) and incubated for 15 min. When the solution became colorless, 160 µL of 50 mM ice-cold $NaBH_4$ was added. After 24 h the solution became bright yellow in color. This solution was centrifuged at 15000 rpm for 15 min in 1:1 methanol-isopropanol mixture and lyophilized to get LAuC.

3.1.2.3 Description Of Experimental Techniques.

UV Visible, fluorescence, FT IR, Zeta potential, MALDI, TEM, XPS, Quantum yield, X-ray CT and optical imaging were monitored as explained in the section 3.1.1.4

3.2 Gold Clusters As A Novel Sensor

3.2.1 Materials

Chloroauric acid, glutathione reduced (GSH), mercaptosuccinic acid (MSA), albumin and glucose was purchased from sigma, Bangalore, India. Sodium borohydride, urea, creatinine and sodium chloride were purchased from Merck India Pvt.Ltd. Urease enzyme was obtained from crest biosystem (Goa, India). All the chemicals were used as such without any further purification unless stated. All the

glass wares were cleaned using aqua regia (1:3 ratios of HCl and HNO_3). The water used in all experiment was Millipore Milli Q grade (18MΩ-cm).

3.2.2 Synthesis Of Gold Quantum Clusters (GAuC):

GMSA were synthesized as explained in section 3.1.1.2

For the synthesis of NIR fluorescing gold nano cluster, GMSA was treated with GSH at 0^oC. In a typical experiment, 2.8 mg GMSA at pH 1.5 and 12 mg GSH (at 0^oC) were dissolved in 30 mL MQ water. After 15 min this system was allowed to react at 70^oC at 500 rpm for 24 hrs. As the time progress, the color of the solution changed from brown to yellow.

3.2.3 Urease Immobilization To AuC (Urease @)GAuC):

For the immobilization of GAuC with urease, 9 mL of AuC was treated with 1 mL (1: 9 ratio of urease and water) urease enzyme which was added sidewise at a pH of 5.3 under very slow stirring at 0^oC and allowed to react for another 2 hrs. Urease@GAuC were centrifuged twice as done for the purification of GAuC.

3.2.4 Description Of Experimental Techniques

UV Visible, fluorescence, FT IR, Zeta potential, MALDI, TEM, XPS and Quantum yield were monitored as explained in the section 3.1.1.4

3.2.4.1 Detection Of Urea In Blood Serum

Blood samples from healthy donors were collected and allowed to clot for 30 min. After removing the clot the blood cells were centrifuged (Biofuge stratus, Heracus

instrument, Germany) at 3000 rpm for 10 min. The serum (supernatant) was separated and was washed repeatedly.

The serum samples were spiked with different amounts of urea and incubated for 30 min. About 10 μg/ mL of Urease@GAuC was treated with 20 μL of control serum and the urea spiked serum. The change in fluorescence intensity at 750 nm was monitored. The procedure was repeated with the serum samples of different patients and the values obtained were compared with those of a clinically followed method.

3.2.4.2 Whole Blood Assay

The blood samples were layered on trisodium citrate (38 mg trisodium citrate for 10 mL blood) to prevent clotting and spiked with different amounts of urea. 20 μL of samples containing different amounts of urea were added to 10 μg/ mL of Urease@GAuC and the variation in fluorescence intensity at 750 nm was monitored in each case.

3.2.4.3 Detection Of Urea In Milk

The milk samples adulterated with different concentration of urea (20 μL) were treated with 10 μg/ mL of Urease@GAuC and the emission intensity at 750 nm was monitored.

3.2.4.5 Comparison With Clinical Method.

For the clinical estimation of urea urease enzyme converts urea into NH_3 and CO_2. The color developing reagent convert NH_3 into a colored complex and the color developed depends on the amount of urea present in it. For quantification, different

concentration of urea was prepared from the stock solution and was quantified using the absorbance value at 600 nm. The obtained result was compared with our method. The change in intensity versus concentration was plotted by known concentration of urea using both methods. From the calibration plot obtained, the unknown concentration can be estimated.

3.3 Gold Clusters For Targeted Tumor Imaging And Photodynamic Therapy

3.3.1 Materials

Chloroauric acid ($HAuCl_4$), lipoic acid (LA), hexamethylenediamine (HMDA), folic acid (FA), 1-Ethyl-3-(3-dimethylaminopropyl)carbodiimide (EDC), *N*-Hydroxysuccinimide (NHS), protoporphyrin IX (PPIX), calcein propedium iodide and hoescht were purchased from Sigma, Bangalore, India. Sodium borohydride ($NaBH_4$) sodium hydroxide (NaOH) and hydrochloric acid (HCl) were obtained from Merck India Pvt. Ltd. Modified Eagle Medium (MEM), Hams F12 medium, fetal bovine serum (FBS) and trypsin were obtained from Himedia. All chemicals were used as such without any further purification unless stated otherwise. All glass wares were cleaned using aqua regia (1:3 ratios of HCl and HNO_3). The water used in all experiment was Millipore Milli Q grade (18 MΩ.cm).

3.3.2 Synthesis Of Lipoic Acid Cluster (LAuC)

LAuCs were synthesized as explained in section 3.1.2

3.3.3 Folic Acid Functionalization To LAuC (FLAuC)

LAuC (2 mg) was dispersed in 5 mL DI water. 0.25 mL EDC (0.05 M) in water was added and the pH was adjusted to 4 and stirred for 2 h. Subsequently, 0.25 mL NHS (0.05 M) in water was added followed by the addition of folic acid (4 mM, 2 mL) under basic pH. The pH of the solution was then adjusted to 9 and the reaction was continued for another 12 h. The reaction mixture was centrifuged at 15000 rpm for 15 min in 1:1 methanol-isopropanol mixture and washed twice with DI water to obtain FLAuC.

3.3.4 Conjugation Of PPIX To FLAuC (PFLAuC)

FLAuC (2 mg) was dispersed in 5 mL DI water. 0.326 mg of Boc protected HMDA in methanol, EDC (0.25 mL, 0.05 M) and NHS (0.25 mL, 0.05 M) were added. After 12 h, HMDA conjugated FLAuC was separated by centrifuging at 15000 rpm for 15 min in 1:1 methanol-isopropanol mixture. This was treated with trifluoroacetic acid (TFA) and water (1:1, 5 mL), stirred for 3 h and the solution was centrifuged at 15000 rpm for 15 min in 1:1 methanol/ isopropanol mixture. The resulting product, AFLAuC was re-suspended in DI water. 2 mg AFL-AuC dispersed in 5 mL DI water was added to EDC/NHS (as mentioned before) activated PPIX (1 mg in 0.001 N NaOH). Reaction was continued for 12 h, followed by centrifugation at 15000 rpm for 15 min in 1:1 methanol/ isopropanol mixture, washed with water twice, dried and used for further study.

3.3.5 Description Of Experimental Techniques

Emission Spectral Measurements, FT-IR, Zeta potential and Particle size analysis, Matrix Assisted Laser Deposition Mass spectroscopy (MALDI), quantum yield measurement, High resolution TEM studies were done as explained in the section Description of Experimental Techniques 3.1.4.

3.3.5.1 Quantification Of Ligand

Number of moles of FA and PPIX present in the FLAuC and PFLAuC were estimated using UV-Visible spectroscopy. A calibration plot was drawn using known concentrations of FA and PPIX. The amount of unbound ligands was determined from the absorption of the supernatant obtained after centrifugation of FLAuC and PFLAuC. Deducting this from the initial value will yield the number of ligands present on FLAuC and PFLAuC.

3.2.5.2 Fluorescence Life Time Measurement

Fluorescence lifetimes of the developed nano system were measured using IBH (FluoroCube) time-correlated picoseconds single photon counting (TCSPC) system. Solutions were excited with a pulsed diode laser (<100 ps pulse duration) at a wavelength of 440 nm (NanoLED-10) with a repetition rate of 1 MHz. The detection system consists of a microchannel plate photomultiplier (5000U-09B, Hamamatsu) with a 38.6 ps response time coupled to a monochromator (5000M) and TCSPC electronics (DataStation Hub including Hub-NL, NanoLED controller and preinstalled Fluorescence Measurement and Analysis Studio (FMAS) software). The

fluorescence lifetime values were determined by deconvoluting the instrument response function with biexponential decay using DAS6 decay analysis software.

3.3.5.2 Singlet Oxygen Efficacy And Quantum Yield

Singlet-oxygen-generation studies were performed with a 200 W mercury lamp light source on an Oriel optical bench with a grating monochromator . The intensity of the light was kept constant throughout the irradiations by measuring the output with an Oriel photodiode detection system.

Quantum yields of the singlet oxygen generation were monitored by dissolving PFLAuC and PPIX in methanol. Absorbance of both the materials was kept same at 530 nm, since the excitation filter used was 530 nm. DPBF (1,3-Diphenylisobenzofuran) is a convenient acceptor because it absorbs in a region of dye-transparency and rapidly scavenges singlet oxygen to give colorless products. 10 μL of DPBF was added to both PFLAuC and PPIX and monitored the decrease in intensity upon irradiation with 530 nm light. The decrease in absorbance was monitored from 0 S to 6 S for both PFLAuC and PPIX.

3.3.5.7 *In Vitro* Cytotoxicity Study

In vitro cytotoxicity of LAuC, FLAuC and PFLAuC were measured by MTT assay which measures the metabolic reduction of MTT reagent to colored formazan by viable cells. For determining the cell viability, normal cell line L929 mouse fibroblast cells were seeded in a 96-well tissue culture plate at 5 $x10^3$ cells/well in

100 µL MEM containing 10 % FBS. After achieving 40 - 50 % confluence cell lines were exposed to various concentrations of LAuC, FLAuC and PFLAuC (1 mg, 0.5 mg, 0.1 mg, 0.05 mg, 0.01 mg, 0.005 mg, 0.001 mg). After 72 h, the derivatives in the medium were removed and washed with phosphate buffered saline. To that 50 µL of MTT (2 mg/mL in MEM) and 200µL of media was added and incubated for 4h under 37^{o}C and 5% CO_2. Four hours later, MTT was removed and 100 µ L of isopropanol was added into each well. The absorbance of the resulting solution was recorded immediately at 570 nm using automated micro plate reader (BioTek Instruments, Vermont, USA). Results were expressed as absorbance after blank (i.e., cells without material) subtraction. Reported values are mean of three replicates.

% Cell Viability = ([Abs]sample/[Abs]Control) x 100.

3.3.5.6 Cellular Uptake

C6 cells were cultured with 1: 1 ratio of MEM and F12 Ham media containing 10% FBS in 5 % CO_2 and 37^{o}C. Cellular uptake and Photodynamic therapeutic efficacy of the nanomaterials were checked. For cellular uptake, to the confluent cell monolayer 1 mg/ mL of the materials (LAuC, FLAuC and PFLAuC) were added and incubated for 3h. The cells were then washed with PBS and stained with hoescht. The uptake efficacy of the developed material was checked using Leica fluorescence microscope (DMI 4000, Germany).

3.3.5.7 Targeted Photodynamic Therapy (PDT) *In Vitro*

For targeted PDT efficacy of the developed material towards cancer cell, C6 cells were incubated with PFLAuC for 3 h. After 3 h of particle incubation to a monolayer

of cells, 530 nm laser was irradiated for 30 S. After 30 S the cells were washed with PBS and stained with calcein propedium iodide. Live and dead cells were assessed using fluorescence microscope (DMI 4000, Germany).

3.3.5.8 Tumor Model Development

C6 rat glial cells were grown in 1 :1 ratio MEM and Hams F12 media supplemented with 10 % FBS. The confluent cell monolayer was trypsinized. The tripsinized cell pellets were resuspended in Matrigel (BD biosys). About 150 µL of the cells were injected subcutaneously in the flank area of mice (Swiss Albino). Tumor volume was monitored in each day.

3.3.5.9 Animal Imaging

When the tumor volume reached around 0.7 cc 0.5 mL (1mg/ mL) nanoparticles (LAuC, FLAuC and PFLAuC) were injected through tail vein injection (i.v). Tumor imaging was done using Xenogen IVIS (Caliper life science) after 3 h of injection.

3.3.5.10 PDT *In Vivo*

For targeted PDT, PFLAuC was injected intravenously and a 532 nm laser was irradiated for 15 min. A tumor bearing mice without particle was irradiated with laser and served as control. Tumor volume was monitored every day using vernier calipers. Also we monitored the collagen concentration based on the peak at 360 nm, total hemoglobin concentration and redox ratio based on the peaks of FAD and NADH using a fiber optic accessory of a spectrofluorimeter (Fluorolog 3) using excitations of 320 nm and 410 nm respectively.

$$\text{Redox ratio} = \frac{\text{Fluorescence intensity ofFAD}}{\text{Fluorescence intensity of (FAD + NADH)}}$$

$$\text{Total hemoglobin concentration} = \frac{\text{Fluorescence intensity at 500 nm}}{\text{Fluorescence intensity at 570 nm}}$$

3.3.5.11 Histopathological Evaluation

On 7th day, the animals were sacrificed and the tissue sections were fixed in formalin. These tissues were processed using standard techniques for histopaathologic study (See the appendix). The Hematoxylene Eoisin stained sections were monitored under microscope (Leica).

3.4 Gold Clusters For Blood Brain Barrier (BBB) Targeted Imaging

3.4.1 BBB Targeting Using GSH Stabilized Quantum Cluster

3.4.1. 1 Materials

Chloroauric acid, glutathione reduced (GSH), mercaptosuccinic acid (MSA), L-dopa, MTT, hoescht, EDC and NHS were purchased from sigma, Bangalore, India. Sodium borohydride was obtained from Merck India. bEnd 3 (BALB/c cerebral endothelial cells)cells were purchased from ATCC. DMEM, FBS, pencilin and streptomycin were obtained from Himedia. All the chemicals were used as such without any further purification unless stated. All the glass wares were cleaned using aqua regia (1:3 ratios of HCl and HNO_3). The water used in all experiment was Millipore Milli Q grade (18MΩ-cm).

3.4.1. 2 Synthesis Of GSH Stabilized Gold Quantum Clusters (GAuC)

GAuC was synthesized by etching of gold nanoparticles with reduced glutathione as explained in section 3.1.2 .

For the synthesis of NIR fluorescing gold nano cluster, GMSA was treated with GSH at 0^oC. In a typical experiment, 2.8 mg GMSA at pH 1.5 and 12 mg GSH (at 0^oC) were dissolved in 30 mL MQ water. After 15 min this system was allowed to react at 70^oC at 500 rpm for 24 hrs. As the time progress, the color of the solution changed from brown to yellow. GAuC were centrifuged at 3000 rpm for 10 minutes.

3.4.1. 3 Conjugation Of L- Dopa To GAuC (Dop@GAuC)

5 mg of synthesized GAuC was dissolved in 5 mL DI water. 0.05 M EDC was added and pH adjusted to 4 and stirred for 2 h. NHS (0.05 M) was added followed by the addition of L- dopa in basic pH. Final pH of the solution was set as 9 and the reaction was continued for another 12 h. Dop@GAuC was centrifuged at 15000 rpm for 15 min in 1:1 methanol isopropanol mixture. Washed twice with DI water to remove excess of unreacted ligands.

3.4.1.4 Development Of In Vitro BBB Model.

For the construction of BBB models, transwell inserts (millipore, 0.4 micron) were first placed into a culture plate well, and DMEM growth medium was added to the basolateral side of each well until the membrane in each insert was completely moistened with the growth medium. Then bEnd.3 cells were seeded onto the inside of the insert above the membrane at a seeding density of 1×10^4 cells/well and

cultured in DMEM growth medium with 10% fetal bovine serum. Cells were maintained at 37 °C and 5% CO_2 in a humidified incubator.

3.4.1.5 Description Of Experimental Techniques

Emission Spectral Measurements, FT-IR, Zeta potential and Particle size analysis, Matrix Assisted Laser Deposition Mass spectroscopy (MALDI), High resolution TEM studies were done as explained in the section Description of Experimental Techniques 3.1.4. Cell viability of the developed materials (GAuC & Dop@GAuC) were assessed using MTT as explained in section 3.3.5.7.

3.4.1.5.1 Barrier Potential Measurement In b-End3 Cell

Barrier potential of the cells were measured using Milli Cell ERS (Millipore). Cells were cultured on a transwell membrane having 0.4 micron pore size (Millipore) by keeping it on a 12 well cell culture plate. Monitored the barrier potential in each day. After 6^{th} day the potential of the cell reached around 1548 ± 35 Ω. For cell material interaction we chose the time as 6 day from the date of seeding.

100 µL of the 1 mg/ mL of GAuC and Dop@GAuC was added to each well and monitored the change in potential for 30 S, 1 h, 2 h, 3 h, 6 h and 24 h. Barrier potential were measured and each material was done in triplicate. Cell without material was served as a control.

3.4.1.5.2 Barrier Permeability Measurement In b-End3 Cell

For the barrier permeability of the material for BBB, after addition of 100 µL of the 1 mg of GAuC and Dop@GAuC, media in the 12 well plates were collected after 1

h, 2 h, 3 h, 6 h and 24 h. Amount of nanoparticles present in the collected media were estimated spectrometrically by drawing the calibration plot of known concentration of GAuC and Dop@GAuC. Cells without material and the millicell insert without bEnd3 cells were served as a control.

3.4.1.5.3 Scanning Electron Microscopy (SEM) Of b-End3 Cell

To confirm the complete monolayer formation of bEnd3 cells after 6^{th} day of cell seeding, SEM (Hitachi 2400) was carried out. Briefly, after 6^{th} day the media in the culture insert were removed and washed twice with PBS. 1% formaldehyde was added to the insert to fix the cells and kept in 4^{o}C for 12 h. Cells were dehydrated with different grades of alcohol. After critical point drying and gold coating cells were viewed under SEM (Hitachi, 2400). Millicell insert without cells and with media were served as a control.

3.4.1.5.4 *In Vitro* Celluar Uptake

Cellular uptake of GAuC and Dop@GAuC were monitored using fluorescence (Leica), and TEM (Jeol) microscope. For this cells were grown on a cover slip with a seeding density of $1x10^5$ cells/ well. When the cells become a complete monolayer 1 mg/ mL of GAuC and Dop@GAuC were added. After 3 h cells were washed with PBS.

For fluorescence microscopic study nucleus were stained with hoesct as per the manufactures instruction. Washed with PBS and fix with 1% paraformaldehyde. Washed with PBS and viewed under Leica fluorescence microscope.

For TEM studies after tripsinization and PBS wash cells were fixed in 1% glutaraldehyde. Cells were post fixed with osmium tetroxide before dehydrating with different grades of alcohol and embeded in beam capsule and bake at 60 ºC . Ultrathin sections of the cells were viewed under TEM. In all the cases cells without material was used as a control.

3.4.1.5.5 Blood Compatibility Study

3.4.1.5.5.1 Hemolysis

Blood samples were collected from healthy individuals to anticoagulant [trisodium citrate (Sigma)] containing vials. Blood was centrifuged at 3000 rpm for 3 min and washed four times in saline. 100 µL of RBC were collected and diluted to 1 mL was used for the studies. For hemolysis different concentration of GAuC and Dop@GAuC (1 mg, 0.5 mg, o.1 mg, 0.05 mg, and 0.01 mg/ mL) was added. As a control same amount of water and saline were added to RBC. Percentage hemolysis was measured using

$$\text{Percentage Hemolysis} = \frac{(\text{Absorbance of sample}) - \text{Absorbance of blank})}{\text{Absorbance of} + \text{ve control}} \text{ x } 100$$

3.4.1.5.5.2 RBC, WBC And Platelet Aggregation

Aggregation of RBC with respect to saline 1 mg of GAuC and Dop@GAuC were added to RBC in 6 well plate. The materials were incubated for 3 h. Aggregation was monitored using phase contrast microscope (Leica)

For the separation of WBC and platelet, histopack (sigma) was layered onto the anticouagulated blood. Kept it for 30 min for the formation of 3 layers. Top 2 layer contains WBC and Platelet. Both these layers were collected carefully and centrifuged at 1000 rpm for 10 min. 1 mg of the samples were added to WBC and platelet and aggregation was monitored under phase contrast microscope.

3.4.1.5.6 *In Vivo* Brain Imaging

Healthy adult mice was chosen as the animal model for early stage diagnosis of brain disorder. The animals were anesthetised using Xylazine (5mg/kg) and Ketamine (50mg/kg) with a premedication of atropine (0.05mg/kg). From 1 mg/ mL of GAuC and Dop@GAuC (0.5 mL) were administered into the mice through tail vein injection. Brain imaging was done after 1 h injection of the material using Xenogen IVIS (caliper life science) instrument. Spectral unmixing was done to remove the noise from the image.

3.4.1.5.7 Fluorescence Signal From The Brain Tissue.

The animals were sacrificed and brain tissue were collected and fix it in formaldehyde. Fluorescence image from the tissuctions were monitored by giving 450 nm excitation and collected in the red region using fluorescence microscope (Leica)

3.4.2 BBB Targeting Using Lipoic acid Stabilized Quantum Cluster

3.4.2.1 Materials

Chloroauric acid, alpha lipoic acid (LA), L- dopa, MTT, hoescht, EDC and NHS were purchased from sigma, Bangalore, India. Sodium borohydride was obtained from Merck India. bEnd 3 (BALB/c cerebral endothelial cells)cells were purchased from ATCC. DMEM, FBS, pencilin and streptomycin were obtained from Himedia. All the chemicals were used as such without any further purification unless stated. All the glass wares were cleaned using aqua regia (1:3 ratios of HCl and HNO_3). The water used in all experiment was Millipore Milli Q grade (18MΩ-cm).

3.4.2.2 Synthesis Of Lipoic Acid Stabilized Gold Quantum Cluster (LAuC)

LAuC was synthesized by one step reaction with $HAuCl_4$ and alpha lipoic acid with sodium borohydride as explained in section 3.2 .

3.4.2.3 Conjugation Of L- Dopa To LAuC (Dop@LAuC)

5 mg of synthesized LAuC was dissolved in 5 mL DI water. 0.05M EDC was added and pH adjusted to 4 and stirred for 2 h. NHS (0.05 M) was added followed by the addition of L dopa in basic pH. Final pH of the solution was set as 9 and the reaction was continued for another 12 h. Dop@LAuC was centrifuged at 15000 rpm for 15 min in 1:1 methanol isopropanol mixture. Washed twice with DI water to remove excess unreacted ligands.

In vitro model and rest of the characterizations were done as explained in the section 3.4.1.1 c to 3.4.1.5.

3.5 Hybrid Nanomaterial For Tumor Targetted Imaging And Photothermal Therapy.

3.5. 1. Materials

Sodium sulphite, Selenium metal powder, Zinc oxide, Cadmium chloride and cysteine were purchased from Merck India Pvt. Ltd. Folic acid, EDC, DCC, NHS,

and DMAP were purchased from Sigma, Bangalore, India. Single wall carbon nano tube (pristine) was obtained from Sigma Aldrich, USA. All the chemicals were used as such without any further purification unless stated. The water used in all experiment was Millipore Milli Q grade (18 MΩ.cm). Breast adenocarcinoma cells (MCF7), Human cell derived from pancreatic cancer: Ductal origin (PANC1) and mouse connective tissue (L929) fibroblast cells were obtained from Riken Bioresource Center, Japan for in vitro cellular assessment of the developed nanosystem. All media and stains for cell culture studies were purchased from Sigma Aldrich and Life Technologies, USA.

3.5.2 Synthesis Of Cadmium Selenium Quantum Dot (Qd):

Selenium stock solution was prepared by dissolving 0.4 M and 0.2 M sodium sulphite and selenium metal powder in 25 mL DI water at 75^{o}C for 3h. 10 mM Cadmium chloride and 10 mM Zinc oxide were dissolved in 10 mL DI water and the pH was adjusted to 11, after adding 1.3 x 10^{-3} moles of cysteine to this mixture. To this solution 10 mM selenium stock solution was added at 60^{o}C. The reaction was continued till the solution became yellowish green. This solution was precipitated in isopropanol and centrifuged twice at 5000 rpm for 15 min.

3.5.3 Synthesis Of Quantum Dot Conjugated Carbon Nanotube (Qd @CNT):

1 mg SWCNT was dissolved in 1% DMF and stirred till the SWCNT was completely dispersed. 0.5 mL of 0.5mM DCC was added to the SWCNT solution and pH was adjusted to 4 and stirred for 2h. After 2h, DMAP was added and stirred for another 30 min. 5 mL of 1% DMF dispersed quantum dot were added to the above solution by making final pH 9. The developed hybrid system was purified by ultra centrifugation at 15000 rpm for 30 min.

3.5.4 Folic Acid Functionalization On Qd @CNT (FaQd@CNT):

Qd@CNT was dispersed in 5 mL DI water. 1.5 $x10^{-5}$ moles of folic acid were added to Qd@CNT using EDC and NHS. Briefly 200 µL of EDC was added to Qd@CNT and pH was adjusted to 4 using 0.001 N HCl and stirred for 3 h. After 3 h, NHS was added to the system followed by addition of 1.5 $x10^{-5}$ moles of folic acid and then pH was adjusted to 9. The reaction was carried out for 12 h.

Synthesized FaQd@CNT was purified by centrifuging at 15000 rpm for 30 min.

3.5.5 *Description Of Experimental Techniques*

Emission Spectral Measurements, FT-IR, Zeta potential and Particle size analysis, High resolution TEM studies were done as explained in the section Description of Experimental Techniques 3.1.4.

3.5.5.1 Raman Spectra

Raman spectra were recorded using LabRAM, HR-800, HORIBA Jobin Yvon. Samples were dried in glass slides and imaged under Raman spectrometer using 720 nm lasers.

3.5.5.2 Photothermal Efficacy

SWCNT, Qd, Qd@CNT, FaQd@CNT solutions were irradiated by 800 nm [Chameleon Ultra diode Pumped Mode Locked- Sub 200 Femtosecond Laser (Coherent 80 MHz repetition rate)] at 1.726 W/cm^2 for 4 minutes, and the temperature was measured with an IR thermal camera [Thermal imager test 881-2 (Testo AG, Lenzkirch Germany)]. All the experiments were conducted at room temperature.

3.5.5.3 *In Vitro* Cytotoxicity

Cyto toxicity of the materials were evaluated using MTT assay in L929, MCF-7 and Panc-1 cells (Rickens, Japan). The protocol used was explained in section 3.2.5.7. MTT was assessed using a microplate reader (multidetection microplate scanner; Dainippon Sumitomo Pharma) by measuring the absorbance of the resultant product.

3.5.5.4 *In Vitro* Cellular Uptake

Selective internalization of nanoparticles by MCF-7 cells was demonstrated with and without folic acid. For folate specific target uptake cells were grown in folate enriched DMEM supplemented with 10 % FBS and antibiotics. Folate depletion of MCF7 cells were done by growing the cells in RPMI media without folic acid. Cells

were cultured in a glass bottom dish in both the condition. 1 mg/ mL of Qd@CNt and FaQd@CNT were added to cells with folate receptor and without folate receptor. After 3 h cells were washed with PBS and the nucleus were stained with hoest as per manufactures instruction. Images were taken using a 100X oil-immersion objective lens. The cells were viewed under a confocal microscope (IX81; Olympus Corp., Tokyo, Japan) with a confocal scanning unit (CSU-X1, Yokogawa Electric Corp., Tokyo, Japan) and a CCD camera (iXon DU897, Andor Technology, Belfast, UK).

3.5.5.5 Cancer Cell Destruction *In Vitro* (PTT)

Cells incubated with particles for 3 h were irradiated with 800 nm laser [Chameleon Ultra diode Pumped Mode Locked- Sub 200 Femtosecond Laser (Coherent 80 MHz repetition rate)] at 1.726 W/cm^2 for 4 minutes, and the temperature was measured with an IR thermal camera [Thermal imager test 881-2 (Testo AG, Lenzkirch Germany)]. Cells were washed with PBS and live dead assay was done using calcein propedium iodide live dead stain. Live dead assay was done as per manufactures instruction. Stains were viewed under confocal microscope using 4X objective.

CHAPTER 4

RESULTS

The size tuneable properties of nanomaterials offer wide range of application in various branches science including biomedical applications. Fluoresccing nanomaterials in the NIR region help to avoid interference with the biological system for various applications like biomolecular sensing, disease diagnosis and therapy. The present study mainly focuses on the use of nanotechnology in the field of bioanalyte detection, early stage disease diagnosis and treatment. NIR emitting gold quantum clusters having varied properties were developed and were analysed to evaluate structure property relation of cluster. A novel nanosensor was developed for the detection of urea in blood and milk using gold quantum cluster. For early stage tumor diagnosis and its therapy were also demonstrated using gold quantum cluster and a hybrid nanomaterial. Gold quantum cluster mediated blood brain barrier targeted brain imaging and drug delivery was evaluated. Detailed results of the above studies are included in this chapter.

4.1 Synthesis And Optimization Of NIR Emitting Gold Quantum Cluster

4.1.1 Synthesis Of Gold Quantum Cluster (AuC) Using Glutathione (GSH)

NIR emitting materials are of much importance in the medical diagnosis owing to its efficacy to overcome autofluorescence from the tissue/ cells. Glutathione stabilized

gold quantum cluster (GAuC) is one among the well studied cluster by utilizing the most beautiful gold thiol chemistry.

Here, we developed four different GAuCs by varying the reaction parameters like addition temperature of GSH to GMSA, reaction pH and reaction temperature for optimizing the property of the cluster and thereby choose the most appropriate one for the rest of the studies. Proposed schematic illustration is shown in figure 27

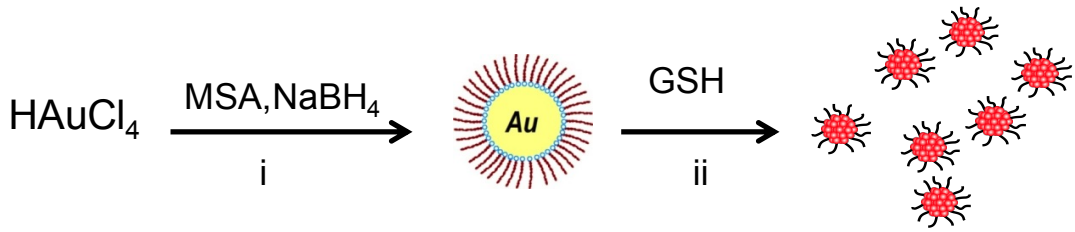

Figure 27: Schematic representation of the synthesis. Reduction of gold chloride using $NaBH_4$ to form gold nanoparticles- GMSA (i). Etching of GMSA with GSH by varying the temperature from 0^oC to 70^oC and pH between 1.5 and 10 (ii).

In the UV- visible spectra all the materials (Figure 28a) showed different band origin. The band origins were found to be 1.53 eV, 1.87 eV, 1.79 eV, and 1.69 eV for samples 1, 2, 3 and 4 respectively.

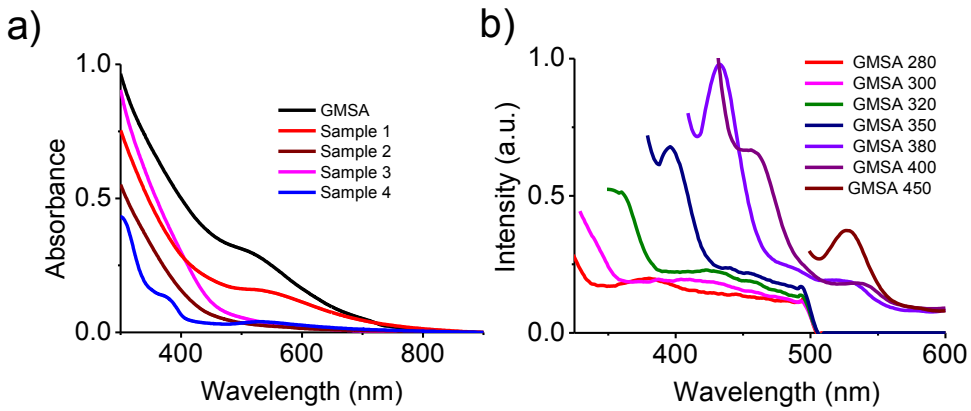

Figure 28: Absorbance spectra of GMSA and the developed sample (a) and fluorescence emission of GMSA upon different excitation (b)

Single photon luminescence of GMSA shows excitation dependent emission characteristics (figure 28b). Fluorescence spectra of different AuC samples were studied for same concentrations. Sample 1, 2, and 3 showed almost same emission wavelength in the range of 750 nm with varying fluorescence intensity upon 450 nm excitation (Figure 29), as 450 nm is the maximum excitation for all these samples. Additionally, there is a peak around 530 nm, which is also having varied intensity in all the three cases. This was attributed due to the fluorescence from GMSA (Figure 28b) from the fluorescence of GMSA at different excitation. However, among the four samples, sample 4 showed emission in the visible region around 410 nm.

The ratios of intensity of 750 nm to 530 nm peaks for sample 1, 2 and 3 were found to be 1.2, 2.5 and 50.42 respectively. Quantum yield of the molecules were calculated in comparison with nile blue (a standard dye), sample 3 showed optical quantum yield of 24% in comparison with sample 1 (0.85%) and sample 2 (2.5%).

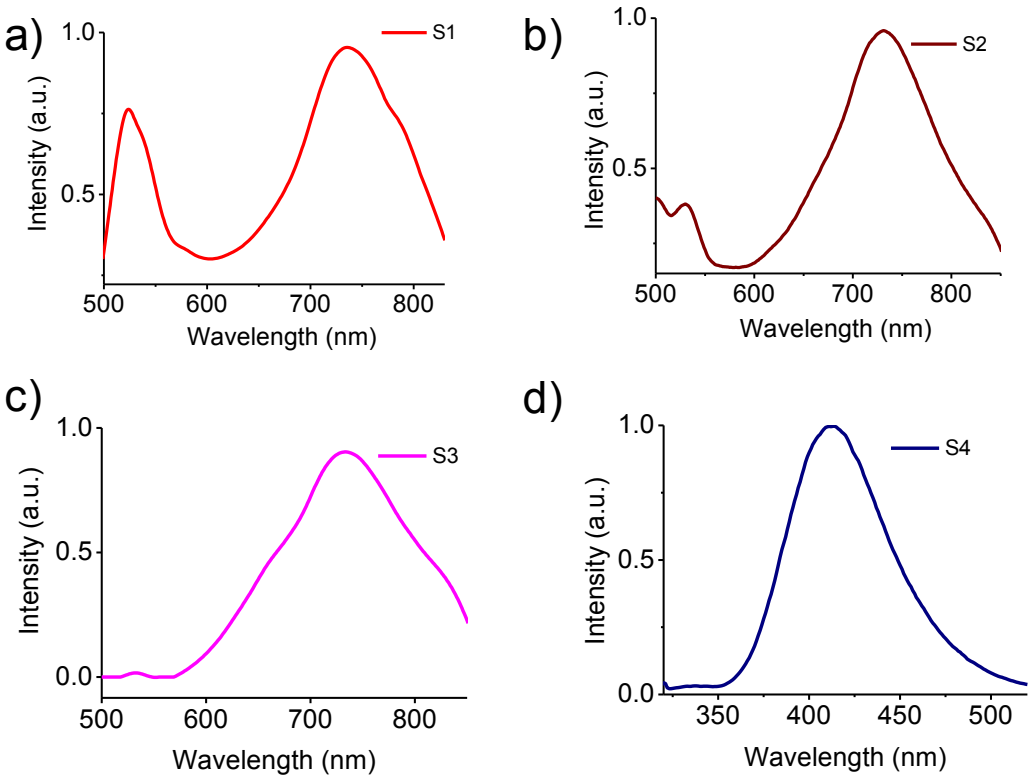

Figure 29: Fluorescence spectra of different AuC samples. Sample 1(a), Sample 2 (b), Sample 3 (c), Sample 4 (d)

Mass analysis was carried out using MALDI MS (Figure 30) method. From the fluorescence and band gap results, the number of gold core atoms was assigned as 33 for sample 1 to 3 and 8 for sample 4. On assigning the number of gold atoms, the number of ligands was calculated from MALDI spectra. The numbers of ligands were found to be 28 for Sample 1 and 2, 11 for sample 3 and 2 for sample 4.

This assignment was confirmed with theoretical mass analysis using *m mass* software. From the experimental and theoretical observation the composition of the developed clusters were assigmed as $(Au)_{33}(SG)_{28}$, $(Au)_{33}(SG)_{28}$, $(Au)_{33}(SG)_{11}$ and $(Au)_8(SG)_2$ for Sample 1, 2, 3 and 4 respectively.

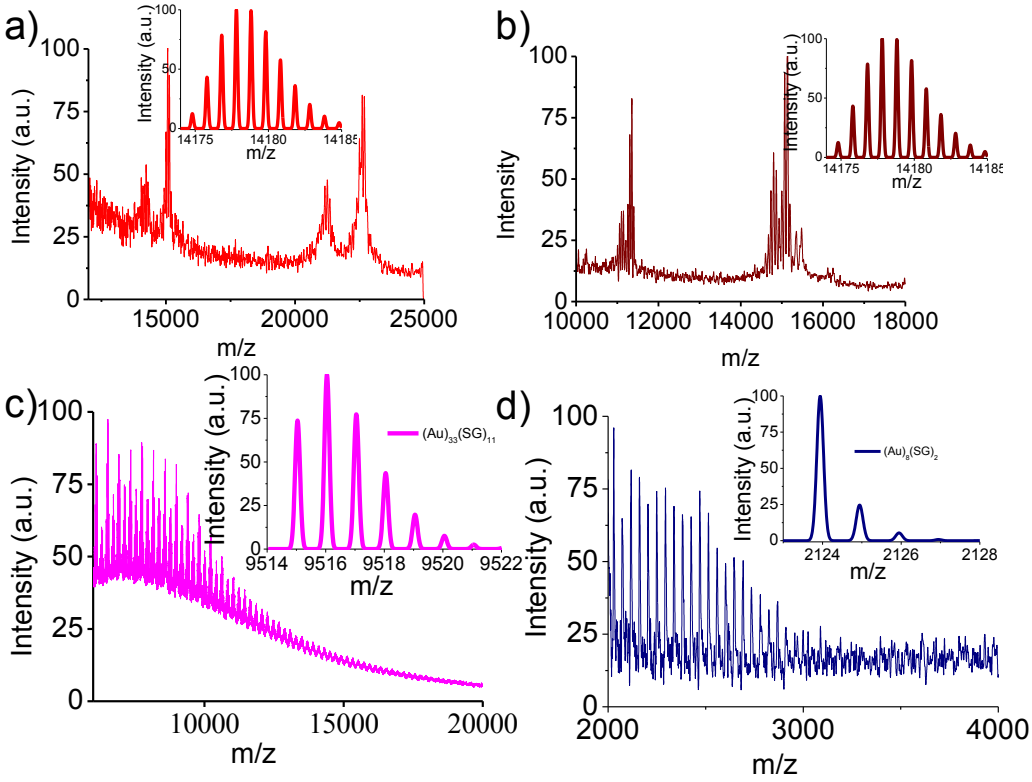

Figure 30: MALDI MS spectra of different clusters. a to d represents sample 1 to 4 respectively. Inset shows the corresponding theoretical mass spectra

In order to find out the reason for fluorescence, band gap and MALDI, we performed TEM (figure 31) to visualize all the samples. GMSA shows an average particle diameter of 7 nm (figure 31 a), Sample 1, 2 and 4 shows a particle diameter of around 1 to 2 nm and sample 3 shows 0.7 nm. TEM shows that samples 1, 2 and 4 tries to form a self assembled structures (figure 31 a, b and d) while sample 3 shows well separated structures.

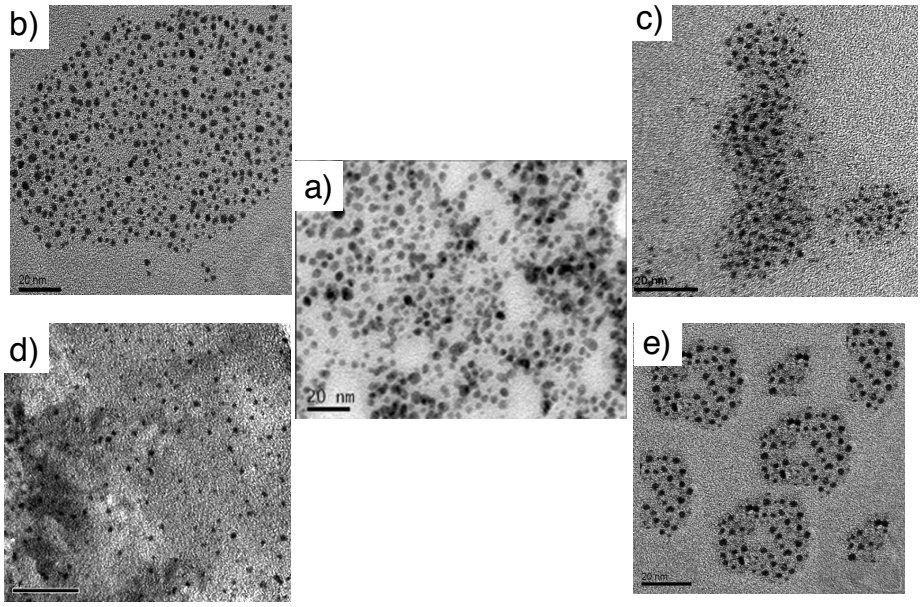

Figure 31: TEM of GMSA (a), Sample 1(b), Sample 2(c), sample 3 (d) and sample 4 (e)

XPS analysis (figure 32) was also carried out for the binding energy evaluation of the developed clusters. 85.18, 85.25, 84.83, 85.21 eV are the binding energies of Au $4f_{7/2}$ peak of Sample 1 to 4 respectively. Similarly, the values for $4f_{5/2}$ peaks are 88.90, 88.99, 88.48, 88.97 eV respectively.

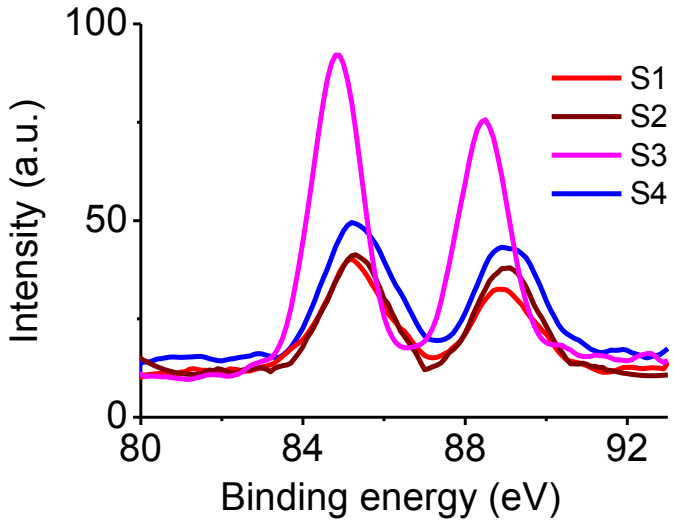

Figure 32: Binding energies of the developed cluster

Zeta potential analysis (figure 33) of the clusters were also evaluated in PBS having pH 7.4 . They showed zeta values of -19.7 mV, -23.33 mV, -20.6 mV, and -41.8 mV for samples 1, 2, 3 and 4 respectively.

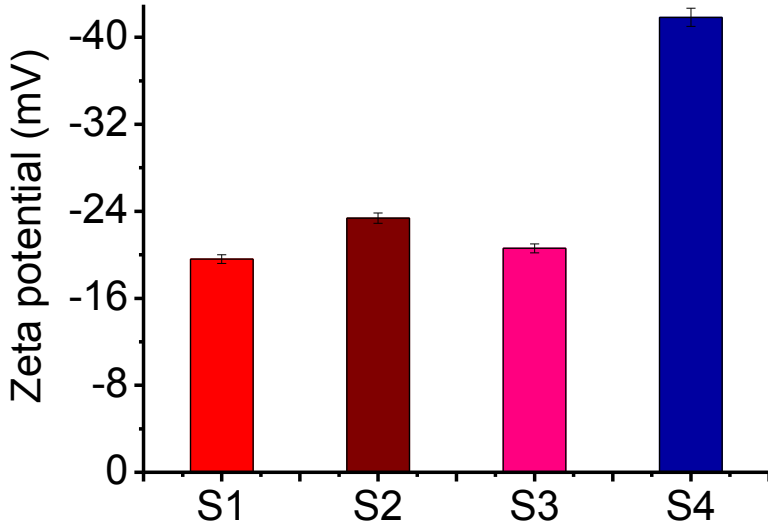

Figure 33: Zeta potential evaluation of the developed cluster

All the developed materials were subjected to fluorescence imaging (figure 34) and Xray CT imaging (Figure 35). Fluorescence imaging shows that S3 has maximum fluorescence intensity than other three samples.

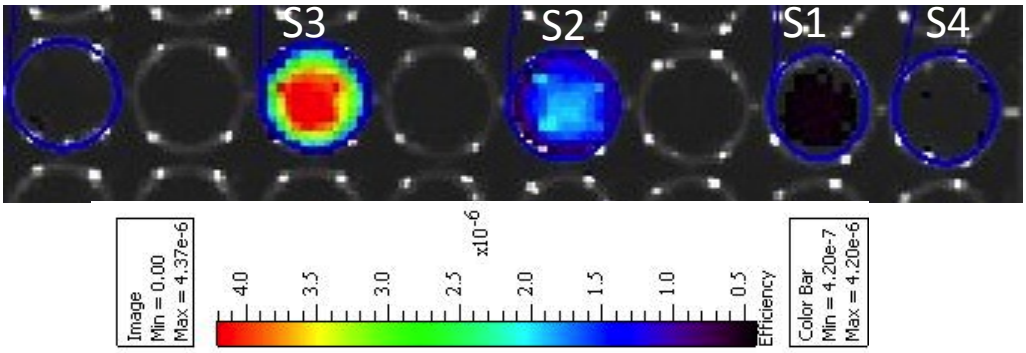

Figure 34: Fluorescence imaging of the developed nano cluster

X ray attenuation of the materials as evaluated using clinical X ray CT scanner shows that S3 is having lower opacity as represented by the least hounsfield unit (figure 35).

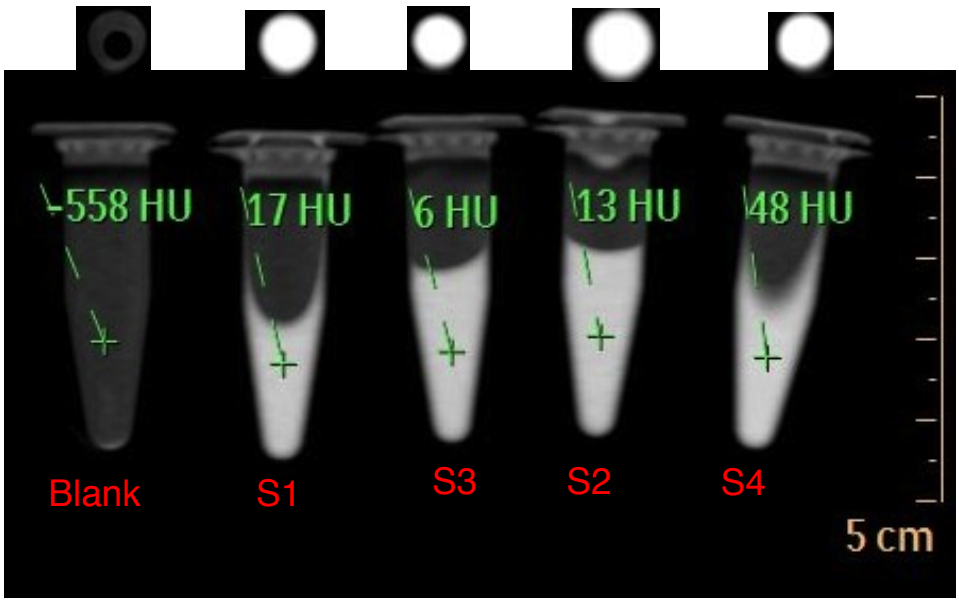

Figure 35: X ray- CT imaging of all samples. X ray intensity was shown in hounsfield unit.

4.1.2. Synthesis Of Gold Cluster Using Lipoic Acid (LAuC)

Lipoic acid stabilized AuCs were synthesized by one step procedure by reducing gold precursor with borohydride using lipoic acid. Schematic representation for the synthesis of LAuC is shown (figure 36)

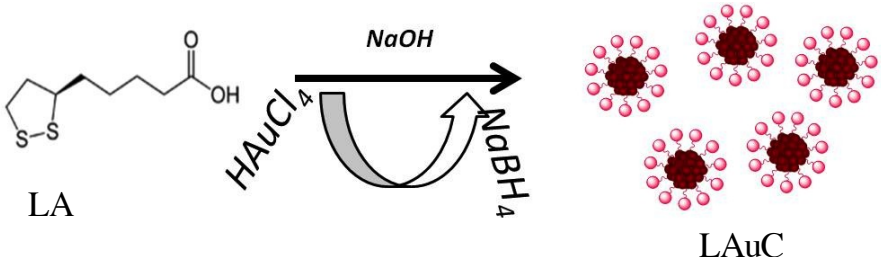

Figure 36: Schematic representation for the synthesis of LAuC

LAuC showed fluorescence emission around 720 nm (Figure 37b) and an average particle diameter c.a. 1.4 nm (Figure 4k d), both of which are characteristics of nanoclusters. HRTEM studies showed a lattice distance of 3.5 A^o for this cluster. The XRD data (figure 38a) also agrees with this result even though it shows broad peaks

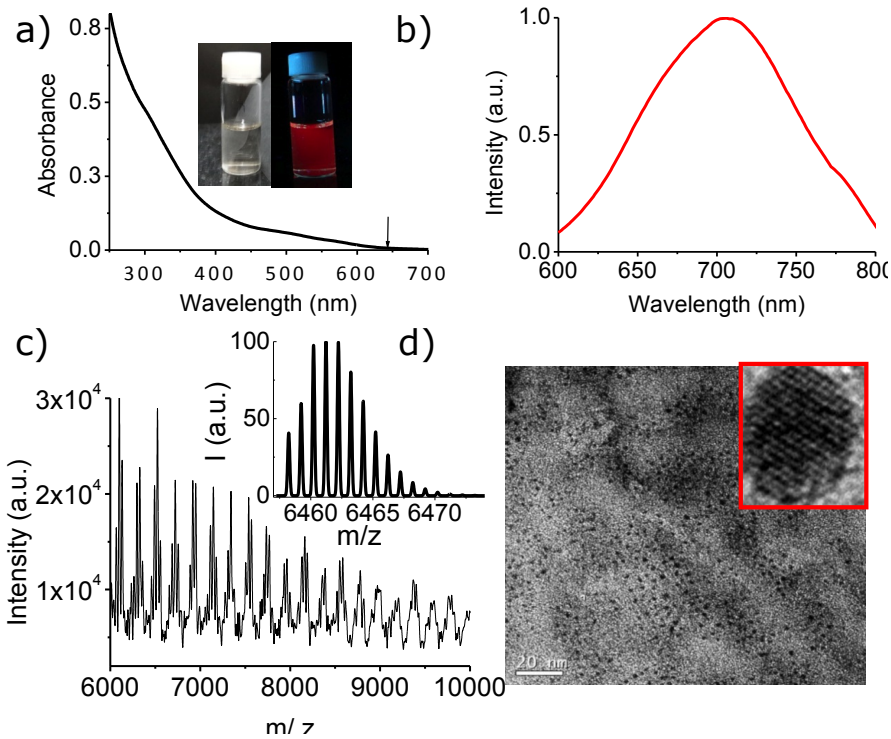

Figure 37: UV- Visible absorption spectrum (a), fluorescence emission spectrum (b) , MALDI- MS spectrum (c) and HRTEM (d) with the lattice spacing(inset) of LAuC. Photograph of LAuC under day light and UV illumination is shown as inset of (a).

Matrix assisted laser desorption ionization mass spectrometric (MALDI) analysis of LAuC showed peaks indicative of the simultaneous desorption of gold and sulphur atoms for each laser fluencies at a power of 160mW (figure 37c). From the UV absorption spectroscopy, optical band gap of LAuC was observed as 1.88 eV (660 nm) (figure 37a), which matches with the reported value for glutathione, stabilized gold cluster with 18 core atoms. Based on the results of mass spectroscopy and the observed resemblance in the optical band gap, Au atoms present in the cluster were assigned as 18. On assigning the number of Au atoms in the total mass of LAuC, the number of ligands present was calculated as 14 from the MALDI-MS peaks.

Further, this assignment was confirmed with theoretical mass spectra of the same combination with the help of mass analysis software (m mass). Theoretical (figure 37c inset) and experimental peak fragmentation showed good agreement justifying the assignment of cluster ligand ratios $(Au)_{18}(LA)_{14}$.

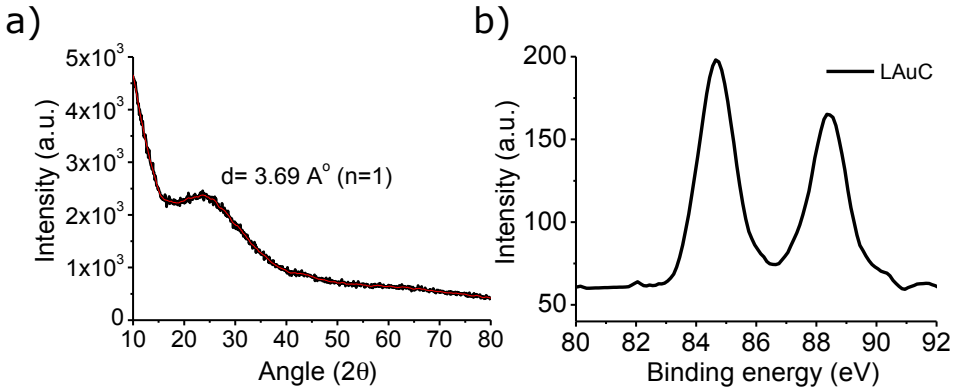

Figure 38: XRD spectra (a) and XPS (b) of LAuC

XPS analysis (figure 38b) shows that 4f $_{7/2}$ peak is situated around 84.6 eV and the $4f_{5/2}$ peaks at 88.43 eV.

FT- IR spectra (figure 39) of LAuC show that LAuC shows the absence of c.a. 2526 cm^{-1} and peaks at 1732 cm^{-1}.

Quantum yield of the developed LAuC is found to be 1%.

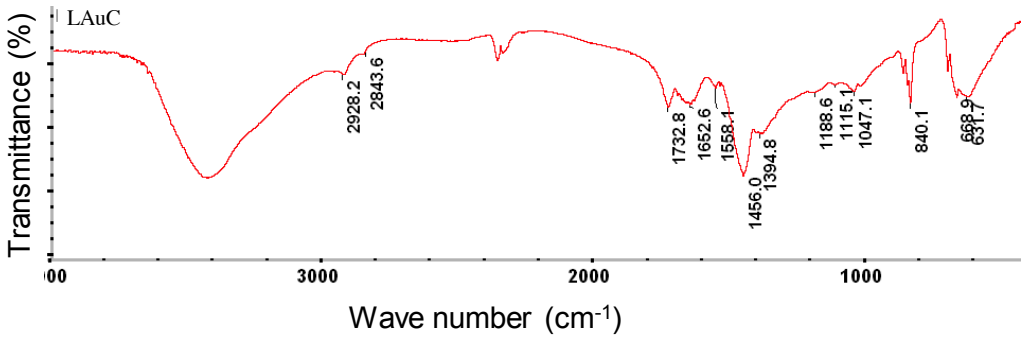

Figure 39: FT- IR spectra of LAuC

Imaging efficacy of lipoic acid stabilized clusters were also monitored using clinical X ray CT and optical imaging instrument (figure 40)

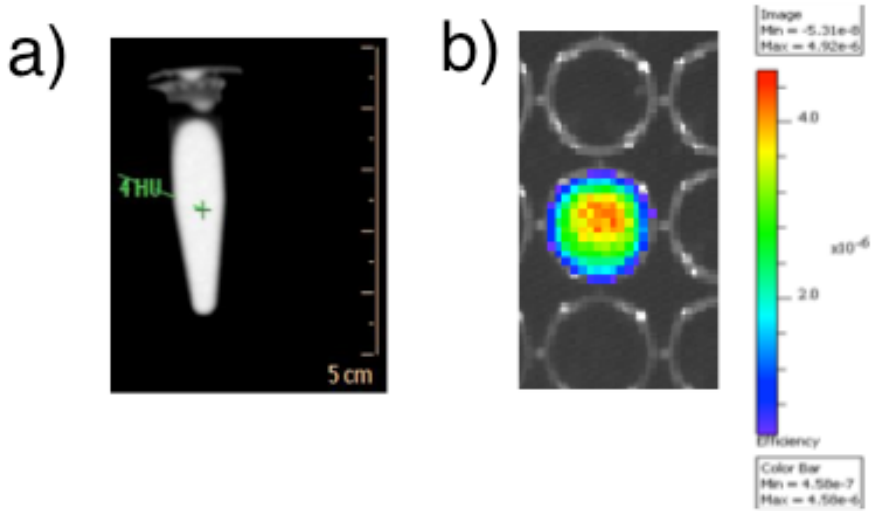

Figure 40: X- ray CT a) and optical images of LAuC b).

4.2. Gold clusters as a Novel Sensor

4.2.1 Synthesis And Characterization Of GAuC

For the development of a novel sensor sample 3 (S3) of section 4.1.1 as the starting material based on the high quantum yield and the monodisperse nature exhibited by the sample. a section. Here after it is abbrivated as GAuC and is synthesized by the process of etching mercapto succinic acid conjugated gold nanoparticles in the presence of glutathione (GSH) at 0^{o}C followed by 20 min incubation and subsequent heating at 70^{o}C, maintaining the pH at 1.5.

The quantum yield of the cluster was estimated as 25±6% using Nile blue as standard.

4.2. 2. Designing Of AuC As A Sensor For Urea

For the biosensor design, GSH protected cluster was mixed with urease which is an enzyme, specific for urea (figure 41)

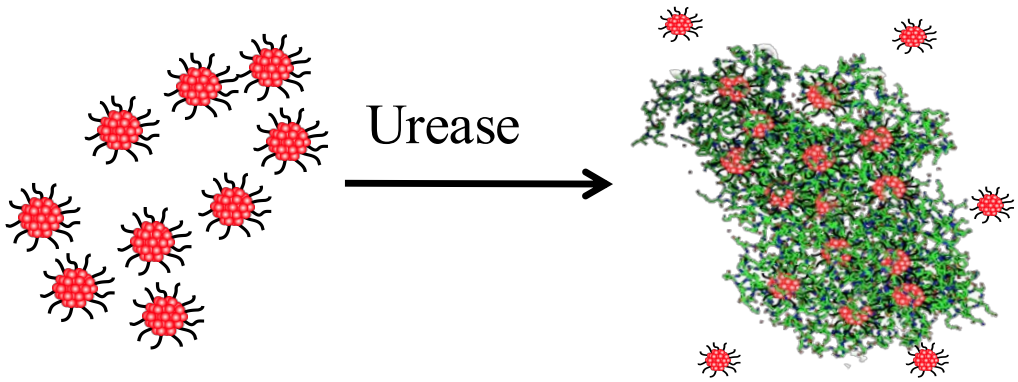

Figure 41: Schematic representation of immobilization of GAuC by urease

The urease-GAuC mixture (Urease@ GAuC) was collected by centrifugation at 8000 rpm, kept under refrigeration and used for the detection of urea.

Addition of urease to GAuC did not show any change in the fluorescence spectrum. However, the negative zeta potential of GAuC (ca. -20 mV) showed a variation to ca. -28 mV upon the addition of urease (figure 42).

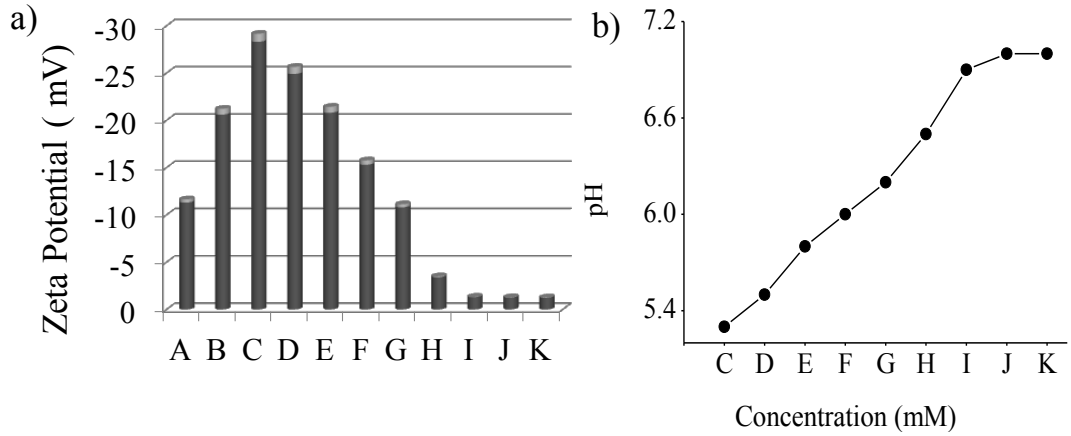

Figure 42: (a) Zeta potential of GMSA (A), GAuC (B) Urease@ GAuC (C) and on addition of 2.5, 5, 7.5, 10, 30, 50, 70 and 100 mM (D-K) of urea, respectively. (b) Corresponding pH variation.

FT- IR spectra (figure 43) of GAuC and urease mediated GAuC's (Urease@GAuC) were recorded for the confirmation of functionalization.

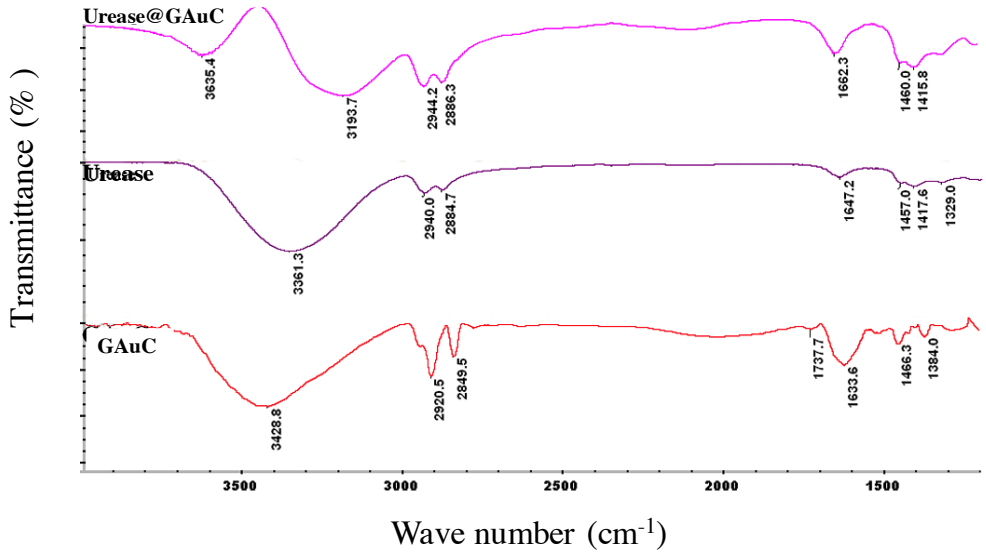

Figure. 43: FT- IR spectra of GAuC, urease and Urease @GAuC.

4.2. 3. Urea Detection Using Urease Immobilized GAuC (Urease@GAuC)

To demonstrate the urea sensing, different concentrations of urea (2.5-70 mM) were added to aqueous solutions of Urease@ GAuC (1 µg mL^{-1}) which exhibited a gradual decrease in the fluorescence emission intensity at 750 nm with the increase in the concentration of urea (figure 44). Nearly 10% fluorescence quenching was observed with addition of 2.5 mM urea, nearly 60% with 7.5 mM and 83% quenching with 50 mM (10 µL). Further addition of urea did not show any considerable quenching.

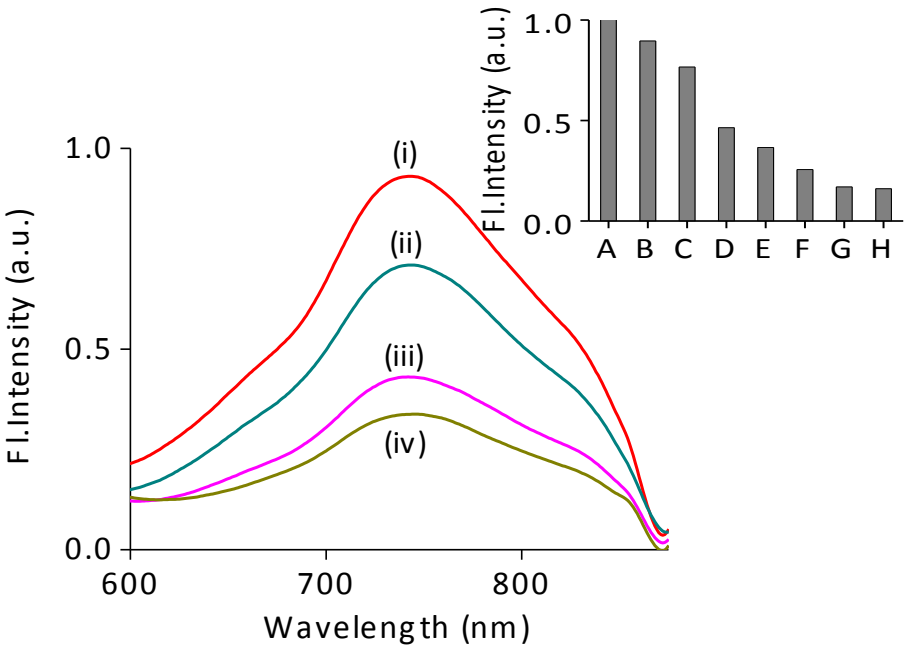

Figure 44: Concentration dependent fluorescence quenching of Urease@GAuC (10 µg/mL) upon titration with urea under aqueous condition. (i) Urease@GAuC; (ii)-(iv) upon addition of 5, 7.5 and 10 mM of urea. Inset shows the variation in the fluorescence intensity(A-H) upon addition of 0, 2.5, 5, 7.5, 10, 30, 50 and 70 mM urea, respectively (λ_{ex} = 450 nm).

The efficacy of the sensor was demonstrated for urea concentrations in blood samples in the range 2.5-10 mM, since the normal blood urea level in a healthy human body ranges from 2.5-7.5 mM and the values above and below this level indicates the need for medical attention. In a series of experiments, blood serum (20 µL samples) of a healthy person was collected and incubated with different concentrations of urea for 30 min. Serum spiked with different amounts of urea was added to Urease@ GAuC (1 µg mL^{-1}) and the fluorescence at 750 nm was recorded which exhibited a concentration dependent decrease in intensity when compared to the control serum sample (Figure 45).

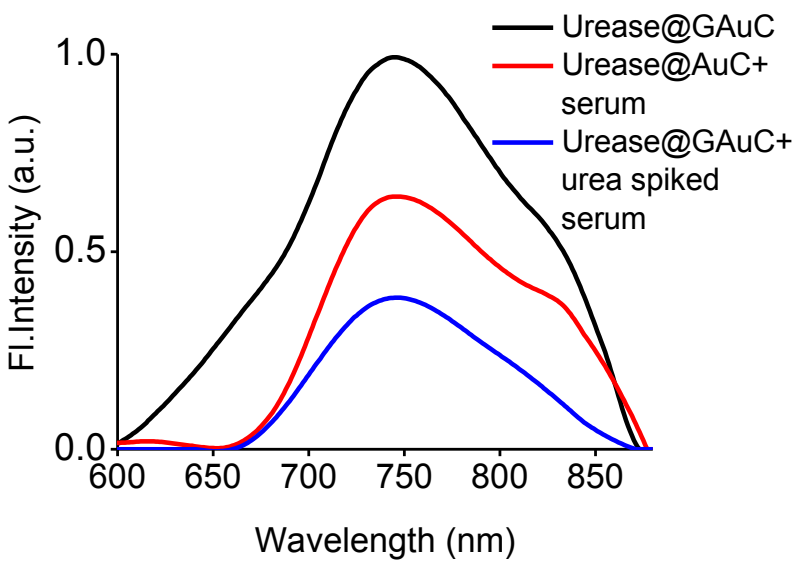

Figure 45: Fluorescence of Urease@GAuC, control serum sample and serum spiked with urea (λ_{ex} = 450 nm).

Particle size of GAuC and Urease@GAuC before and after the addition of different amounts of urea was analysed using TEM micrographs (Figure 46). GAuC and Urease@GAuC both showed an average particle size of 0.7 nm (Figure 46 a, b).The HR-TEM images after the addition of urea to Urease@GAuC showed significant increase in the size of the clusters (Figure 46 c, d).

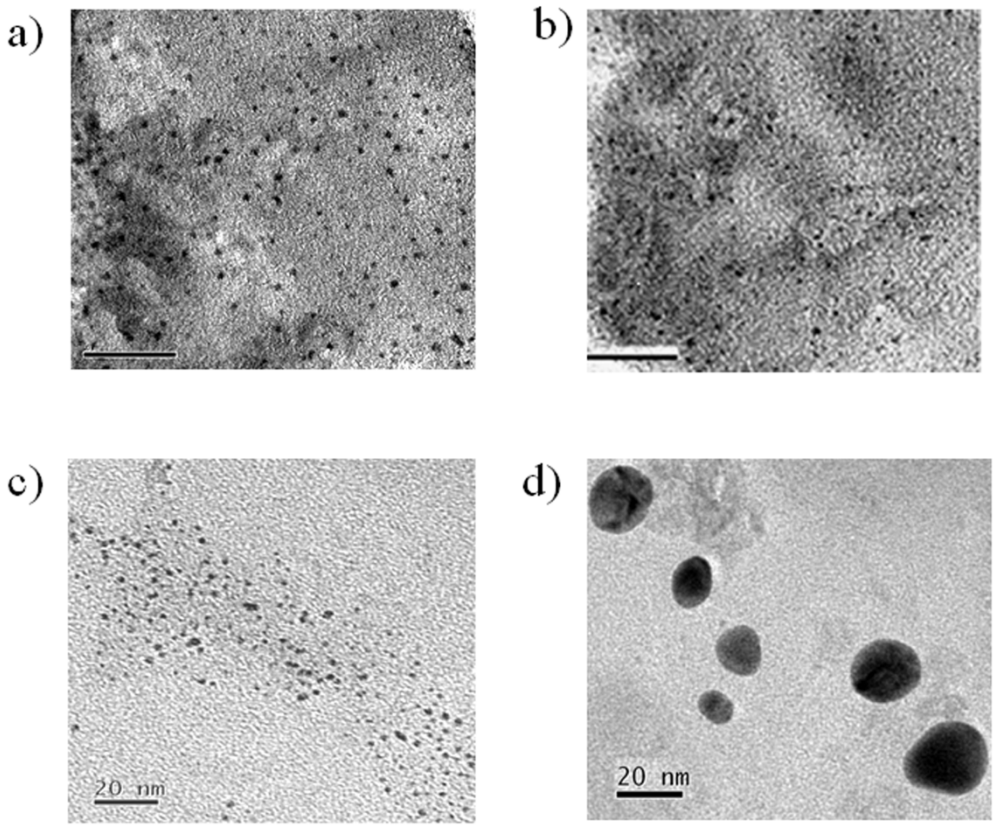

Figure 46: HR-TEM images of GAuC (a), Urease@ GAuC (b) and on addition of 2.5 (c) and 30 (d) mM of urea.

The size distribution analysis was done using TEM (figure 46). The histograms (figure 47) after the addition of 2.5 mM urea showed an average particle size of 3 nm which considerably increased to 18 nm upon addition of 30 mM urea.

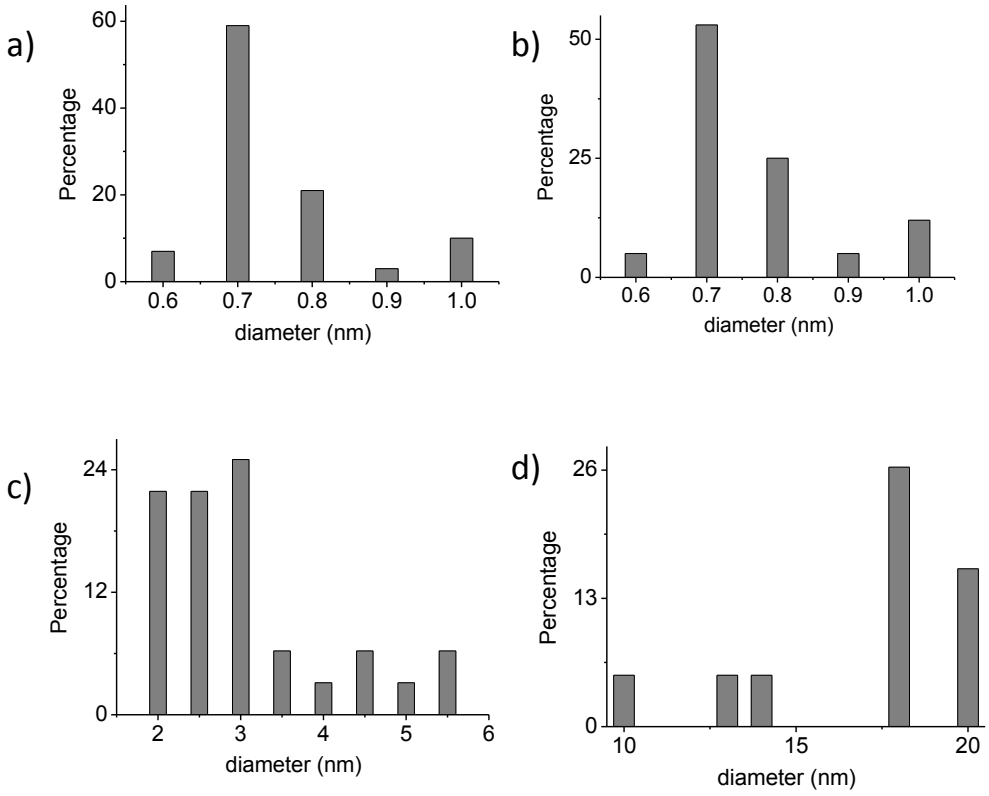

Figure 47: Size distributions by HR-TEM analysis (a) GAuC, (b) Urease@ GAuC, size distributions of Urease@ GAuC on addition of 2.5 (c) and 30 (d) mM of urea respectively.

Zeta potential of Urease@ GAuC gradually decreased from -28.3 mV to 0 mV with increase in the urea concentration (figure 42a). With the addition of 50 mM of urea, the zeta potential dropped from -28 mV to nearly zero. pH of the solution was evaluated after addition of urea. The initial pH of the Urease@ GAuC solution was 5.3 which slowly increased on the addition of urea (Figure 42b).

Effect of ammonium ions (NH_4^+) towards GAuC was carried out for the better understanding of the sensing mechanism. Presence of NH_4^+ ions showed a concentration dependent fluorescence quenching (figure 48)

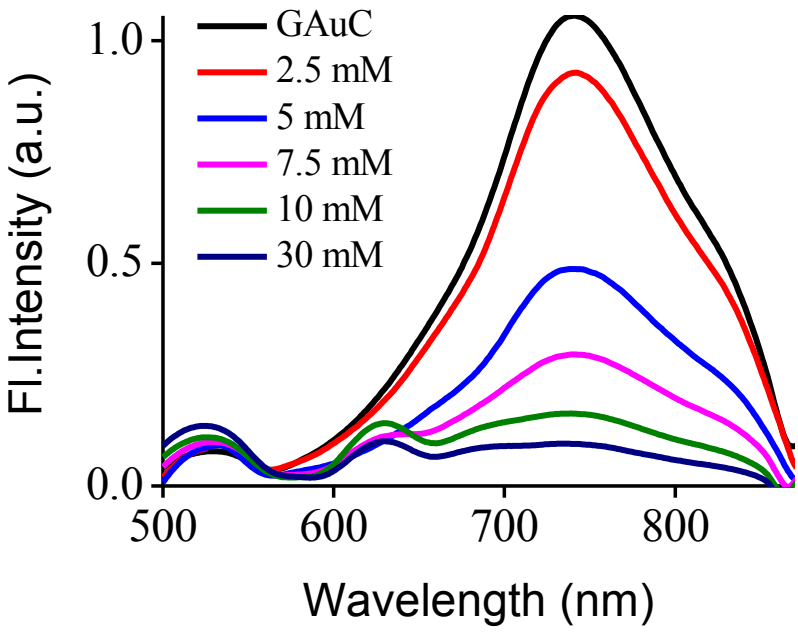

Figure 48: Effect of ammonium carbonate on GAuC (λ_{ex} = 450 nm) to establish the role of ammonium ions and pH on the fluorescence quenching.

The change in particle size of GAuC after addition of urea was monitored by TEM analysis. TEM micrographs show an increase in size upon addition of ammonia (figure 49)

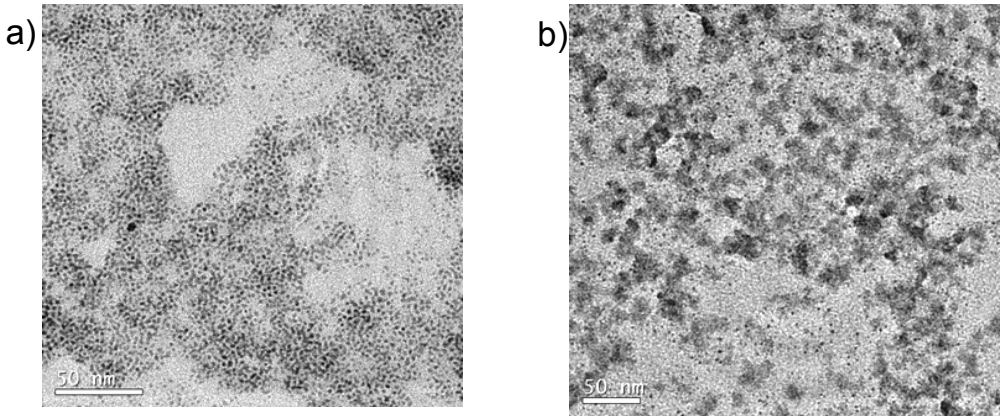

Figure 49: Effect of ammonium carbonate on GAuC to establish the ammonium ion mediated aggregation of gold clusters to large particles**.** TEM image upon addition of 2.5 mm (a) and 30 mm (b) NH_4CO_3.

Selectivity of the Urease@ GAuC for blood urea sensing was demonstrated in the serum sample collected from a healthy person. 20 μL serum was spiked with different analytes such as creatinine, glucose, uric acid, Albumin, cystein and NaCl separately followed by incubation for 30 min. Subsequently, these samples were added to Urease@ GAuC (1 μg mL^{-1}) and the fluorescence intensity at 750 nm was monitored which revealed no considerable variation. However, when a definite amount of urea was added to these solutions significant fluorescence quenching was observed indicating high selectivity of Urease@ GAuC towards urea (figure 50a). The limit of detection for urea was estimated to be 1 mM for a 5-7% quenching of fluorescence intensity when the urease to AuC ratio was maintained at 1:9 v/v.

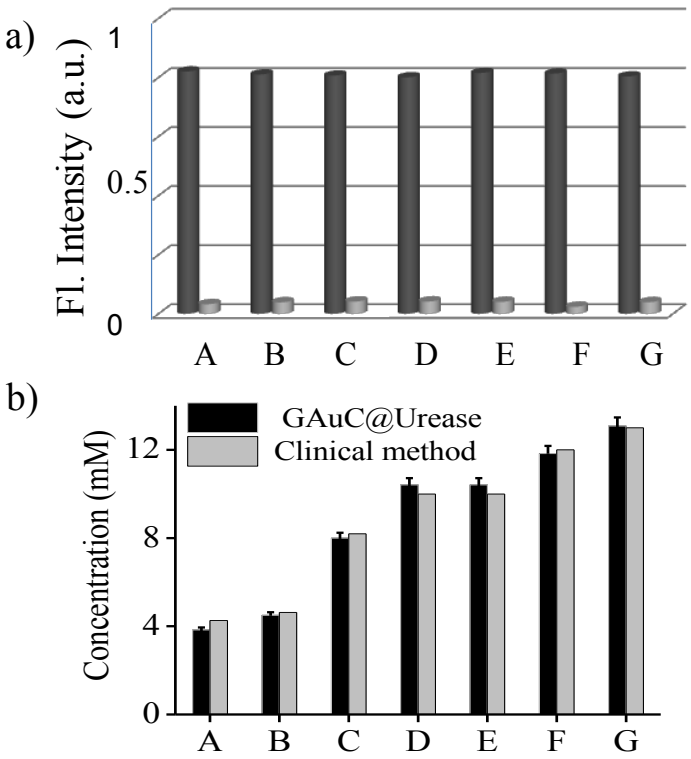

Figure 50: (a) Fluorescence intensity of Urease@ GAuC in the presence of different analytes; (A) Sensor alone (black) and after addition of urea (gray); (B-G) Sensor in presence of creatinine, albumin, glucose, uric acid, cysteine, and NaCl (black) and after addition of urea (gray). (b) Validation of Urease@ GAuC method with the currently practiced clinical method. (A-G) serum samples spiked with different concentrations of urea.

This method of sensing has also been validated for its accuracy against currently adopted methods in clinical diagnosis. For this purpose, urea estimation was done on blood serum samples collected from patients with different unknown urea levels using the standard clinical and the Urease@ GAuC methods (Table S1). The blood urea level was quantified using a calibration plot drawn for known concentrations of urea against changes in the fluorescence intensity. By this method, the unknown concentration of urea in blood was calculated and the values were compared with those obtained by independent clinical analysis and found to be within ±3% error limit (figure 50b, Table S1).

Sample code	Urease@ GAuC [mm]	Clinical Method [mm]
A	3.83 ± 0.4	4.26
B	4.50 ± 0.3	4.63
C	8.00 ± 0.5	8.19
D	10.41± 0.3	10.00
E	10.41± 0.3	10.00
F	11.83 ± 0.4	12.00
G	13.08 ± 0.3	13.00

Table 1. Comparison of urea levels detected by Urease@ GAuC method with an independent clinical detection method. A-G are different serum samples containing varying amounts of urea.

For a real time analysis of a specific analyte in blood, it is advantageous to use whole blood rather than blood serum. Since the autofluorescence of blood samples occur at 620 nm (λ_{ex} @ 450 nm, Figure 51), we speculated that the NIR emission of Urease@ GAuC at 750 nm may not interfere and hence will be ideal for the detection of urea in whole blood. Moreover, since the fluorescence quantum yield of blood is relatively low (0.1% with reference to Rhodamine B) when compared to that of Urease@ GAuC, interference by the autofluorescence of blood for detection of urea is negligible. For the whole blood analysis, the fluorescence change of Urease @GAuC in blood samples spiked with different concentrations of urea were measured (figure 51b) and compared with that of the native blood. Further, the data

of the whole blood were compared with those of the same blood samples (figure 51a).

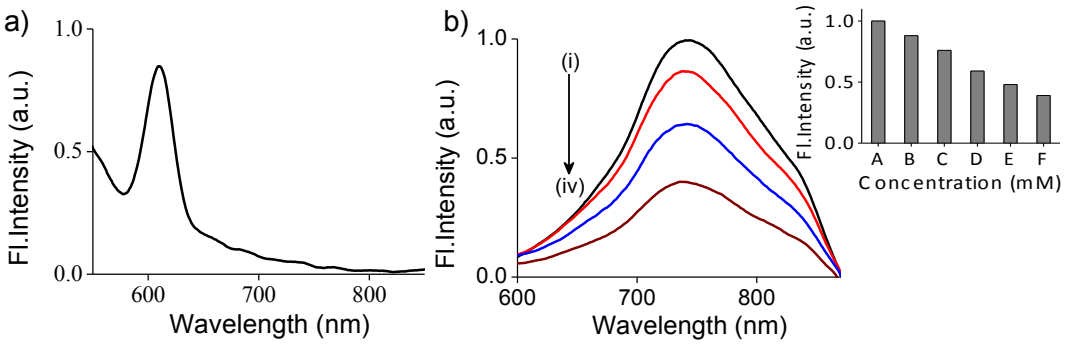

Figure 51: (a) Fluorecence emission of whole blood (λ_{ex} = 450 nm), (b) Fluorescence quenching of Urease@ GAuC on addition of urea in whole blood (i) Urease@ GAuC; On addition of (ii) control blood and (iii and iv) 5 and 10 mM urea. Inset shows the intensity variation of Urease @ GAuC (A) at 750 nm on addition of blood (B) with different amounts of urea (C-F: 2.5, 5, 7.5, 10mM).

Further to the results of urea detection in blood and serum, the efficiency of Urease@GAuC was tested to detect the urea content in milk.Urea adultration in milk is a growing thread Asian and African countries. Urea adultration in milk is mainly to increase the SNF value (solid not fat) of milk. Also milk from the diseased cow is contaminated with urea. Milk samples were adulterated with different amounts of urea and subjected to analysis. When Urease@GAuC is added to the native and the adulterated milk samples, concentration dependent fluorescence quenching was observed as shown in figure 52.

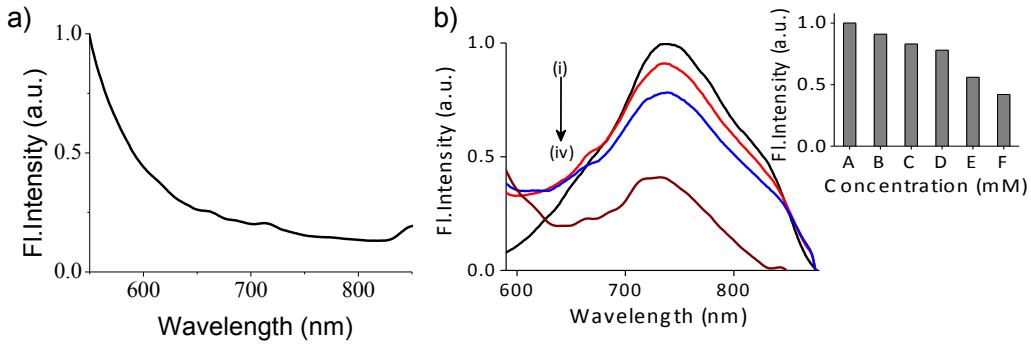

Figure 52: a) Fluorecence emission of pure milk (λ_{ex} = 450 nm) to establish that there is no overlap of the NIR emission of Urease@ GAuC; b) Fluorescence quenching of Urease@ GAuC on addition of urea in milk (i) Urease@ GAuC; On addition of (ii) control milk and (iii and iv) 5 and 10 mM urea. Inset shows the intensity variation of Urease@ GAuC (A) at 750 nm on addition of milk (B) with different amounts of urea (C-F: 2.5, 5, 7.5, 10mM).

4.3 NIR Emitting Gold Quantum Clusters For Targeted Tumor Imaging And Photodynamic Therapy

4.3.1 Preparation Of Protoporphyrin IX Conjugated Gold Cluster

To facilitate dual functions of targeted PDT and imaging applications, lipoic acid protected gold cluster (LAuC) with NIR emission was synthesized and used. To this cluster, cancer targeting moiety, folic acid (FA) and the photo dynamic therapeutic agent protoporphyrin IX (PPIX) were functionalized by EDC-NHS chemistry to get the desired final system (PFLAuC). For incorporating PPIX to folate conjugated cluster, hexamethilenediamine (HMDA), an intermediate coupling agent for both folate and PPIX was integrated to FLAuC by protecting one of the amine groups of

HMDA (Fig 1C). For this, a concentration of HMDA equivalent to 1/10th of the final concentration of FA was chosen. To the resultant system (AFLAuC), PPIX was conjugated by EDC and NHS chemistry to get the final system. Various stages of preparation of PFLAuC are represented in the schematic diagram (figure 53)

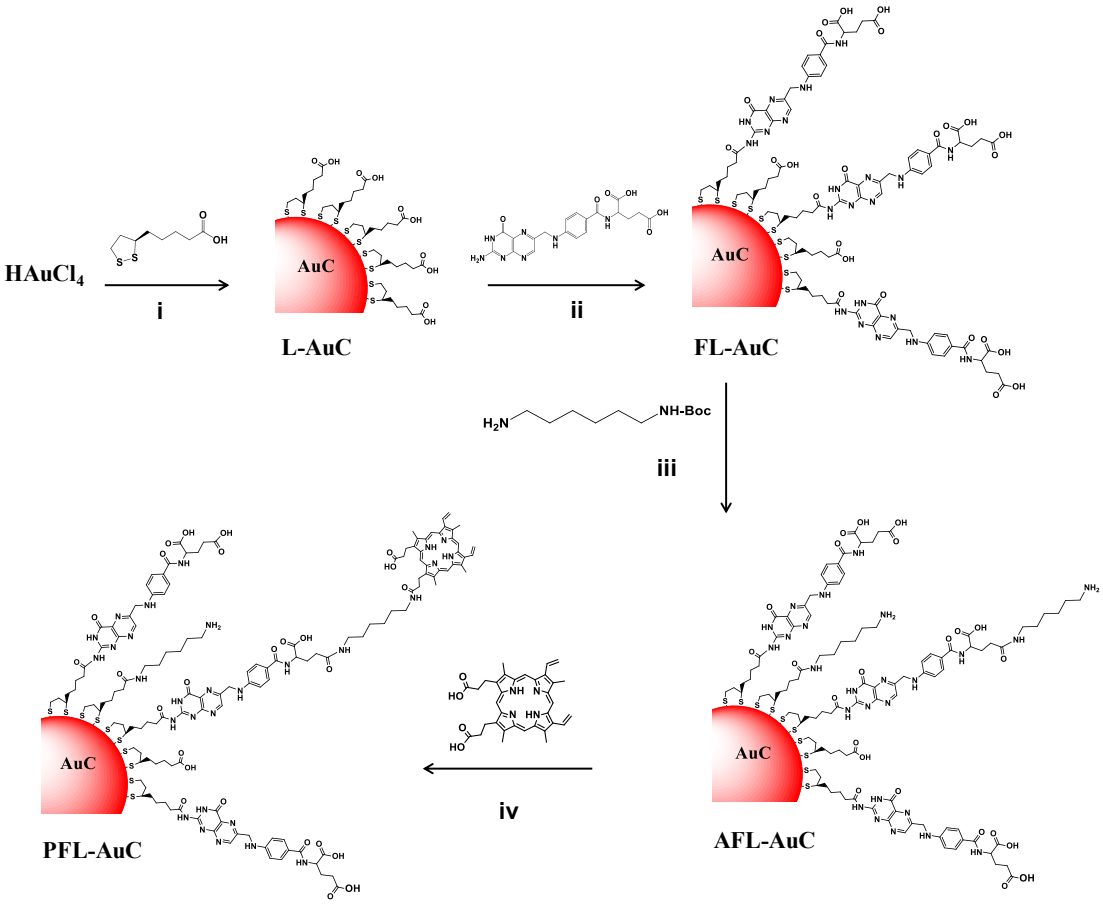

Figure 53: Schematic representation of the overall reaction of porphyrin conjugated LAuC.

LAuC showed fluorescence emission around 720 nm (figure 37b) and an average particle diameter c.a. 1.4 nm (figure 37d), both of which are characteristics of nanoclusters. HRTEM studies showed a lattice distance of 3.5 A^{o} for this cluster. The XRD data (figure 38a) also agrees with this result even though it shows broad peaks.

Folic acid functionalization was carried out on as-prepared LAuC to specifically target to the cancer cells without affecting the normal cells. Negative zeta potential of -36 mV exhibited by LAuC decreased to -28 mV on addition of FA (figure 54). Characteristic absorption of folic acid (figure 55a) observed in the UV-Vis absorption spectrum of FLAuC also demonstrates the presence of folate moiety on the surface of LAuC.

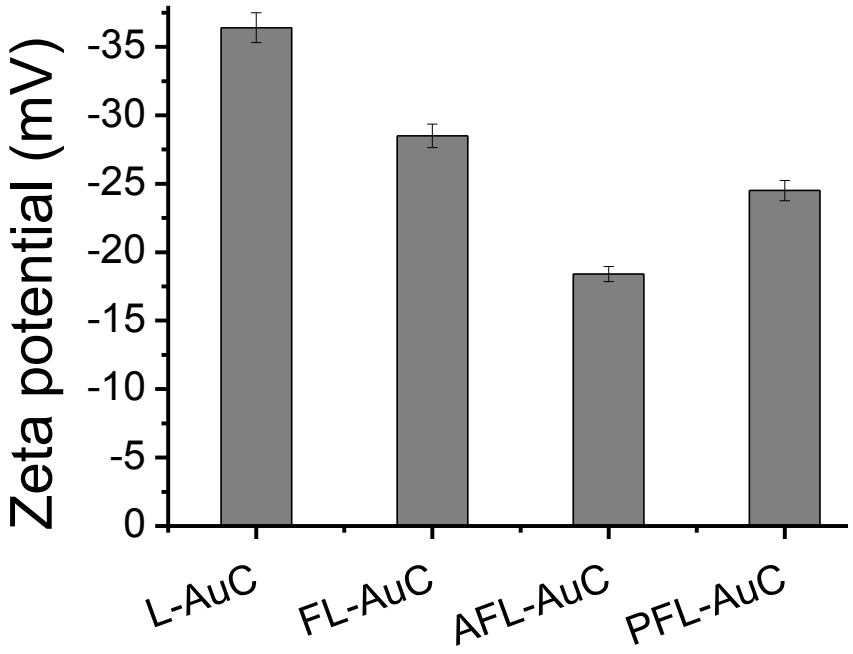

Figure 54: Zeta potential study of LAuC and different stages of functionalization.

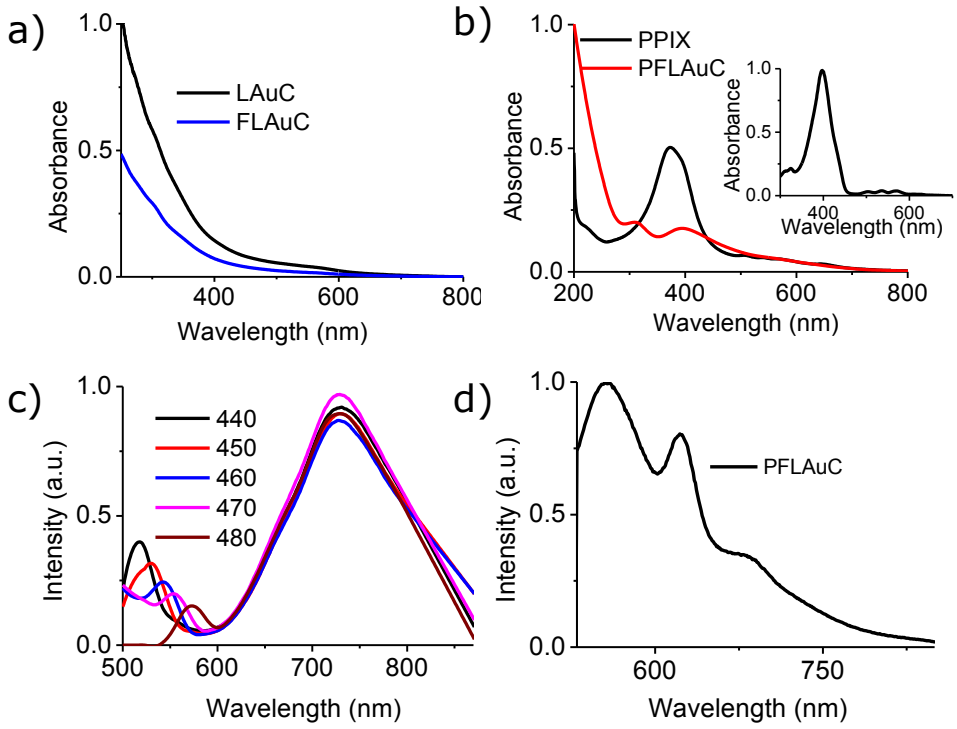

Figure 55: Absorption and emission spectra of FLAuC (a & c) and PFLAuC (b and d). Inset (b) is the higher concentration of PFLAuC.

In the FT-IR spectra there is a peak around 1642.9 cm^{-1} of FLAuC (figure 56).

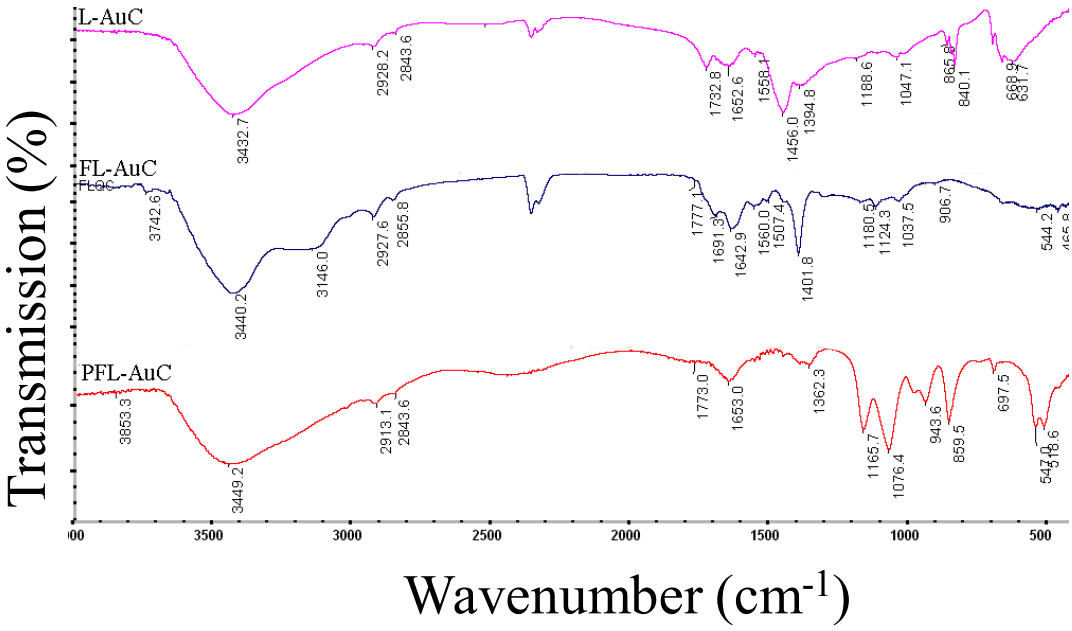

Figure 56: FT- IR spectra of LAuC, FLAuC and PFLAuC

For enabling targeted PDT, PPIX was conjugated to the FLAuC. Here also the presence of FA and PPIX was evident in the absorption spectra of final system (figure 54b). The negative zeta potential of -28mV of FLAuC further decreased on addition of HMDA (c.a. -19 mV) and increased to the order of -25mV (figure 54) on addition of PPIX. The particle size of FLAuC and PFLAuC remains the same as that of LAuC as is evident from the TEM results (figure 57).

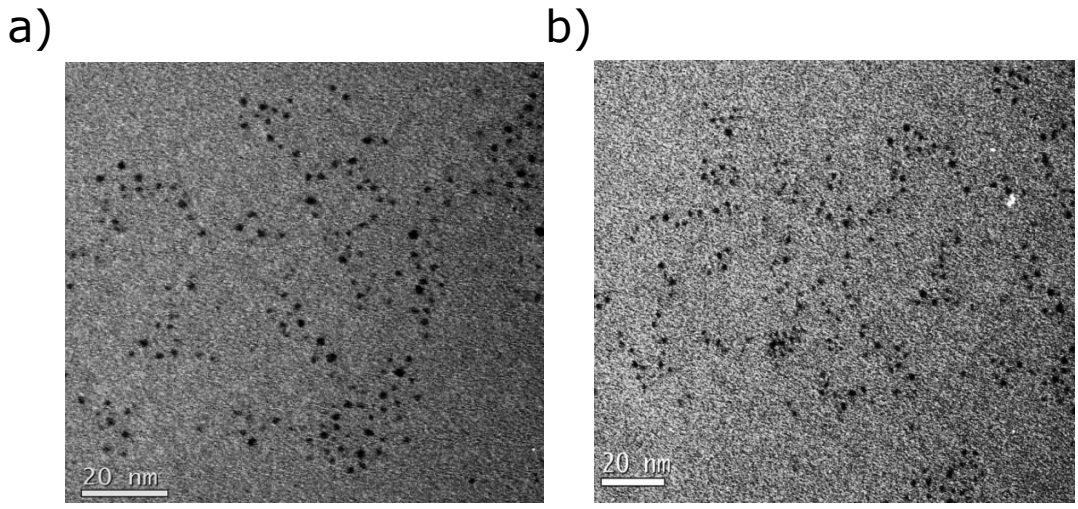

Figure 57: TEM of FLAuC (a) and PFLAuC (b)

Fluorescence lifetime of LAuC is 401 ns and is increased to 37 ms upon functionalization of folic acid (FLAuC) (figure 58 a, b). The fluorescence life time (figure 58c) of PFAuQC decreases to 5.68 pS from 37 mS of that of FLAuC

The fluorescence quantum yield measurement (figure 58d) shows a high quantum yield of 10% for FLAuC compared to 1.86% of LAuC, which reduces to 5.1% in PFLAuC on conjugation with porphyrin.

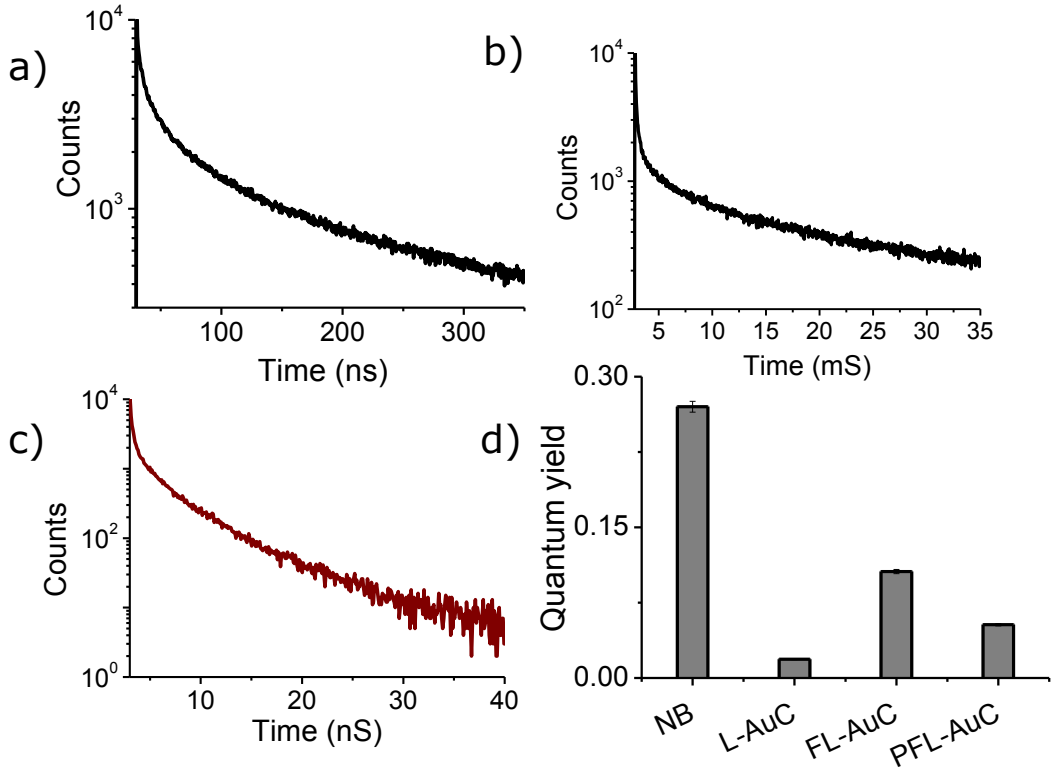

Figure 58: Fluorescence life time of LAuC (a), FLAuC (b), PFLAuC at 720 nm emission (c) and Quantum yield evaluation of control, LAuC, FLAuC and PFLAuC (d).

At every stage of functionalization, ligand concentration on the cluster surface was quantified using UV- Vis absorption spectroscopy. The number of moles of lipoic acid, FA and PPIX present on LAuC at each stages of functionalization are evaluated as 1.35×10^{-6}, 1.67×10^{-6} and 1.40×10^{-7} respectively.

In order to use the developed system as photo sensitizer for photodynamic therapy, the singlet oxygen generation efficiency of PFLAuC was demonstrated. This is achieved by the direct spectroscopic observation of singlet oxygen emission at 1270 nm by 530nm excitation (figure 59a).

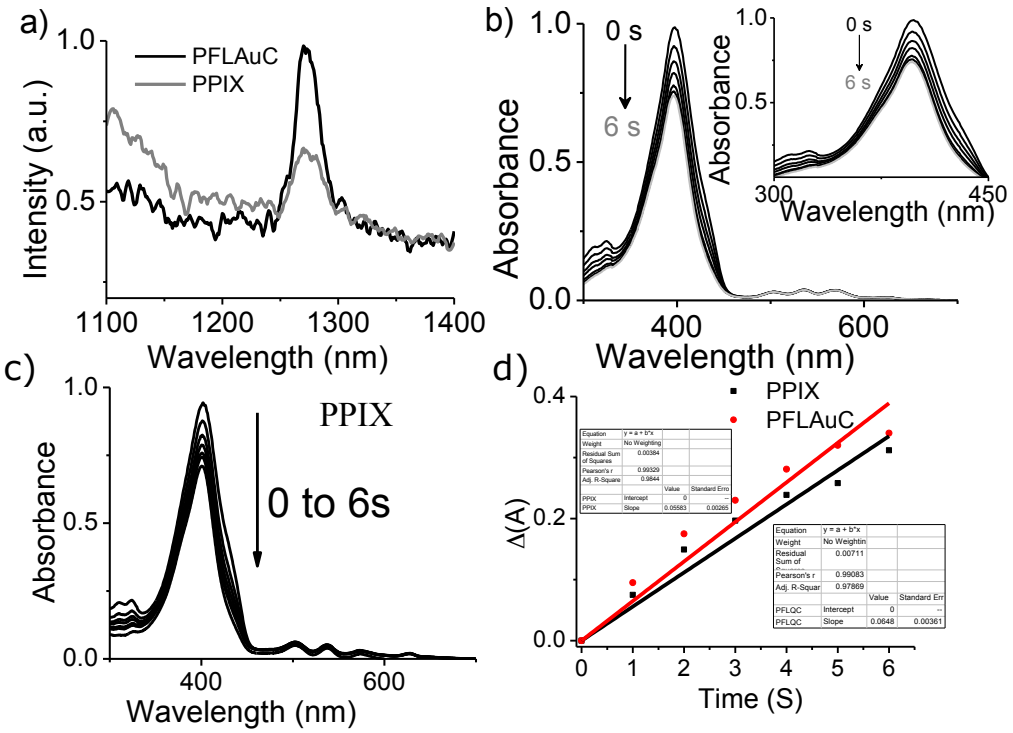

Figure 59: Singlet oxygen generation of PFLAuC and PPIX detected by measuring the phosphorescence of singlet oxygen at 1270 nm upon excitation by a 530 nm laser (a) and the same detected by DPBF method (b) singlet oxygen generation of PPIX using DPBF probe (c) and time dependent linear response of PPIX and PFLAuC (d).

The singlet oxygen production was reconfirmed by another method using diphenylisobenzofuran (DPBF). DPBF readily reacts with singlet oxygen with an observed decrease in absorption of DPBF with the increase in singlet oxygen concentration (figure 59 b- d). Singlet oxygen yield of PFLAuC was 80% compared to 63% of PPIX.

The high singlet oxygen efficiency enables the use of lower concentrations of the currently developed system for efficient PDT. Moreover, the targeting property of PFLAuC also helps to reduce the dose and will leave the normal cells unaffected.

4.3.2 In *Vitro* Cellular Imaging And Therapy

The feasibility of using the developed material for *in vitro* imaging and PDT was checked with folate over expressed cancer cell line (c6 rat glial cell) and the non toxicity of the developed system was confirmed with L929 mouse fibroblast. Cytocompatibility of the developed nanocarrier was confirmed by the activity of mitochondrial reductase using MTT assay (figure 60). All the materials showed good cellular viability at all concentration.

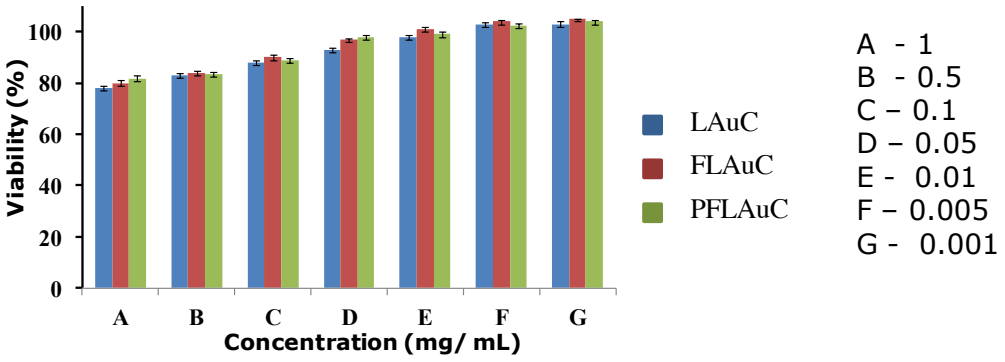

Figure 60: MTT assay of the developed nano carrier with different concentrations.

The targeting and non targeting efficacy of the material was studied by incubating 1 mg/ mL of LAuC, FLAuC and PFLAuC (figure 61). The initial material, LAuC showed less entry into the C6 glial cells compared to its folate conjugated and porphyrin conjugated counter parts FLAuC and PFLAuC. The targeting capability of folic acid conjugated materials to the folate over expressed cells accounted for the increased uptake of FLAuC and PFLAuC in glial cells.

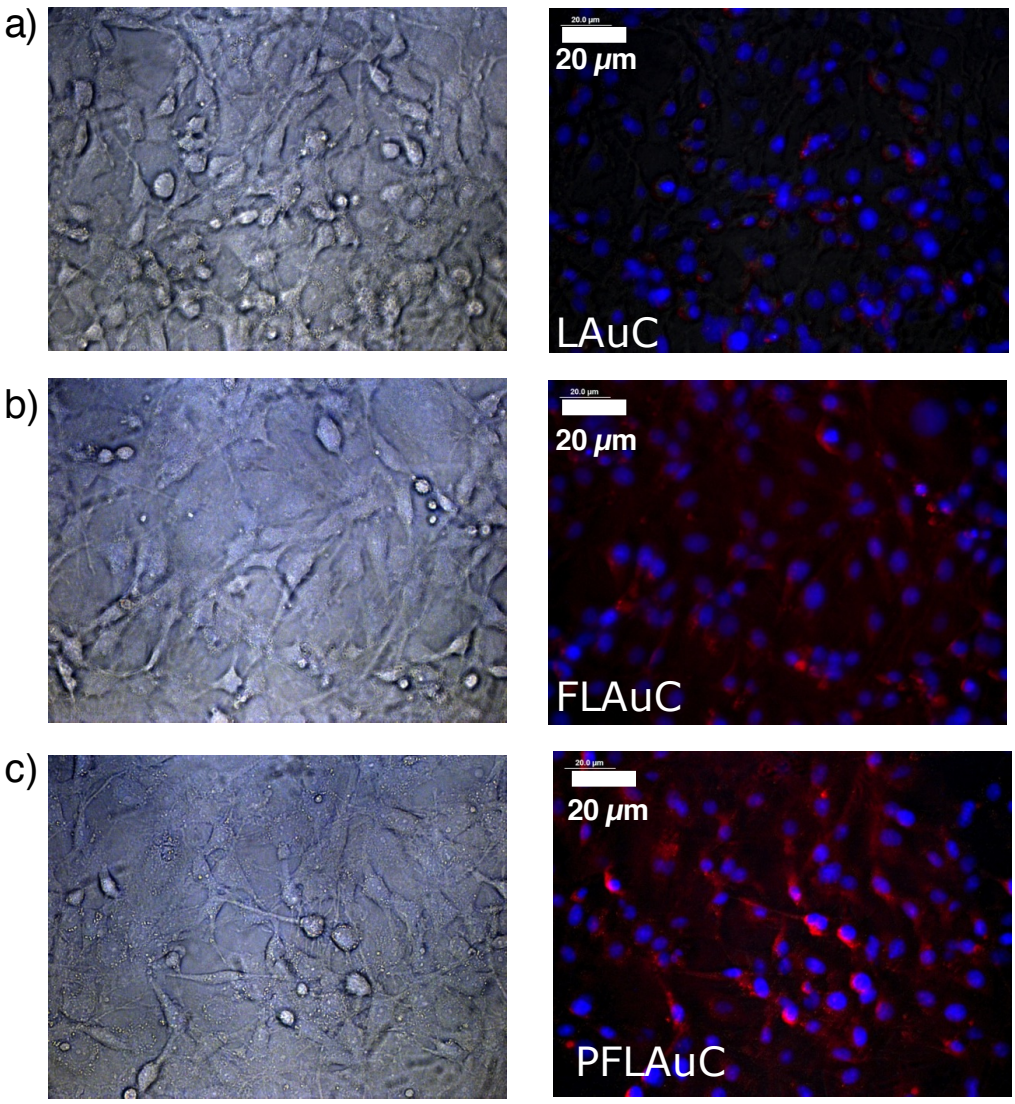

Figure 61: Cellular uptake of LAuC (a), FLAuC (b) and PFLAuC (c). Figure in the left represents the bright field image and second row is the merged bright field and fluorescence image (Red color from nano cluster and blue color hoescht)

Photodynamic therapeutic efficiency of the final system PFLAuC was assessed at the cellular level using folate over expressed cells using calcein propidium iodide staining to assess the live and dead cells. Cells incubated with PFLAuC were irradiated with laser for 30 S. A batch of cells without PFLAuC also received laser irradiation at same dosage and another batch with PFLAuC and without laser

irradiation served as controls (figure 62). Irradiated cells were washed with PBS and stained with calcein propidium iodide stain to differentiate live and dead cells as per the manufacturer's protocol. As seen from figure 62, cell death is negligible in the case of control cells after 30 S of laser irradiation whereas significant cell death was observed in the cells carrying PFLAuC. Cells incubated with PFLAuC and did not receive laser treatment (figure 62 a) also showed no cell death.

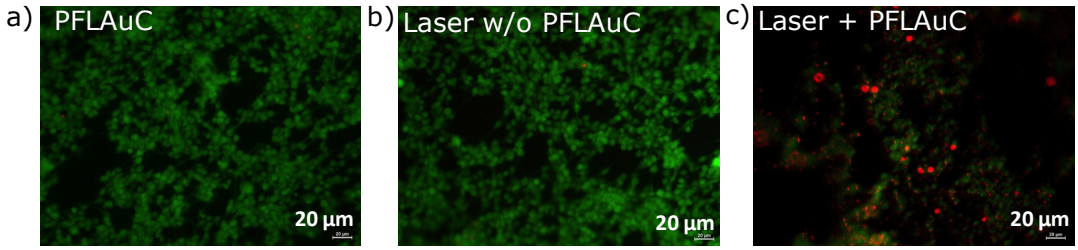

Figure 62: Live dead assay of C6 cells on irradiating with 530 nm laser.

Concentration dependent PDT efficacy of PFLAuC was demonstrated by measuring the cell viability on addition of both PPIX and PFLAuC before (figure 63a) and after (figure 63b) laser irradiation. Percentage viability was assessed using MTT with different concentrations (80 µg, 60 µg, 40 µg, 20 µg, 10 µg, 8 µg and 5 µg) of PPIX and PFLAuC. IC 50 value of PFLAuC is 60 µg whereas a corresponding concentration of PPIX shows more than 70% cell viability (figure 63a).

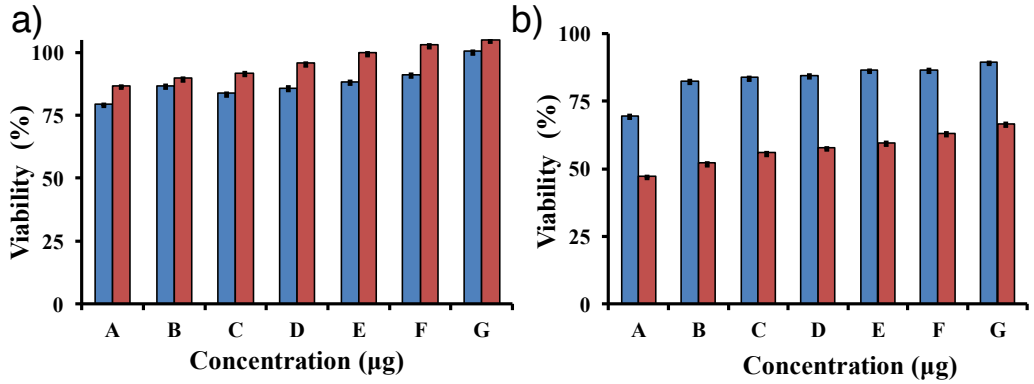

Figure 63: Percentage cell viability of PPIX (blue) and PFLAuC (brown) after 3 h of incubation before (a) and after (b) laser irradiation. A, B, C, D, E, F, and G represents 80 μg, 60 μg 40 μg, 20 μg, 10 μg, 8 μg and 5 μg concentration respectively

4.3.3 Targeted Tumor Imaging *In Vivo*

To demonstrate the tumor targeting efficacy of the developed materials, the nanoclusters were injected intravenously to tumor bearing mice and imaged under live animal optical imaging system (Xenogen, IVIS). In the case of FLAuC and PFLAuC more particle internalization is observed in the tumor region (figure 64)

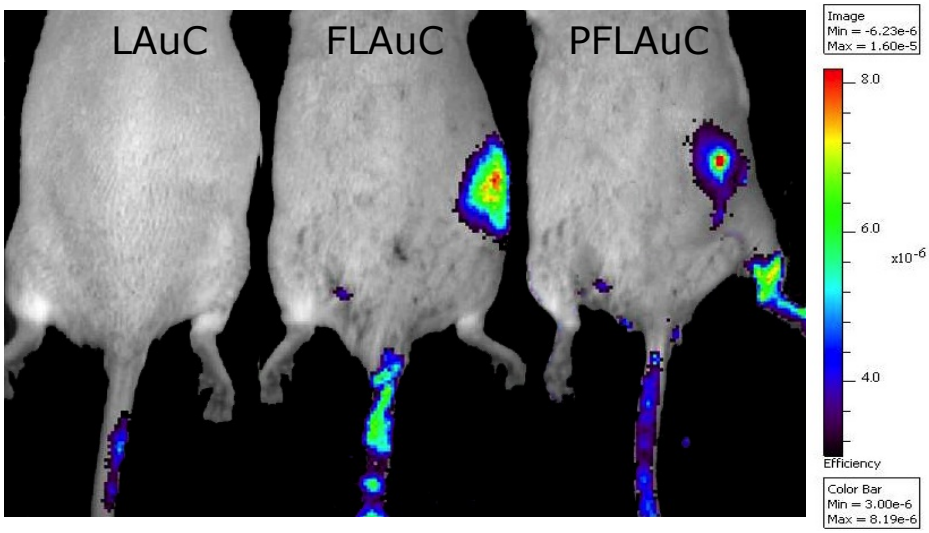

Figure 64: Tumor imaging using the developed nanocluster (LAuC, FLAuC and PFLAuC) *in vivo*.

4.3.4 PDT Efficacy Of PFLAuC *In Vivo*

In order to demonstrate the PDT efficacy of PFLAuC, the animals were irradiated with 532 nm laser (1.5 W) for 15 min after 3 h of injection of the materials. Tumor bearing animals without materials served as control. The effect of treatment was monitored upto 7^{th} day of laser irradiation by measuring the reduction in tumor volume (figure 65a). The therapeutic efficacy was also ascertained using fluorescence spectroscopy by evaluating the total hemoglobin concentration, redox ratio and collagen level (figure 65) from the emission of endogenous fluorophores.

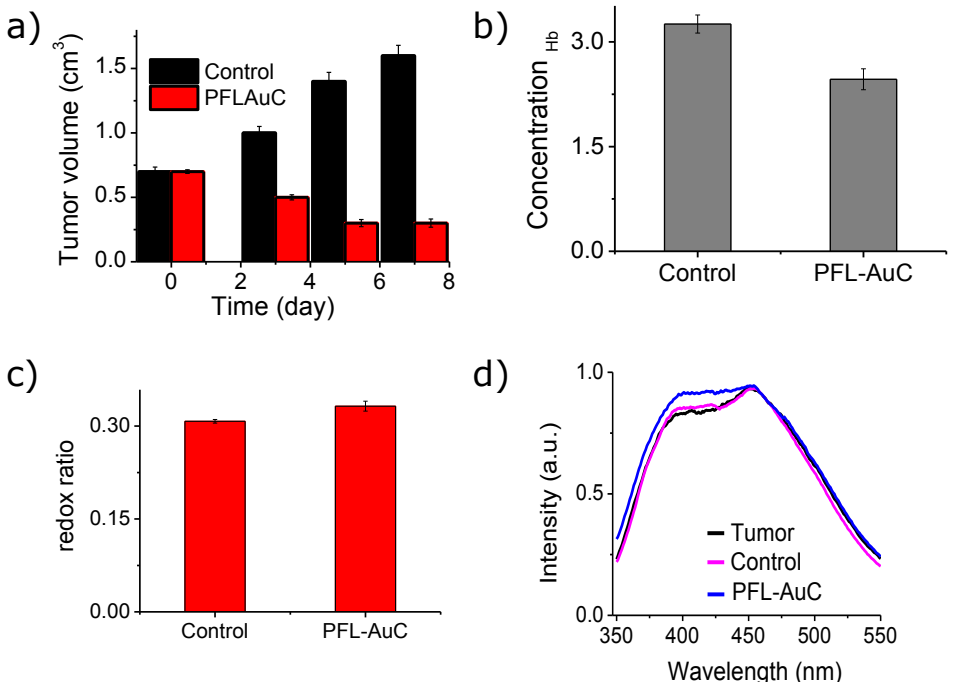

Figure 65: Tumor volume in control and treated mice upto seven days, after laser irradiation (a). Total hemoglobin concentration (b) , Redox ratio (c) and Autofluorescence spectra of collagen, NADH and FAD in different group of mice with 320 nm excitation *in vivo*.

4.3.5 Histopathological Evaluation

Animals were sacrificed after 7th day of administration of materials and laser treatment.The presence of nodules in the H& E stained sections of tumor bearing mice with and without laser irradiation indicates the well developed tumor model. In both the controls dividing cells are clearly visible (indicated by arrow figure 66 a, b) where as in the case of PFLAuC treated animal with laser exposure show more necrotic cells (figure 66c).

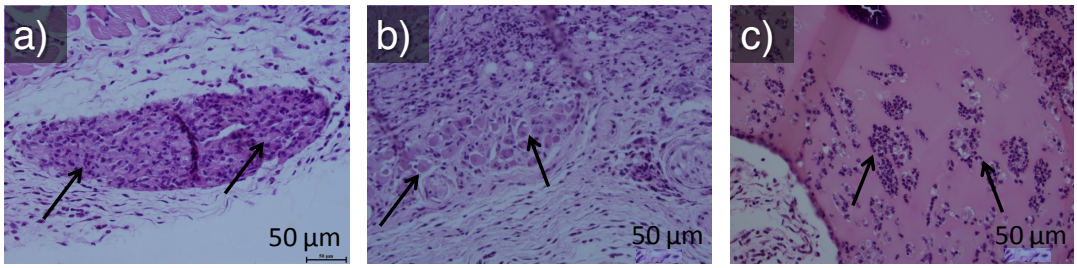

Figure 66: H&E stained sections of mice showing tumor and the arrow mark represents the dividing cells present in the skin (a), Mice bearing tumor with laser alone showing dividing cells (arrow mark) (b), tumor mice treated with PFLAUC and laser showing necrotic cells in the skin (e)

4.4 NIR Emitting Gold Clusters For Blood Brain Barrier (BBB) Targeted Imaging

4.4.1 BBB Targeting Using Glutathione Stabilized Cluster

4.4.1.1 Synthesis Of GAuC And Dop@GAuC

Glutathione gold nano cluster (GAuC) was prepared by etching gold nanoparticles with reduced glutathione. Synthesis of GAuC with GSH is schematically shown in figure 27.

The developed GAuC was tuned to emit at 750 nm (figure 29c). The average size of the particle was estimated as 0.7 nm (figure 31d). Extremely smaller size and NIR fluorescence emission of the cluster makes it a suitable carrier for diagnostic and therapeutic applications, both *in vivo* and *in vitro*.

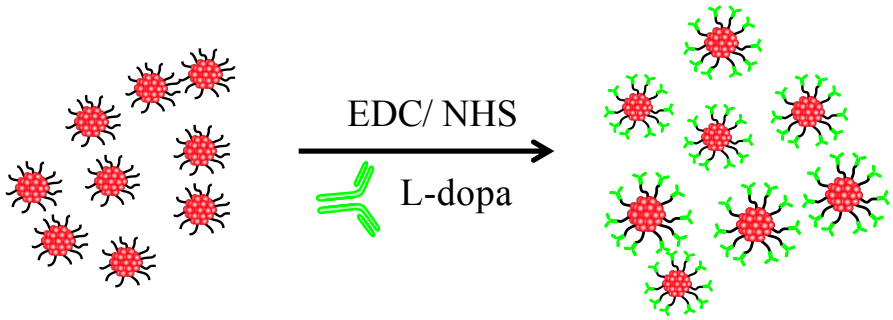

Figure 67: Schematic representation of the synthesis of Dop@GAuC

L- dopa was conjugated to GAuC through EDC- NHS coupling chemistry (figure 67). A systematic characterization of the materials in terms of their physico chemical properties, blood and cell compatibility have been carried out before the *in vitro* and *in vivo* BBB permeability evaluation.

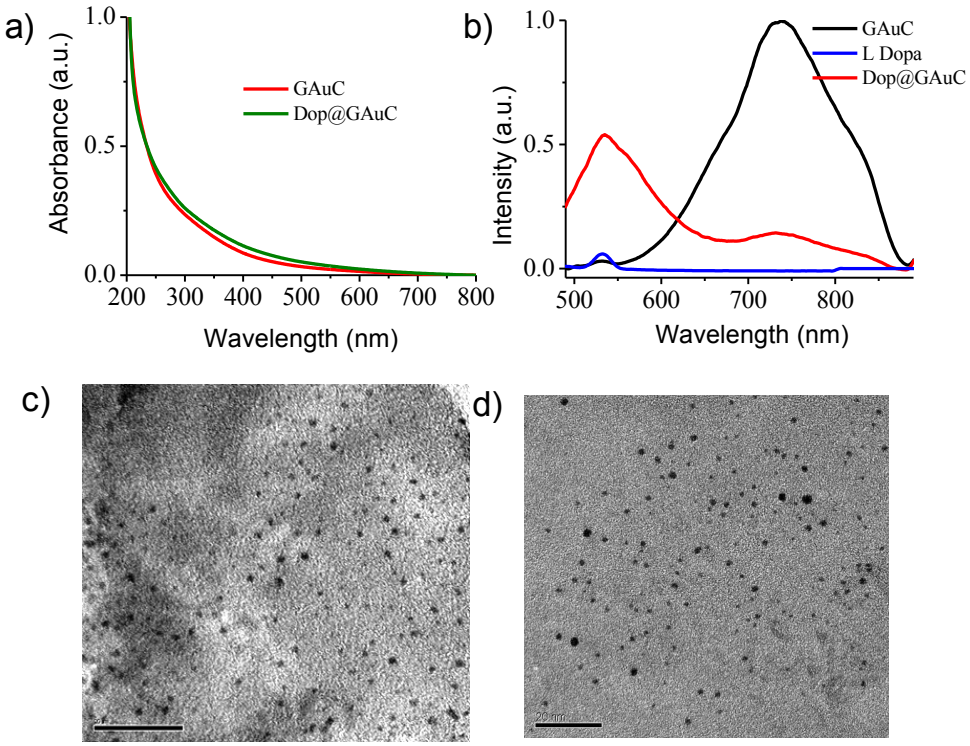

Figure 68: UV- Visible absorbance spectra of GAuC, Dopa@GAuC (a), Photoluminescence spectra (b), and TEM of GAuC (c) and Dop@GAuC (d)

Absorbance spectra (figure 68a) shows valley like absorbance profile. In the fluorescence spectrum (figure 68b) in addition to the peak at 750 nm there is a peak around 534 nm observed for Dop@GAuC. Size analysis using TEM shows that the GAuC shows an average particle diameter of 0.7 nm (figure 68c) and Dop@GAuC shows 1.4 nm (figure 68d).

In the FT- IR spectra GAuC shows characteristics peak at 1734, 1691, 1522 and 1400 cm^{-1}. Dop@GAuC shows IR peak at 1726, 1649, 1588 and 1452 cm^{-1} (figure 69).

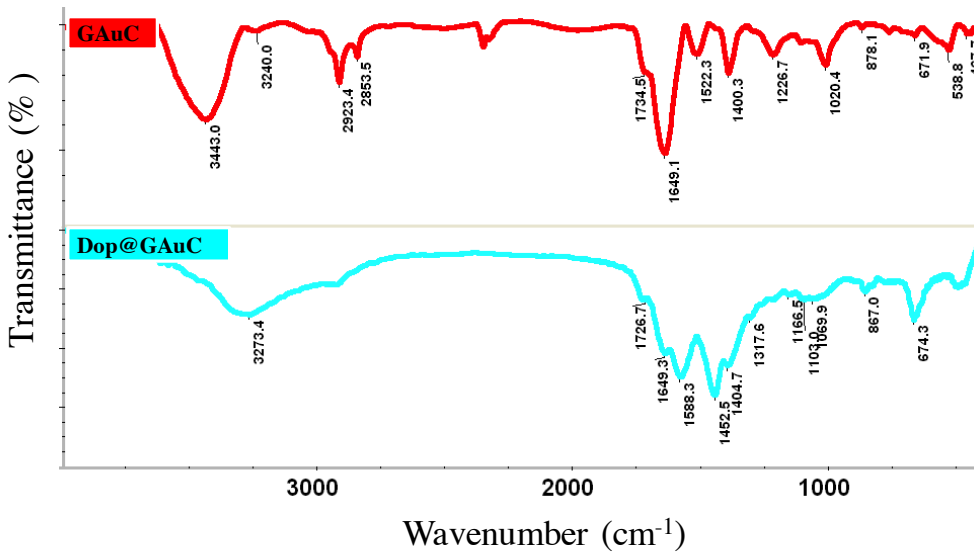

Figure 69: FT- IR spectra of GAuC and Dop@GAuC

XPS analysis shows that the binding energy of GAuC and Dop@GAuC has a slight variation for both Au $4f_{7/2}$ and Au $4f_{5/2}$ states. 85.93 eV (Au $4f_{7/2}$) of GAuC changes to 87.34 eV for Dop@GAuC. Similarly the Au $4f_{5/2}$ peak of GAuC changes from 82.22 eV to 83.83 eV (figure 70).

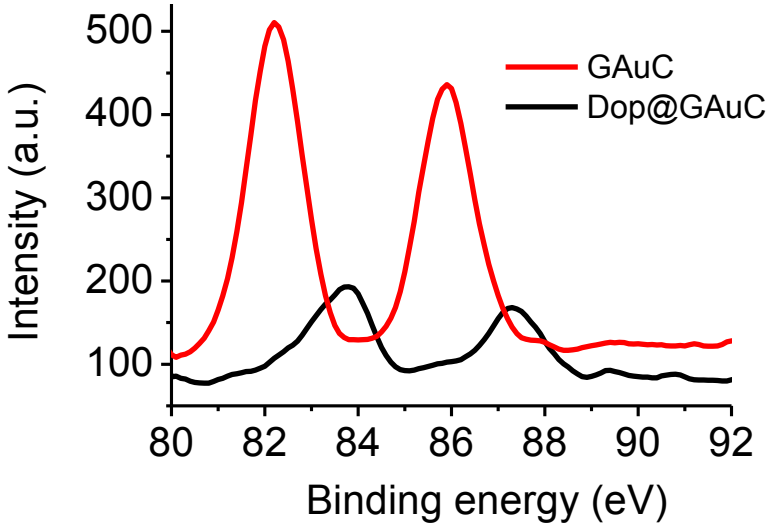

Figure 70: XPS spectra of GAuC and Dop@GAuC

4.4.1.2 *In Vitro* Studies

Cell viability of the developed material was evaluated using MTT assay (figure 71) in L929 mouse fibroblast. MTT assay shows that the viability of cells is found to be more than 75% upon incubating with different concentrations of GAuC and Dot@GAuC.

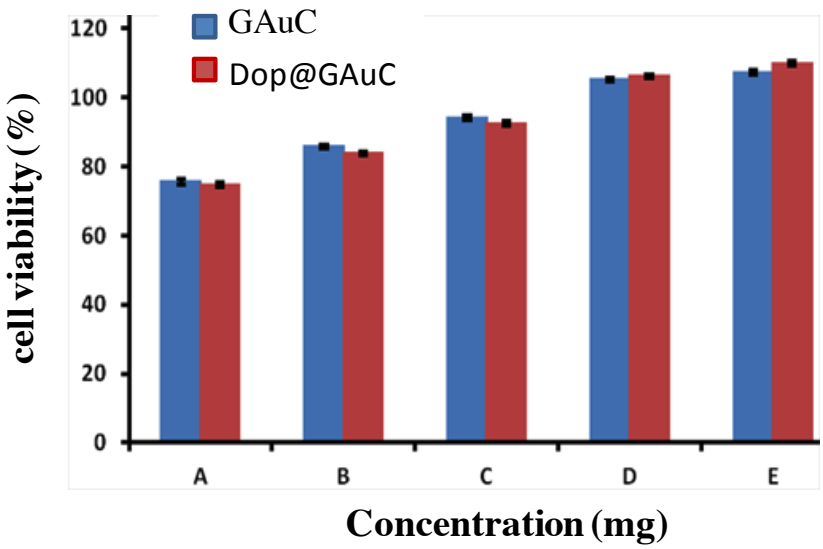

Figure 71: Viability of the cells by the addition of different concentrations of GAuC and Dop@GAuC using MTT assay. A, B, C, D, and E represents 1 mg, 0.5 mg, 0.1 mg, 0.05 mg, and 0.01 mg/ mL of material respectively.

4.4.1.3 Barrier Potential, Permeability And Uptake By b-End3 Cell Line

In order to prove the *in vitro* BBB permeability of the developed material, brain endothelial cells of mice origin (b-End3 from ATCC) were grown on milli cell insert with a pore size of 0.4 µm. Barrier potential of the cells was regularly monitored to ascertain the confluence of the cells and the monolayer formation so that it exactly mimics the BBB. Completely confluent monolayer with barrier potential of the order

of 1400 Ω was considered as in vitro model for BBB. To the developed BBB model, 1 mg/ mL (100 µL) of of GAuC and Dop@GAuC was added separately. On addition of GAuC and Dop@GAuC, the original barrier potential of c.a~ 1400 Ω dropped to 812 Ω and 982 Ω respectively within 30 min. Later, the potential of the cells regained almost completely within 2-3 h (figure 72b).

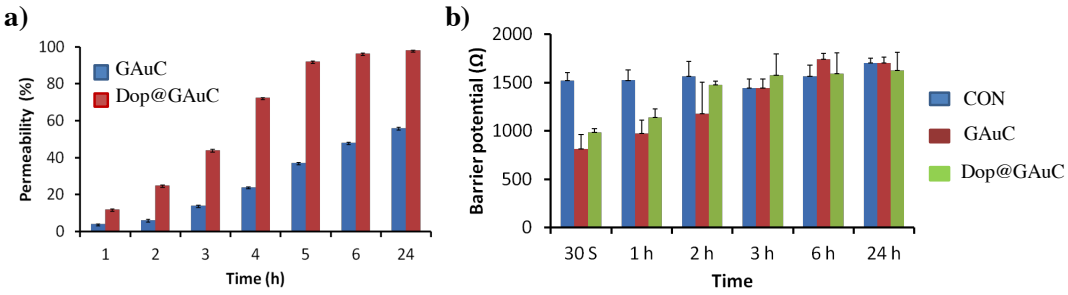

Figure 72: Barrier permeability (a) and barrier potential measurement (b) in b-End3 cells by the addition of 1 mg/ mL of GAuC and Dop@GAuC at different time period.

Figure 72a shows the concentration of GAuC and Dop@GAuC that has crossed the BBB and has evaluated by UV visible spectroscopy through the millicell. At 3h, 44% of Dop@GAuC were found in the outside chamber (figure 72a) where as only 14% of GAuC were observed during this time. It took nearly 24 h for 56% of the material to come out in the later case. More than 90% Dop@GAuC came out in 5 h.

Monolayer formation over the surface of millicell insert was confirmed using SEM analysis (figure 73).

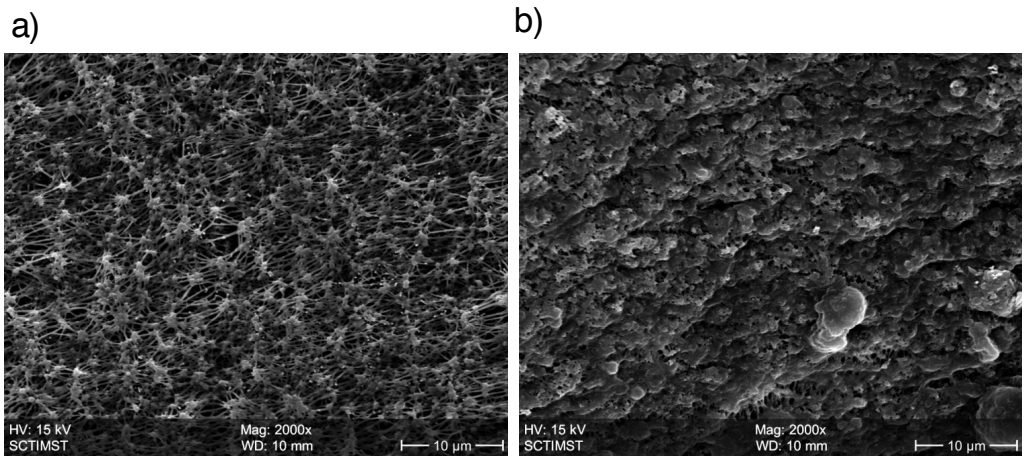

Figure 73: SEM image of the b-End3 cells grown on milli cell insert

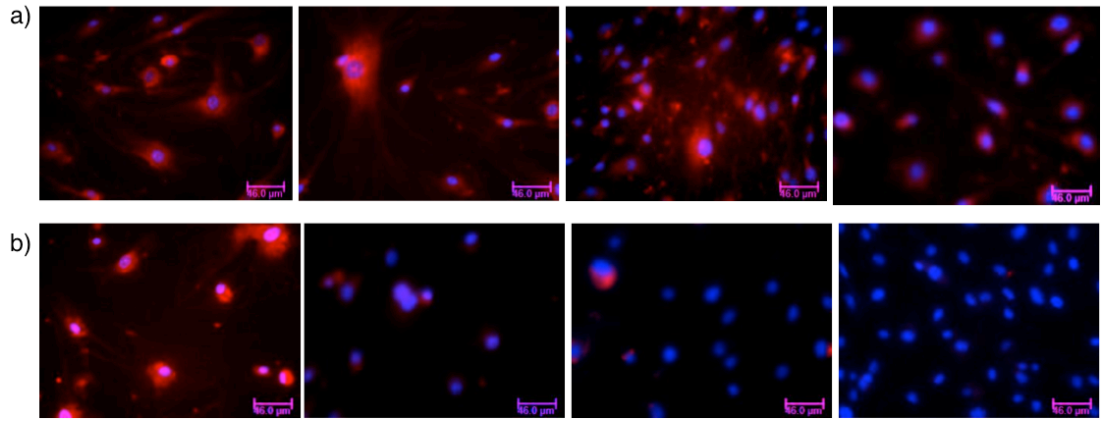

Figure 74: Cellular uptake of the material for 3, 6, 12 and 24 h using fluorescence microscope. (a) b-End3 cells with GAuC for 3 h, 6 h, 12 h and 24 h and (b) represents the same with Dop@GAuC.

Figure 74 shows the fluorescence image of the cells after incubating the particle for 3, 6, 12 and 24 h. Nucleus were counter stained with hoescht. These images shows the particle uptake efficacy of GAuC and Dop@GAuC by the barrier cell. In the figure it is observed that upto 24 h, fluorescence is visible from the particles uptaken by the cells but in the case of Dop@GAuC the fluorescence intensity diminishes upto

6h and at 24 h there is no fluorescence.

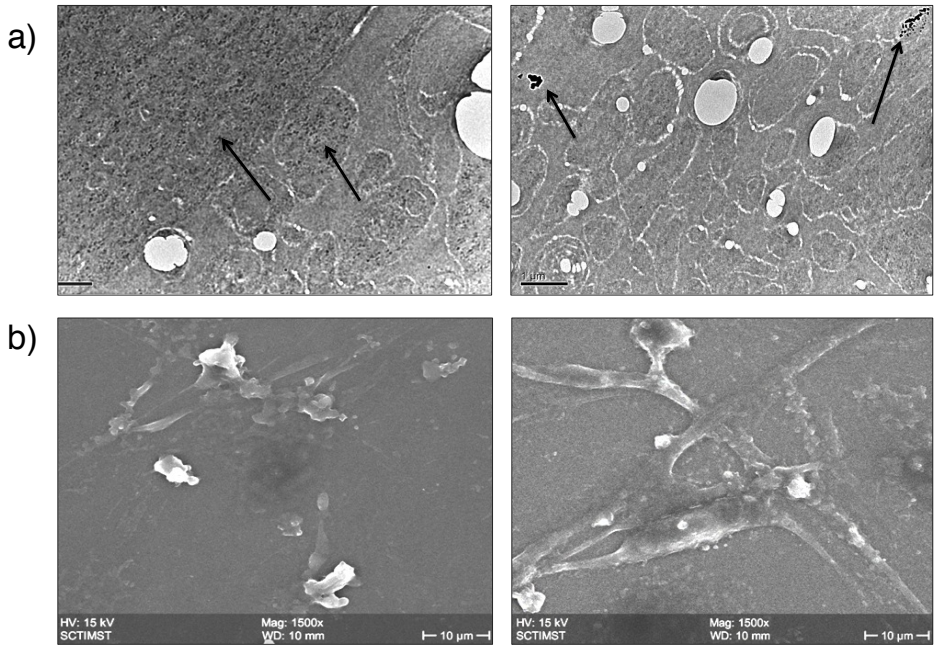

Figure 75: Electron microscopic evaluation of BBB cells with GAuC and Dop@GAuC after 3 h incubation transmission electron micrograph (a) and Scanning electron micrograph (b)

In order to substantiate the fluorescence data, and barrier permeability data the cells were fixed for electron microscopy after 3h of particle incubation. From the TEM micrograph (figure 75a) it is clear that in the case of GAuC more particles are internalized inside the cell where as lesser number of particles only are observed in the case of Dop@GAuC treated cells at 3h. SEM (figure 75b) micrographs shows the intactness of the cells upon electron exposure and particle treatment.

4.4.1.4 Blood Compatibility Evaluation

Blood material interactions were also carried out before doing *in vivo* BBB studies. In all the concentrations studied both GAuC and Dop@GAuC showed below 0.3% hemolysis (figure 76).

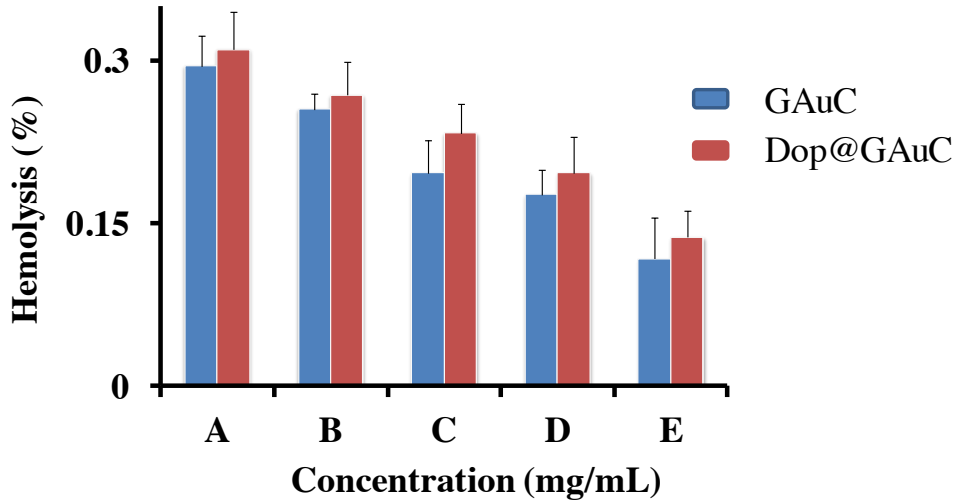

Figure 76: Percentage hemolysis of GAuC and Dop@GAuC. A, B, C, D, and E represents material concentration of 1 mg, 0.5 mg, 0.1 mg, 0.05 mg, and 0.01 mg/ mL.

Aggregation of blood cells upon incubation of material was monitored. Bright field microscopic image shows (figure 77) no aggregation for RBC, WBC and platelet due to the material.

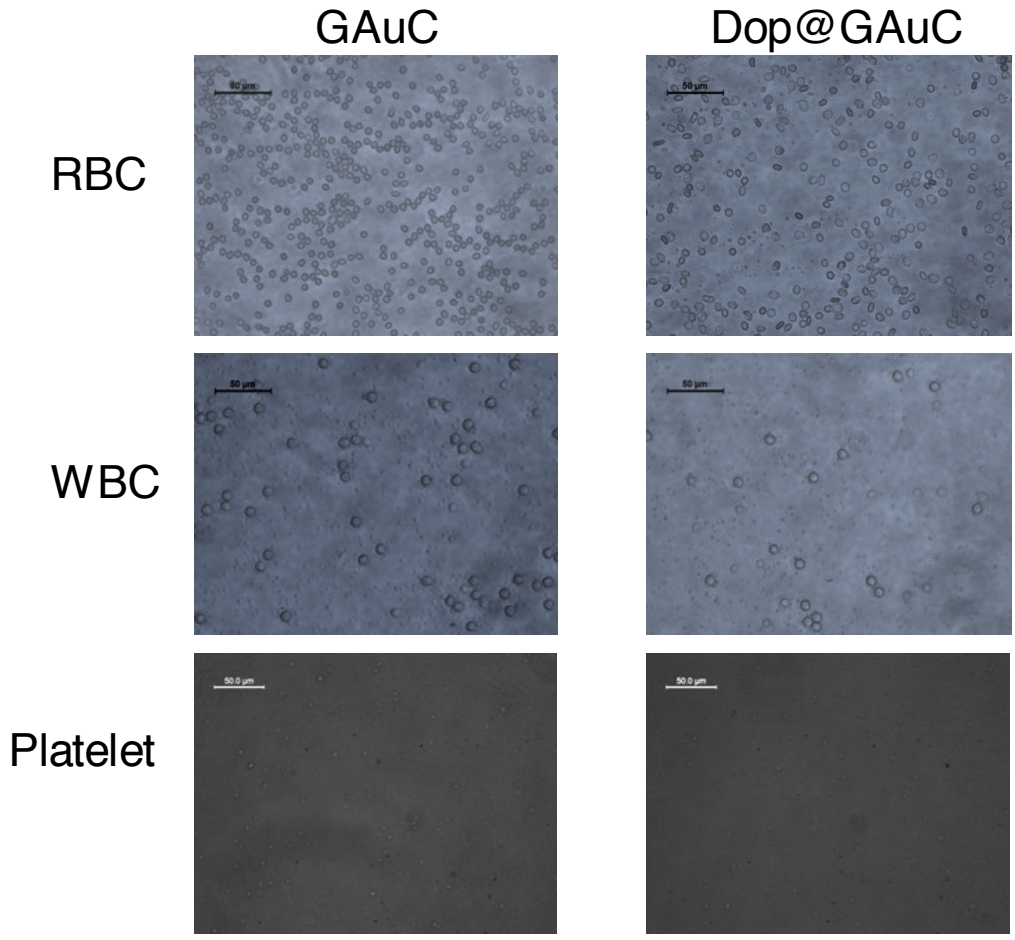

Figure 77: Bright field images of RBC, WBC and platelet upon incubation of GAuC and Dop@GAuC for 3h.

4.4.1.5 In Vivo Brain Imaging

The BBB permeability of the materials was demonstrated in vivo using normal albino Swiss mice. The institutional animal ethical committee approved all animal studies. GAuC and Dop@GAuC were administered intravenously through tail vein at a dose of 1 mg/ mL (0.5 mL). The animals were imaged after 1hr using IVIS spectrum imaging system with 604 nm excitation and 740 nm emission wavelengths.

The NIR emission of the gold cluster facilitated imaging of the fluorescence signal from the brain and avoided the auto fluorescence signal from the animal body. Residual autofluorescence was eliminated by spectral unmixing of the image after image acquisition using live image software. Signal from the brain was observed for GAuC and Dop@GAuC injected animals. However the signal intensity of Dopa@GAuC injected animal was more than that of GAuC injected animal (figure 78 a).

The fluorescence images of the excised brain after 2 hours also showed similar result (figure 78 b). In the case of GAuC injected mice the brain shows a weak signal compared to that of Dop@GAuC injected one.

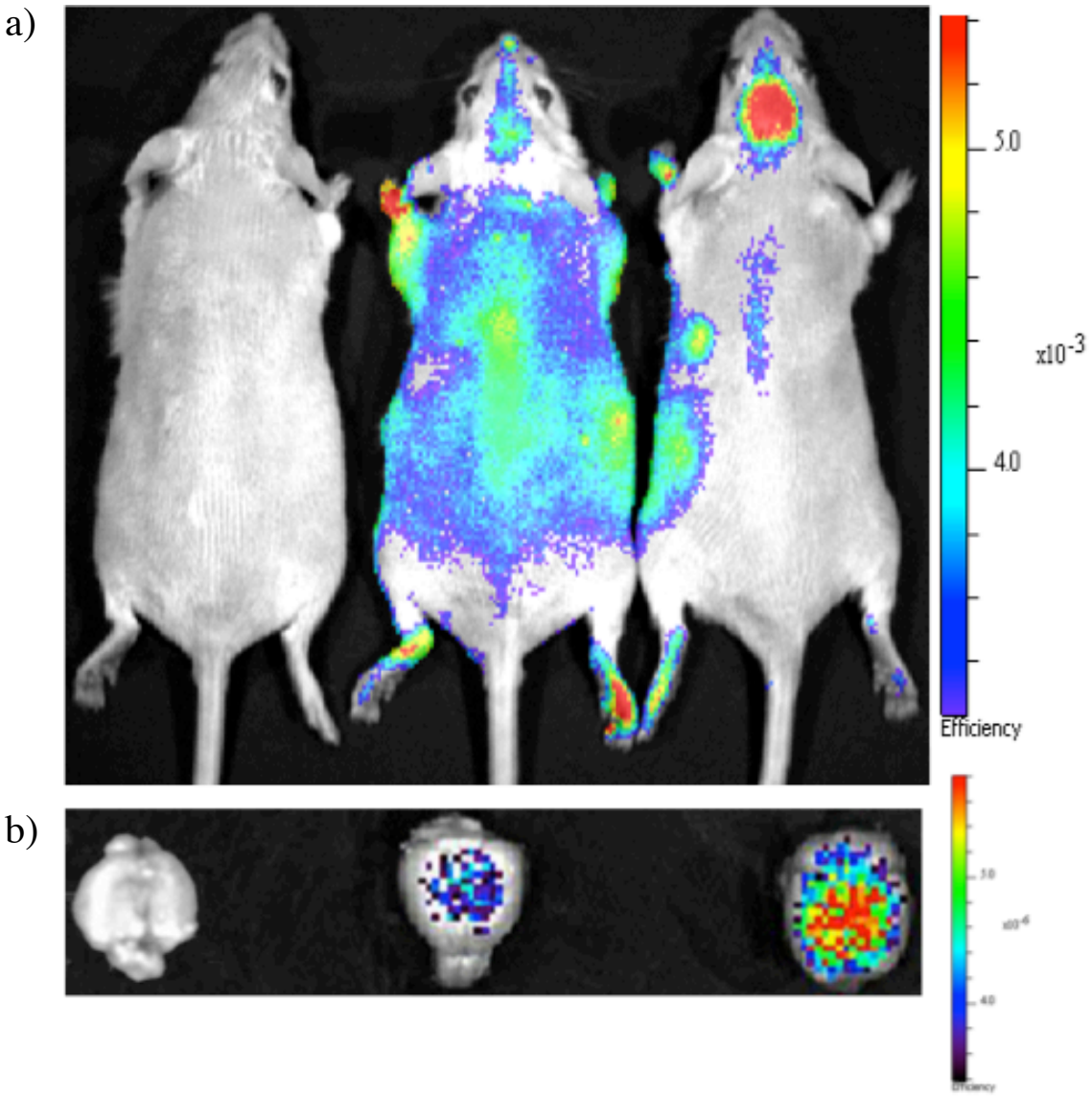

Figure 78: BBB targeting with GAuC and Dop@GAuC *in vivo* (a). *Ex- vivo* (b) study to indicate the signal in the mice brain.

4.4.1.6 Fluorescence Microscopic Evaluation From Brain Sections

Fluorescence microscopic evaluation of the excised brain sections (400 micron thick) shows fluorescence signal from within the blood vessel in the case of GAuC treated animals where as more fluorescence is observed from within the brain in the case of Dop@GAuC (figure 79).

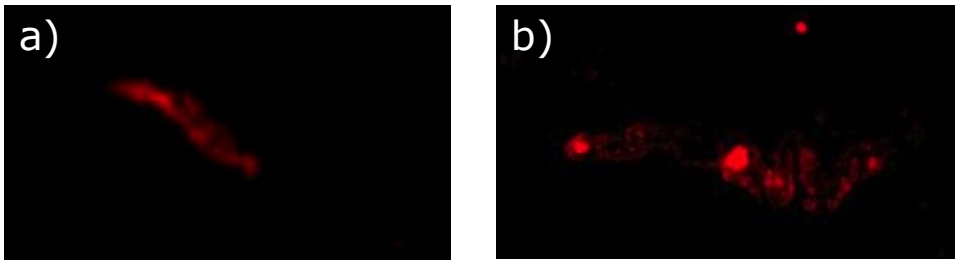

Figure 79: Fluorescence from brain sections of GAuC (a) treated, and Dop@GAuC (b) treated mice brain.

4.4.2. Blood Brain Barrier Targeting Using Lipoic Acid Stabilized Gold Cluster

4.4.2.1 Synthesis Of LAuC And Dop@LAuC

Lipoic acid gold nano cluster (LAuC) was prepared by one step method explained in section 4.1.2.

The developed LAuC was tuned to emit at 720 nm (figure 37). The average size of the particle was estimated at 1.4 nm (figure 37c). The smaller size and NIR fluorescence emission of the cluster makes it a suitable carrier for diagnostic and therapeutic applications, both *in vivo* and *in vitro*.

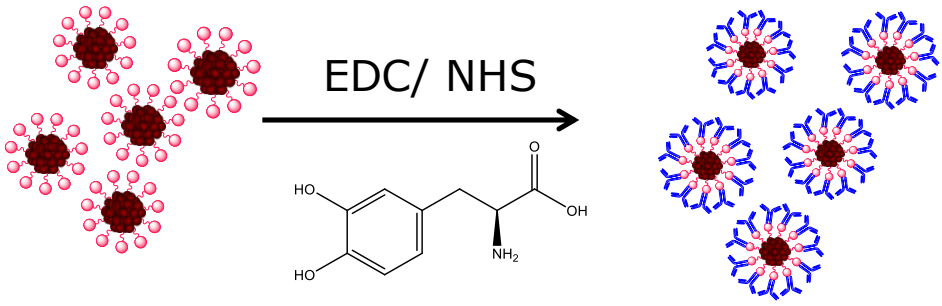

Figure 80: Schematic representation of the synthesis of Dop@LAuC

L dopa was conjugated to LAuC through EDC- NHS coupling chemistry (figure 80). A systematic characterization of the materials in terms of their physico chemical properties, blood and cell compatibility have been carried out before the *in vitro* and *in vivo* BBB permeability evaluation.

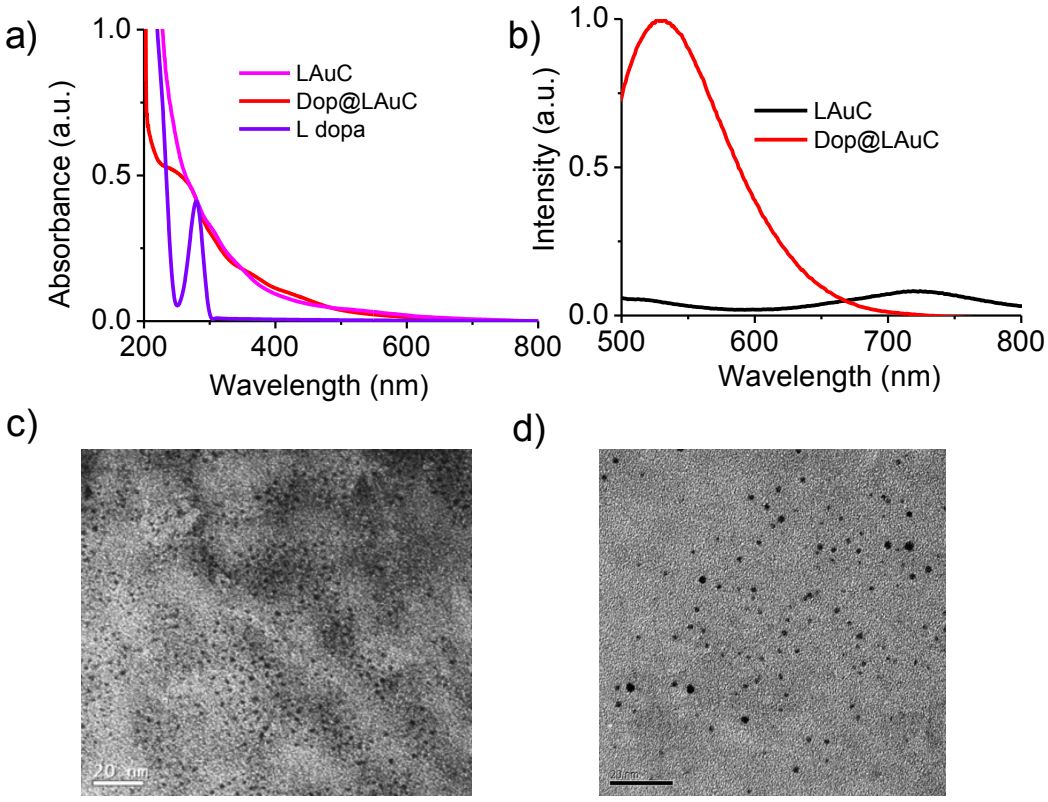

Figure 81: UV-Vis absorbance spectra of LAuC, L- dopa, Dop@LAuC (a), Photoluminescence spectra (b), and TEM of LAuC (c) and Dop@LAuC (d) [scale bar is 20 nm]

Absorbance spectra of Dop@LAuC (figure 81a) show an absorbance around 250 nm. In the fluorescence spectra (figure 81b) emission around 534 nm is observed for Dop@LAuC. Size analysis using TEM shows that the LAuC is having an average particle diameter of 1.4 nm (figure 81c). But in the case of Dop@LAuC slightly varied size from 1.4 to 2 nm (figure 81d).

FT- IR (figure 82) study shows that LAuC is having major vibrational modes at 1632.8, 16552.6, 1558 cm^{-1} where as Dop@LAuC is showing around 1729, 1652, 1563, 1463 cm^{-1}.

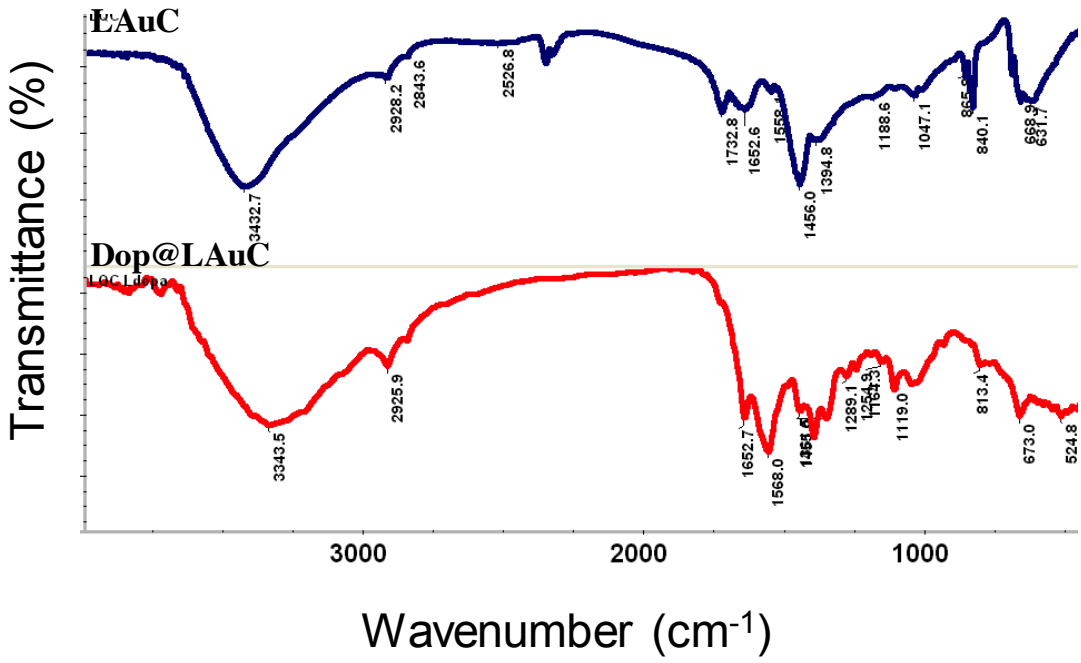

Figure 82: FT IR spectra of LAuC and Dop@LAuC

XPS analysis (figure 83) shows that the binding energy of LAuC and Dop@LAuC shows a slight variation for both Au $4f_{7/2}$ and Au $4f_{5/2}$ states. LAuC is having binding energy at 82.8 eV and 86.58 eV for $4f_{5/2}$ and $4f_{7/2}$ of Au respectively. When LAuC is bound with L dopa there is a slight change in the binding energy profile. Dop@LAuC shows peak position at 82.51 eV and 86.12 eV for $4f_{5/2}$ and $4f_{7/2}$ of Au respectively.

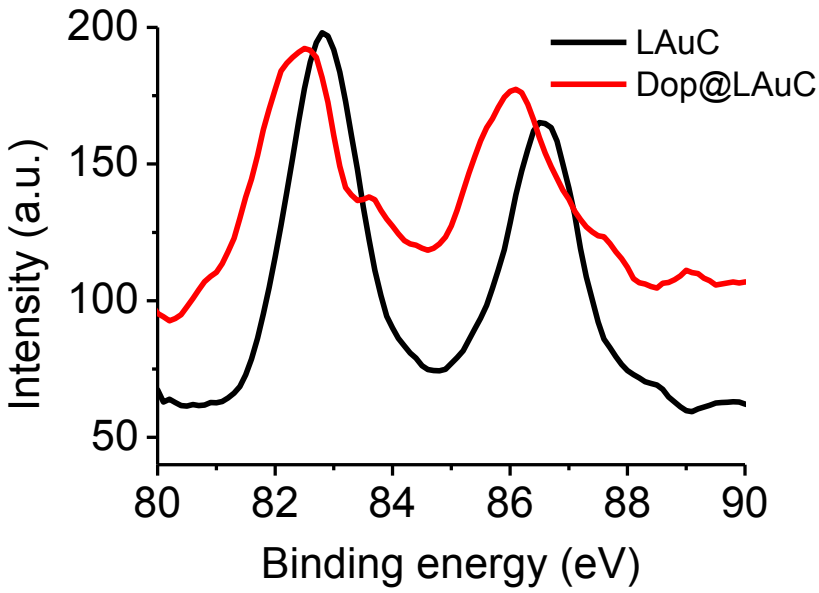

Figure 83: XPS spectra of LAuC and Dop@ LAuC.

4.4.2.2 In Vitro Studies

Cell viability of the developed material was evaluated using MTT assay (figure 84) in L929 mouse fibroblast.

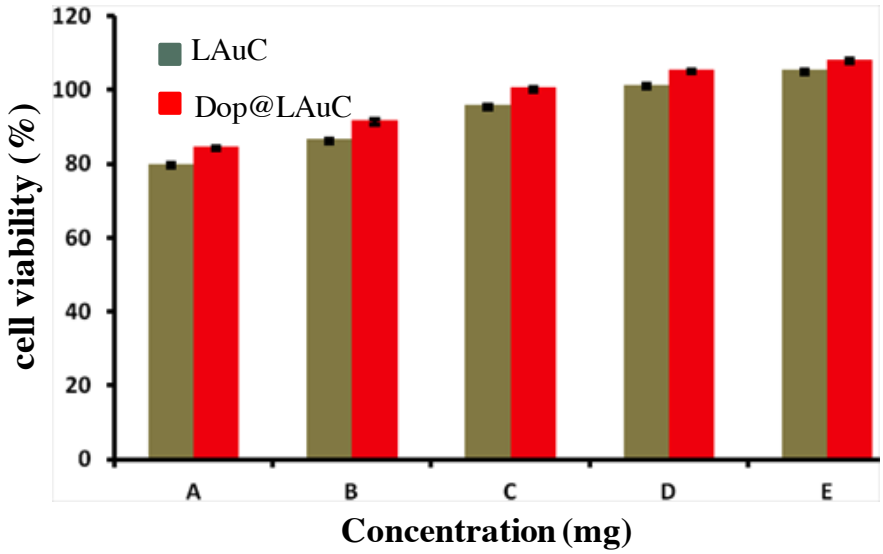

Figure 84: Viability of the cells by the addition of different concentrations of material using MTT assay. A, B, C, D, and E represents 1 mg, 0.5 mg, 0.1 mg, 0.05 mg, and 0.01 mg/ mL of material respectively.

4.4.2.3 BBB Potential, Permeability And Uptake Of LAuC and Dop@LAuC By The Cell

In order to prove the *in vitro* BBB permeability of the developed material, brain endothelial cells of mice origin (bEnd3 from ATCC) were grown on milli cell insert with a pore size of 0.4 µm. Barrier potential of the cells was regularly monitored to ascertain the confluence of the cells and the monolayer formation so that it exactly mimics the BBB. Completely confluent monolayer with barrier potential of the order of 1400 Ω was considered as in vitro model for BBB. To the developed BBB model, 1 mg/ mL (100 µL) of of LAuC and Dop@LAuC was added separately. In the case of LAuC the potential drastically reduced to 500 Ω with in 30 s. As the time proceeds the potential is trying to increase from 30 s to 24 h. The potential regaining by the cells was slow. But in the case of Dop@LAuC the potential reduced to 574 Ω

and it regains its original potential with in 2 h (figure 85a).

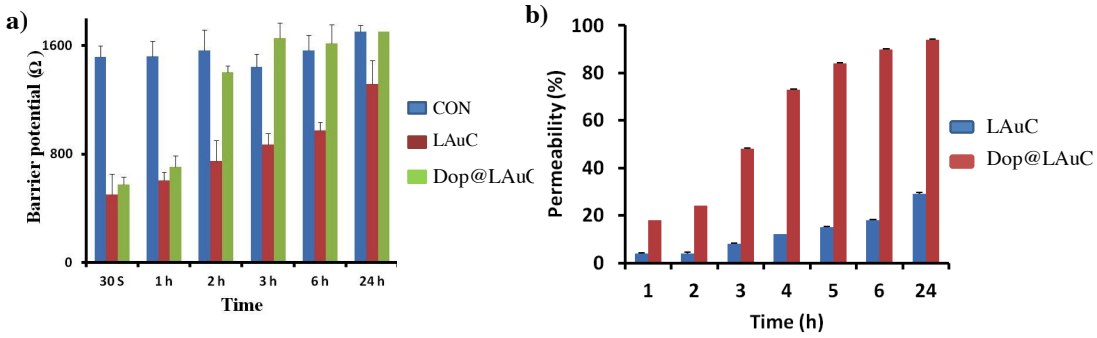

Figure 85: Barrier potential (a) and barrier permeability measurement (b) in b-End3 cells by the addition of 1 mg/ mL of LAuC and Dop@LAuC at different time period.

Figure 85b shows the barrier permeability of LAuC and Dop@LAuC by the BBB model cell. At 3h, ~50 % of Dop@LAuC were found in the outside chamber where as only 10% of LAuC were observed during this time. 25% of LAuC only is observed in the outside chamber at 24h where as more than 90% of particles are seen in the case of Dop@LAuC.

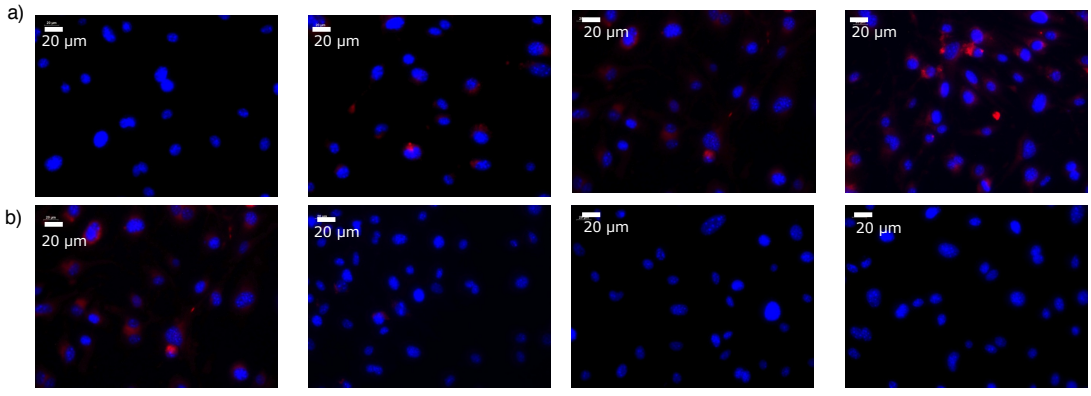

Figure 86: Cellular uptake using fluorescence microscope. b-End3 cells incubated with LAuC for 3 h, 6 h, 12 h and 24 h (a) and same with Dop@LAuC (b).

Figure 86 shows the fluorescence image of the cells after incubating the particle for 3, 6, 12 and 24 h. Nucleus were counter stained with hoescht. These images show the particle uptake efficacy of LAuC and Dop@LAuC by the micro vascular brain endothelial cells. In the figure 86 it is observed that in the case of LAuC, the intensity of the particle is increasing from 3 h to 24 h while in the case of Dop@LAuC fluorescence intensity diminishes upto 6 h and at 24 h there is no fluorescence observed in the cells.

4.4.2.4 Blood Compatibility Of LAuC And Dop@LAuC

Blood material interactions were also carried out before doing *in vivo* BBB studies. In all the concentration both the material shows below 0.45% hemolysis (figure 87).

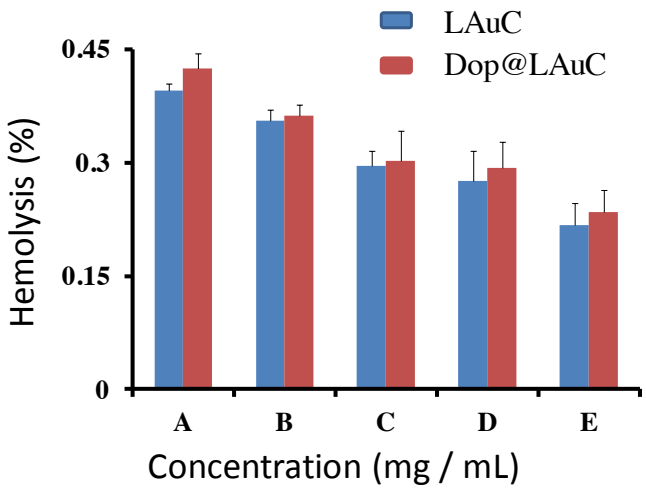

Figure 87: Percentage hemolysis of LAuC and Dop@LAuC. A, B, C, D, and E represents 1 mg, 0.5 mg, 0.1 mg, 0.05 mg, and 0.01 mg/ mL of material respectively.

4.4.2.5 *In Vivo* BBB Analysis

The BBB permeability of the materials was demonstrated *in vivo* using normal adult Swiss albino mice. The institutional animal ethical committee approved all animal studies. Dop@LAuC were administered intravenously through tail vein at a dose of 1 mg/ mL (0.5 mL). The animals were imaged after 1hr using IVIS spectrum imaging system. The NIR emission of the gold cluster facilitated imaging of the fluorescence signal from the brain and avoided the auto fluorescence signal from the animal body. Residual autofluorescence was eliminated by spectral unmixing of the image after image acquisition using live image 3.2 software. The enhanced signal intensity of Dopa@LAuC injected animal was evident in comparison with control animal (Figure 88a).

The fluorescence images of the excised brain after 2 hours also show similar result (figure 88b). In the case of Dop@LAuC injected mice is having fluorescence compared with control mice brain without any material treatment.

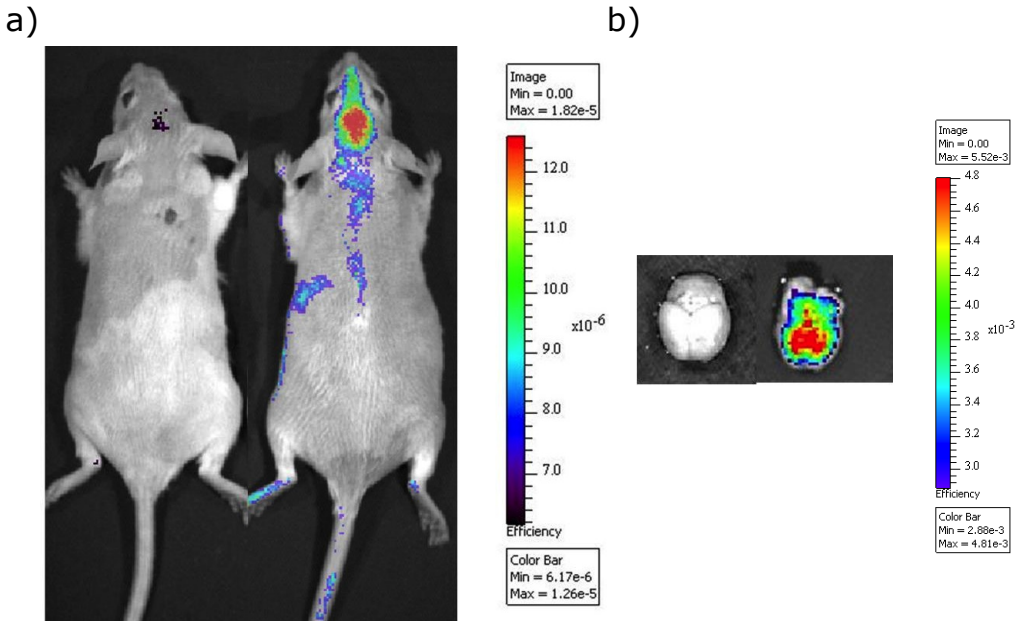

Figure 88: BBB targeting with LAuC and Dop@LAuC *in vivo* (a). Ex- vivo study to indicate the signal in the mice brain (b).

4.4.3 Delivery Of Therapeutics Into The Brain

Targeted delivery of drug into the brain is demonstrated by conjugating a model drug, pilocarpine, into GSH stabilized gold quantum cluste (GAuC). Drug release profile of pilocarpine nanoclusters were studied in different environments like phosphate buffered saline (PBS- pH 7.3), artificial cerebrose spinal fluid (ACSF) and phosphate buffer (pH 5). Cumulative drug release was shown in figure 89.

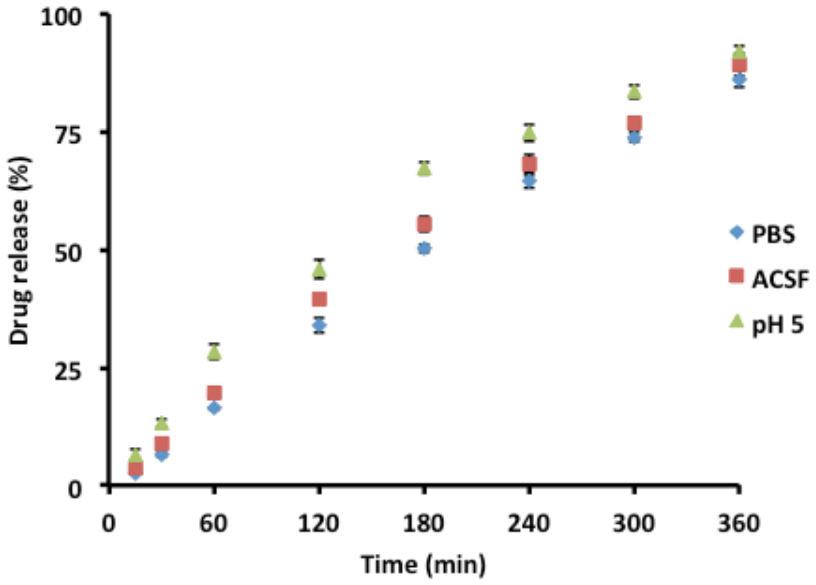

Figure 89: Cumulative drug release profile of drug treated gold cluster in PBS (pH 7.3), ACSF and phosphate buffer (pH5)

Behavioural changes in the animals were also monitored by injecting drug conjugated nanocluster to a healthy mouse. Observations are shown in table 2.

	Activity	Salivation	Tail stiffness	Seizure
1. Pilocarpine	+++	+++	++	+++
2. Pilocarpine-Dopa@GAuC	++	+	-	-
3. Dopa@GAuC	++	-	-	-

Table 2 : showing animal behavior upon injection of different materials to a healthy mice

4.5 Hybrid Nanomaterials For Imaging And Therapy In Vitro

4.5.1 Synthesis Of Quantum Dot Conjugated Single Wall Carbon Nanotube

Single wall carbon nanotube and quantum dot got wide attention in the medical field because of its unique properties. SWCNT is proven to be highly efficient in photothermal destruction where as Qd offers disease diagnosis due to the fluorescence property of the same. Here we developed a hybrid nanosystem with SWCNT and Qd (Qd@CNT) for cancer diagnosis and its treatment. Synthesis of Qd@CNT is shown schematically (figure 90)

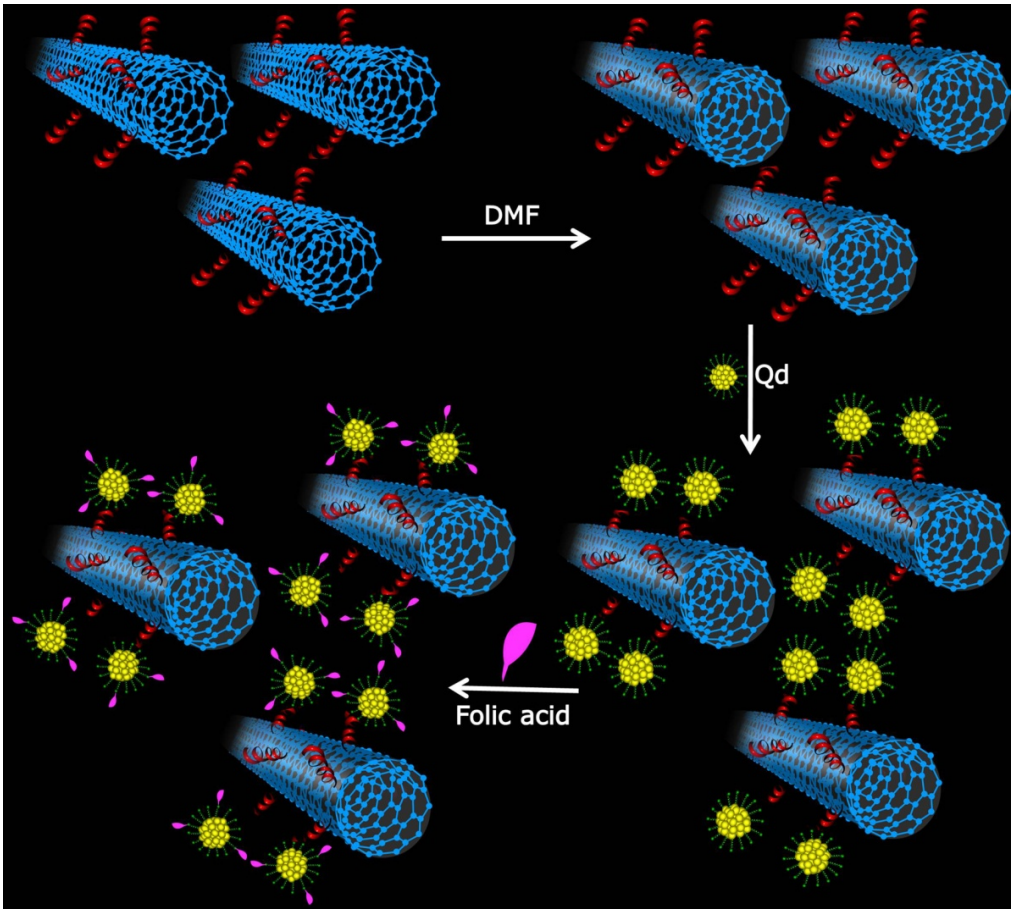

Figure 90: Schematic representation of the development of hybrid nanosystem FaQd@CNT.

The developed quantum dot exhibits a photoluminescence emission around 556 nm (Figure 91b).

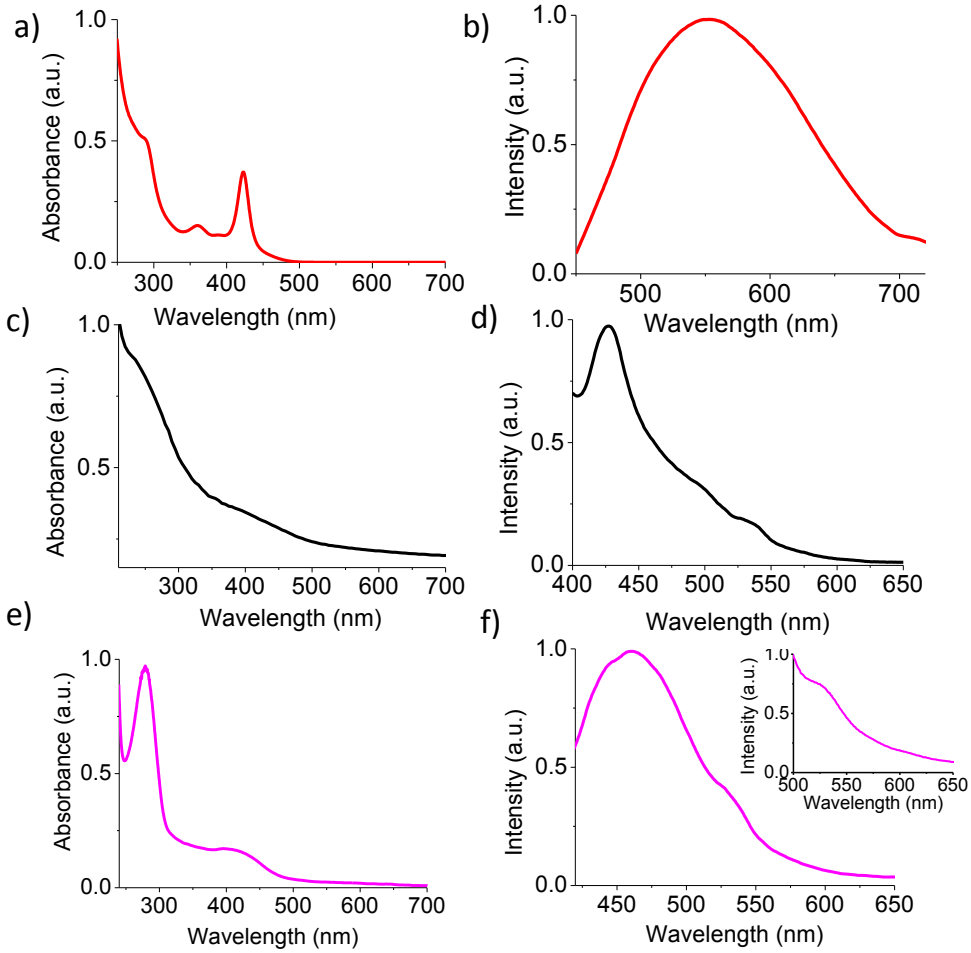

Figure 91: Absorbance spectra of Qd (a), Qd@CNT (c), FaQd@CNT (e) and corresponding fluorescence (b), (d) and (f)

Qd shows an average particle diameter of 4 nm (figure 92a). Particle size distribution of the Qd using image j software is shown in figure 93a.

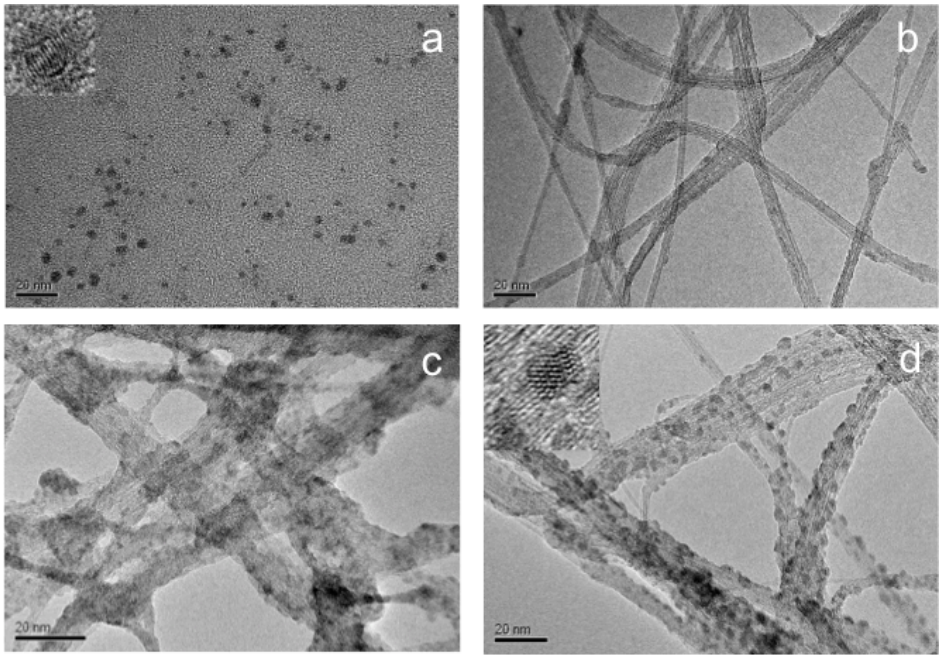

Figure 92: TEM images showing different stages of functionalization. Quantum dots (a), COOH functionalized SWCNT (b), Qd@CNT (c) and FaQd@CNT (d). Inset shows the plane orientation of the nanocrystals. Scale bar is 20 nm

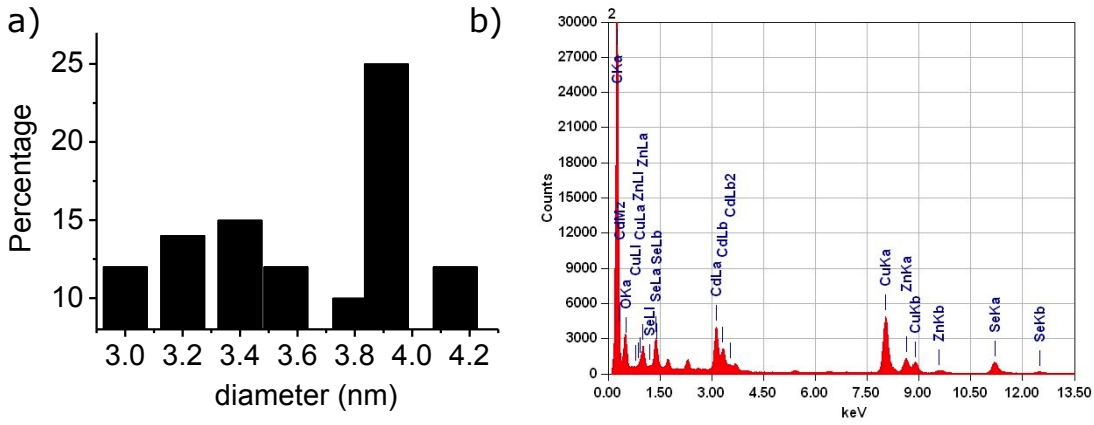

Figure 93. Size distribution by TEM (a) and EDX spectra (b) of FaQd@CNT.

Single wall carbon nanotubes were purified and acid functionalized as per the reported procedure (Kumar et al., 2013).

The aquous solubility of Qd@CNT increased tremendously compared to SWCNT. Presence of Qd over the surface of SWCNT is clearly evident under the TEM image (figure 92c, d). Crystallinity of the material is evident in the TEM (inset of figure 92) and the elemental composition of FaQd@CNT was checked using TEM- EDX (figure 93b). From EDX it is observed that FaQd@CNT shows te peak for C, Cd, Zn and Se.

The developed Qd@CNT in water showed an emission at 556 nm (figure 91d) whose intensity has been considerably reduced from that of pure Qd.

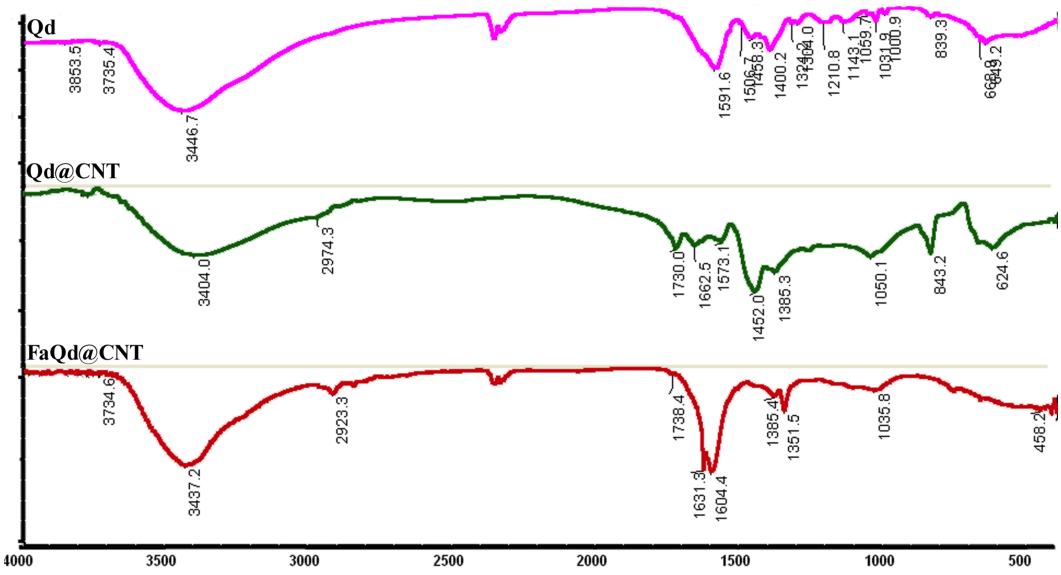

Figure 94: FT- IR spectra of Qd, Qd@CNT and FaQd@CNT

For targeting specifically to the cancer cells folic acid was conjugated to Qd@CNT. FaQd@CNT showed an absorption peak ca. 250 nm. FT- IR spectra shows a peak at

1630 cm^{-1}. The number of moles of folic acid present on FaQd@CNT was quantified using UV spectrometre and it shows value of 0.835x 10^{-5} moles of FA.

Zeta potential measured at various stages of functionalization shows that initial Qd had a zeta potential of -40± 2 mV which changes to -27± 1.5 mV (figure 95) on conjugation with SWCNT. Upon folic acid conjugation zeta potential became c.a. -23 mV.

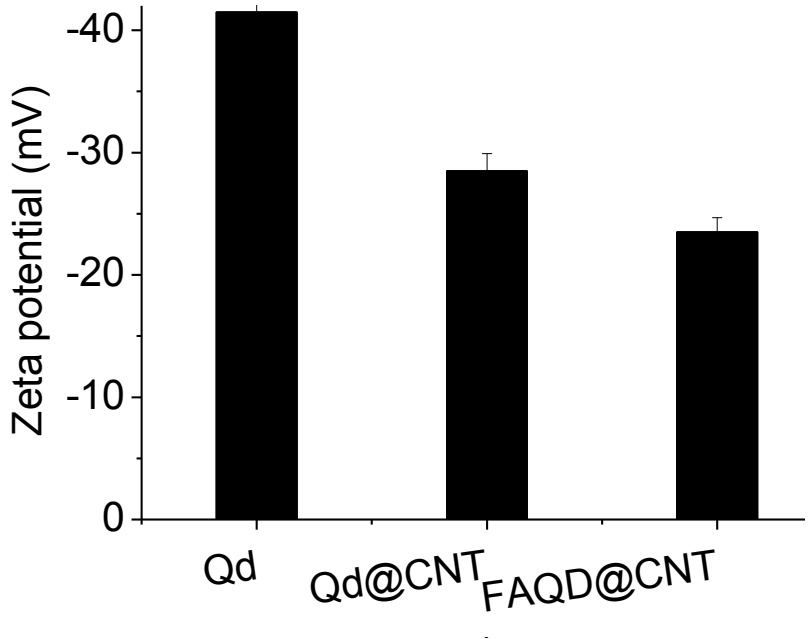

Figure 95: Zeta potential measurement of Qd, Qd@CNT and FaQd@CNT

The developed hybrid systems were again evaluated using Raman spectral analysis, since Raman is the most widely used tool for the analysis of carbon nanotubes and for its purity. SWCNT shows an areal breathing mode in the lower wavenumber region along with G band and D band.

Purified SWCNT, Qd@CNT and FaQd@CNT shows prominent peak around 200 cm^{-1}, 1600 and 1300 cm^{-1} (figure 96a).

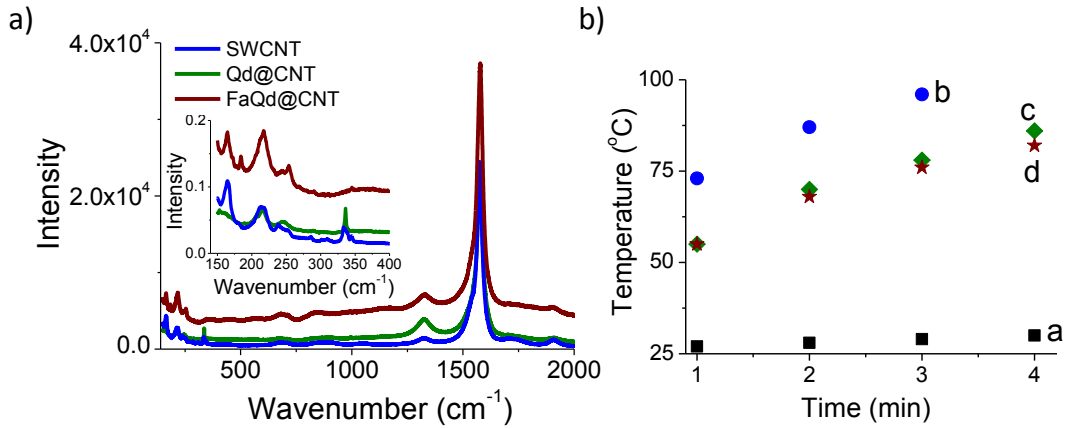

Figure 96: (a) Raman spectra of SWCNT, Qd@CNT, FaQd@CNT. Inset shows the expanded view of the arial breathing mode. (b) Temperature generation of Qd (a), SWCNT (b), Qd@CNT (c) and FaQd@CNT (d) on excitation of 800 nm laser.

Photothermal responsiveness of the materials was evaluated using a 800 nm laser of 1.726 W/cm^2 power radiated for 4 minutes. The temperature was measured with an IR thermal camera on equal concentrations of (1 mg/ mL) Qd, SWCNT, Qd@CNT and FaQd@CNT. Significant increase in temperature was observed in the combination materials where SWCNT was incorporated (figure 96b). Corresponding thermal camera photographs are shown in figure 97. In the case of Qd alone, there was no rise in temperature for laser irradiation for upto 4 min. A significant rise in temperature to 90^{o}C was observed in the case of SWCNT on 3 min laser irradiation while in the case of Qd@CNT and FaQd@CNT the temperature rise was 75^{o}C and 67^{o}C respectively.

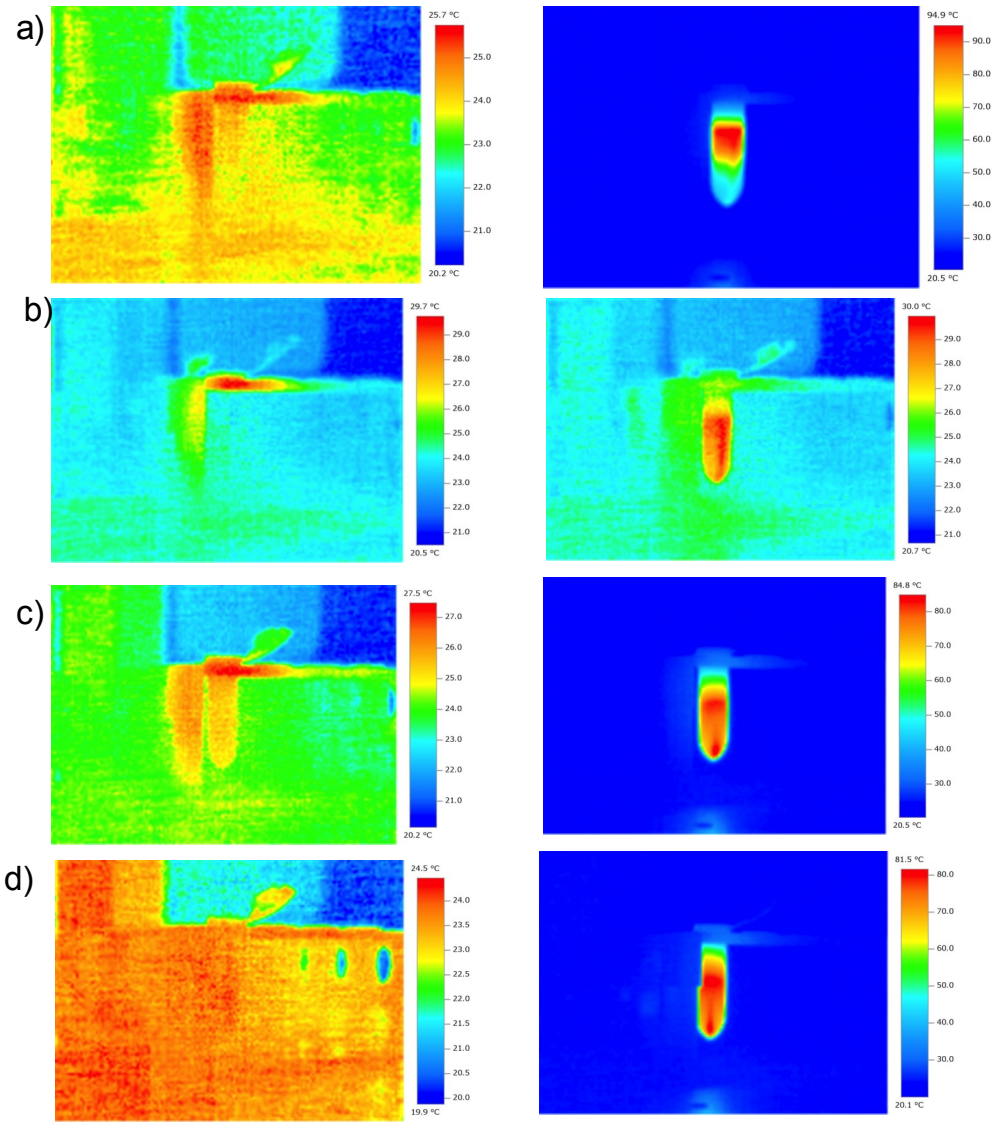

Figure 97: Thermal camera image of the developed nanosystems SWCNT (a), Qd (b), Qd@CNT (c) and FaQd@CNT (d). Left side shows temperature at 0 min and right at 4 min respectively.

4.5.2 In Vitro Studies

Cell viability of the system was tested using MTT assay in mice fibroblast (L929), and two cancerous, viz, breast (MCF7) and pancreatic (Panc1) cell lines. Developed hybrid nanosystems were incubated with the cells for 24 hrs. All the cells showed

more than 80% viability for all the concentrations of Qd@CNT and FaQd@CNT (figure 98) eventhough Qd alone showed toxicity at higher concentrations.

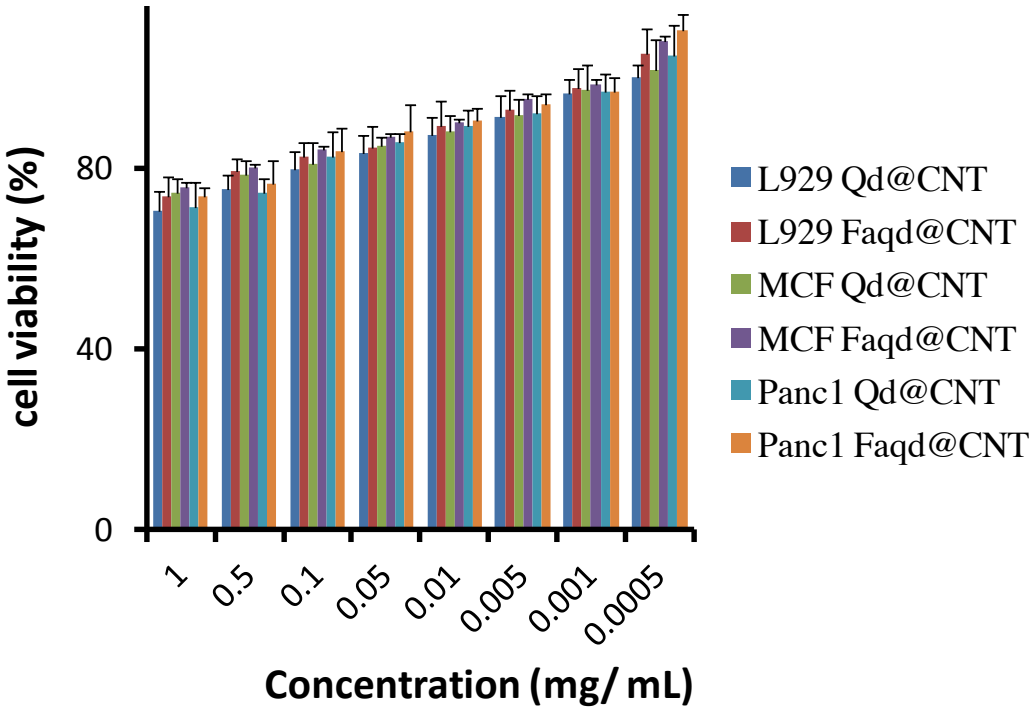

Figure 98: MTT assay of Qd@CNT and FaQd@CNT on normal (L929) and cancerous (MCF-7 & Panc 1) cell lines.

4.5.3 *In Vitro* Cellular Targeting

The MCF- 7 cells were grown in folate enriched DMEM media and the particle uptake was monitored. Both Qd@CNT and FaQd@CNT were added to the cells for 3 h. Fluorescence microscopic images shows that Qd@CNT treated cells have lesser particle uptake than FaQd@CNT. Phase and fluorescence images are shown in figure 99.

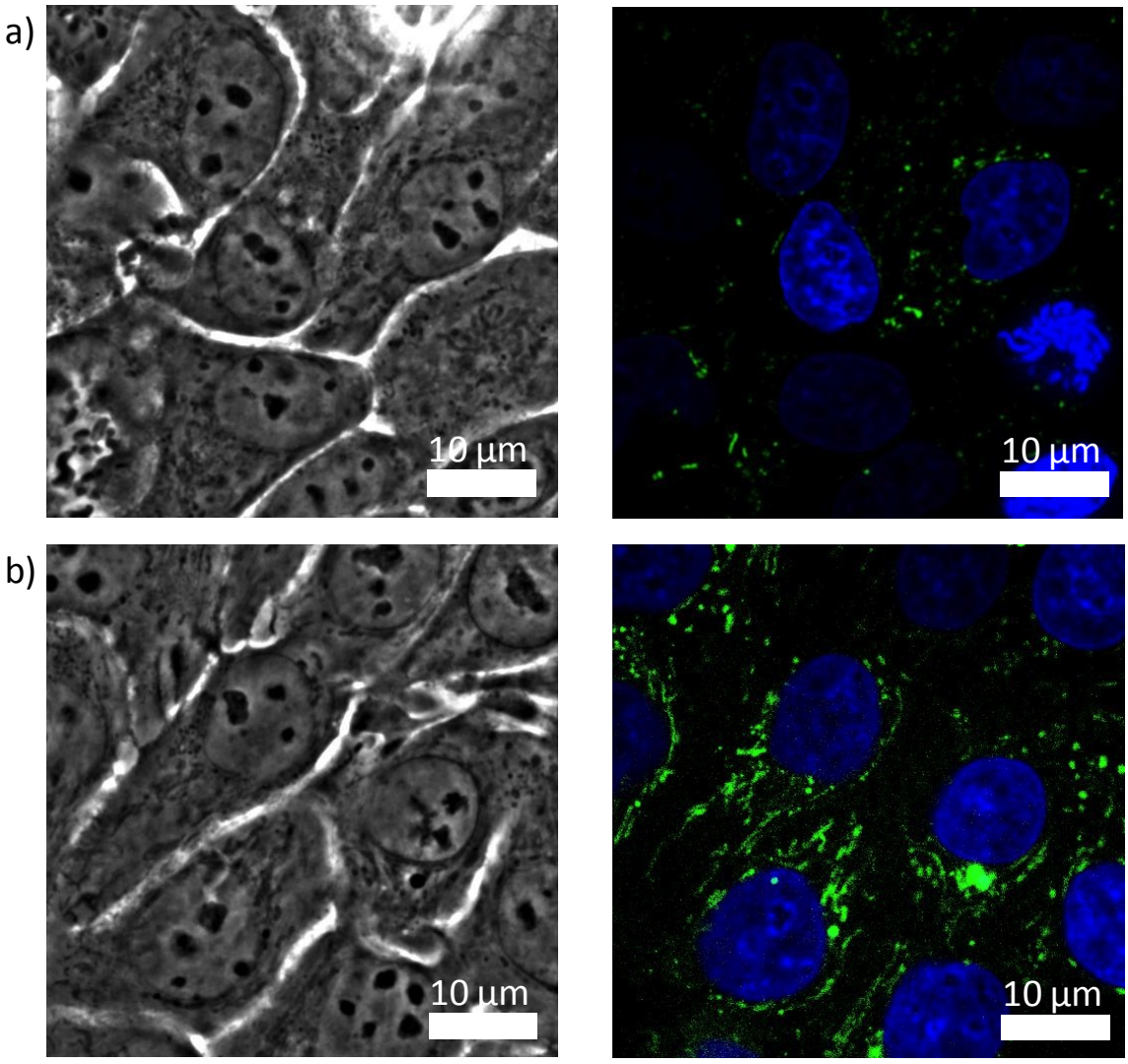

Figure 99: Particle uptake in MCF7 breast cancer cell line. First row represents the cell with Qd@CNT (a) and second row the same cell with FaQd@CNT (b) .

In order to prove the targeting efficacy of the material towards the cells, folate receptor in the cells were depleted by growing in RPMI media without folic acid. The folate depletion was done as per the reported procedure (Habeeb Muhammed et al., 2010) . MCF cells without folate receptor shows negligible uptake in the case of Qd@CNT and FaQd@CNT (figure 100).

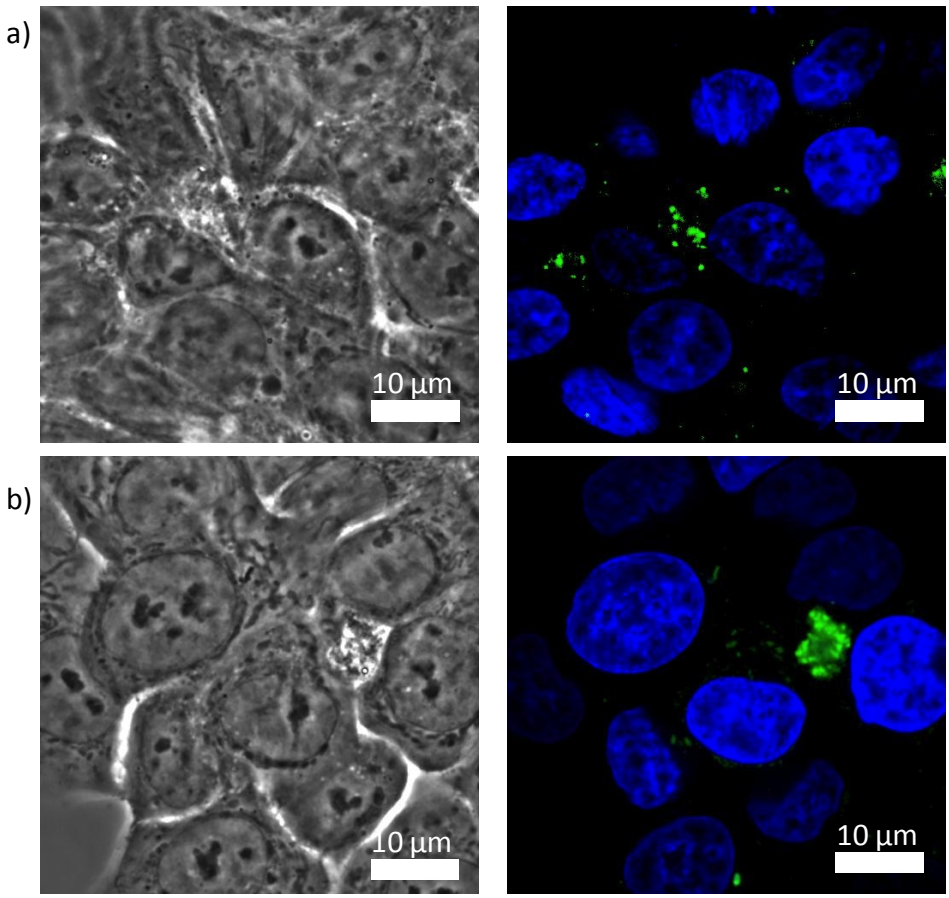

Figure 100: Particle uptake in MCF7 cell line in RPMI media. First row represents the cell with Qd@CNT (a) and second row the same cell with FaQd@CNT (b)

4.5.4 Photothermal Therapy Of Hybrid Nanomaterial

To demonstrate the photothermal therapeutic potential of the developed system, phototoxicity of Qd@CNT and FaQd@CNT was evaluated using 800 nm laser, after 3 hrs of incubation of the particles (1mg/ mL) with the cells. During laser irradiation, variation in the temperature inside the cells was continuously monitored using a thermal camera. After 4 min, the temperature of FaQd@CNT reached 50-60^{o}C where as the observed temperature rise was only upto 37^{o}C in the case of Qd@CNT which remained unchanged even after 10 min of laser irradiation. Cell death was assessed

in both cases using calcein propidium iodide stain to assess live and dead cells (figure 101). In the case of Fa Qd@CNT we observed complete cell death after 4 min laser exposure.

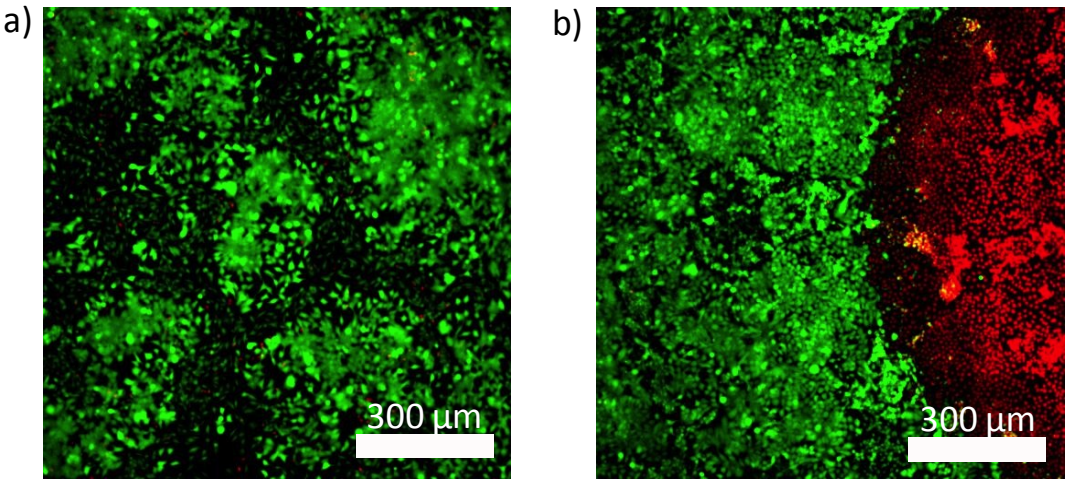

Figure 101: Calcein propedium iodide stained cells with Qd@CNT (a) and FaQd@CNT showing cell death (b).

CHAPTER 5

DISCUSSION

The success of a sensor, imaging probes and therapeutic agents depend on its efficacy to detect or transfer the drugs/ agent successfully to the target site. Relatively nonspecific action of the conventional sensors and therapeutic agents restricts its use to detect/ cure the disease in its early stage. Toxicity due to higher concentration of drug molecule and the need for the use of hazardous external stimulation like light, radiation etc again restricts its usage in large extent. Therefore it is of great importance to design strategies to detect and to cure diseases specifically to target disease causing agents or diseased region as precisely as possible. In this study the uniqueness of nanotechnology as a prime tool to achieve above said goal is explored. For that a NIR emitting gold nanocluster has been developed for sensing imaging and therapy. NIR emission of these materials enables us to avoid the autofluorescence isssues that may arise due to the visible light interaction with tissues. Urease conjugated NIR emitting AuC with GSH were utilized as a model system to diagnose blood urea from the whole blood. A novel gold cquantum luster based image guided photodynamic therapy was demonstrated for the target specific tumor detection and its treatment using PDT. The present study also includes a novel strategy to target the brain in its early stage by utilizing amino acid transport pathway mechanism using L dopa conjugated AuCs to cross BBB. A hybrid nano system has also been developed to target the tumor and its treatment using photothermal destruction.

This section of the thesis critically discusses the results emerged from the study, which includes,

1. Synthesis, structural and property evaluation of AuC with GHS and LA
2. Nanotechnology as a sensor for early stage detection of urea in whole blood and milk
3. Tumor targeting and its selective cell destruction using singlet oxygen generation of photosensitizer
4. Blood brain barrier targeting by utilizing NIR emission property of the nanocluster (GAuC and LAuC) and L dopa
5. Hybrid nanoconstruct for effective tumor targeting efficacy and selective cell destruction in vitro by photothermal abalation.

5.1. Synthesis And Optimization Of NIR Emitting Gold Quantum Cluster

5.1.1 Synthesis Of AuCs Using Glutathione

NIR emitting gold nano clusters are one of the most interesting candidates in the biomedical field because of its ability to reduce the autofluorescence during imaging application and its non toxic property. The size of the nanocluster lies below 2 nm which enhances the reactivity of the material compared to bulk and nano particle counter part. Tuning of the optical property can be achieved by varying the reaction conditions like pH , temperature, concentration of ligand etc. Emission property can be manipulated from blue to red by properly modifying the reaction condition.

Monolayer protected gold cluster attained huge interest where its property can be suitably modified by changing the gold thiol interaction. Depending on the degree of aggregation the gold thiol binary system exhibit unique structural and functional characteristics which in turn is useful for various applications like water purification, sensing of toxic element and various biomedical applications. The ratio of gold and thiol usually plays an important role in the properties of the material because it depends on the degree of polymerization of gold thiol system. Another factor which affects the structural and functional properties of the system is that Au (I) atoms with a d^{10} closed-shell electronic configuration tend to form aggregate due to aurophilic interaction.

Initially, gold nanoparticles (GMSA) were synthesised using mercapto succinic acid (MSA) for stabilisation. As synthesized GMSA showed broad absorbance, c.a. 530 nm and excitation dependent emission characteristics (figure 28a,b) in the visible region. It has an average particle diameter of 7 nm (figure 31a). Later, during the cluster formation, glutathione (GSH) replaced MSA at different reaction conditions while keeping the GMSA- GSH ratio constant (1:4 W/W%).

In the first case (S1), GSH was added to GMSA at room temperature and the reaction also continued at the same temperature. In order to evaluate the effect of temperature on the etching process of GSH on GMSA, a second cluster (S2) was prepared by adding GSH at room temperature followed by reaction at 70^{o}C. In the third case (S3), GSH was added at 0^{o}C and the reaction was continued at 70^{o}C. Further, to check the effect of pH and temperature on the cluster formation, GSH was added to GMSA at

room temperature and system pH was adjusted to 10 and the reaction was continued at 70^{o}C (S4).

The synthesized clusters showed different band origin of 1.79, 1.53, 1.87 and 1.69 eVs (figure 28a) respectively for S1, S2, S3 and S4 indicating the formation of different clusters. It was unusual to observe that S1, S2 and S3 exhibited comparatively similar photoluminescence emission property (figure 29) with emission peak around 750 nm, eventhough the band gaps are different in all these cases. In addition, the first two clusters showed an extra prominent emission band at 530 nm (for 450 nm excitation). Ratio of 750 to 530 nm peaks is found to be 1.2, 2.5, and 50.42 respectively for S1, S2 and S3. Quantum yield with respect to nile blue was found to be 0.85%, 2.5 % and 24 % respectively for S1, S2 and S3. Excitation and emission of S4 shifts to lower wavelength of 300 nm and 412 nm respectively as expected for the cluster prepared at higher pH (Habeeb Muhammed et al., 2008). A critical analysis of the UV- Vis spectra was carried out to explain the optical property exhibited by the clusters (figure 28a). S3 is not giving any surface plasmon peak due to the extremely smaller size where as other three samples shows the presence of plasmon peak around 500 nm to 650 nm. Origin of these plasmon peaks in a system where quantum confinement can prevails can be due to the assembly of these clusters in the solution state. The appearance of strong emission characteristics of quantum clusters further strengthens this argument. If the Plasmon peaks were from the aggregated bigger particle the fluorescence emission would not have observed. Slight variation in the plasmon peak among all the samples indicates the difference in the formation of assembly. Shoulder peak around 500 to 600 nm in

S2 again indicates the assembly of the cluster in comparison with S3. In the case of S4, absorption around 370 nm is observed which gives an indication of the lesser number of atoms which again is evident from the blue shift in the fluorescence emission.

Fluorescence of gold nano cluster and nanoparticles is explained based on the quantum confinement and the Mooradian explanation respectively. When the dimension of nanoparticle reduces to the order of approximately fermi wavelength of electron, it shows discrete energy level because of the quantum confinement which enhances the fluorescence efficiency of quantum cluster (Qian et al., 2012). Origin of fluorescence of gold is mainly due to the excitation of 5d valence electron to 6sp band followed by scattering and recombination from sp band resulting photon emission (Mooradian, 1969). El Sayed and co workers have also explained the same as surface fluorescence in the case of gold nanorod (Mohamed et al., 2000).

Appearance of additional emission peak around 530 nm in the first two cases could be either due to the presence of bigger nanoparticles, GMSA (figure 28b), in the final cluster colloid or due to the arrangement of gold clusters in such a way that the distance between individual cluster is very less to overcome interaction with one another, giving rise to combined emission similar to that of gold nanoparticles.

To find a more specific reason for this observation, TEM analysis was done (figure 31) where S1 and S2 shows plate like and helical structures respectively in which the diameter of S1 ranges from 0.7 to 2 nm where as that of S2 ranges from 0.7 to 1.5 nm. The absence of GMSA particles in TEM apparently ruled out the first possibility.Moreover, it is clear from the TEM images that in both cases, the distance

between individual nanoclusters is less than 1 nm, and shows a self assembled pattern which strengthens the second possibility for the appearance of additional emission peak. The absence of a prominent emission peak around 530 nm in S3 further confirms this argument where mono dispersed and well separated clusters with diameter of the order of 0.7nm are observed, without self assembly. Repeated units of similar assembled patterns in TEM confirm self assembly.Appearance of repeated regular assembled patterns rules out the solvent evaporation assembly or coalescence due to electron beam. From these observations, we propose that contribution from the combined electronic transitions of the self assembled structure has resulted in the enhancement of 530 nm emission peak while discrete energy transition within the energy level has resulted in the 750 nm peak. Particle diameter of 2 nm with a self assembled symmetrical patterns was noted for S4. It is evident from the fluorescence peaks of GMSA (figure 28b) that there is no strong emission at 412 nm for 300 nm excitation, as observed in the case of S4. This explains that the emission property of S4 also has no contributions from bigger particles.

To further extend the knowledge on details like cluster ionization and number of atoms and ligands present in the nanocluster, MALDI -MS analysis was performed. Number of core atoms and ligands present in the material plays a crucial role in the optical property of the cluster. It is reported that 750 nm emitting cluster consists of 33 core atoms and 410 nm emitting cluster consists of 8 atoms (Habeeb Muhammed et al., 2008). Assigning the core atoms accordingly, the number of ligands has been evaluated from the MALDI spectra (figure 30). Likewise, the compositions of the clusters were estimated as $(Au)_{33}(SG)_{28}$, $(Au)_{33}(SG)_{28}$, $(Au)_{33}(SG)_{11}$ and $(Au)_{8}(SG)_{2}$

for S1, S2, S3 and S4 respectively. These assignments are further validated theoretically using *m mass* software (figure 30 insets). The fragmentation in the MALDI spectra can be either due to the existence of atomic cluster with minor changes in mass or due to the breakage of gold-thiol bond of the same atomic cluster (Tanaka et al., 2003) (Negishi et al., 2005) as a result of laser irradiation. Based on the isolation procedure that we have adopted in this study, we do not expect the presence of atomic cluster with significant mass change. So we conclude that the fragmentation is based on the breakage of gold –thiol bonds. Previous reports also agree this type of fragmentation (Negishi et al., 2005). Further strict isolation of the cluster with minor mass change would result in the reduction of material yield significantly, and hence is not considered in this study. Moreover, such isolation is not very essential in the context of a particular application like imaging. Incomplete ionization observed in the MALDI spectra of S1 and S2 and the complete fragmentation in S3 further supports the formation of assembly in S1 and S2. In S1 and S2 the laser energy has been utilized to break the assembly to individual nano cluster in addition to the fragmentation of Au-thiol bond. Complete fragmentation observed in S3 for the same laser power (160mW), where self assembly is absent justifies this. But conversely, in S4, complete ionization was achieved even when there is a well established self assembled structure (figure 30d). This is due to the presence of comparatively lesser number of core atoms and ligands, which enabled the desorption of individual cluster and also the Au thiol-bond for the applied laser power.

Developed nanoclusters were further studied for their geometric and structural evaluation using XPS (figure 32). A chemical shift was observed in the $4f_{7/2}$ peak for all the clusters (85.18, 85.25, 84.83, 85.21 eV respectively for S1 to S4). Based on the $4f_{7/2}$ peak, Negishi et al and Tanaka and co workers have explained the mechanism of photoemission by de-convoluting the $4f_{7/2}$ peak in the binding energy spectrum of gold (Tanaka et al., 2003), (Negishi et al., 2004). The peak shift has been explained based on the 'initial state effect' due to electronic transition from gold core to thiolates, which applies to the observed shift in the present study also (Negishi et al., 2005). Slightly higher chemical shift observed for self assembled structures (S1, S2 and S4) is attributed to the electronic transition from self assembled electron to gold core/ surface gold atoms.

From the TEM results, formation of self assembly was noted in cases where GSH was added at room temperature and that too is more prominent in the case of S1, S2 and S4. Compiling the results of number of atoms per cluster, size of the cluster and observed self assembly, a plausible mechanism is explained in correlation with the reaction conditions. Accordingly, in the first case of S1, where the reaction takes place at room temperature, equilibrium of GSH is between two carboxylic groups, amine group and one SH group when the pH is 1.5. GSH is known to have a tendency to form linear assembly because of the presence of acid and amine moiety in it (Sudeep et al., 2005). During this reaction, MSA gets replaced by GSH through the S- moiety forming 33 atoms to form S1. Further, COO^- will tend to form assembly with NH_3^+ moiety of another S1 and the assembly continues. While balancing between the formation of stable cluster and self assembly at room

temperature, uniformity is compromised which resulted in the occurrence of different sized particles in the TEM (figure 31b). But when GSH was added at room temperature and reaction is continued at 70^{o}C (S2), etching takes place uniformly. Here, addition of GSH at room temperature results in the assembly between COO^{-} of one cluster and NH_3^{+} of another cluster, exhibiting a helical appearance to the assembly. When GSH was added at 0^{o}C and the reaction was performed at 70^{o}C (S3), the system overcomes the tendency to form self assembly accomplishing the most stable cluster of the study.

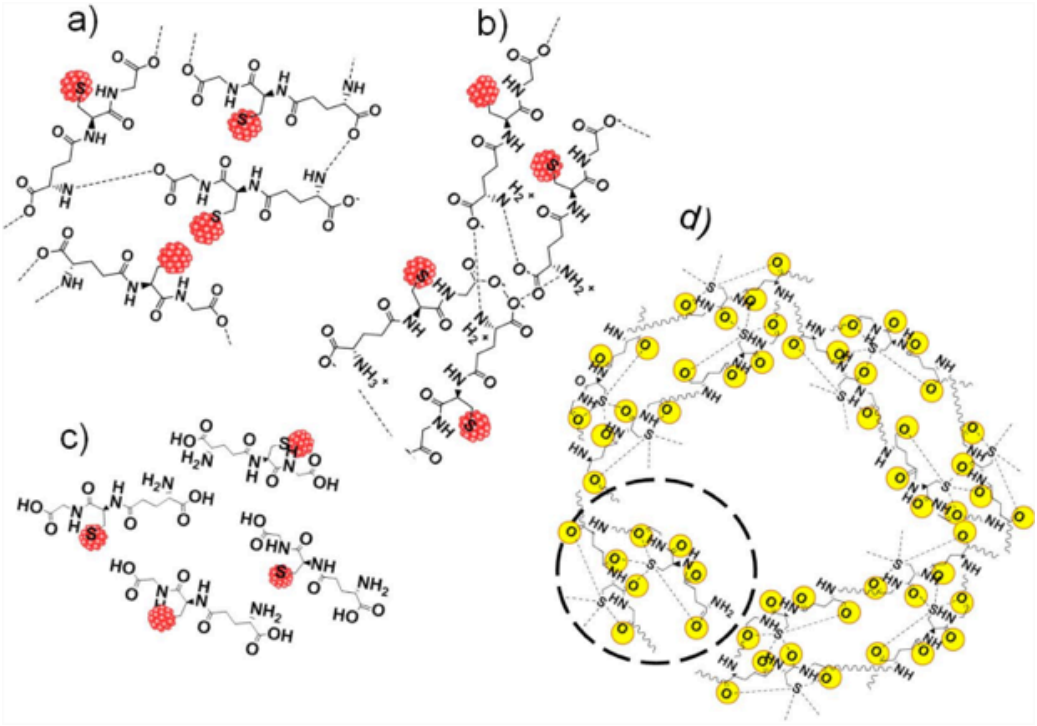

Figure 102: Mechanism for the formation of different cluster by varying the reaction condition

In the fourth case, at pH 10 the GSH equilibrium is between four carboxylic oxygen atom, amino group and thiol group. MALDI and TEM observations reveal that eight gold atoms form a cluster with two GSH ligands, but with an increase in the particle size compared to other clusters. This is because the individual eight atoms of gold

are slightly separated in S4 compared to thirty three atoms in S1 and S2 imparting bigger size for S4 in the TEM image. The most suitable way to explain the mismatch between number of atoms and size is, the arrangement is in such a way that 8 gold atoms interact with the negative charges of four carboxylic groups together with a centralized interaction by the thiol group so that it forms a spherical shape with spacing at the centre (figure 31d). Formation of different cluster is depicted schematically in figure 102.

X-ray contrast for CT imaging (figure 35) and optical imaging potential of the developed clusters shows that, CT Number was maximum for AuC4 (48 HU) with the best image contrast and minimum for S3 (8HU). Extremely small size and the mono disperse nature of S3 would have caused the less CT contrast compared to self assembled ones. For optical imaging S3 (figure 34) leads with very good imaging potential as expected from its highest quantum yield originated due to its unique optical property.

5.1.2 Synthesis And Characterization Of LAuC

Lipoic acid stabilized gold cluster showed fluorescence emission around 720 nm (figure 37b) and an average particle diameter c.a. 1.4 nm (figure 37d), which confirms the quantum confinement of the developed nano construct. HRTEM studies showed a lattice distance of 3.5 A^o for this cluster. The XRD data (figure 38a) also agrees with this result even though it shows broad peaks. Peak broadening can be attributed to the extremely smaller size. Assignment of LAuC as $(Au)_{18}(LA)_{14}$, the magic numbered cluster was confirmed theoretically.

From XPS (figure 38b) analysis it is evident that here also a chemical shift is observed and is due to the initial state effect as discussed in the case of GSH cluster. LAuC is found to be lesser quantum yield than GAuC.

Absence of S-H peak in the FT- IR spectrum (figure 39) of LAuC is an indication of the ligation of both the thiols of lipoic acid. Since both thiol groups are linked to the Au atoms we hypothesize that $(Au)_{18}(La)_{14}$ is arranged in such a way that 12 atoms of gold have adopted an icosahedral symmetry utilizing one of the thiol groups of lipoic acid, while the remaining 6 atoms of gold are connected via another thiol group (i.e, S-Au-S-Au bond). This might be the most possible way of the system to minimize the potential energy to form a stable system.

5.2 Gold Quantum Cluster As A Novel Sensor

Urea is a byproduct of protein metabolism that is formed in the liver, carried by the blood and excreted through the kidney in urine. Therefore, urea is an important marker for evaluating uremic toxin levels and kidney and hepatocellular functions. Urea detection is also important in the estimation of non-protein nitrogen in food products such as milk since it is known that urea adulteration is utilized as an indicator of protein feeding efficiency. Nanosensors based on metal nanoparticles have got wide attention during the past couple of decades because of their enhanced selectivity and sensitivity towards specific analytes. There are several reports on nanosensors for the detection of urea, most of which are based on electrochemical or amperometric sensing.

The design of the nanosensor started with the preparation of GAuC by the process of etching mercapto succinic acid conjugated gold nanoparticles (GMSA, 5-7 nm,

figure 31a) in the presence of glutathione (GSH) at 0^{o}C followed by 20 min incubation and subsequent heating at 70^{o}C, maintaining the pH at 1.5. The color of the solution changed from dark brown to light yellow with etching process. The cluster exhibited a broad fluorescence emission with a maximum around 750 nm (figure 29c) which agrees well with the reported value for Au_{33}. The quantum yield of the cluster was estimated as 25±6% using Nileblue as standard, which is much higher than the reported value for Au_{33}. The increase in quantum yield may be attributed to the modulation of the HOMO–LUMO gap, the intraband transitions and the stabilizing ligand used. This observation is supported by a previous report by Dickson et al. on clusters exhibiting wide range of fluorescence properties and quantum yield of 10-70% (Zheng et al., 2007).

For the biosensor design, GSH protected AuC (GAuC) was mixed with urease which is an enzyme, specific for urea. The urease-AuC mixture (Urease@GAuC) was collected by centrifugation at 8000 rpm, kept under refrigeration and used for the detection of urea. Addition of urease to GAuC did not show any change in the fluorescence spectrum. However, the negative zeta potential of AuC (ca. -20 mV) showed a variation to ca. -28 mV upon the addition of urease (figure 42a). Since the spectral data did not show any considerable change in the optical properties of GAuC and Urease@GAuC, we hypothesized that the GAuC could be physically entrapped within the urease. To demonstrate the urea sensing, different concentrations of urea (2.5-70 mM) were added to aqueous solutions of AuC@Urease(1 μg mL^{-1}) which exhibited a gradual decrease in the fluorescence emission intensity at 750 nm with the increase in the concentration of urea (figure 44). Nearly 10% fluorescence quenching was observed with addition of 2.5 mM urea, nearly 60% with 7.5 mM and

83% quenching with 50 mM (10 μL). Further addition of urea did not show any considerable quenching. The efficacy of the sensor was demonstrated for urea concentrations in blood samples in the range 2.5-10 mM, since the normal blood urea level in a healthy human body ranges from 2.5-7.5 mM and the values above and below this level indicates the need for medical attention. In a series of experiments, blood serum (20 μL samples) of a healthy person was collected and incubated with different concentrations of urea for 30 min. Serum spiked with different amounts of urea was added to Urease@GAuC (1 μg mL^{-1}) and the fluorescence at 750 nm was recorded which exhibited a concentration dependent decrease in intensity when compared to the control serum sample (figure 45).

A possible explanation for the urea mediated fluorescence quenching of Urease@GAuC could be the aggregation of GAuCs in the presence of urea. This hypothesis is confirmed by the TEM analysis of the GAuC and Urease@GAuC before and after the addition of different amounts of urea (figure 46). The extremely small size and the inherent fluorescence exhibited by the cluster limit the use of DLS for the estimation of the particle size and size distribution. Hence the size distribution analysis was done using TEM (figure 47). GAuC and Urease@GAuC both showed an average particle size of 0.7 nm (figure 46a, b).The HR-TEM images after the addition of urea to Urease@GAuC showed significant increase in the size of the clusters (figure 46c, d). The histograms after the addition of 2.5 mM urea showed an average particle size of 3 nm which considerably increased to 18 nm upon addition of 30 mM urea. Interestingly, the initial zeta potential of Urease@GAuC (-28.3 mV) gradually decreased with increase in the urea concentration (figure 42a). With the addition of 50 mM of urea, the zeta potential dropped from -28 mV to nearly zero.

The drop in the zeta potential value could be the result of the urease catalysed conversion of urea into NH_3 and CO_2 leading to the generation of ammonium ions and the consequent pH variation (Wang and Tarr, 1955).The initial pH of the Urease@GAuC solution was 5.3 which slowly increased on the addition of urea (figure 42b). The positively charged ammonium ions neutralize the negative surface charge of the gold clusters which induce instability, resulting in the aggregation and the consequent quenching of fluorescence. Based on these observations, a plausible mechanism for the detection of urea is shown in figure 103. To validate the above proposed sensing mechanism, we have checked the effect of added ammonium ions on GAuC. As expected, the fluorescence intensity of GAuC was quenched after adding different quantities of ammonium ions (figure 48). Furthermore, TEM analysis of the GAuC after addition of ammonium ions (figure 49) showed larger particles as observed with the addition of urea to Urease@GAuC (figure 46). These observations clearly support the mechanism proposed in figure 103.

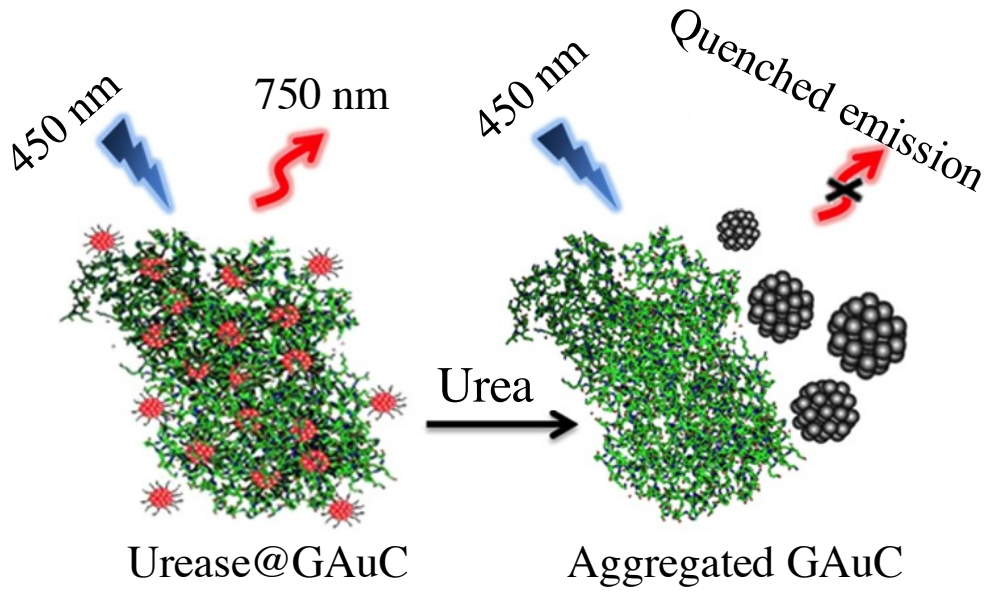

Figure 103: Mechanism of urea detection by urease treated GAuC

One of the limitations of sensors based on nanoparticle aggregation induced fluorescence quenching is the potential interference by other analytes, which often hampers the selectivity. To prove the selectivity of the Urease@GAuC for blood urea sensing, the serum sample collected from a healthy person was divided into 20 μL portions and was spiked with different analytes such as creatinine, glucose, and uric acid followed by incubation for 30 min. Subsequently, these samples were added to Urease@GAuC (1 μg mL^{-1}) and the fluorescence intensity at 750 nm was monitored which revealed no considerable variation. However, when a definite amount of urea was added to these solutions significant fluorescence quenching was observed indicating high selectivity of Urease@GAuC towards urea (figure 50a). The limit of detection for urea was estimated to be 1 mM for a 5-7% quenching of fluorescence intensity when the urease to GAuC ratio was maintained at 1:9 v/v. Another potential interference may be from thiol containing amino acids such as cysteine and homocysteine present in the blood due to the high affinity of the thiol moiety towards GAuC. However, the fluorescence intensity did not show any considerable change after incubating AuC@Urease with cysteine (figure 50a F) indicating that thiol containing molecules have no effect on urea sensing. In addition, aggregation based assays can also be influenced by the presence of proteins and salts. This possibility was ruled out by testing with a protein (albumin) and NaCl (figure 50a C and G). Thus, the described sensor based on enzyme specific aggregation induced fluorescence quenching of GAuCs is selective for urea and shows no interference due to any other analytes present in blood.

The new sensing method has also been validated for its accuracy against currently adopted methods in clinical diagnosis. For this purpose, urea estimation was done on

blood serum samples collected from patients with different unknown urea levels using the standard clinical and the Urease@GAuC methods (Table 1). The blood urea level was quantified using a calibration plot drawn for known concentrations of urea against changes in the fluorescence intensity. By this method, the unknown concentration of urea in blood was calculated and the values were compared with those obtained by independent clinical analysis and found to be within±3% error limit (figure 50b, Table S1). For a real time analysis of a specific analyte in blood, it is necessary to use whole blood rather than blood serum. Since the autofluorescence of blood samples occur at 620 nm (λ_{ex} @ 450 nm, figure 51a), we speculated that the NIR emission of Urease@GAuC at 750 nm may not interfere and hence will be ideal for the detection of urea in whole blood. Moreover, since the fluorescence quantum yield of blood is relatively low (0.1% with reference to Rhodamine B) when compared to that of Urease@GAuC, interference by the autofluorescence of blood for detection of urea is negligible. For the whole blood analysis, the fluorescence change of Urease@GAuC in blood samples spiked with different concentrations of urea were measured (figure 51b) and compared with that of the native blood. Further, the data of the whole blood were compared with those of the same blood serum samples. These data indicate that direct urea detection in whole blood is possible with Urease@GAuC without any considerable interference by other analytes present. In order to demonstrate further application of Urease@GAuC, we have carried out the urea analysis in milk samples. In the case of diseased cows, the urea content in the milk is reported to be high. In addition, in many Asian and African countries, locally available milk is adulterated with urea, to increase the solid-not-fat (SNF) value, and hence urea contamination needs to be monitored. Therefore, milk samples

were adulterated with different amounts of urea and subjected to analysis. When Urease@GAuC is added to the native and the adulterated milk samples, concentration dependent fluorescence quenching was observed as shown in figure 52. Since the developed sensor system does not interfere with the autofluorescence of milk (figure 52a) or with other biological analytes present, it offers a suitable way to monitor the urea content in adulterated milk.

5.3 Gold Cluster For Tumor Targeted Imaging And PDT

To facilitate dual functions of targeted PDT and imaging applications, lipoic acid protected gold cluster (LAuC) with NIR emission was synthesized and used. To this cluster, cancer targeting moiety, folic acid (FA) and the photo dynamic therapeutic agent protoporphyrin IX (PPIX) were functionalized by EDC-NHS chemistry to get the desired final system (PFLAuC). For incorporating PPIX to folate conjugated cluster, hexamethilenediamine (HMDA), an intermediate coupling agent for both folate and PPIX was integrated to FLAuC by protecting one of the amine groups of HMDA. For this, a concentration of HMDA equivalent to one third of the final concentration of FA was chosen. To the resultant system (AFLAuC), PPIX was conjugated by EDC and NHS chemistry to get the final system. Various stages of preparation of PFLAUC are represented in the schematic diagram (figure 53)

LAuC showed fluorescence emission around 720 nm (figure 37b) and an average particle diameter c.a. 1.4 nm (figure 37d), both of which are characteristics of nanoclusters. HRTEM studies showed a lattice distance of 3.5 A^o for this cluster. The XRD data (figure 38) also agrees with this result even though it shows broad peaks, which may be due to the extremely smaller size of the cluster. The observed

fluorescence of cluster is attributed to the intra/ inter band transition within the conduction band.

The photophysical properties of cluster based nano systems are characterized by the number of atoms which constitutes the cluster. The effect of stabilizing ligand has also been found to contribute remarkably to the optical properties of AuCs. A typical top down approach were adopted of preparation, where the bulk gold is reduced to nanoparticle using a reducing agent and **α-**lipoic acid as a stabilizer. As the reaction proceeds α-lipoic acid gets reduced to dihydrolipoic acid (DHLA) which further etches gold nanoparticles to smaller cluster (LAuC). The freshly reduced DHLA etches gold nanoclusters through the formation of strong dithiol-Au bonds in such a way that the acid head group points towards the solution.

Matrix assisted laser desorption ionization mass spectrometric (MALDI) analysis of LAuC showed peaks indicative of the simultaneous desorption of gold and sulphur atoms for each laser fluencies at a power of 160mW (figure 37c). From the UV absorption spectroscopy, optical band gap of LAuC was observed as 1.88 eV (660 nm) (figure 37a) which matches with the reported value for glutathione stabilized gold cluster with 18 core atoms (Negishi et al., 2004), (Negishi et al., 2005). Based on the results of mass spectroscopy and the observed resemblance in the optical band gap, we have assigned 18 number of Au atoms present in the cluster. On assigning the number of Au atoms in the total mass of LAuC, the number of ligands present was calculated as 14 from the MALDI-MS peaks. The metal-ligand ratio of $(Au)_{18}(La)_{14}$ assigned likewise represents a magic number which imparted the stability to the cluster, justifying the assignment. Further, this assignment was confirmed with theoretical mass spectra of the same combination with the help of

mass analysis software (m mass). Theoretical (figure 37 inset) and experimental peak fragmentation showed good agreement justifying the assignment of cluster ligand ratios $(Au)_{18}(LA)_{14}$.

Folic acid functionalization was carried out on as-prepared LAuC to specifically target to the cancer cells without affecting the normal cells. Negative zeta potential of -36 mV exhibited by LAuC decreased to -28 mV on addition of FA (figure 54). Characteristic absorption of folic acid (figure 55a) observed in the UV-Vis absorption spectrum of FLAuC also demonstrates the presence of folate moiety on the surface of LAuC. The observed shift in the amide bands of FLAuC in the FT- IR spectrum (figure 56) also supports the functionalization. Folic acid conjugated nano cluster, FLAuC shows red edge excitation emission, a phenomenon in which the emission peak red shifts as the excitation increases (Chattopadhyay and Mukherjee, 1999). This phenomenon was observed initially in the case of folic acid at basic pH and later in FLAuC. Red edge excitation occurs due to the change in dipole moment of the folic acid and the rate of reorientation of the water molecules as a result of a change in the FA-water interaction in the ground and excited states. This difference in excitation is also maintained in the fluorescence lifetime of FLAuC which showed a lifetime of 37 ms compared to 401 ns of LAuC (figure 58a,b). Also, in the case of FLAuC, an increase in the intensity of 720 nm emission peak is observed which may be attributed to the fluorescence resonance energy transfer (FRET) between LAuC and the folic acid ligand. Occurrence of FRET can be due to the fact that in FLAuC, emission of FA, which is bound over the lipoic acid, is overlapping with the excitation of LAuC.

For enabling targeted PDT, PPIX was conjugated to the folate functionalized LAuC. Here also the presence of FA and PPIX was evident in the absorption characteristics which demonstrate both the functionality over LAuC (figure 55b). The negative zeta potential of -28mV of FLAuC further decreased on addition of HMDA (c.a. -19 mV) and increased to the order of -25mV on addition of PPIX indicating the changes in the functionality onto the surface of LAuC at different stages of functionalization (figure 54). Again, the shift observed in the amide peaks in the FTIR spectrum of PFLAuC is indicative of the functionalization of porphyrin. The photoluminescence emission of PFLAuC showed all the characteristics emission peaks of folic acid, PPIX and gold confirming the presence of these components in the final system. The particle size of FLAuC and PFLAuC remains the same as that of LAuC as is evident from the TEM results (figure 57).

The fluorescence quantum yield measurement (figure 58d) shows a high quantum yield of 10% for FLAuC compared to 1.86% of LAuC, which reduces to 5.1% in PFLAuC on conjugation with porphyrin. The fluorescence life time (figure 58) of PFLAuC also decreases to 5.68 pS from 37 mS of that of FLAuC. The decrease in the fluorescence quantum yield of PFLAuC at 720 nm is due to the increase in the distance between PPIX and core atom (figure 53). As a result, most of the excitation energy is utilized by the surface groups rather than by the inner Au core. At every stage of functionalization, ligand concentration on the cluster surface was quantified using UV- Vis absorption spectroscopy. The number of moles of lipoic acid, FA and PPIX present on LAuC at each stages of functionalization are evaluated as 1.35×10^{-6}, 1.67×10^{-6} and 1.40×10^{-7} respectively.

In order to use the developed system as photo sensitizer for photodynamic therapy, the singlet oxygen generation efficiency of PFLAuC was demonstrated. This is achieved by the direct spectroscopic observation of singlet oxygen emission at 1270 nm by 530nm excitation (figure 59a). The singlet oxygen production was reconfirmed by another method using diphenylisobenzofuran (DPBF) DPBF readily reacts with singlet oxygen with an observed decrease in absorption of DPBF with the increase in singlet oxygen concentration (figure 59b-d). Singlet oxygen yield of PFLAuC was 80% compared to 63% of PPIX. The high singlet oxygen efficiency enables the use of lower concentrations of the currently developed system for efficient PDT. Moreover, the targeting property of PFLAuC also helps to reduce the dose and will leave the normal cells unaffected.

The feasibility of using the developed material for *in vitro* imaging and PDT was checked with folate over expressed cancer cell line (c6 rat glial cell) and the non toxicity of the developed system was confirmed with L929 mouse fibroblast. Cytocompatibility of the developed nanocarrier was confirmed by the activity of mitochondrial reductase using MTT assay (figure 60). All the materials showed good cellular viability.

The targeting and non targeting efficacy of the material was studied by incubating 1 mg/ mL of LAuC, FLAuC and PFLAuC (figure 61). The initial material, LAuC showed less entry into the C6 glial cells compared to its folate conjugated and porphyrin conjugated counter parts FLAuC and PFLAuC. The targeting capability of folic acid conjugated materials to the folate over expressed cells accounted for the increased uptake of FLAuC and PFLAuC in glial cells. From this it can found out

that the nanoparticles were entered into the cell via folate receptor mediated path ways.

PDT efficiency of the final system PFLAuC was assessed at the cellular level using folate over expressed cells using calcein propidium iodide staining to assess the live and dead cells. Cells incubated with PFLAuC and cells were irradiated with laser for 30 S. A batch of cells without PFLAuC also received laser irradiation at same dosage and another batch with PFLAuC and without laser irradiation served as controls (figure 62). As seen from figure 62, cell death is negligible in the case of control cells after 30 S of laser irradiation whereas significant cell death was observed in the cells carrying PFLAuC. This is due to the more uptake of the particle by the cell and its efficacy to form singlet oxygen. The cells incubated with PFLAuC which did not receive laser treatment (figure 62) also showed no cell death. This clearly indicates the laser power used was not sufficient to kill the cells. The cell death mainly occurs due to the generation of singlet oxygen by the particle upon laser exposure. Based on these observations a schematic representation for the entry of the particle and therapy is shown (figure 104).

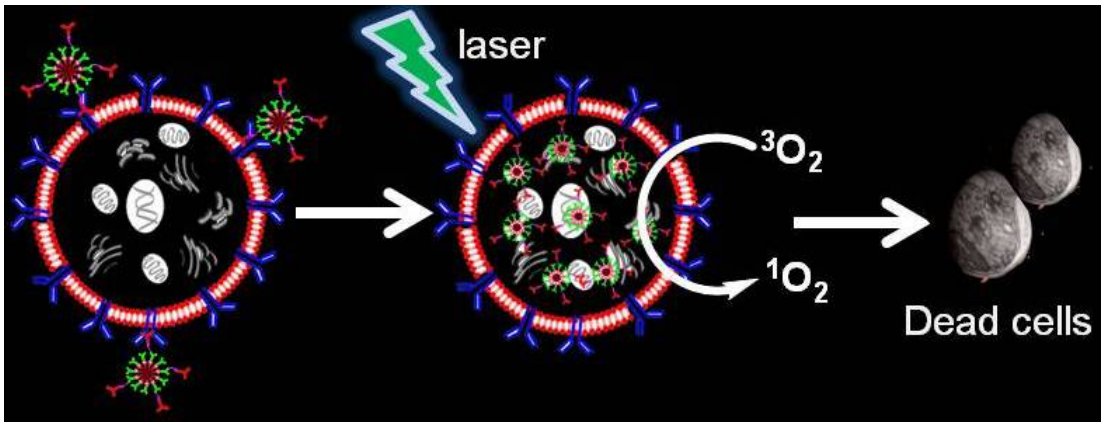

Figure 104: Schematic representation of imaging and PDT efficacy of PFLAuC upon irradiating with 530 nm laser

To demonstrate the in vivo tumor targeting efficacy of the developed materials, the nanoclusters were injected intravenously to tumor bearing mice and imaged under live animal optical imaging system (Xenogen, IVIS). The results (figure 64) show animals injected with LAuC has no signal output from the tumor compared to the other two systems. This is due to the uniform distribution of the material throughout the body in absence of targeting moiety. The lesser quantum yield of LAuC compared to other two systems again restricts the signal, even if there is less amount of particle uptake by the cancer cells. As expected, tumor imaging efficacy is highest for FLAuC which is in agreement with the quantum efficiency of the same compared to other systems.

In order to demonstrate the PDT efficacy of PFLAuC, the animals were irradiated with 532 nm laser (1.5 W) for 15 min after 3 h of injection of the materials. Tumor bearing animals without materials served as control. The effect of treatment was monitored upto 7^{th} day of laser irradiation by measuring the reduction in tumor volume. The therapeutic efficacy was also ascertained using fluorescence spectroscopy by evaluating the collagen level (figure 65), total hemoglobin concentration and redox ratio from the emission of endogenous fluorophores. In the case of PFLAuC treated animals, the tumor volume remained unchanged after 5^{th} day whereas there was considerable increase in the tumor volume among the control animals (figure 65a). On seventh day, the collagen level, ratio of NADH and FAD (redox ratio) and total hemoglobin concentration of the PFLAuC treated animals showed a close similarity to that of normal ones.

Tumor development and treatment efficacy was also confirmed histopathologically on sacrificing the animals on the 7^{th} day ((figure 66). More necrotic cells present in

the test material clearly indicate the cell death in vivo due to the generation of singlet oxygen by PFLAuC.

5.4 NIR Emitting Gold Clusters For Blood Brain Barrier (BBB) Targeted Imaging

5.4.1 BBB Targeting Using Glutathione Stabilized Nano Cluster

We have developed a GAuC with very small size of the order of 0.7 nm and tuned its emission around 750 nm to enable the fluorescence imaging of the particles as they enter the BBB. Gold based nanocarriers dominate over other nanomaterials because of its size tunable optical property and non toxicity. Among the various size and shape of gold nanomaterials, gold clusters have got wide attention in the field of bio imaging due to its inherent fluorescence emission. Recent reports on the use of gold clusters include cell labeling, diagnosis and sensing applications. Little efforts have been made to study the blood brain barrier permeability of gold cluster based fluorescent nanocarriers.

It is reported that glutathione (GSH) enter the brain through a carrier mediated transport and is not susceptible to any further oxidation. The present study is designed to provide a proof of this concept by rationally choosing the GAuC tuned to emit in the NIR region. The key regulatory pathways of BBB in facilitating brain uptake of essential nutrients like amino acids and glucose is utilized for the entry the materials of the study. L- dopa is one of the most common drugs used for the treatment of Parkinson's disease clinically. Specific membrane protein (large neutral amino acid transporter -LAT1) is present on BBB to enable the entry of L dopa to the brain. But in order to increase the bioavailability of L- dopa usually it is

administrated along with carbidopa.

In addition to the GSH cluster, we have also evaluated the effect of L-dopa cluster to understand the difference in the transport mechanism if any on BBB permeability. The effect of both systems have been evaluated on *in vitro* BBB model comprising rat brain endothelial cells and *in vivo* on normal animals whose BBB is expected to be intact.

For BBB permeability studies, L dopa was conjugated to GAuC through EDC- NHS coupling chemistry. A systematic characterization of the materials in terms of their physico chemical properties, blood and cell compatibility have been carried out before the *in vitro* and *in vivo* BBB permeability evaluation. Absorbance spectra (figure 68a) of GAuC and Dop@GAuC show the quantum confinement of both the clusters. L-Dopa conjugated GAuC retained its NIR emission with an additional peak due to the emission of L dopa at 534 nm (figure 68b). Functionalisation of L-Dopa over GAuC was evident from the FT- IR spectroscopy (figure 69). The occurrence of amide band at 1588 cm^{-1} and a shift in the C=O peak is an evidence for the functionalization of L dopa onto the surface of GAuC through an amide bond between GSH and L dopa.

Particle size of GAuC and Dop@GAuC as observed in TEM images ranges from 0.7 to 1.4 nm respectively. Binding energy evaluated using XPS (figure 70) study shows a difference of 1.61 eV and 1.41 eV respectively for the Au $4f_{7/2}$ and Au $4f_{5/2}$ states of GAuC and Dopa@GAuC. This difference in the binding energy (BE) is due to the minor change in the average particle size of Dopa@GAuC .Increase in the particle size is due to the binding of the amine moiety of L-Dopa to either one or

both the carboxylic acid present in GSH. Since the L-Dopa conjugated final system had size in the acceptable range to serve the purpose of this study, further purification on the basis of the different types of bonding has not been attempted.

Cell compatibility (figure 71) of different concentrations of the two materials considered was proven by standard MTT assay in L929 mouse fibroblast cell lines.

For the *in vitro* BBB model, bEnd- 3, mouse brain endothelial cells have been used, as it is accepted that the cerebral endothelial cell layer is the principal site of the BBB in mammals. These cells are demonstrated to have high electrical impedance restricting the entry of even ions to the brain. These cells have been widely accepted as an ideal *in vitro* model for BBB.

In order to prove the *in vitro* BBB permeability of the developed material, brain endothelial cells of mice origin (Bend3 from ATCC) (Guarnieri et al., 2013) were grown on milli cell insert with a pore size of 0.4 μm. Barrier potential of the cells was regularly monitored to ascertain the confluence of the cells and the monolayer formation so that it exactly mimics the BBB. Completely confluent monolayer with barrier potential of the order of 1400 Ω was considered as *in vitro* model for BBB. To the developed BBB model, 1 mg/ mL of GAuC and Dop@GAuC was added, separately. On addition of GAuC and Dop@GAuC, the original barrier potential of c.a~ 1400 Ω dropped to 812 Ω and 982 Ω respectively within 30 min. Later, the potential of the cells regained almost completely within 2-3 h ((figure 72b). The concentration of the materials that crossed the barrier cells and passed out through the insert at different time interval was quantified using UV/ Vis absorbance

spectroscopy. At 3h, 44% of Dop@GAuC crossed the *in vitro* barrier and cleared out from the cells ((figure 72a) where as only 14% of GAuC crossed and cleared out during this time. It took nearly 24 h for 56% of the material to come out in the later case. More than 90% Dop@GAuC crossed the cells in 5h. From this result, it is clear that entry of Dopa@GAuC through the barrier cells and its clearance take place faster than that of GAuC.

The particle uptake efficacy of GAuC and Dop@GAuC by the barrier cells was monitored using fluorescence microscope at 3, 6, 12 and 24 h. (figure 74). Evident from the NIR emission of gold nano cluster, more particles of GAuC remain inside the cell compared to Dop@GAuC. At different time intervals, the uptake efficacies of both the materials are in good agreement with the permeability study (figure 72a). Barrier permeability study is a clear indication of the fact that both the particles are taken up by the cells initially before crosses and comes out. This also indicates that bEnd-3 cells allows the entry of the developed nanoparticles. At 6^{th} h more intense fluorescence of the gold cluster is observed in the case of GAuC where as this is very less in the cells with Dopa@GAuC. This confirms the finding that Dopa@GAuC clears from the BBB cells quickly.

TEM (figure 75a) studies of the cells after 3 h of particle incubation also supports these findings of cell uptake and permeability of b End-3 cell line. At 3 h, more GAuC can be seen inside the cell where as only very few particles of Dop@GAuC are visible. Aggregated particles of Dopa@GAuC that got cleared from the cells during late phase of trans-cytosis is also seen (figure 75a). This is not observed in the case of GAuC where most of the particles are still inside the cell.

Presence of transporters on both luminal and abluminal side of the brain endothelial

cells facilitates the quick intake and clearance of dop@GAuC. But in the case of GAuC, non enzymatic degradation nature of GSH delayed the intake which caused an initial delay in the uptake and clearance. However around 50% of the GAuCs crossed the cells with in 24 h. It is reported that GSH can be transported across the BBB by a saturable and specific mechanism where as L- dopa is transported through large aminoacid transporter pathways. The difference in rate of transport of GAuC and Dop@GAuC through BBB can be attributed to the difference in the internalization by the microvascular endothelial cells.

Based on these observations we hypothesize that the GAuC cluster enters the cell through a carrier mediated glutathione pathway by the activation of γ-glutamyl transpeptidase (Meister, 1973) (Kannan et al., 1990) while Dop@GAuC entres through large amino acid path ways (LAT1), which may be the most promising way these particles would have entered into the cells. The schematic illustration of the entry of the particle in brain through BBB is shown in figure 105.

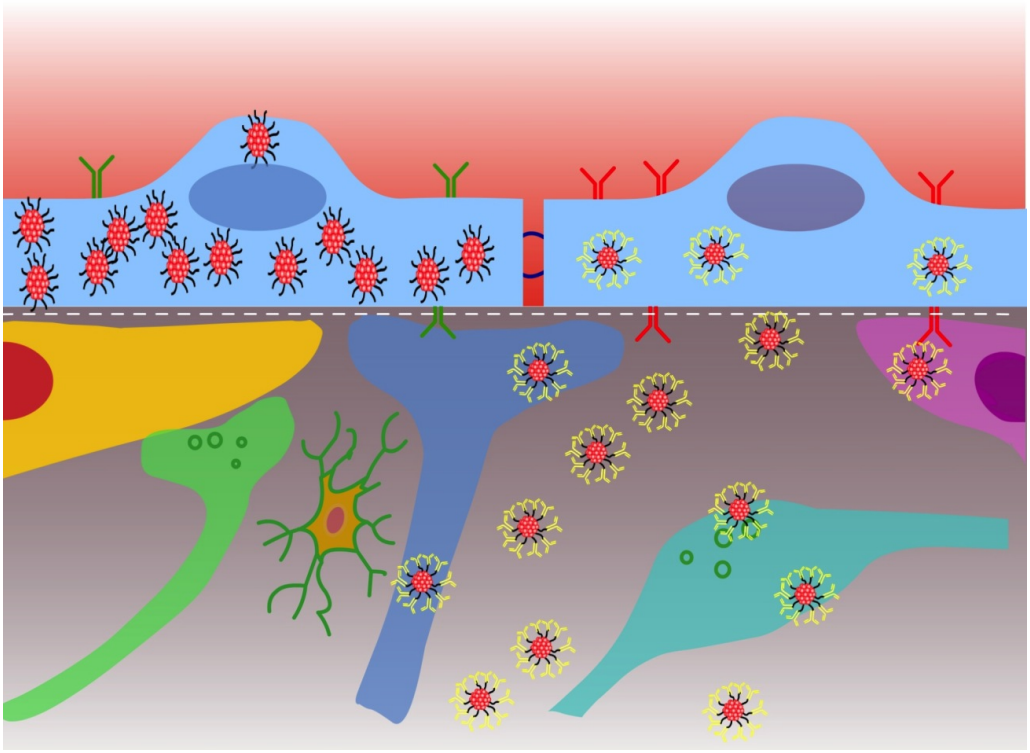

Figure 105: Schematic representation of the entry of GAuC (left) and Dop@GAuC (right) by the BBB cell

Blood compatibility studies indicate that the developed probes are highly blood compatible.

Animal studies again confirm our hypothesis. GAuC and Dop@GAuC were administered intravenously through tail vein at a dose of 1 mg/ mL (0.5 mL). The animals were imaged after 1hr using IVIS spectrum imaging system with 604 nm excitation and 740 nm emission wavelengths. The NIR emission of the gold cluster facilitated imaging of the fluorescence signal from the brain and avoided the auto fluorescence signal from the animal body. Residual autofluorescence was eliminated by spectral unmixing of the image after image acquisition using live image software. The signal intensity of Dopa@GAuC injected animal was more than that of GAuC

injected animal (figure 78a). This implies that the barrier permeability of Dopa@GAuC is more at 1hr.This is in good agreement with the permeability study and the in vitro barrier study where faster uptake and clearance of Dopa@GAuC was observed compared to GAuC. With respect to commercially available NIR emitting dyes, good fluorescence signal could be achieved from the biocompatible material developed in this study, on crossing the BBB. This could be used for the early stage diagnosis of neurological diseases, when the barrier is not disrupted. The fluorescence image of the excised brain after 2 hours also shows inline with the in vivo observation (figure 78b). In the case of GAuC injected mice, the brain shows a weak signal compared to that of Dop@GAuC injected one. Enhanced fluorescence signal from the brain is due to accumulation of more Dopa@GAuC in the short time period by the fast permeability of the same through BBB. (figure 105). Fluorescence microscopic evaluation of the excised brain sections shows fluorescence signal from within the blood vessel due to the delayed entry in the case of GAuC treated animals where as more fluorescence is observed from within the brain in the case of Dop@GAuC due to the fast entry(figure 79) agreeing with other findings.

5.4.2 BBB Targeting Using Lipoic Acid Stabilized Nano Cluster

Similar to GAuC cluster LAuC cluster functionalized with L dopa was also used to target the brain. Functionalization of L dopa over LAuC cluster was confirmed with UV- Vis spectra, fluorescence and FT- IR (figure 81& 82).

LAuC shows a broad absorbance while a peak around 250 nm in Dop@LAuC is a clear indication of L dopa on LAuC. In the fluorescence spectra along with a peak at 720 nm there is a strong fluorescence in the green region with higher intensity than L

dopa. This peak is also an evidence for L dopa. The increase in the fluorescence might be due to the electronic interaction of gold in the green region with L- dopa. Also we observed extremely weaker fluorescence peak of 720 nm this is mainly due to the lesser quantum yield of LAuC in comparison with GAuC. An amide peak in the FT- IR spectra (figure 82) is also a clear indication of Dopa on LAuC in the case of Dop@LAuC.

The average particle diameter of Dop@LAuC remains as that of LAuC. In XPS (figure 83) analysis there is slight decrease in binding energy of 0.29 eV and 0.46 eV for the Au $4f_{7/2}$ and Au $4f_{5/2}$ peaks of LAuC and Dop@LAuC. This difference bindinding energy is due to the increase of distance gold core after functionalizing with L- dopa.

In vitro cell culture studies on L929 mouse fibroblast cells shows that both LAuC and Dop@LAuC are cyto-compatible (figure 84).

Similar to GAuC nano cluster barrier permeability, barrier potential (figure 85) and cellular uptake (figure 86) were carried out. *In vitro* imaging of bEnd3 cells shows that maximum fluorescence signal was observed at 24 h for LAuC whereas Dop@LAuC shows more particles within 3h and reduced the signal thereafter. Similarly the barrier pearmeability measurement in BBB shows that around 50% and 10% of Dop@LAuC and LAuC were crossed the brain endothelial cell within 3h incubation respectively. All these data shows that the brain microvascular endothelial cells uptake LAuC and release very slowly to the brain while Dop@LAuC entered and release faster. The entry of LAuC by the BBB cell is not clear but we believe that this might be some sort of adsorptive transport arise due to smaller size and

charge of LAuC. Entry of Dop@LAuC is fascilitated by LAT1 transporter pathway.

Blood compatibility studies were also carried out and found to be highly blood compatible

In vivo studies shows that similar to GAuC cluster, Dop@LAuC were injected through tail vein. The signal fluorescence signal from the brain clearly demonstrate the brain imaging efficacy of Dop@LAuC in vivo.

5.4.3. Delivery Of Therapeutics Into The Brain

Pilocarpine treated Dop@GAuC was used to demonstrate the delivery efficacy of therapeutics into the brain by the AuCs. Cumulative drug release profile of drug conjugated Dop@GAuC shows a sustained release of drug from the nanocluster. The sustained release of this model drug formulated nanosystem could be an option for the treatment of brain diseases. Sustained release of pilocarpine from pilocarpine treated Dop@GauC is also evident in the in vivo experiment. All the parameters like the activity of animal, salivation, tail stiffness and seizure occurance reflected the slow and steady release of drug in the case of pilocarpine treated Dop@GAuC case compared to pilocarpine alone.

5.5 Hybrid Nanomaterials For Targeted Imaging And Therapy In Vitro

Developed a quantum dot with Cd and Zn (CdSe/ ZnSe) by wet chemical method using cysteine as the stabilizing ligand. The developed quantum dot exhibits a photoluminescence emission around 556 nm (figure 91b). Qd shows an average

particle diameter of 4 nm (figure 92a). Particle size distribution of the Qd using image j software is shown in figure 93a.

Single wall carbon nanotubes were purified and acid functionalized as per the reported procedure. Photothermal destruction of cancer cells has been demonstrated previously using similar SWCNT (Kumar et al., 2013).

Initial attempts to conjugate the two systems resulted in a fluorescence quenching of the Qds by SWCNT. So, before conjugating to Qds, a layer of dimethylformamide (DMF) was introduced onto the surface of SWCNT which acts as a spacer between the two and reduces the fluorescence quenching property. Quantum dots were bound to the COOH moiety of SWCNT through the DMF layer. A plausible mechanism for the formation of combined Quantum dot- single wall carbon nanotube (Qd@CNT) is shown schematically in figure 90. The aquous solubility of Qd@CNT increased tremendously compared to SWCNT due to the presence of hydrophilic quantum dots on the surface of carbon nanotube. Presence of Qd over the surface of SWCNT is clearly evident under the TEM image (figure 92c, d). Crystallinity of the material is evident in the TEM (inset of figure 92) and the elemental composition of FaQd@CNT was checked using TEM- EDX (figure 93b). From EDX it is clear that FaQd@CNT shows the peak for C, Cd, Zn and Se. Broad absorbance of Qd@CNT (figure 91c) again confirms the presence of Qd on SWCNT.

The developed Qd@CNT in water showed emission at 556 nm (figure 91d) whose intensity has been considerably reduced from that of pure Qd. In spite of the presence of DMF spacer between Qd and SWCNT, the observed decrease in fluorescence intensity of Qd indicates the strong bonding between them. Qd was

conjugated to the SWCNT through DMF using DCC and DMAP. In comparison with quantum yield of the developed quantum dot, FaQd@CNT shows 32% of quantum yield. Stability of FaQd@CNT was checked for a period of one month in room temperature and at 4^{o}C. In both the cases the system was found to be stable. Samples were found to be stable for longer time period upon lyophilisation.

In order to prove the cellular targeting efficacy, the developed Qd@CNT system was functionalized with folic acid, whose over expression is established in most of the cancer cells. Folic acid functionalization was confirmed by UV- visible, fluorescence (figure 91) and FT IR (figure 94) spectroscopy. FaQd@CNT showed an absorption peak ca. 250 nm corresponding to the absorption (figure 91e) of folic acid. The amide peak at 1630 cm^{-1} in the FT-IR spectrum also confirms the folic acid binding onto Qd@CNT. The number of moles of folic acid present on FaQd@CNT was quantified using UV spectrometre and it shows value of 0.835x 10^{-5} moles of FA.

Zeta potential measured at various stages of functionalization shows that initial Qd had a zeta potential of -40± 2 mV which changes to -27± 1.5 mV (figure 95) on conjugation with SWCNT. This change in zeta potential is attributed to the binding of amine groups of the cysteine moiety of Qd to the acid group of SWCNT, making it more biocompatible.

Additionally, formation of a hybrid nanostructure has been confirmed using Raman spectra at different stages (figure 96a). The results are consistent with the formation of desired system with functionalized SWCNT, Qd@CNT and FaQd@CNT showing the arial breathing mode around 200 cm^{-1}, and characteristic high frequency G mode and a weak D mode around 1600 and 1300 cm^{-1} respectively. The other peaks are

assigned to the peaks of DMF, reconfirming the presence of bound DMF in the hybrid nano structure.

Photothermal responsiveness of the materials was evaluated using a 800 nm laser at 1.726 W/cm^2 for 4 minutes, and the temperature was measured with an IR thermal camera on equal concentrations of (1 mg/ mL) Qd, SWCNT, Qd@CNT and FaQd@CNT. Significant increase in temperature was observed in the combination materials where SWCNT was incorporated (figure 96b). Corresponding thermal camera photographs are shown in figure 97. In the case of Qd alone, there was no rise in temperature for laser irradiation of upto 4 min.A significant rise in temperature to 90^{o}C was observed in the case of SWCNT on 3 min laser irradiation while in the case of Qd@CNT and FaQd@CNT the temperature rise was 75^{o}C and 67^{o}C respectively. This decrease in temperature compared to SWCNT is due to the presence of quantum dot and folic acid on the surface of SWCNT in Qd@CNT and FaQd@CNT.

Cell viability of the system was tested using MTT assay in mice fibroblast (L929), and two cancerous, viz, breast (MCF7) and pancreatic (Panc1) cell lines. Developed hybrid nanosystems were incubated with the cells for 24 hrs. All the cells showed more than 80% viability for all the concentrations of Qd@CNT and FaQd@CNT (figure 98) eventhough Qd alone showed toxicity at higher concentrations. Toxicity of Qd is mainly due to the observed high zeta potential of the same which is higher than the desired value for the physiological condition (Nel et al., 2009).

Cellular targeting and uptake efficiency of the material was performed on three different cancer cells. The targeting efficacy of Qd@CNT and FaQd@CNT was

proved using different cell lines with and without folate over expression. In the case of human breast cancer cells MCF-7, grown in folic acid enriched DMEM medium, the cellular uptake for FaQd@CNT (figure 99) was more compared to Qd@CNT. The experiment was repeated with the same cells by depleting the folate receptor by growing them in RPMI media without folic acid. The folic acid depletion was done as per the reported procedure by Muhammed et al (Habeeb Muhammed et al., 2010). When the cells were grown in folic acid depleted medium, the uptake of particles was considerably less (figure 100). This is due to the lack of folate receptor on the cell surface which prevented the effective uptake of the particles. Observed difference in the uptake of particles by same cells grown in different conditions clearly indicates the targeting efficacy of the developed material in breast cancer cell lines.

To demonstrate the photothermal therapeutic potential of the developed system, phototoxicity of Qd@CNT and FaQd@CNT was evaluated using 800 nm laser, after 3 hrs of incubation of the particles (1mg/ mL) with the cells. During laser irradiation, variation in the temperature inside the cells was continuously monitored using a thermal camera. After 4 min, the temperature of FaQd@CNT reached 50-60^{o}C where as the observed temperature rise was only upto 37^{o}C in the case of Qd@CNT which remained unchanged even after 10 min of laser irradiation. Cell death was assessed in both cases using calcein propidium iodide stain to assess live and dead cells (figure 101). In the first case a complete cell death was observed, where as the cells with Qd@CNT showed no considerable cell death due to the less uptake of this system leading to a decreased temperature rise which was not sufficient to destroy

the cancer cells. This proves the selective uptake, which leads to efficient targeting and also the therapeutic potential of folate conjugated Qd@CNT hybrid nanosystem. The overall mechanism is shown schematically (figure 106)

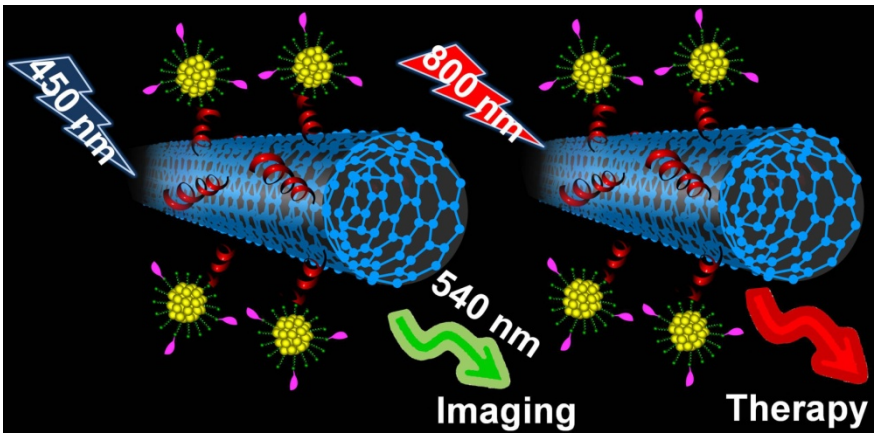

Figure 106: Schematic illustration of imaging and therapeutic efficacy of quantum dot conjugated single wall carbon nanotube.

CHAPTER 6

SUMMARY AND CONCLUSION

This thesis is focused on the use of nanotechnology in the field of disease diagnosis, sensing of bio analyte and targeted distruction of the disease at its early stage using non toxic near infra red emitting fluorescing nanomaterials. It also includes a section on the use of hybrid nanomaterial for in vitro imaging and photothermal therapy.

This chapter of the thesis summarizes the overall findings along with conclusion and future prospects of the present study,

First part of the thesis deals with the development of NIR emitting AuC and its structure property evaluation. For this AuCs ,with distinct fluorescence behavior were developed by etching with GSH for evaluating their structural and physical properties. By the etching of gold nanoparticles with GSH, three different Au_{33} clusters and one Au_8 cluster were prepared with different geometrical arrangement of atoms within the cluster. These clusters having size in the range 0.7 to 2 nm were synthesized by changing reaction temperature from 0^oC to 70^oC and pH between 1.5 and 10. Self assembly of atoms observed in the TEM images of three clusters was explained with the support of MALDI-MS and XPS studies. Solution phase assembly is clearly evident in absorbance spectra by the appearance of SPR band in the visible region. This study demonstrates the role of self assembly of atoms and its arrangement in the characteristic properties of the cluster. Among the developed AuCs, GSH AuC's (GAuC) with 24% quantum yield were selected to estimate urea contents in blood and adulterated milk samples and also to target the brain through

BBB. Similar to GAuC another AuCs made of lipoic acid was also developed in a one step method. The so developed AuCs was found to have 18 core atom having emission in 720 nm with 1% quantum yield.

This part concludes with the finding that reaction conditions like temperature and pH have major responsibility in the cluster formation. The contribution of these factors on the size, number of atoms of the cluster, and the fluorescence properties has been explained. It is found that initial temperature and the reaction temperature plays a crucial role in the self assembly of monolayer protected AuCs where as pH of the reaction determines the number of core atoms and ligands. Based on the results of absorbance, emission properties and MALDI, a probable composition was assigned for all the AuCs studied. A correlation between the number of atoms, fluorescence emission and particle diameter is reported for the first time using GSH stabilized AuCs. With both optical and CT imaging efficacy, these materials have potential applications in multimodal imaging.

The second part demonstrates the use of a nanosensor based on urease enzyme immobilized NIR emitting (λem = 750 nm) gold cluster (Urease@GAuC) for the selective detection of urea in whole blood which is an advantage over the existing clinical method. The blood urea level estimated in whole blood and blood serum using this method was comparable and the data were validated against a currently used clinical method for blood serum. Finally, the generality of the nanosensor is demonstrated by detecting urea in adulterated milk samples. Since the detection is by NIR emission change associated with an enzyme specific conversion of urea leading to a pH induced aggregation of AuC, the method does not interfere with other

analytes. To conclude, NIR emitting GAuC can be used as a selective fluorescent nanosensor for the diagnosis of urea content in blood and milk samples by conjugating them with a specific enzyme, which has significant relevance in human health care and food safety measures. The future prospect of the desired system is the tuning of the AuC as a marker for deadly diseases like cancer, diabetic, cardiac and brain related diseases.

Tumor diagnosis and treatment is achieved by developing a biocompatible LAuC based multifunctional nanosystem for fluorescence imaging directed PDT applications. Even though the fluorescence quantum yield of the LAuC is relatively low when compared to that of Qd or organic fluorophore, the localization of the clusters on tumor cells allowed fluoresce imaging with reasonably good resolution. Singlet oxygen efficiency of PFLAuC is found to be significantly high (80%) when compared to that of the PPIX (63%) alone. The enhanced local concentration of the AuC bound PPIX and better localization of the PFLAuC on tumor cells facilitated the use of very small amount of PPIX (a few micrograms) for considerable cell death with a sufficiently low dose of laser irradiation. 60 μg of PPIX was sufficient to kill 50% of cell population. Moreover, the NIR emission of PFLAuC facilitates real time tracking of the progress of PDT. In vivo study shows that the developed nanocluster is useful for monitoring and effective destruction of tumor cells. The future prospect of the described system is to use it as a suitable therapeutic agent for clinical practice.

BBB targeted brain imaging and drug delivery was demonstrated using GSH and LA stabilized AuCs upon L dopa conjugation. NIR emission of AuCs was retained after

functionalization, enabling optical imaging. Time dependent *in vitro* studies for BBB permeability showed Dopa treated AuC crossed more particle through *in vitro* barrier in 3h compared to AuC alone. The barrier potential remained in the normal level with in 30 min of particle incubation indicating the non disruption of BBB during the crossing of nanosystem. Live animal imaging study showed the particle internalization in the brain. Model drug delivery through BBB was demonstrated by the behavioural changes (like movement, tail stiffness, salivation, general activity etc) of the animal. The future prospect of the described system is to use to identify the molecular/ bio chemical changes of brain in normal versus diseased brain. To study changes in the brain after administration and also to study the effect of drug release in the brain diseased conditions are also comes under the future scope of this study.

In the last part a hybrid nanosystem based on Qd and SWCNT was developed for imaging and targerted PTT. The developed nanosystem addresses most of the issues encountered while using the individual parental systems for similar applications. Importantly, it is found to be more cyto compatible eventhough the parental systems have certain cytotoxic effects when considered individually. Tumor targeting efficacy of the nanosystem is considerably enhanced in folate receptor over expressing cells. To conclude, the quantum dot conjugated single wall carbon nanotube can be used for tumour diagnosis and selective destruction. Future prospect of this study is the development of NIR emiting Qd conjugated SWCNT for in vivo tumor imaging and therapy.

BIBLIOGRAPHY

Abbott N Joan, Rönnbäck Lars, Hansson Elisabeth (2006) Astrocyte-endothelial interactions at the blood-brain barrier. *Nat. Rev. Neurosci.* 7: 41–53.

Abrams MJ, Murrer BA (1993) Metal compounds in therapy and diagnosis. *Science* 261: 725–730.

Alagarasi A (2015) Introduction To Nanomaterials. In *Introd. Nanomater.* National acentre for catalysis research.

Alivisatos AP (1996) Semiconductor Clusters, Nanocrystals, and Quantum Dots. *Science* 271: 933–937.

Apell P, Monreal R, Lundqvist S (1988) Photoluminescence of noble metals. *Phys. Scr.* 38: 174–179.

Ballabh Praveen, Braun Alex, Nedergaard Maiken (2004) The blood–brain barrier: an overview. *Neurobiol. Dis.* 16: 1–13.

Banerjee Sarbajit, Wong Stanislaus S (2003) In Situ Quantum Dot Growth on Multiwalled Carbon Nanotubes. *J. Am. Chem. Soc.* 125: 10342–10350.

Bao Jie, Chen Wei, Liu Taotao, Zhu Yulin, Jin Peiyuan, Wang Leyu, Liu Junfeng, Wei Yongge, Li Yadong (2007) Bifunctional Au-Fe_3O_4 Nanoparticles for Protein Separation. *ACS Nano* 1: 293–298.

Barhoumi H, Maaref A, Rammah M, Martelet C, Jaffrezic-Renault N, Mousty C, Cosnier S, Perez E, Rico-Lattes I (2005) Insulator semiconductor structures coated with biodegradable latexes as encapsulation matrix for urease. *Biosens. Bioelectron.* 20: 2318–2323.

Begley David J, Brightman Milton W (2003) Structural and functional aspects of the blood-brain barrier. In *Pept. Transp. Deliv. Cent. Nerv. Syst.*, ed. Laszlo Prokai, Katalin Prokai-Tatrai, 39–78. Basel

Borst Jan Willem, Visser Antonie JWG (2010) Fluorescence lifetime imaging microscopy in life sciences. *Meas. Sci. Technol.* 21: 102002. doi:10.1088/0957-0233/21/10/102002.

Chattopadhyay Amitabha, Mukherjee Sushmita (1999) Red Edge Excitation Shift of a Deeply Embedded Membrane Probe: Implications in Water Penetration in the Bilayer. *J. Phys. Chem. B* 103: 8180–8185.

Chaudhari Kamalesh, Xavier Paulrajpillai Lourdu, Pradeep Thalappil (2011) Understanding the Evolution of Luminescent Gold Quantum Clusters in Protein Templates. *ACS Nano* 5: 8816–8827.

Chen Mei-Ling, He Ye-Ju, Chen Xu-Wei, Wang Jian-Hua (2012) Quantum Dots Conjugated with Fe_3O_4 -Filled Carbon Nanotubes for Cancer-Targeted Imaging and Magnetically Guided Drug Delivery. *Langmuir* 28: 16469–16476.

Chen Wei-Yu, Lin Ju-Yu, Chen Wei-Jen, Luo Liyang, Wei-Guang Diau Eric, Chen Yu-Chie (2010) Functional gold nanoclusters as antimicrobial agents for antibiotic-resistant bacteria. *Nanomed*. 5: 755–764.

Chen Wenbin, Tu Xijuan, Guo Xiangqun (2009) Fluorescent gold nanoparticles-based fluorescence sensor for Cu^{2+} ions. *Chem. Commun*. 17-36.

Daniel Marie-Christine, Astruc Didier (2004) Gold nanoparticles: assembly, supramolecular chemistry, quantum-size-related properties, and applications toward biology, catalysis, and nanotechnology. *Chem. Rev*. 104: 293–346.

Dickerson E, Dreaden E, Huang X, Elsayed I, Chu H, Pushpanketh S, Mcdonald J, Elsayed M (2008) Gold nanorod assisted near-infrared plasmonic photothermal therapy (PPTT) of squamous cell carcinoma in mice. *Cancer Lett*. 269: 57–66.

Duan Hongwei, Nie Shuming (2007) Etching Colloidal Gold Nanocrystals with Hyperbranched and Multivalent Polymers: A New Route to Fluorescent and Water-Soluble Atomic Clusters. *J. Am. Chem. Soc*. 129: 2412–2413.

Durgadas CV, Sharma CP, Sreenivasan K (2011) Fluorescent gold clusters as nanosensors for copper ions in live cells. *The Analyst* 136: 933–940.

Eustis Susie, El-Sayed Mostafa A (2006) Why gold nanoparticles are more precious than pretty gold: Noble metal surface plasmon resonance and its enhancement of the radiative and nonradiative properties of nanocrystals of different shapes. *Chem. Soc. Rev*. 35: 209.

Fan Hai-Ming, Olivo Malini, Shuter Borys, Yi Jia-Bao, Bhuvaneswari Ramaswamy, Tan Hui-Ru, Xing Gui-Chuan, Ng Cheng-Teng, Liu Lei, Lucky Sasidharan S, Bay Boon-Huat, Ding Jun (2010) Quantum Dot Capped Magnetite Nanorings as High Performance Nanoprobe for Multiphoton Fluorescence and Magnetic Resonance Imaging. *J. Am. Chem. Soc*. 132: 14803–14811.

Fernández-Suárez Marta, Ting Alice Y (2008) Fluorescent probes for super-resolution imaging in living cells. *Nat. Rev. Mol. Cell Biol*. 9: 929–943.

Ferrari Mauro (2005) Cancer nanotechnology: opportunities and challenges. *Nat. Rev. Cancer* 5: 161–171.

Foster Lynn E (2006) Nanotechnology: science, innovation and opportunity. Upper Saddle River, NJ: Prentice Hall.

Frangioni John V (2003) In vivo near-infrared fluorescence imaging. *Curr. Opin. Chem. Biol*. 7: 626–634.

Ghosh Sujit Kumar, Pal Tarasankar (2007) Interparticle Coupling Effect on the Surface Plasmon Resonance of Gold Nanoparticles: From Theory to Applications. *Chem. Rev*. 107: 4797–4862.

Gole Anand, Stone John W, Gemmill William R, zur Loye Hans-Conrad, Murphy Catherine J (2008) Iron Oxide Coated Gold Nanorods: Synthesis, Characterization, and Magnetic Manipulation. *Langmuir* 24: 6232–6237.

Guarnieri Daniela, Falanga Annarita, Muscetti Ornella, Tarallo Rossella, Fusco Sabato, Galdiero Massimiliano, Galdiero Stefania, Netti Paolo A (2013) Shuttle-Mediated Nanoparticle Delivery to the Blood-Brain Barrier. *Small* 9: 853–862.

Habeeb Muhammed Madathumpady Abubaker, Ramesh Subramani, Sinha Sudarson Sekhar, Pal Samir Kumar, Pradeep Thalappil (2008) Two distinct fluorescent quantum clusters of gold starting from metallic nanoparticles by pH-dependent ligand etching. *Nano Res*. 1: 333–340.

Habeeb Muhammed Madathumpady Abubaker, Verma Pramod Kumar, Pal Samir Kumar, Retnakumari Archana, Koyakutty Manzoor, Nair Shantikumar, Pradeep Thalappil (2010) Luminescent Quantum Clusters of Gold in Bulk by Albumin-Induced Core Etching of Nanoparticles: Metal Ion Sensing, Metal-Enhanced Luminescence, and Biolabeling. *Chem. - Eur. J*. 16: 10103–10112.

Hawkins Brian T, Davis Thomas P (2005) The blood-brain barrier/neurovascular unit in health and disease. *Pharmacol. Rev*. 57: 173–185.

Hostetler Michael J, Wingate Julia E, Zhong Chuan-Jian, Harris Jay E, Vachet Richard W, Clark Michael R, Londono J David, Green Stephen J, Stokes Jennifer J, Wignall George D, Glish Gary L, Porter Marc D, Evans Neal D, Murray Royce W (1998) Alkanethiolate Gold Cluster Molecules with Core Diameters from 1.5 to 5.2 nm: Core and Monolayer Properties as a Function of Core Size. *Langmuir* 14: 17–30.

Huang Chih-Ching, Chen Chao-Tsen, Shiang Yen-Chun, Lin Zong-Hong, Chang Huan-Tsung (2009a) Synthesis of Fluorescent Carbohydrate-Protected Au Nanodots for Detection of Concanavalin A and *Escherichia coli*. *Anal. Chem*. 81: 875–882.

Huang Chih-Ching, Chiang Cheng-Kang, Lin Zong-Hong, Lee Kun-Hong, Chang Huan-Tsung (2008a) Bioconjugated Gold Nanodots and Nanoparticles for Protein Assays Based on Photoluminescence Quenching. *Anal. Chem*. 80: 1497–1504.

Huang Chih-Ching, Liao Hao-Ying, Shiang Yen-Chun, Lin Zong-Hong, Yang Zusing, Chang Huan-Tsung (2009b) Synthesis of wavelength-tunable luminescent gold and gold/silver nanodots. *J Mater Chem* 19: 755–759.

Huang Chih-Ching, Yang Zusing, Lee Kun-Hong, Chang Huan-Tsung (2007) Synthesis of Highly Fluorescent Gold Nanoparticles for Sensing Mercury(II). *Angew. Chem. Int. Ed*. 46: 6824–6828.

Huang Peng, Lin Jing, Wang Shouju, Zhou Zhijun, Li Zhiming, Wang Zhe, Zhang Chunlei, Yue Xuyi, Niu Gang, Yang Min, Cui Daxiang, Chen Xiaoyuan (2013)

Photosensitizer-conjugated silica-coated gold nanoclusters for fluorescence imaging-guided photodynamic therapy. *Biomaterials* 34: 4643–4654.

Huang Xiaohua, Jain Prashant K, El-Sayed Ivan H, El-Sayed Mostafa A (2008b) Plasmonic photothermal therapy (PPTT) using gold nanoparticles. *Lasers Med. Sci.* 23: 217–228.

Huang Xin, Luo Yi, Li Zhen, Li Buyi, Zhang Hui, Li Luo, Majeed Irfan, Zou Ping, Tan Bien (2011) Biolabeling Hematopoietic System Cells Using Near-Infrared Fluorescent Gold Nanoclusters. *J. Phys. Chem. C* 115: 16753–16763.

Jang Boseung, Park Jin-Young, Tung Ching-Hsuan, Kim In-Hoo, Choi Yongdoo (2011) Gold Nanorod–Photosensitizer Complex for Near-Infrared Fluorescence Imaging and Photodynamic/Photothermal Therapy *In Vivo*. *ACS Nano* 5: 1086–1094.

Jia Nengqin, Lian Qiong, Shen Hebei, Wang Chen, Li Xingyu, Yang Zhongnan (2007) Intracellular Delivery of Quantum Dots Tagged Antisense Oligodeoxynucleotides by Functionalized Multiwalled Carbon Nanotubes. *Nano Lett.* 7: 2976–2980.

Kannan R, Kuhlenkamp JF, Jeandidier E, Trinh H, Ookhtens M, Kaplowitz N (1990) Evidence for carrier-mediated transport of glutathione across the blood-brain barrier in the rat. *J. Clin. Invest.* 85: 2009–2013.

Katz Eugenii, Willner Itamar (2004) Integrated Nanoparticle-Biomolecule Hybrid Systems: Synthesis, Properties, and Applications. *Angew. Chem. Int. Ed.* 43: 6042–6108.

Khandelia Rumi, Bhandari Satyapriya, Pan Uday Narayan, Ghosh Siddhartha Sankar, Chattopadhyay Arun (2015) Gold Nanocluster Embedded Albumin Nanoparticles for Two-Photon Imaging of Cancer Cells Accompanying Drug Delivery. *Small*: doi:10.1002/smll.201500216.

Kulakovich Olga, Strekal Natalya, Yaroshevich Alexandr, Maskevich Sergey, Gaponenko Sergey, Nabiev Igor, Woggon Ulrike, Artemyev Mikhail (2002) Enhanced Luminescence of CdSe Quantum Dots on Gold Colloids. *Nano Lett.* 2: 1449–1452.

Kumar Sakthi, Hasumura Takashi, Nagaoka Yutaka, Yoshida, Maekawa Toru, Jeymohan Prashanti (2013) Accelerated killing of cancer cells using a multifunctional single-walled carbon nanotube-based system for targeted drug delivery in combination with photothermal therapy. *Int. J. Nanomedicine*: 2653. doi:10.2147/IJN.S46054.

Lee Dongil, Donkers Robert L, Wang Gangli, Harper Amanda S, Murray Royce W (2004) Electrochemistry and optical absorbance and luminescence of molecule-like Au38 nanoparticles. *J. Am. Chem. Soc.* 126: 6193–6199.

Lévy Raphaël, Shaheen Umbreen, Cesbron Yann, Sée Violaine (2010) Gold nanoparticles delivery in mammalian live cells: a critical review. *Nano Rev.* 1. doi:10.3402/nano.v1i0.4889. http://www.nano-reviews.net/index.php/nano/article/view/4889.

Lin Cheng-An J, Yang Ting-Ya, Lee Chih-Hsien, Huang Sherry H, Sperling Ralph A, Zanella Marco, Li Jimmy K, Shen Ji-Lin, Wang Hsueh-Hsiao, Yeh Hung-I, Parak Wolfgang J, Chang Walter H (2009) Synthesis, Characterization, and Bioconjugation of Fluorescent Gold Nanoclusters toward Biological Labeling Applications. *ACS Nano* 3: 395–401.

Lin Shu-Yi, Chen Nai-Tzu, Sum Shu-Pin, Lo Leu-Wei, Yang Chung-Shi (2008) Ligand exchanged photoluminescent gold quantum dots functionalized with leading peptides for nuclear targeting and intracellular imaging. *Chem. Commun*. 4762.

Lin Shu-Yi, Chen Nai-Tzu, Sun Shu-Pin, Chang Jerry C, Wang Yu-Chao, Yang Chung-Shi, Lo Leu-Wei (2010) The Protease-Mediated Nucleus Shuttles of Subnanometer Gold Quantum Dots for Real-Time Monitoring of Apoptotic Cell Death. *J. Am. Chem. Soc*. 132: 8309–8315.

Link Stephan, El-Sayed Mostafa A (2003) Optical Properties and Ultrafast Dynamics of Metallic Nanocrystals. *Annu. Rev. Phys. Chem*. 54: 331–366.

Liu Chien-Liang, Ho Mei-Lin, Chen Yu-Chun, Hsieh Cheng-Chih, Lin Yi-Chih, Wang Yu-Hsiu, Yang Meng-Ju, Duan Hsin-Sheng, Chen Bo-So, Lee Jyh-Fu, Hsiao Jong-Kai, Chou Pi-Tai (2009) Thiol-Functionalized Gold Nanodots: Two-Photon Absorption Property and Imaging In Vitro. *J. Phys. Chem. C* 113: 21082–21089.

Liu Lihong, Guo Kun, Lu Jia, Venkatraman Subbu S, Luo Dan, Ng Kian Chye, Ling Eng-Ang, Moochhala Shabbir, Yang Yi-Yan (2008) Biologically active core/shell nanoparticles self-assembled from cholesterol-terminated PEG-TAT for drug delivery across the blood-brain barrier. *Biomaterials* 29: 1509–1517.

Liu Yanlan, Ai Kelong, Cheng Xiaoli, Huo Lihua, Lu Lehui (2010) Gold-Nanocluster-Based Fluorescent Sensors for Highly Sensitive and Selective Detection of Cyanide in Water. *Adv. Funct. Mater*. 20: 951–956.

Lockman PR, Mumper RJ, Khan MA, Allen DD (2002) Nanoparticle Technology for Drug Delivery Across the Blood-Brain Barrier. *Drug Dev. Ind. Pharm*. 28: 1–13.

Luo Xiliang, Morrin Aoife, Killard Anthony J, Smyth Malcolm R (2006) Application of Nanoparticles in Electrochemical Sensors and Biosensors. *Electroanalysis* 18: 319–326. doi:10.1002/elan.200503415.

Meister A (1973) On the Enzymology of Amino Acid Transport. *Science* 180: 33–39.

Mohamed Mona B, Volkov Victor, Link Stephan, El-Sayed Mostafa A (2000) The `lightning' gold nanorods: fluorescence enhancement of over a million compared to the gold metal. *Chem. Phys. Lett*. 317: 517–523.

Mooradian A (1969) Photoluminescence of Metals. *Phys. Rev. Lett*. 22: 185–187.

Muhammed MA Habeeb, Pradeep Thalappil (2010) Luminescent Quantum Clusters of Gold as Bio-Labels. In *Adv. Fluoresc. Report. Chem. Biol. II*, ed. Alexander P. Demchenko, 9333–353. Berlin, Heidelberg: Springer Berlin Heidelberg.

Muhammed Madathumpady Abubaker Habeeb, Verma Pramod Kumar, Pal Samir Kumar, Kumar RC Arun, Paul Soumya, Omkumar Ramakrishnapillai Vyomakesannair, Pradeep Thalappil (2009) Bright, NIR-emitting Au23 from Au25: characterization and applications including biolabeling. *Chem. - Eur. J.* 15: 10110–10120.

Negishi Yuichi, Nakazaki Tafu, Malola Sami, Takano Shinjiro, Niihori Yoshiki, Kurashige Wataru, Yamazoe Seiji, Tsukuda Tatsuya, Häkkinen Hannu (2015) A Critical Size for Emergence of Nonbulk Electronic and Geometric Structures in Dodecanethiolate-Protected Au Clusters. *J. Am. Chem. Soc.* 137: 1206–1212.

Negishi Yuichi, Nobusada Katsuyuki, Tsukuda Tatsuya (2005) Glutathione-Protected Gold Clusters Revisited: Bridging the Gap between Gold(I)–Thiolate Complexes and Thiolate-Protected Gold Nanocrystals. *J. Am. Chem. Soc.* 127: 5261–5270.

Negishi Yuichi, Takasugi Yoshimitsu, Sato Seiichi, Yao Hiroshi, Kimura Keisaku, Tsukuda Tatsuya (2004) Magic-Numbered Au $_n$ Clusters Protected by Glutathione Monolayers (n = 18, 21, 25, 28, 32, 39): Isolation and Spectroscopic Characterization. *J. Am. Chem. Soc.* 126: 6518–6519.

Nel Andre E, Mädler Lutz, Velegol Darrell, Xia Tian, Hoek Eric MV, Somasundaran Ponisseril, Klaessig Fred, Castranova Vince, Thompson Mike (2009) Understanding biophysicochemical interactions at the nano–bio interface. *Nat. Mater.* 8: 543–557.

Oh Eunkeu, Hong Mi-Young, Lee Dohoon, Nam Sung-Hun, Yoon Hyun C, Kim Hak-Sung (2005) Inhibition Assay of Biomolecules based on Fluorescence Resonance Energy Transfer (FRET) between Quantum Dots and Gold Nanoparticles. *J. Am. Chem. Soc.* 127: 3270–3271.

OV Salata (2004) Applications of nanoparticles in biology and medicine. *J. Nanobiotechnology* 2: 1 – 6.

Pahuja Richa, Seth Kavita, Shukla Anshi, Shukla Rajendra Kumar, Bhatnagar Priyanka, Chauhan Lalit Kumar Singh, Saxena Prem Narain, Arun Jharna, Chaudhari Bhushan Pradosh, Patel Devendra Kumar, Singh Sheelendra Pratap, Shukla Rakesh, Khanna Vinay Kumar, Kumar Pradeep, Chaturvedi Rajnish Kumar, Gupta Kailash Chand (2015) Trans-Blood Brain Barrier Delivery of Dopamine-Loaded Nanoparticles Reverses Functional Deficits in Parkinsonian Rats. *ACS Nano* 9: 4850–4871.

Pardridge William M (2012) Drug transport across the blood–brain barrier. *J. Cereb. Blood Flow Metab.* 32: 1959–1972.

Park Ji-Ho, von Maltzahn Geoffrey, Ruoslahti Erkki, Bhatia Sangeeta N, Sailor Michael J (2008) Micellar Hybrid Nanoparticles for Simultaneous Magnetofluorescent Imaging and Drug Delivery. *Angew. Chem. Int. Ed.* 47: 7284–7288.

Peer Dan, Karp Jeffrey M, Hong Seungpyo, Farokhzad Omid C, Margalit Rimona, Langer Robert (2007) Nanocarriers as an emerging platform for cancer therapy. *Nat. Nanotechnol.* 2: 751–760.

Polavarapu Lakshminarayana, Manna Manoj, Xu Qing-Hua (2011) Biocompatible glutathione capped gold clusters as one- and two-photon excitation fluorescence contrast agents for live cells imaging. *Nanoscale* 3: 429–434.

Pons Thomas, Medintz Igor L, Sapsford Kim E, Higashiya Seiichiro, Grimes Amy F, English Doug S, Mattoussi Hedi (2007) On the quenching of semiconductor quantum dot photoluminescence by proximal gold nanoparticles. *Nano Lett*. 7: 3157–3164.

Qian Huifeng, Zhu Manzhou, Wu Zhikun, Jin Rongchao (2012) Quantum Sized Gold Nanoclusters with Atomic Precision. *Acc. Chem. Res*. 45: 1470–1479.

Ramakrishna Guda, Varnavski Oleg, Kim Junhyung, Lee Dongil, Goodson Theodore (2008) Quantum-Sized Gold Clusters as Efficient Two-Photon Absorbers. *J. Am. Chem. Soc*. 130: 5032–5033.

Retnakumari Archana, Setua Sonali, Menon Deepthy, Ravindran Prasanth, Muhammed Habeeb, Pradeep Thalappil, Nair Shantikumar, Koyakutty Manzoor (2010) Molecular-receptor-specific, non-toxic, near-infrared-emitting Au cluster-protein nanoconjugates for targeted cancer imaging. *Nanotechnology* 21: 055103. doi:10.1088/0957-4484/21/5/055103.

Röcker Carlheinz, Pötzl Matthias, Zhang Feng, Parak Wolfgang J, Nienhaus G Ulrich (2009) A quantitative fluorescence study of protein monolayer formation on colloidal nanoparticles. *Nat. Nanotechnol*. 4: 577–580.

Rosi Nathaniel L, Mirkin Chad A (2005) Nanostructures in Biodiagnostics. *Chem. Rev*. 105: 1547–1562.

Roy K, Mao HQ, Huang SK, Leong KW (1999) Oral gene delivery with chitosan--DNA nanoparticles generates immunologic protection in a murine model of peanut allergy. *Nat. Med*. 5: 387–391.

Roy Subhasish, Palui Goutam, Banerjee Arindam (2012) The as-prepared gold cluster-based fluorescent sensor for the selective detection of AsIII ions in aqueous solution. *Nanoscale* 4: 2734.

Sadikovic B, Al-Romaih K, Squire J, Zielenska M (2008) Cause and Consequences of Genetic and Epigenetic Alterations in Human Cancer. *Curr. Genomics* 9: 394–408.

Sanchez Clément, Belleville Philippe, Popall Michael, Nicole Lionel (2011) Applications of advanced hybrid organic–inorganic nanomaterials: from laboratory to market. *Chem. Soc. Rev*. 40: 696. doi:10.1039/c0cs00136h.

Santra Swadeshmukul, Yang Heesun, Stanley Jessie T, Holloway Paul H, Moudgil Brij M, Walter Glenn, Mericle Robert A (2005) Rapid and effective labeling of brain tissue using TAT-conjugated CdS:Mn/ZnS quantum dots. *Chem. Commun. Camb. Engl*. 3144–3146.

Sathe Tushar R, Agrawal Amit, Nie Shuming (2006) Mesoporous Silica Beads Embedded with Semiconductor Quantum Dots and Iron Oxide Nanocrystals: Dual-Function Microcarriers for Optical Encoding and Magnetic Separation. *Anal. Chem.* 78: 5627–5632.

Schaeffer Nicolas, Tan Bien, Dickinson Calum, Rosseinsky Matthew J, Laromaine Anna, McComb David W, Stevens Molly M, Wang Yiqian, Petit Laure, Barentin Catherine, Spiller David G, Cooper Andrew I, Lévy Raphaël (2008) Fluorescent or not? Size-dependent fluorescence switching for polymer-stabilized gold clusters in the 1.1–1.7 nm size range. *Chem. Commun.* 3986.

Shang Li, Azadfar Naghmeh, Stockmar Florian, Send Winfried, Trouillet Vanessa, Bruns Michael, Gerthsen Dagmar, Nienhaus G Ulrich (2011a) One-pot synthesis of near-infrared fluorescent gold clusters for cellular fluorescence lifetime imaging. *Small Weinh. Bergstr. Ger.* 7: 2614–2620.

Shang Li, Dörlich René M, Brandholt Stefan, Schneider Reinhard, Trouillet Vanessa, Bruns Michael, Gerthsen Dagmar, Nienhaus G Ulrich (2011b) Facile preparation of water-soluble fluorescent gold nanoclusters for cellular imaging applications. *Nanoscale* 3: 2009. doi:10.1039/c0nr00947d.

Shang Li, Nienhaus G Ulrich (2012) Gold nanoclusters as novel optical probes for in vitro and in vivo fluorescence imaging. *Biophys. Rev.* 4: 313–322.

Shenhar Roy, Rotello Vincent M (2003) Nanoparticles: Scaffolds and Building Blocks. *Acc. Chem. Res.* 36: 549–561. doi:10.1021/ar020083j.

Shi D, Guo Y, Dong Z, Lian J, Wang W, Liu G, Wang L, Ewing RC (2007) Quantum-Dot-Activated Luminescent Carbon Nanotubes via a Nano Scale Surface Functionalization forin vivo Imaging. *Adv. Mater.* 19: 4033–4037. doi:10.1002/adma.200700035.

Shi Jinjun, Zhu Yongfa, Zhang Xinrong, Baeyens Willy RG, García-Campaña Ana M (2004) Recent developments in nanomaterial optical sensors. *TrAC Trends Anal. Chem.* 23: 351–360.

Shibu Edakkattuparambil Sidharth, Pradeep Thalappil (2011) Quantum Clusters in Cavities: Trapped Au_{15} in Cyclodextrins. *Chem. Mater.* 23: 989–999.

Shrivastava Siddhartha, Dash Debabrata (2009) Applying Nanotechnology to Human Health: Revolution in Biomedical Sciences. *J. Nanotechnol.* 2009: 1–14.

Silva Gabriel A (2008) Nanotechnology approaches to crossing the blood-brain barrier and drug delivery to the CNS. *BMC Neurosci.* 9: S4. doi:10.1186/1471-2202-9-S3-S4.

Srivastava Rajesh K, Srivastava Saurabh, Narayanan Tharangattu N, Mahlotra Bansi D, Vajtai Robert, Ajayan Pulickel M, Srivastava Anchal (2012) Functionalized Multilayered Graphene Platform for Urea Sensor. *ACS Nano* 6: 168–175.

Sudeep PK, Joseph ST Shibu, Thomas K George (2005) Selective detection of cysteine and glutathione using gold nanorods. *J. Am. Chem. Soc.* 127: 6516–6517.

Sun Cuiji, Yang Hui, Yuan Yi, Tian Xin, Wang Liming, Guo Yi, Xu Li, Lei Jianlin, Gao Ning, Anderson Gregory J, Liang Xing-Jie, Chen Chunying, Zhao Yuliang, Nie Guangjun (2011) Controlling Assembly of Paired Gold Clusters within Apoferritin Nanoreactor for in Vivo Kidney Targeting and Biomedical Imaging. *J. Am. Chem. Soc.* 133: 8617–8624.

Tanaka Akinori, Takeda Yuitsu, Imamura Masaki, Sato Shigeru (2003) Dynamic final-state effect on the Au 4 f core-level photoemission of dodecanethiolate-passivated Au nanoparticles on graphite substrates. *Phys. Rev. B* 68. doi:10.1103/PhysRevB.68.195415.

Wang Hui, Shen Jing, Li Yingyu, Wei Zengyan, Cao Guixin, Gai Zheng, Hong Kunlun, Banerjee Probal, Zhou Shuiqin (2014) Magnetic iron oxide–fluorescent carbon dots integrated nanoparticles for dual-modal imaging, near-infrared light-responsive drug carrier and photothermal therapy. *Biomater. Sci.* 2: 915. doi:10.1039/c3bm60297d.

Wang Jui H, Tarr Donald A (1955) On the Mechanism of Urease Action. *J. Am. Chem. Soc.* 77: 6205–6206.

Wang Xiaojing, Wang Chao, Cheng Liang, Lee Shuit-Tong, Liu Zhuang (2012) Noble Metal Coated Single-Walled Carbon Nanotubes for Applications in Surface Enhanced Raman Scattering Imaging and Photothermal Therapy. *J. Am. Chem. Soc.* 134: 7414–7422.

Wei Hui, Wang Zidong, Yang Limin, Tian Shiliang, Hou Changjun, Lu Yi (2010) Lysozyme-stabilized gold fluorescent cluster: Synthesis and application as Hg2+ sensor. *The Analyst* 135: 1406.

Weiss Nicolas, Miller Florence, Cazaubon Sylvie, Couraud Pierre-Olivier (2009) The blood-brain barrier in brain homeostasis and neurological diseases. *Biochim. Biophys. Acta BBA - Biomembr.* 1788: 842–857.

Wu Xu, He Xiaoxiao, Wang Kemin, Xie Can, Zhou Bing, Qing Zhihe (2010) Ultrasmall near-infrared gold nanoclusters for tumor fluorescence imaging in vivo. *Nanoscale* 2: 2244. doi:10.1039/c0nr00359j.

Xavier Paulrajpillai Lourdu, Chaudhari Kamalesh, Pradeep Thalappil (2012) Protein-protected luminescent noble metal quantum clusters: an emerging trend in atomic cluster nanoscience. *Nano Rev.* 3. doi:10.3402/nano.v3i0.14767. http://nano-reviews.net/index.php/nano/article/view/14767.

Xavier Paulrajpillai Lourdu, Chaudhari Kamalesh, Verma Pramod Kumar, Pal Samir Kumar, Pradeep Thalappil (2010) Luminescent quantum clusters of gold in transferrin family protein, lactoferrin exhibiting FRET. *Nanoscale* 2: 2769–2776.

Xia Yunsheng, Song Lei, Zhu Changqing (2011) Turn-On and Near-Infrared Fluorescent Sensing for 2,4,6-Trinitrotoluene Based on Hybrid (Gold Nanorod)–(Quantum Dots) Assembly. *Anal. Chem.* 83: 1401–1407.

Xie Jianping, Zheng Yuangang, Ying Jackie Y (2009) Protein-Directed Synthesis of Highly Fluorescent Gold Nanoclusters. *J. Am. Chem. Soc.* 131: 888–889.

Xu Zhichuan, Hou Yanglong, Sun Shouheng (2007) Magnetic Core/Shell Fe_3O_4/Au and Fe_3O_4/Au/Ag Nanoparticles with Tunable Plasmonic Properties. *J. Am. Chem. Soc.* 129: 8698–8699.

Yan Huihui, Wang Lu, Wang Jiyao, Weng Xiaofu, Lei Hao, Wang Xuxia, Jiang Lu, Zhu Jianhua, Lu Weiyue, Wei Xunbin, Li Cong (2012) Two-Order Targeted Brain Tumor Imaging by Using an Optical/Paramagnetic Nanoprobe across the Blood Brain Barrier. *ACS Nano* 6: 410–420.

Yi Dong Kee, Selvan S Tamil, Lee Su Seong, Papaefthymiou Georgia C, Kundaliya Darshan, Ying Jackie Y (2005) Silica-Coated Nanocomposites of Magnetic Nanoparticles and Quantum Dots. *J. Am. Chem. Soc.* 127: 4990–4991.

Yu Junhua, Choi Sungmoon, Richards Chris I, Antoku Yasuko, Dickson Robert M (2008) Live Cell Surface Labeling with Fluorescent Ag Nanocluster Conjugates †. *Photochem. Photobiol.* 84: 1435–1439.

Yuan Xun, Yu Yong, Yao Qiaofeng, Zhang Qingbo, Xie Jianping (2012) Fast Synthesis of Thiolated Au_{25} Nanoclusters via Protection–Deprotection Method. *J. Phys. Chem. Lett.* 3: 2310–2314.

Zandonella Catherine (2003) Cell nanotechnology: The tiny toolkit. *Nature* 423: 10–12.

Zheng Jie, Nicovich Philip R, Dickson Robert M (2007) Highly fluorescent noble-metal quantum dots. *Annu. Rev. Phys. Chem.* 58: 409–431.

Zheng Jie, Zhang Caiwei, Dickson Robert M (2004) Highly Fluorescent, Water-Soluble, Size-Tunable Gold Quantum Dots. *Phys. Rev. Lett.* 93. doi:10.1103/PhysRevLett.93.077402.

Zhou Renjia, Shi Minmin, Chen Xiaoqiang, Wang Mang, Chen Hongzheng (2009) Atomically Monodispersed and Fluorescent Sub-Nanometer Gold Clusters Created by Biomolecule-Assisted Etching of Nanometer-Sized Gold Particles and Rods. *Chem. - Eur. J.* 15: 4944–4951.

List of Publications

International Journals

1. **Lakshmi. V. Nair,** Shaiju S. Nazeer, Ramapurath S. Jayasree , Ayyappanpillai Ajayaghosh, "*Fluorescence Imaging Assisted Photodynamic Therapy Using Photosensitizer-Linked Gold Quantum Clusters"*, ***ACS Nano,*** 2015, *doi: 10.1021/acsnano.5b00406*
2. **Lakshmi. V. Nair** , Yutaka Nagaoka , Toru Maekawa , D. Sakthikumar , Ramapurath. S. Jayasree, *"Quantum Dot Tailored to Single Wall Carbon Nanotubes: A Multifunctional Hybrid Nanoconstruct for Cellular Imaging and Targeted Photothermal Therapy"* **Small,** *10,* No. 14, 2771–2775, *July,* 2014. **(Back Cover Page)**
3. **Lakshmi. V. Nair,** Divys S. Philips, Ramapurath S. Jayasree , Ayyappanpillai Ajayaghosh, " *A near Infrared Fluorescent Nanosensor (AuC@Urease) for the selective detection of blood urea***" Small,** *9,* No. 16, 2673- 2677, *February,* 2013.
4. C.V. Durgadas, **V. Nair Lakshmi**, C.P. Sharma, K. Sreenivasan, *" Sensing of lead ions using glutathione mediated end to end assembled gold nanorod chains***", Sensors and Actuators B,** *156,* No. 2, 791-797, *August*, 2011
5. **V. Nair Lakshmi**, V. Nair Resmi, R. S. Jayasree, "*Role of self assembly in probing the response of size and number of atoms of gold nanocluster in tuning the optical property".* **(Under review)**
6. **V. Nair Lakshmi,** T. Anoopkumar, R. S. Jayasree, "*L dopa mediated transport of NIR emitting gold cluster for blood brain barrier targeted brain Imaging"*. **(Communicated)**

Manuscript under preparation

1. **Lakshmi. V. Nair**, Jayasree. R.S, *"Gold quantum cluster conjugated gold nanorod hybrid nanosystem- An alternate system for imaging and photothermal therapy"*
2. **Lakshmi. V. Nair,** Jayasree. R. S, " *Blood brain barrier targeted brain imaging using L dopa conjugated lipoic acid cluster"*
3. **Lakshmi. V. Nair,** Jayasree. R. S, *"Detection of Endosulfan at Femto Molar Level and its Clearance from Ground Water using Cadmium Selenium Quantum dots"*

Patents

1. *" Method of preparation of urease and gold quantum clusters mediated nanobiosensor for the detection of blood urea and the process involved"* ***(Indian patent no: 1567/ CHE/12)***
2. *"Detection of endosulfan and its clearance from ground water using cadmium selenium quantum dots"****(Applied for Indian patent)***
3. *"Blood brain barrier targeting using L dopa mediated gold quantum clusters"* ***(Applied for Indian patent).***

Conference Presentation

1. **Lakshmi. V. Nair,** Jayasree. R. S , *"Synthesis and Biocompatibility Evaluation of NIR emitting Gold Quantum Clusters"* Indian Analytical Science Congress, Kanniakumari, January 27- 28 **2012** ***(Best Poster Award)***
2. **Lakshmi. V. Nair,** Jayasree. R. S, *"Gold Quantum Cluster as a Biomaterial for Biomedical Imaging and Therapy"* , International Congress on Advances in Human Healthcare Systems ' Healthcare India, Delhi, 21-24 February **2012**
3. **Lakshmi. V. Nair,** Jayasree. R. S, *"Detection of Endosulfan at Femto Molar Level and its Clearance from Ground Water using Cadmium Selenium Quantum dots"* 26th Kerala Science Congress, Pookode, Wayanad from 28th to 31st January **2014** ***(Selected for best paper award category)***
4. **Lakshmi. V. Nair,** Jayasree. R. S, *"Quantum dot functionalized singlewall carbon nanotube for cancer cell imaging and targetted photothermal therapy"* National Conference on Materials Science and Technology , Thiruvananthapuram, July 11-13 **2014** ***(Oral presentation)***
5. **Lakshmi. V. Nair,** Jayasree. R. S, "*Multifunctional Gold nanocluster:An insight into cancer diagnosis and treatment",* Material Research Society of India , Thiruvananthapuram, January 30, **2014** ***(Best Presentation Award).***
6. **Lakshmi V Nair,** Jayasree R S, *"Cancer cell Imaging and Targeted therapy using quantum dot conjugated carbon nanotube"* Indo-Australian Conference on biomaterials, tissue engineering, drug delivery systems and regenerative medicine (BiTERM) , Chennai, February 5-7, **2015** ***(Oral presentation)***

CURRICULAM VITAE

Education

05/2011 – Present: **Ph D Scholar** at Sree Chitra Tirunal Institute for Medical Sciences and Technology, Biomedical Technology Wing,Trivandrum, Kerala, India. Advisor: Dr. R.S Jayasree.

08/2009 – 07/ 2010: **MPhil Student** at Sree Chitra Tirunal Institute for Medical Sciences and Technology, Biomedical Technology Wing, Trivandrum, Kerala, India. Advisor: Dr. K. Sreenivasan.

10/2006 – 10/ 2008: **Masters of Science in Physics**, University of Kerala, India

06/2003 – 06/2006: **Bachelors of Science in Physics**

Professional Experience

09/2010 – 12/2010: **Technical Assistant- Instrument** at Sree chitra Tirunal Institute for Medical Sciences and Technology, Biomedical Technology Wing, Trivandrum, Kerala, India. Location: Dental Product Laboratory